The use of functionalized polymers to make hollow carbon spheres to be used as supports in catalysis

By

Pumza Mente (MSc)

A thesis submitted to the Faculty of Science, University of the Witwatersrand, Johannesburg, in fulfillment of requirements for the Degree of **Doctor of Philosophy in Chemistry**

Supervisor: Prof Neil J. Coville

Co-supervisor: Dr. Roy P. Forbes

Declaration

I declare that this is my work and has never been submitted to any other university. It is being submitted for the Doctor of Philosophy at the University of the Witwatersrand, Johannesburg.

Signature: 

Date: 1 July 2021

Abstract

Metal particle agglomeration is known to be one of the factors responsible for the reduction in catalytic activity (even selectivity) of catalysts when they are supported on carbon. In this study, an approach using functional groups attached to a polymeric support was used to reduce metal catalyst agglomeration. This study reports the functionalization of polystyrene (PS) spheres using poly(acrylic acid) (PAA), poly(ethylene glycol), poly(ethyl cyano acrylate) and poly(methyl methacrylate). Co_xO_y nanoparticles were supported on both PS and the functionalized PS templates (5%, 10%, and 15% Co loading). The Co_xO_y/template composites were coated with resorcinol-formaldehyde (RF). Thermal removal of the templates and annealing of the RF yielded Co_xO_y@HCS materials. The use of functionalized polymer templates allowed small Co particles to be easily transferred from the template to the RF to give Co_xO_y@HCS. The Co_xO_y nanoparticles were also supported outside HCSs to give Co_xO_y/HCSs and their catalytic activity with that of Co_xO_y@HCSs. The synthesized Co_xO_y@HCS and Co_xO_y/HCS materials were evaluated in the oxidation of benzyl alcohol reaction. PXRD studies indicated that the Co oxidation state varied for the different catalysts due to reduction of the Co by the carbon, and a metal oxidation step prior to the benzyl alcohol oxidation enhanced the catalytic activity. The catalytic activity decreased with increasing metal loading, possibly due to pore filling effects. All the catalysts showed similar activity and selectivity towards benzaldehyde formation (70% selectivity at 50% conversion). No poisoning was observed due to product build-up in the HCSs. The catalysts were also evaluated in the hydrogenation of cinnamaldehyde reaction. The hydrogenation of cinnamaldehyde is usually performed in the liquid phase in batch mode. In this study, a vapour phase flow system has been used to evaluate the catalytic activity of both Co_xO_y@HCS and Co_xO_y/HCS. The influence of temperature, hydrogen flow rate and catalyst mass on the hydrogenation reaction was investigated. The products produced by this reaction were hydrocinnamaldehyde, 3-phenyl propanol and cinnamyl alcohol. The data revealed that the Co@HCS showed better activity and product selectivity compared to the Co/HCS. The catalysts with smaller particle sizes (ca. 6 nm) were more efficient than big particles (30 – 40 nm). An increase in reaction temperature (200 – 300°C) resulted in a lower cinnamaldehyde conversion and a poor product selectivity. TPR studies revealed that the Co@HCSs had stronger metal-support interaction than the Co/HCSs catalysts. Catalyst recycling studies revealed that only the Co/HCSs could be regenerated (4 cycles) and post-reaction analysis of the catalysts revealed that this was due to HCS pore blockage and not Co sintering.

Acknowledgements

- I wish to express my sincere appreciation to my supervisor Prof Neil Coville for his abundant support throughout this work. He has been a very understanding supervisor, I have never felt under pressure, he always provided very quick responses to all science-related queries.
- I thank my Co-supervisor Dr. Roy Forbes for his contributions towards the completion of this work.
- I would like to thank all members of the CATMAT research group who attended the weekly research seminars and always gave valuable input. I am grateful to have been part of such a strong research group.
- I will forever be grateful to the following lab-mates who always made being in the lab a very fun session: Dr. Victor Mashindi for being a consistent lab partner who would always show up in the lab at any hour of the day or night. Without these night sessions we could not have completed this work; William Mokone for his positive energy that always motivated me to work, Dr. Tumelo Phaahlamohla for the brains that challenged some of the ideas in this work; and also Kamogelo Modisane, Mamma Sebake, Alice Magubane, Thelma Majola, Yongezile Mhlana, Thuli Buthelezi, Orlette Mkhari and Themba Ntuli.
- This work could not have been completed without the financial support from the National Research Foundation (NRF), the Department of Science and Innovation-NRF Centre of Excellence in Strong Materials (DSI-NRF CoE-SM) and The WITS Postgraduate Merit Award.
- The microscopy analysis of samples reported in this work was conducted at the WITS Microscopy and Microanalysis Unit. I am grateful to this facility and its staff members.
- I am grateful for the support and patience of my family, particularly my mother, Noxolo Mente and my grandmother Nokhaya Mente for their love and support throughout the years of my study.
- I am grateful for the moral support from my friends: Ndivhuwo Shumbula, Sinaye Mtimba and Sendibityosi Gandidzwanwa.

Publications, Awards, Presentations and workshops

Publications related to this work

- **Pumza Mente**, Tumelo N. Phaahlamohlaka, Victor Mashindi and Neil J. Coville, Polystyrene-b-poly(acrylic acid) nanospheres for the synthesis of size-controlled cobalt nanoparticles encapsulated inside hollow carbon spheres, ***J. Mater, Sci*. (2021),** 56, 2113-2128. DOI: 10.1007/s10853-020-05323-w.
- **Pumza Mente**, Victor Mashindi, Tumelo N. Phaahlamohlaka, Thabo Monyatsi, Roy P. Forbes and Neil J. Coville, The oxidation of benzyl alcohol using cobalt oxide supported inside and outside hollow carbon spheres. ***(Accepted Manuscript, ChemistryOpen, 2021).***
- **Pumza Mente**, Victor Mashindi, Alice Magubane, Tumelo N. Phaahlamohlaka, Prakash M. Gangatharan, Roy P. Forbes and Neil J. Coville, The hydrogenation of cinnamaldehyde using cobalt nanoparticles supported inside and outside hollow carbon spheres. **(*Submitted to Can. J. Chem)*.**

Publications arising from collaborations

- Victor Mashindi, **Pumza Mente**, Tumelo N. Phaahlamohlaka, Ofentse Makgae, Roy Forbes, Kenneth I. Ozoemena, Pieter B. Levecque and Neil J. Coville, Platinum supported on pristine and nitrogen doped bowl-like broken hollow carbon spheres as oxygen reduction catalysts, ***J. Appl. Elctrochem. (2021)*** https://doi.org/10.1007/s10800-021-01554-0
- Alice Magubane, Prakash M. Gangatharan, **Pumza Mente**, Tumelo Phaahlamohlaka, Manoko S. Maubane-Nkadimeng, Michael Lee, Jacques O'Connell and Neil J. Coville, Hydrogenation of cinnamaldehyde using carbon dots reduced palladium nanoparticles. ***(Prepared Manuscript)***

Awards

- **2019:** NRF travel grant
- **2018:** Poster award (1st place) from the Microscopy Society of Southern Africa (MSSA).
- **2017 – 2021:** NRF Postgraduate Scholarship

- **2018 – 2021:** Postgraduate Merit Award from WITS university

Presentations

- **Research Poster Presentation**, 14th International Conference on Materials Chemistry, Birmingham, United Kingdom **(2019)**
- **Research Poster Presentation**, 29th Annual Conference of the Catalysis Society of South Africa (CATSA), Western Cape, South Africa **(2019)**
- **Research Poster Presentation**, DST-NRF Centre of Excellence in Strong Materials (CoE-SM) Student Presentation Workshop, WITS University **(2019)**
- **Research Oral Presentation**, 29th Annual Conference of the Catalysis Society of South Africa (CATSA), Limpopo, South Africa **(2018)**
- **Research Poster Presentation** (1st place), 2018 Microscopy in Materials Science Workshop, Microscopy Society of Southern Africa (MSSA), Johannesburg, South Africa **(2018)**
- **Science Slam Talk/ Presentation**, Wits National Science Week, WITS University **(2018)**
- **Research Poster Presentation**, 28th Annual Conference of the Catalysis Society of South Africa (CATSA), North West, South Africa **(2017)**

Workshops

- **Attendance**, Chromatography Training Workshop: Capillary GC for the 21st Century, Johannesburg, South Africa **(2019)**
- **Attendance**, 2018 Microscopy in Materials Science Workshop, Microscopy Society of Southern Africa (MSSA), Johannesburg, South Africa **(2018)**

Table of Contents

Table of Contents

List of Figures

Chapter 1:

Chapter 3

Chapter 4

Chapter 5

Chapter 6

Chapter 7

Appendix A

Appendix B

Appendix C

Appendix D

Appendix E

List of Tables

Chapter 2

Chapter 3

Chapter 4

Chapter 5

Chapter 6

Chapter 7

Appendix A

Appendix B

Appendix D

Appendix E

List of Abbreviations

Abbreviation	Description
UNESCO	United Nations Educational, Scientific and Cultural Organization
SDGS	Sustainable development goals
HCSs	Hollow Carbon Spheres
PS	Polystyrene
PE	Polyethylene
PP	Polypropylene
RESS	Rapid Expansion Supercritical Solution
RESSOLV	Rapid Expansion Supercritical Solution into the Liquid Solvent
PMA	Poly(methacrylic acid)
PESA	Poly(ethylene sulfonic acid)
PVAm	Poly(vinyl amine)
PEI	Polyethyleneimine
PVA	Poly(vinyl alcohol)
PEO	Poly(ethylene oxide)
PVP	Poly(vinyl pyrrolidone)
PEG	Poly(ethylene glycol)
PEO-b-PB	Poly(ethylene oxide)-block-polybutadiene
PS-b-PB-b-PMMA	Polystyrene-block-polybutadiene-block-poly(methyl methacrylate)
PEO-b-PBO	Poly(ethylene oxide)-block-poly(butylene oxide)
PHA	Poly(hydroxamic acid)
RF	Resorcinol Formaldehyde
PANi	Polyaniline
PPy	Polypyrrole
PAA	Poly(acrylic acid)
PDDA	Poly(dimethyl diallyl ammonium chloride)
3AP-F	3-aminophenol formaldehyde
CTAB	Cetyltrimethylammonium bromide
CTAT	Cetyltrimethylammonium tosylate
SDBS	Sodium dodecyl benznesulfonate
TMOS	Tetramethoxysilane
SO	Sodium Oleate
PEO-PPO-PEO	Poly(ethylene oxide)-block-poly(propylene oxide)-block-poly(ethylene oxide)
PDA	Polydopamine
HF	Hydrofluoric acid
CVD	Chemical vapour deposition
PAN	Polyacrylonitrile
FTS	Fischer Tropsch synthesis
NHCSs	Nitrogen-doped hollow carbon spheres
BHCSs	Boron doped hollow carbon spheres
M@HCSs	Metal inside hollow carbon spheres
M/HCSs	Metal outside hollow carbon spheres
PSSs	Polystyrene spheres
PS-b-PAA	Polystyrene-block-poly(acrylic acid)
FTIR	Fourier-Transform Infrared Spectroscopy

SEM	Scanning Electron Microscopy
TEM	Transmission Electron Microscopy
PXRD	Powder X-aay Diffraction
ICP-OES	Inductively Coupled Plasma Optical Emission spectroscopy
BET	Brunauer-Emmett-Teller
TPR	Temperature-programmed reduction
TGA	Thermogravimetric analysis
DTA	Derivative thermal analysis
PNIPAAm	Poly(N-Isopropylacrylamide)
PECA	Poly(ethyl cyano acrytate)
AA	Acrylic acid
ID	Internal diameter
ST	Shell thickness
SA	Surface area
MSA	Micropore surface area
PD	Pore diameter
PV	Pore volume
XPS	X-ray Photoelectron Spectroscopy
PS-PMMA	Polystyrene-block-poly(methyl methacrylate)
MMA	Methyl methacrylate
DMF	N,N-dimethyl formamide
BE	Binding energy
GC	Gas chromatogram
FID	Flame ionization detector
CALD	Cinnamaldehyde
HCALD	Hydrocinnamaldehyde
CAL	Cinnamyl alcohol
THF	Tetrahydrofuran

Chapter 1: Introduction

1.1. Background to the study

The scientific study of novel materials is one of the most important fields in science and it promises to make contributions towards the achievement of the UNESCO 17 sustainable development goals (SDGs) [1]. Three of the SDGs deal with the issues of clean water and sanitation, affordable and clean energy, and sustainable industrialization and innovation. Catalysts can play a role in these three goals. Catalysis is one of the areas that have made positive contributions in water treatment methods, evolution of clean energy and sustainable industrial processes. Catalytic reactions have been used for several decades for the industrial preparation of various products such as fine chemicals, pharmaceutical drugs, fuels and other essential consumer products. Catalysis technology accounts for about 60% of industrial processes and 90% of industrial products, while 20-30% of the industrial world is directly dependant on catalysis to produce and manufacture products of some form [2]. Catalysis is also used to tackle environmental problems such as water and air pollution [3]. The demand for novel catalysts is constantly growing and this signifies the importance of the field. Due to this high demand, there is a constant need to improve the available catalysts and develop cheaper, more efficient and more environmentally friendly catalyst materials that can operate under varying reaction conditions. This can be achieved through further research to improve our fundamental understanding of catalyst systems at an atomic level [4].

Catalysis processes can be broadly classified into two categories, which are homogeneous and heterogeneous catalysis. Homogeneous catalysis is the process where the catalyst is in the same phase as the reactants. It typically involves catalysts and reactants that are in the liquid phase. Heterogeneous catalysis refers to a process where the catalyst and the reactants are in different phases. This typically involves the use of a solid catalyst in a reaction involving liquid or gas phase reactants. Heterogeneous catalysis is generally preferred in the industry due to the ease of catalyst recovery, catalyst recyclability and catalyst stability [5]. Heterogeneous catalysis reactions normally occur via a catalytically active metal or metal oxide surface. For an efficient catalytic process, the catalytically active atoms must be exposed to the reaction medium [6]. The number of active atoms can be maximized by having the catalyst in a finely dispersed form to increase the number of atoms that will encounter reactants. However, small catalyst particles normally sinter/agglomerate at elevated temperatures, resulting in the formation of large

particles, which are less catalytically active (Figure 1.1(a)). Thermal sintering occurs mainly because the catalyst particles are in close contact with one another. Therefore, sintering can be minimized if the catalyst particles are well dispersed or isolated, or by metal-support interactions which reduces migration and stabilizes the metal nanoparticles [7] [8]. The latter effect can be achieved by attaching the catalyst to a thermally stable support material as shown in Figure 1.1(b).

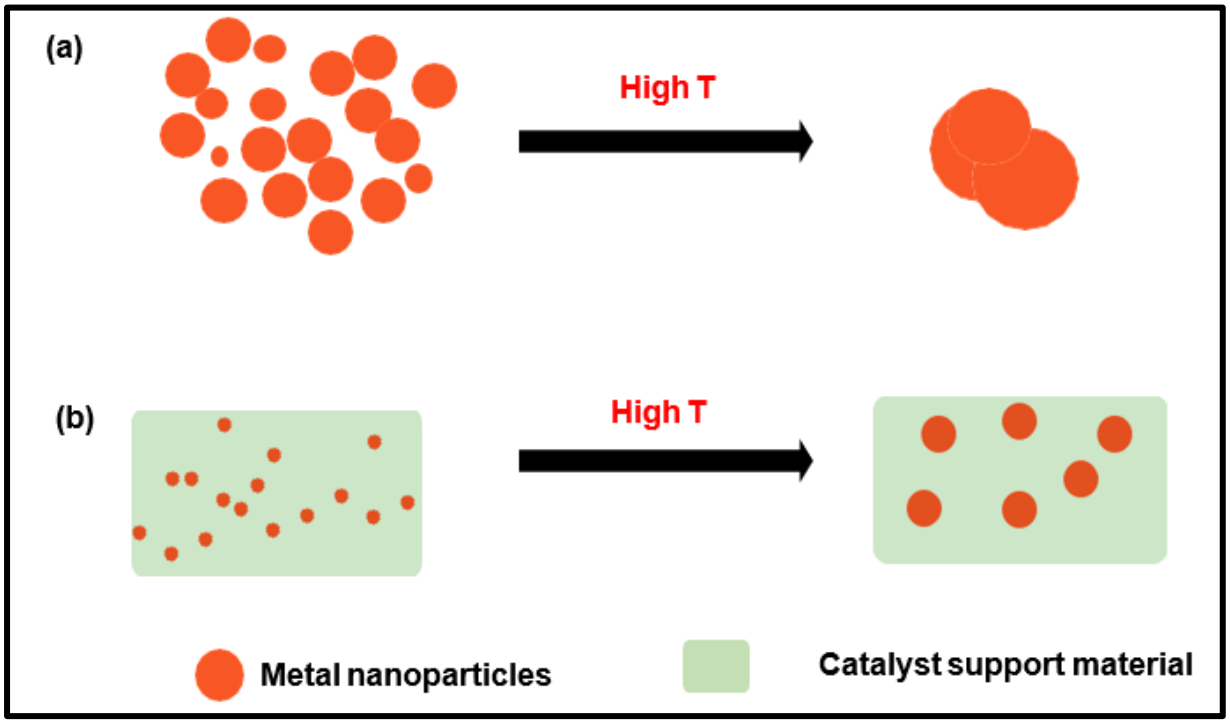

Figure 1.1: Illustration of particle sintering and growth at high reaction temperatures for a non-supported catalyst (a) and a supported catalyst (b).

Supported metal nanoparticles are easier to maintain as uniformly dispersed particles, as opposed to unsupported nanoparticles which may have random shapes with a wide particle size distribution. A high metal dispersion means the particles are highly dispersed on the support material. This is facilitated by the deposition procedures as well as the support material having a high surface area. The choice of the support material is therefore very crucial in catalyst design, as it determines the behaviour, performance, and cost-effectiveness of the catalyst [9].

Catalyst performance and efficiency are evaluated based on their activity, selectivity and stability [10]. The support material is thus one of the more important factors which influence catalytic selectivity and activity [11]. Parameters such as density, hardness, porosity (pore volume, size, and distribution), particle size and shape can also determine the performance of

the support material [12]. An ideal catalyst support material should have corrosion resistance, entail moderate metal-to-support interactions, and have a large surface area, mesoporous structure and ideally, the catalyst should be easy to recover [13]. The material should also be easy to synthesize reproducibly, at relatively low cost using environmentally friendly synthetic conditions. If these criteria are met, catalysts may help further the UNESCO SDGs.

Several catalyst support materials have been reported in literature, including titania, indium oxide, alumina, silica, tungsten oxide, polymer-based and carbon-based supports [13] [14]. The most used industrial catalyst supports are silica, titania and alumina [15]. A large class of carbon-based supports have also been developed and they include nanofibers, nanotubes, spheres, hollow spheres, nanodiamonds, graphene and carbon black [16] [17]. However, metal oxide supports have the disadvantage of forming strong interactions with the metal nanoparticles leading to the formation of metal-support compounds, which are less catalytically active. However, carbon supports are relatively chemically inert, and therefore only moderate metal-to-support interactions are formed when using as a support material [18].

Generally, carbon materials contain useful properties and advantages which make them interesting and preferable over conventional catalyst supports (such as silica and alumina). These include, but are not limited to, availability in various shapes (granules, nanofibers, nanotubes, spheres, pellets), control of polarity and hydrophobicity by chemical modification, easy catalyst recovery made possible by simply heating the carbon material, acid/base resistance and also cost-effectiveness [19] [20]. For reasons to be described in the next sections, this research was focused on using hollow carbon spheres (HCSs) as a catalyst support for cobalt metal catalysts.

1.2. Hollow carbon spheres

A carbon sphere can be described as a spherical carbon material that consists of graphene-like layers arranged to form spherical particles [21]. As seen in Figure 1.2(a), the sphere shown is made of small carbon domains. A hollow carbon sphere (HCS) can be described as a carbon sphere in which the inside region has been removed, to leave behind a thin carbon layer (shell). This can be considered to consist of graphene-like layers, similar to those found in solid carbon spheres but with a hollow core. The diameter, shell thickness and porosity of HCSs can be varied by controlling the synthesis conditions. Figure 2(b) shows a microscopy image of HCSs and the shell thickness and diameter are indicated with red arrows and blue lines, respectively.

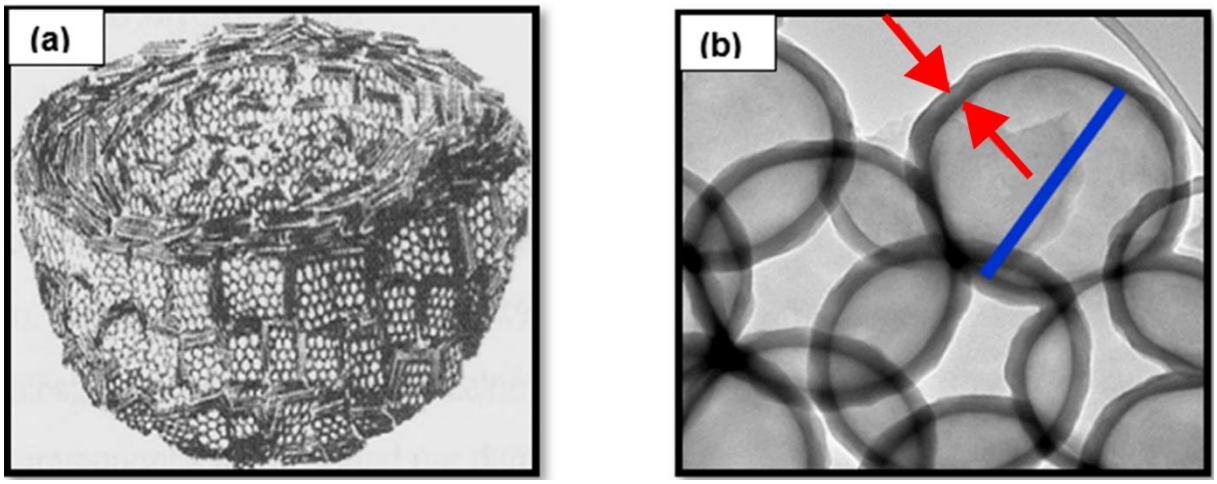

Figure 1. 2: (a) Model showing arrangement of graphene-like sheets forming a carbon sphere [21] and (b) TEM micrograph of HCSs showing their internal hollow diameter (blue line) and carbon shell thickness (red line). [21]

HCSs have found applications in various fields, including catalysis, gas storage, as a template in the synthesis of other hollow spheres, electrode materials for lithium-ion batteries and water purification [22] [23]. They find use in all these different applications because of the unique desirable structural characteristics that they possess. For example, HCSs offer superior properties such as high surface area, low density, a mesoporous shell, uniform particle size, narrow pore size distribution and a relatively high oxidation stability [9] [24]. The carbon shell can be porous such that catalytically active materials can be encapsulated inside and/or outside the HCSs. Catalytically active metals which have been placed inside HCSs include platinum, palladium, rhodium, rhenium, iron, nickel, cobalt, silver, gold as well as some alloys [25].

1.3. Advantages of encapsulating catalyst nanoparticles inside HCSs

Most catalytic reactions occur under harsh conditions such as high temperature and pressure and may occur in the presence of a high potential and acidic/basic pH in the case of electrocatalysis. These conditions promote catalyst sintering and growth through migration of the metal nanoparticles on the surface of the catalyst support, as shown in Figure 1.3. One way to overcome this is by use of HCSs where metal particles present on an isolated HCS are restricted from interacting with metal particles that are in an adjacent HCS. This is depicted in Figure 1.4 which shows how nanoparticles encapsulated inside HCSs are protected within each hollow sphere and cannot interact with nanoparticles in the neighbouring hollow spheres.

Ultimately, this encapsulation reduces the extent of particle interaction and therefore limits sintering and metal particle growth.

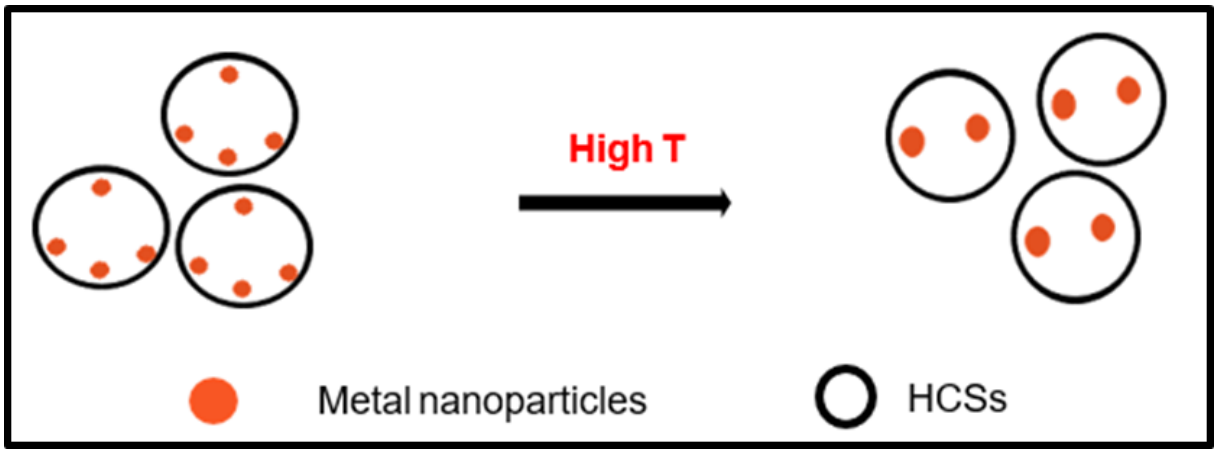

Figure 1.3: Schematic of metal nanoparticles encapsulated inside HCSs.

1.4. Research aim and objectives

This work aimed to control the size of Co nanoparticles encapsulated inside HCSs and evaluate the prepared materials through the achievement of the following objectives:

- Development of a synthesis method for the preparation of polystyrene spheres with surface functional groups.
- Synthesis of Co nanoparticles supported inside HCSs using modified polystyrene spheres.
- The characterization of these materials using various surface and bulk characterization techniques.
- Evaluation of the prepared materials by catalytic oxidation and hydrogenation reactions.
- Comparison of the properties and catalytic activity of the catalysts supported inside HCSs and catalysts supported outside HCSs.

1.5. Thesis outline

Chapter 1 provides the background and objectives of this study.

Chapter 2 is divided into two sections discussing the literature on the preparation of functional polymers and their use to stabilize metal nanoparticles and literature on hollow spheres and catalysis with metal nanoparticles inside and outside HCSs

Chapter 3 reports on studies on the use of polystyrene-*b*-poly (acrylic acid) for the synthesis of Co nanoparticles encapsulated inside HCSs.

Chapter 4 presents the synthesis and characterization of Co nanoparticles encapsulated inside HCSs, prepared with PS nanospheres and PS nanospheres functionalized by coating with poly(acrylic acid), poly(ethylene glycol) and poly(ethyl cyanoacrylate).

Chapter 5 reports on the synthesis and characterization of polystyrene-*b*-poly(methyl methacrylate) nanospheres and their use in the synthesis of Co@HCSs

Chapter 6 discusses the catalytic activity and selectivity of cobalt oxide nanoparticles supported inside and outside HCSs in the oxidation of benzyl alcohol.

Chapter 7 discusses the catalytic activity and selectivity of cobalt oxide nanoparticles supported inside and outside HCSs in the hydrogenation of cinnamaldehyde.

Chapter 8 provides the conclusions and recommendations.

References

[1] "UNESCO and Sustainable Development Goals," United Nations Educational, Scientific and Cultural Organization (UNESCO), [Online]. Available: https://en.unesco.org/sustainabledevelopmentgoals. [Accessed 18 September 2020].

[2] K. Engeblad, J. Rass-Hansen, C. C. Marscden, E. Taarning and C. H. Christensen, "Heterogeneous catalysis for production of value-added chemicals from biomass," in Catalysis, vol. 21, J. J. Spivey and K. M. Dooley, Eds., Royal Society of Chemistry, 2009, pp. 13-50.

[3] C. Descorme, P. Gazellot, C. Geantet and G. Christian, "Heterogenous catalysis: A key tool towards sustainability," ChemCatChem, vol. 4, pp. 1897-1906, 2012.

[4] K. F. Kalz, R. Kraehnert, M. Dvoyashkin, R. Dittmeyer, R. Gläser, U. Krewer, k. Reuter and J.-D. Grunwaldt, "Future challenges in heterogeneous catalysis: Understanding catalysts under dynamic reaction conditions," ChemCatChem, vol. 9, pp. 19-29, 2017.

[5] M. Lombardo and C. Trombini, "Catalysis in non-conventional reaction media," in Eco-friendly synthesis of fine chemicals, R. Ballini, Ed., Royal Society of Chemistry, 2009, pp. 1-79.

[6] T. Valdes-Solis, P. Valle-Vigon, M. Sevilla and A. B. Fuertis, "Encapsulation of nanosized catalysts in the hollow core of a mesoporous carbon capsule," J. Catalysis, vol. 251, pp. 239-243, 2007.

[7] R. Augustine, Heterogeneous catalysis for the synthetic chemist, New York: Marcel Dekker Inc, 1995.

[8] L. Perez, M. R. Axet, D. Yi, P. Serp and K. Soulantica, "Selective hydrogenation of cinnamaldehyde by unsupported and few-layer graphene supported platinum concave nanocubes exposing {110} facets stabilized by long-chain amine," Catalysis Today, 2019.

[9] S. Li, A. Pasc, V. Feirro and A. Celzard, “Hollow carbon spheres, synthesis and applications: a review,” J, Mater. Chem. A, vol. 4, pp. 12686-12713, 2016.
[10] P. S. Lamoureux, K. T. Winther, J. A. Torres, V. Streibel, Z. Meng, M. Bajdich, F. Abild-Pedersen and T. Bliggard, “Machine learning for computational heterogeneous catalysis,” ChemCatChem, vol. 11, pp. 3581-3601, 2019.
[11] L. J. Garces, B. Hincapie, R. Zerger and S. L. Suib, “The effect of temperature and support on the reduction of cobalt oxide: An in-situ X-ray diffraction study,” Journal of Physical Chemistry C, vol. 119, pp. 5484-5490, 2015.
[12] G. Ertl, H. Knozinger and J. weitkamp, Preparation of solid catalysts, Weinheim: Wiley - VCH, 1999.
[13] S. Shama and B. G. Pollet, “Support Materials for PEMFC and DMFC electrolytes - A review,” J. Power Sources, vol. 208, pp. 96-119, 2012.
[14] F. Rodrigues-Reinoso, “The role of carbon materials in heterogeneous catalysis,” Carbon, vol. 36, pp. 159-175, 1998.
[15] D. I. Enache, B. Rebours, M. Roy-Auberger and R. Revel, “In situ XRD study of the influence of thermal treatment on the characteristics and the catalytic properties of cobalt-based Fischer-Tropsch catalysis,” J. Catal, vol. 205, pp. 346-353, 2002.
[16] H. Xiong, M. Moyo, N. K. Rayner, L. L. Jewell, D. G. Billing and N. J. Coville, “Autoreductin and catalytic performance of a cobalt Fischer-Tropsch synthesis catalyst supported on nitrogen-doped carbon spheres,” ChemCatChem., vol. 2, pp. 514-518, 2010.
[17] C. Galeano, J.C. Meier, V. Peinecke, H. Bongard, I. Katsounaros, A. A. Topalov, A. Lu, K. J. J. Mayrhofer and F. Schuth, “Toward highly stable electrocatalyst via nanoparticle pore confinement,” J. Am. Chem. Soc., vol. 134, pp. 20453-20465, 2012.
[18] K. Cheng, V. Subramanian, A. Carvelho, V. V. Ordomsky, Y. Wang and A. Y. Khodakov, “The role of carbon pre-coating for the synthesis of highly efficient cobalt catalysts for Fischer-Tropsch synthesis,” J. Catal., vol. 337, pp. 260-271, 2016.
[19] F. Rodriguez-Reinoso and A. Sepulveda-Escribano, “Chapter 4: Carbon as catalyst support,” in Carbon materials for catalysis, P. Serp and J. L. Figueiredo, Eds., New Jersey, Wiley & Sons Inc, 2009, pp. 131-155.
[20] P. Serp and B. Machado, Nanostructured carbon materials for catalysis, Cambrige: Royal Society of Chemistry, 2015.
[21] M. Wissler, “Graphite and carbon powders for electrochemical applications,” Journal of Power Sources, vol. 156, pp. 142-150, 2006.
[22] F. bottger-Hiller, P. Kampe, G. Cox, A. Panchenko, N. Janssen, A. Petzold, T. Thurn-Albrecht, L. Borchardt, M. Rose, S. Kaskel, C. Georgi, H. Lang and S. Spange, “Twin polymerization at spherical hard templates: An approach to size-adjustable carbon hollow spheres with micro or mesoporous shells,” Angew. Chem. Int. Ed., vol. 52, pp. 6088-6091, 2013.

[23] I. Nongwe, V. Ravat, R. Meijboom and N. J. Coville, “Pt supported nitrogen doped hollow carbon spheres for the catalysed reduction of cinnamaldehyde,” Applied Catalysis A: General, vol. 517, pp. 30-38, 2016.
[24] J. H. Kim, B. Fang, M. Kim and J. Yu, “Hollow spherical carbon with mesoporous shell as a super anode catalyst support in proton exchange membrane fuel cell,” Catalysis Today, vol. 146, pp. 25-30, 2009.
[25] C. Lurhs, J. Philips, M. N. Richard and A. M. Knapp, “Hollow carbon spheres”. United States of America Patent 0215960, 26 August 2010.

Chapter 2: Literature review

2.1. Polymers

2.1.1. Introduction

Polymers are macromolecules containing one or more sets of repeating chemical units joined together by chemical bonds to form a molecule with a chain-like structure. The repeating chemical unit is referred to as a monomer [1] [2]. If there is one set of repeating units, the polymer is referred to as a homopolymer, and when more than one repeating chemical unit is present the polymer is referred to as a copolymer. Both natural and synthetic polymers exist; natural polymers include cellulose, starch, chitosan, gelatin and others [3] [4]. Synthetic polymers include polystyrene (PS), polyethylene (PE), polypropylene (PP), various polyolefins, and others. Synthetic polymers can be synthesized by either step-growth or chain-growth polymerization techniques, which are discussed in the next section [5].

Even though polymers can be synthesized into various sizes (macro, micro and nano), there has been an increased interest in the investigation of polymer nanomaterials. This is due to their promising applications in various fields such as drug delivery [6], optics, catalysis, chemical sensing [7], electrochemistry [8] and environmental technology [9]. Their tunable size, shape and surface functionality extends their application range [10]. Polymer nanomaterials can exist in different shapes such as nanorods, nanofibers, nanotubes, core-shell nanoparticles, hollow nanoparticles and nanospheres which all find suitable applications in various fields [11]. For instance, they have become one of the preferred templates for the synthesis of nanostructures and hollow nanostructures [12] [13]. Most, especially those with surface functional groups, have also become the preferred materials for the adsorption of metal ions and the growth of metal nanoparticles [14] [15].

The synthesis of high purity metal nanoparticles with controlled shape and size and good stability and dispersity has been important for the development and use of catalysts. Several methods have been developed to tune the properties of metal nanoparticles such that they complement the requirements for specific applications. Polymers have shown promise for use the growth and stabilization of metal nanoparticles with controllable size and shape [16]. As a result, the control and tuning of a polymers' properties through surface functional groups has been the subject of many studies. Due to the importance of surface functional groups in the

adsorption and growth of metal nanoparticles, the polymers can sometimes require modification to improve their surface properties.

2.1.2. General synthesis of polymers

Polymerization mechanisms

The types of polymerization mechanisms are classified into addition and condensation polymerization [17], which can also be referred to as chain growth and step-growth polymerization, respectively [18]. They can be defined as follows:

Addition/ chain-growth polymerization occurs in the presence of vinyl monomers (unsaturated molecules). It can be defined as a chain-growth reaction where the polymerization occurs in a chain-like manner with chain propagation and in one direction. It occurs by 3 mechanisms, which are called free-radical, anionic and cationic polymerization reactions. All these mechanisms include 3 steps, namely initiation, propagation and termination. Initiation is the splitting of initiator molecules to form free radicals which then react with the monomer molecules and start to form the polymer chains thus "initiating" the polymeric reaction. Propagation is the continuous addition of the monomer molecules. Termination occurs when two radicals react with each other, and the polymerization process stops [17] [19] [20] [21].

Condensation/ step-growth polymerization occurs in the presence of monomers with two or more functional groups which can form chemical bonds. The polymerization occurs by a step-growth reaction with slow and non-spontaneous chain growth, with the elimination of a small molecule, typically water or methanol. Typical monomers are esters, amides and urethanes [21] [22] [23].

Polymerization techniques

Polymerization techniques can be classified into bulk, solution, slurry, suspension, emulsion and gas polymerization [17] [24]. These techniques are described briefly in Table 2.1

Table 2. 1: Classification of polymerization techniques

No.	Classification of polymerisation synthesis techniques
1	**Bulk polymerization**
	Bulk polymerization is the addition or condensation polymerization of a pure monomer. The reaction mixture only contains the monomer and the initiator (catalyst). The advantage of this process is the formation of a high purity product [25].
2	**Solution polymerization**
	In Solution polymerization, an inert solvent with a boiling point corresponding to the polymerization temperature is used. The product is separated from the solvent at the end of the reaction [17] [26].
3	**Slurry polymerization**
	Slurry polymerization makes use of a catalyst dispersed/dissolved in a solvent in which the monomer is dissolved or in a liquid monomer. The polymer is not soluble in the reaction medium and therefore precipitates as a slurry on the catalyst [17] [27].
4	**Suspension polymerization**
	In suspension polymerization the monomer is dispersed in water, forming small droplets. The polymer then precipitates as small spherical particles in the solution. Protective colloids/ stabilizing agents are used to prevent agglomeration of the particles and to produce uniform particles [24] [28].
5	**Emulsion polymerization**
	Emulsion polymerization involves the dispersion of a monomer in water. An emulsifier (surfactant) is used to create very small droplets of the monomer (smaller than in suspension polymerization). The formed polymer molecules are dispersed and form spherical particles [29].
6	**Gas-phase polymerization**
	Gas-phase polymerization makes use of a gaseous monomer in the presence of a heterogeneous catalyst supported on a material such as silica. The polymer forms on the active sites of the catalyst [30].

2.1.3. Synthesis of polymer spheres

Polymer nanospheres can be synthesized by the dispersion of already synthesized polymers or by direct polymerization of the monomers following the processes illustrated in Scheme 2.1 [9] [31].

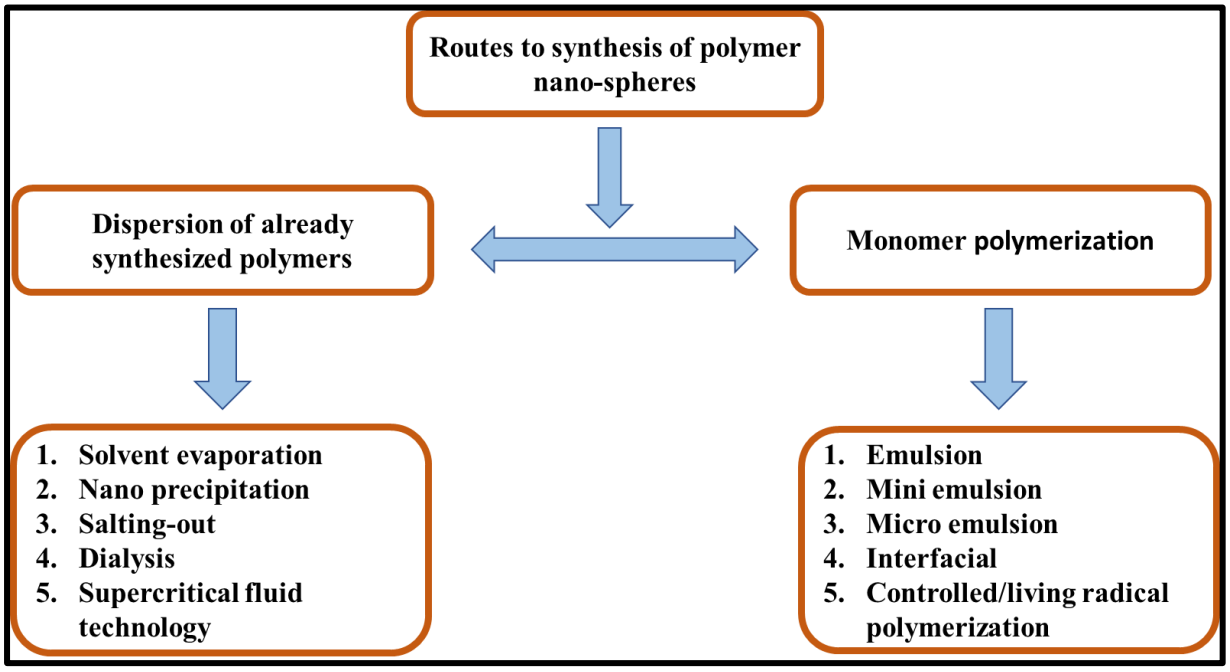

Scheme 2.1: 1Schematic representation of various techniques for the preparation of polymer nanoparticles [9].

Synthesis of polymer spheres by dispersion of pre-synthesized polymers

The different techniques are explained in Table 2.2.

Table 2. 2: Techniques for the preparation of polymer spheres by dispersion of pre-synthesized polymers.

No.	Synthesis techniques
1	**Solvent evaporation**
	During solvent evaporation, a polymer is dissolved in a volatile solvent by ultrasonication or highspeed homogenization to form an emulsion. The solvent is then evaporated at room temperature and/or under reduced pressure. Once the solvent has evaporated, the nanoparticles are formed from the emulsion and collected by ultra-centrifugation or filtration [32] [33].

2	**nanoprecipitation**
	In **nanoprecipitation**, the polymer is dispersed in a water-miscible organic solvent to form a suspension with a polymer precipitate. This suspension is added to water containing a surfactant while stirring. The precipitated polymer nanoparticles deposit on the interface between the water and the organic solvent, forming a colloidal suspension. The nanoparticles can be separated from the suspension by solvent evaporation at room temperature or using a rotavapor followed by centrifugation or freeze-drying [34] [35].
3	**Salting-out**
	Salting-out involves the dissolution of the polymer in an organic solvent such as acetone, which forms an emulsion. This is transferred into an aqueous gel containing a salting-out agent (such as magnesium chloride, calcium chloride, magnesium acetate or sucrose) and a surfactant (e.g., polyvinylpyrrolidone or hydroxyethylcellulose). The acetone diffuses into the aqueous phase, leading to the formation of nanospheres. The nanoparticles are collected by crossflow filtration or centrifugation [9] [31].
4	**Dialysis**
	With **dialysis**, the polymer is dissolved in an organic solvent and placed inside a dialysis tube/membrane. The tube is placed inside a non-solvent which is miscible in the organic solvent. Inside the tube, solvent displacement occurs, causing the polymer to aggregate due to loss of solubility and this leads to the formation of a homogeneous suspension of nanoparticles [9].
5	**Supercritical fluid technology**
	Supercritical fluid technology occurs by two techniques, namely, the rapid expansion of supercritical solution (RESS) and rapid expansion of supercritical solution into the liquid solvent (RESSOLV). In RESS the polymer is dissolved in a supercritical fluid, forming a solution that is subsequently expanded rapidly across a capillary nozzle into ambient air. Supersaturation and rapid reduction in pressure results in homogeneous nucleation, and well-dispersed nanoparticles are then formed. RESSOLV is a modified version of RESS where the supercritical solution is expanded into a liquid solvent instead of ambient air. The RESS produces spheres in the micro- and nano-size range, while RESSOLV produces only nano-sized spheres [9] [36].

Synthesis of polymer spheres by polymerization of monomers

The different techniques are explained on Table 2.3.

Table 2.3: Techniques for the preparation of polymer spheres by polymerization of monomers

No.	Synthesis techniques
1	**Emulsion polymerization**
	Emulsion polymerization is the most widely used method for the synthesis of polymer nanospheres and can be classified as conventional and surfactant-free emulsion polymerization. Conventional emulsion occurs in a mixture of water, monomer (low water solubility), water-soluble initiator and surfactant. The mixture may require an elevated temperature for the polymerization to start. Removal of the surfactant is often challenging in this method. In a surfactant-free emulsion**,** the initiator and monomer are dissolved in a two-phase solution consisting of oil and water phases. The monomer also acts as a surfactant, and well-dispersed polymer spheres are formed. The control of temperature, monomer and initiator concentrations are necessary for controlling the size of the polymer spheres [10] [32] [37].
2	**Mini emulsion**
	Mini emulsion makes use of water, monomer, surfactant, initiator, co-stabilizer and a high-speed device such as an ultra-sonicator to achieve a stable suspension. The co-stabilizer is normally a low-molecular-weight and water-insoluble compound [38].
3	**Micro-emulsion**
	Micro-emulsion produces very small particles and is the most widely used method for the preparation of polymer colloids. A water-soluble initiator is added to a thermodynamically stable microemulsion containing swollen micelles. High quantities of surfactant (~ 10% of total mass) are used to create a very low interfacial tension at the oil/water interface. The particles formed are completely covered in surfactant. Initiation does not occur simultaneously, and therefore the polymer chains only form in some droplets. Ultimately, the small nanoparticles co-exist with empty micelles in the final product [39].
4	**Interfacial polymerization**

	Interfacial polymerization is another widely used method for the preparation of polymer spheres. It occurs in two phases (continuous and dispersed phase) in the presence of two reactive monomers. The reaction takes place at the interface of the two immiscible solvents. The reaction may occur by the addition of an initiator in one of the monomers, or the monomers may initiate a reaction by themselves. For certain cases ultraviolet light may be used to initiate a reaction at the interface between the two phases [40].

2.1.4. Stabilization of metal nanoparticles on functionalized polymers

Functional polymers are used in solutions where they bring a special physical or chemical effect or function. Monomers that can be used to synthesize functional polymers must have specific properties that can result in functional surface properties [41]. These include anionic charged (acidic) monomers, cationic charged (alkaline) monomers, electrically neutral/highly polar monomers and zwitterionic monomers [22]. Most commercial functional polymers are based on homopolymers and copolymers of acrylic acid, vinylpyrrolidone and vinyl acetate monomers. Acrylate and methacrylate monomers are other important examples [16] [22].

Functional polymers can be synthesized through copolymerization, which modifies the chain structure by making use of two or more monomers [17]. The surface properties of polymer particles can also be modified by coating or encapsulation with a preferred functional material. This can modify properties such as surface charge, reactivity, stability and the dispersion of the encapsulated polymer particles [42]. Apart from chemical modifications, engineering the topology and porosity of polymer materials can be achieved by templating and/or molecular imprinting. This creates opportunities with which to control properties such as permeability, mechanical strength, transparency and adsorption capacity [43].

Metal nanoparticles can be stabilized in different ways, which include ligand protection, immobilization on a solid support and stabilization by polymers [44] [45]. Metal ions can be absorbed and converted to metal nanoparticles on the surface of polymers containing surface functional groups [46]. Furthermore, these nanoparticles can adsorb strongly onto the polymer surface through van der Waals forces, causing a reduction in the surface energy of the nanoparticles and consequently prevent their aggregation [47].

Metal nanoparticles with small average diameters and wide particle size distribution have been synthesized using polymers as reducing agents and stabilizers [48]. The polymers used for the synthesis of metal nanoparticles must be dispersible in the solvent and thermally stable at the temperature used for the synthesis of the nanoparticles [49].

Two mechanisms are responsible for the stabilization of metal nanoparticles by polymer materials. These are electrostatic and steric mechanisms and are detailed in the review by Saldias et al. [16]. The types of polymers which can be used as metal stabilizers are polyelectrolytes, non-ionic polymers, and block copolymers [50]. Polyelectrolytes are polymers containing a charged monomer, making the polymer positively or negatively charged. Examples include polyacrylic acid, poly(methacrylic acid) (PMA), poly(ethylene sulfonic acid) (PESA), poly(vinyl amine) (PVAm) and polyethyleneimine (PEI) [51]. These polymers can stabilize metal nanoparticles by electrostatic stabilization [50]. Non-ionic polymers are uncharged polymers that contain polar functional groups. These include poly (vinyl alcohol) (PVA), poly (ethylene oxide) (PEO), poly (vinyl pyrrolidone) (PVP) and poly (ethylene glycol) (PEG) [52]. These polymers can stabilize metal nanoparticles by steric stabilization [50]. Block copolymers are polymers that contain two or more monomers arranged into blocks, where each block represents a homopolymer corresponding to the original monomer [53]. Examples include, PEO-block- polybutadiene (PEO-b-PB), PS-block-PB-block-poly (methyl methacrylate) (PS-b-PB-b-PMMA) and PEO-block-poly (butylene oxide) (PEO-b-PBO) [54]. These polymers can stabilize metal nanoparticles by both steric and electrostatic stabilization [47] [50]. Non-functional polymers such as polystyrene, which do not have surface functional groups can be functionalized to introduce functional groups that can make them suitable also for metal nanoparticle stabilization [42].

Modification of polymer surface properties by copolymerization

Copolymers can be classified as random, alternating, block or graft copolymers depending on how the monomer units are arranged in the polymer chain. Core-corona polymer nanospheres with functional groups can be synthesized by copolymerization of hydrophilic and hydrophobic monomers [55]. The hydrophobic polymer forms the core, while the hydrophilic polymer forms the corona. In a study by Mayer and Mark [56], Pt and Pd nanoparticles with small particle sizes and narrow size distributions were synthesized by reduction with potassium borohydride and stabilization with PS-b-PMAA and PS-b-PEO. PMAA and PEO are hydrophilic, while

polystyrene is hydrophobic. The presence of the hydrophilic polymers introduced functional groups on the PS surface. These functional groups were responsible for the controlled growth of small Pt and Pd nanoparticles. Zhang and co-workers [57] also synthesized functional polymer spheres by modifying the synthesis of PS spheres. This was achieved by using styrene as a major monomer and (vinyl benzyl) trimethylammonium chloride as a functional monomer. This method afforded the synthesis of copolymer spheres with quaternary ammonium groups on the surface. The functional polymer spheres were then used as templates in the synthesis of hollow silica spheres. Removal of the polymer template was achieved by thermal degradation. Sidorov and co-workers [58] prepared Pt, Pd, Rh and Cu nanoparticles stabilized with (PEO-b-PEI) copolymers. They achieved the control of the size and morphology of the nanoparticles in water, through effective control of particle nucleation and growth and obtained small metal nanoparticles (1-12 nm). The combination of the two polymers gave carboxylic and amino functional groups which are known to be responsible for the adsorption of metal ions. Cao and co-workers [59] copolymerized styrene and hydroxamic acid to prepare a PS-poly (hydroxamic acid) (PS-PHA) copolymer. The spherical PS did not have surface functional groups and therefore was not useful in terms of metal adsorption. PHA contained the desired functional groups but could not form spheres. The combination of the two polymers gave a co-polymer that could be synthesized as spheres and contained surface functional groups that were useful for metal adsorption.

Modification of polymer surface properties by chemical treatment

In studies by Yang et al. [60], He et al. [61] and Yuan et al. [62], PS spheres were modified by treatment with concentrated sulfuric acid to obtain sulfonated PS spheres with improved surface polarity and hydrophilicity. These microspheres were then used as templates for the synthesis of various hollow polymer spheres including, polyaniline (PANi), polypyrrole (PPy), PMMA, polyvinyl acetate. Sulfonation of the PS surface was done to allow easy absorbance of the various polymers. The removal of the sulfonated polystyrene template was achieved by washing with water. Wickramaratne and Jaroniec [63] modified the surface of resorcinol-formaldehyde (RF) spheres using cysteine, to introduce -SH, -NH_2 and -OH groups. Au, Ag, Ru, Mn, Gd and Fe nanoparticles were synthesized with diameters of less than 10 nm on the surface of functionalized RF spheres. The size of the nanoparticles was attributed to the presence of chelating functional groups on the surface of the polymer spheres. Han et al. [64]

synthesized small Au nanoparticles (2 - 10 nm) supported on polyaniline nanofibers. A redox reaction between a $AuHCl_4$ salt and PANi gave stable Au nanoparticles with a small diameter. The dispersion of the Au nanoparticles was further improved by using a doping acid (thioglycolic acid). The method could be reproduced for Pt and Ag nanoparticles. Liu et al. [65] prepared acrylonitrile/methyl acrylate copolymer spheres modified with hydroxylamine hydrochloride to introduce amidoxime functional groups. The synthesized polymer spheres were used for the adsorption of various metal ions, including Ag^{+}, Cu^{2+} and Hg^{2+}. The untreated copolymer contained cyano groups, however, they were unable to adsorb the metal ions. The cyano groups were converted to amidoxime groups upon reaction with hydroxylamine hydrochloride. The amidoxime groups generally have a high affinity for metal ions and therefore resulted in good adsorption of the metal ions on the polymer surface. Surface-modified polyacrylonitrile spheres were used for the adsorption of Pb and Cu ions in the research that was carried out by Godjevargova and co-workers [66]. The polymers were modified by chemical treatments with sodium hydroxide, hydroxylamine and hydrazine hydrochloride. These treatments were done to introduce hydrazine, amidoxime and carboxylic groups, which have a high affinity for adsorption of metal ions. Schuetz et al. [67] used an electrostatic layer-by-layer deposition method [68] to coat polystyrene microspheres with layers of polyacrylic acid and poly (allylamine hydrochloride) polyelectrolytes. The coated layers introduced carboxylate and ammonium functional groups on the PS surface. PbS (< 2 nm) and Au (3-4 nm) nanoparticles were synthesized through metal ion adsorption of metal nanoparticles onto the active surface of the polymer spheres followed by precipitation of metal nanoparticles from the adsorbed ions. Yang et al. [69] prepared a spherical polyelectrolyte consisting of a PS core and a poly (acrylic acid) (PAA) shell. This was achieved by photopolymerization of the acrylic acid monomer under UV radiation on the surface of pre-synthesized polystyrene spheres. The carboxylic acid groups introduced by the PAA layer assisted with capturing and immobilization of Ag ions by electrostatic interaction.

2.2. Hollow spheres

2.2.1. Introduction

Hollow structures are materials that consist of a porous shell of a certain thickness, with a hollow void in the center. Macro and nano colloidal hollow structure materials have attracted great attention in various fields including, but not limited to, medicine and materials science [70] [62]. These materials offer unique and superior properties such as low density, large specific surface area, surface permeability and the ability to encapsulate other molecules [13]. Due to their microencapsulation abilities, hollow structured materials can easily be applied in cosmetics, inks, pigment, chemical reagents and to facilitate the controlled release of drugs [71]. These structures have also been used for the encapsulation of small molecules, enzymes and catalytic metal nanoparticles [72]. The methods for the fabrication of hollow structures have been well documented in the literature. Such methods are classified as either template-free synthesis or template synthesis. Template synthesis can be further classified into hard and soft templating [57] [73]. The history and scientific literature of hollow materials are well documented in many reviews [74] [75] [101] [77] [78] [79].

Hollow materials are very important in catalysis and they can function as catalysts or catalyst supports. When used as catalysts they must have a particular composition that allows them to be active for a particular application [74]. For example, hollow Co_3O_4 particles have previously been synthesized and could be used as anode materials in Li-ion batteries [80]. CeO_2 hollow spheres have also been synthesized and used as photocatalysts [81]. When used as catalyst supports, they can be loaded with catalytically active metal nanoparticles. The nanoparticles can be placed on the outside of the shell, the inside of the shell and within the mesoporous shell [101]. When the active catalysts are loaded on the inside of the shell, then the control of the shell thickness and porosity is usually necessary to ensure the effective transportation of reactants and products to and from the active sites. This is usually done by the incorporation of surfactants during shell synthesis [79].

2.2.2. Synthesis of hollow spheres

Template-free synthesis

Template-free synthesis strategies include self-templating, Ostwald ripening and the Kirkendall effect [82] [83] [84] [85].

Ostwald ripening takes advantage of crystallite size variation within the polydisperse crystallites. The smaller crystallites will dissolve and deposit onto the larger particles, leaving hollow voids [74]. An example of a template-free synthesis method by Ostwald ripening was reported by Lou et al. [86]. In a simple one-step synthesis method, hollow SnO_2 spheres were synthesized using a hydrothermal synthesis method in a water-ethanol mixture using potassium stannate trihydrate ($K_2SnO_3.3H_2O$) as a precursor. The mechanism involved the hydrolysis of stannate to form solid SnO_2 spheres. After prolonged hydrothermal treatment, the solid spheres underwent an inside-out Ostwald ripening, forming hollow SnO_2 spheres. A detailed report of this mechanism can be found in a review by Weng et al. [87], for the synthesis of TiO_2, VO_2, MnO_2, Fe_3O_4 and SnO_2 hollow spheres.

The Kirkendall effect takes advantage of the diffusion rate differences in core-shell structures. If the outward diffusion rate (shell to the core) is higher than the inward diffusion rate (core to the shell) small voids are formed leaving a hollow core [74] [88]. One such example was employed by Huang and co-workers in the synthesis of hollow Co_3O_4 nanoparticles (d = 12 nm) using a template-free synthesis strategy that involved calcining solid Co_3O_4 nanoparticles in air at 290 °C [84]. Chu and co-workers [89] also employed this procedure for the synthesis of hollow NiO nanospheres. In their study, pre-synthesized Ni nanoparticles were (12 nm) were calcined in air at 400 and 500 °C. Hollow NiO nanospheres were formed due to the slow inward diffusion of oxygen atoms and faster outward diffusion of Ni atoms which resulted in the formation of hollow voids.

Self-templating approaches usually make use of a material that can act as a solid template as well as a hollow shell precursor [90]. This occurs by the transformation of the solid template into a hollow structure [91]. This transformation can occur by various mechanisms which include surface protected etching, structural difference etching, cationic surfactant-assisted etching, galvanic replacement and dissolution regrowth [82] [83]. The surface-protected etching mechanism was used by Zhang and co-workers [92] for the synthesis of hollow SiO_2 spheres, using PVP as a protecting ligand and NaOH as an etching solution. The carbonyl

groups from PVP could form strong hydrogen bonds with the hydroxyl groups from SiO_2. This resulted in the selective etching of the interior, leaving a hollow void and forming a hollow SiO_2-PVP composite. An example of structural difference etching can be found in a report by Chen et al. [93]. Ren et al. [94] reported on the fabrication of hollow silica spheres by using a cationic surface-assisted etching. A layer of cationic poly (dimethyl diallyl ammonium chloride) (PDDA) was coated on the surface of pre-synthesized SiO_2 spheres. The composite was treated with an ammonia solution, which resulted in the dissolution of SiO_2. The cationic layer interaction with the anionic SiO_2 oligomers resulted in the creation of a hollow void and a shell of PDDA/SiO_2. The hollow PDDA/SiO_2 was calcined at 550 °C to remove the cationic polymer. Examples of the galvanic replacement method can be found in the studies by Yu et al. [95], Falchevskaya et al. [96], and Liu et al. [97]. An example of the dissolution regrowth method was demonstrated by Zhang et al [98] for the synthesis of hollow SiO_2 spheres. The core of the solid SiO_2 spheres (360 nm) stabilized with a PVP surfactant could dissolve in the presence of $NaBH_4$. The dissolved SiO_2 core redeposited on the outer surface of the SiO_2, with the assistance of PVP, to give hollow SiO_2 spheres (330 nm). A self-templating approach for the synthesis of hollow carbon spheres was reported by Qiu et al. [99] using 3-aminophenol-formaldehyde (3AP-F) polymer spheres as a spherical template and carbon source. The synthesized polymer spheres were treated with acetone at room temperature, to remove the interior of the nanospheres. The formed hollow 3AP-F shell was carbonized at 800 ° C to give nitrogen-doped HCSs.

Template synthesis

Soft templating uses micelles and microemulsions formed from surfactant molecules as templates [82]. When surfactants are dispersed in water, they form micelles, and microemulsions when dispersed in water and oil. These micelles can form different structures including rods and spheres, depending on the surfactant concentration [100]. A mesoporous shell of the desired material with a hollow interior is formed simultaneously with the micelle formation in a one-step or one-pot synthesis method [101]. The template can be removed by thermal decomposition, washing with a solvent, and sometimes by evaporation. With this method, it is difficult to control the size of the micelles (soft template) and this, therefore, results in poor size distribution of the hollow particles [82]. Ren et al. [101] prepared TiO_2 hollow microspheres, using decaoxyethylene cetyl ether surfactant as a soft template and

titanium tetrapropoxide (Ti $(OPr)_4$) as a TiO_2 precursor. The TiO_2 precursor was hydrolyzed in a mixture containing ethanol and the surfactant. Hydrothermal treatment of the resulting suspension gave TiO_2 spheres containing the surfactant. The surfactant was removed by Soxhlet extraction in ethanol over a 36 h period. Hollow SiO_2 spheres (60 - 120 nm) were synthesized by Hentze and co-workers [102] using mixtures of cetyltrimethylammonium bromide (CTAB) and sodium perfluorooctanoate and cetyltrimethylammonium tosylate (CTAT) and sodium dodecyl benzenesulfonate (SDBS). These surfactant mixtures could form micelles in water and the addition of tetramethoxysilane (TMOS) as a SiO_2 source under acidic conditions led to the formation of a SiO_2 shell. Their study did not mention how the soft templates were removed after SiO_2 formation. Soft template synthesis of hollow carbon spheres was reported by Wang et al. [103] using a combination of two surfactants, sodium oleate (SO) and PEO-b-poly (propylene oxide)-b-PEO (PEO-PPO-PEO; P123) as a soft template. Hydrothermal synthesis of the carbon source in the presence of the co-surfactants gave hollow polymer spheres, which were ultimately transformed to HCSs upon pyrolysis. The templates were removed during the hydrothermal process, and therefore, no additional step was required for template synthesis.

Hard templating is the most common method and involves the coating of a hard template with a layer(s) of the desired material or its precursor and subsequent removal of the template by calcination or chemical dissolution [71]. This method offers advantages that other methods cannot offer. Such advantages include the control of the shape, size and porosity of the resulting hollow shell [104]. Previously synthesized types of hollow spheres are polymer [105], silica [13], carbon, metal and metal oxides [106]. Hollow silica spheres (HSSs) were synthesized by Yang and co-workers [69] using a PS template functionalized with PAA. It was reported that the carboxylic acid functional groups on the surface of the functionalized polymer spheres interacted with the ammonium ions (catalyst for the sol-gel synthesis of silica). This interaction resulted in the uniform coating of the silica shell on the surface of the spherical polymer. The HSSs were obtained by calcination of the polymer spheres. Wang et al [80] synthesized hollow Co_3O_4 spheres using a hard templating method with carbon microspheres as templates. The reaction parameters such as temperature and solvent composition were varied to synthesize multi-shelled hollow spheres with double-, triple- and quadruple-shelled hollow Co_3O_4 spheres. The synthesized spheres showed superior performance when compared to that of common lithium-ion batteries (LIB's), owing to their microporous multi-shelled structure. The best performance was obtained with the triple-shelled hollow spheres. Liu et al. [107] used

SiO_2 nanospheres for the synthesis of hollow carbon spheres using polydopamine (PDA) as a carbon source. Dopamine was polymerized on the surface of the silica spheres forming a SiO_2@PDA composite. The formed composite was annealed at 800 °C under a N_2(g) atmosphere to form the SiO_2@C. The SiO_2 template was removed by hydrofluoric acid (HF) etching to obtain the HCSs. Another interesting method for the synthesis of HCSs and HSSs was reported by Su and co-workers [108]. SiO_2 spheres were used as a template for the synthesis of HCSs using a chemical vapour deposition (CVD) method and benzene as a carbon source. The dissolution of SiO_2 in HF gave HCSs. The synthesized HCSs were then used as templates in the synthesis of HSSs using the CVD method and $SiCl_4$ as SiO_2 source. Calcination at 700 ° C in air removed the HCSs and produced hollow SiO_2 spheres. The hard templating method is the most effective strategy for the synthesis of hollow carbon spheres (HCSs) as it allows for the easy control of morphology and dispersity of the hollow spheres [79]. As seen above, the other methods are best suited to the synthesis of hollow metals and hollow metal oxides.

Synthesis of the HCS shell during hard template synthesis

The HCSs can be prepared by sol-gel synthesis using polymers as carbon precursors coated on a hard template [109]. They can also be synthesized by chemical vapor deposition (CVD) using hydrocarbon vapors (e.g., toluene, acetylene, methane, benzene, acetonitrile) as a carbon source [108] [110]. The sol-gel process is compatible with both polymer and metal oxide templates. However, the CVD method is usually performed at very high temperatures (> 700 °C) and is therefore not compatible with polymer templates as they decompose at high temperatures. Furthermore, shell porosity control is generally easier with the sol-gel synthesis as opposed to the CVD method; this is because with the sold-gel method the shell, porosity can be manipulated by modification of the precursor used in the synthesis method. For instance, surfactants can be added during synthesis, to introduce pores into the HCS shell [111]. The surfactants usually settle within the shell and are removed during template decomposition, leaving behind pore structures within the hollow shell [112] [113].

Several types of carbon precursors have been proposed, such as polydopamine (PDA) [114]. PDA has the advantage of acting as both a carbon source and a nitrogen source and therefore the method makes it easy to prepare nitrogen-doped HCSs without an additional doping step [114] [115]. Other polymers that can act as both carbon and nitrogen sources include PANi,

polyacrylonitrile (PAN) [109] and 3-aminophenol-formaldehyde [99]. RF is another popular precursor used for carbon synthesis [116]

2.2.3. Catalysis reactions with HCSs decorated with metal nanoparticles

Metal nanoparticles can be supported on the outer surface of HCSs in two ways, (i) by reduction of a metal salt in the presence of HCSs, or (ii) by deposition of pre-synthesized metal nanoparticles on the surface of HCSs. Metal nanoparticles can also be loaded on the inner surface of hollow carbon spheres in two ways, (i) deposition of metal nanoparticles on a hard template (usually a polymer) followed by the synthesis of a carbon precursor on the surface of the template loaded with metal nanoparticles. During carbonization, the template gets removed by thermal decomposition and the metal nanoparticles remain on the inner surface of the hollow carbon spheres. In the other method, (ii) the diffusion of metal ions through the shell of pre-synthesized HCSs and subsequent reduction of the metal ions to form metal nanoparticles inside the HCSs is used. Metal nanoparticles can also be loaded within the shell of the hollow carbon spheres by the simultaneous synthesis of the metal nanoparticles and the carbon precursor on the surface of a hard template [117] [118].

Metal-decorated HCSs in hydrogenation reactions

Metal@HCSs

Yang et al [119] loaded PdAg nanoparticles inside HCSs by diffusion of Ag^{+} and Pd^{2+} ions into the inner surface of pre-synthesized HCSs and subsequent reduction by $NaBH_4$. The particle size of the PdAg was found to be 2.8 nm and was controlled by introducing an amino polymer (polyethylene diamine) inside the HCSs before loading the nanoparticles. The polymer was also introduced by diffusion and subsequent polymerization of a monomer inside the HCSs. Without the polymer, larger particles (50 nm) were obtained, therefore, the polymer effectively stabilized and capped the metal nanoparticles. Their method effectively placed small PdAg nanoparticles inside HCSs, however, some of the particles could be found within the shell of the HCSs. The catalyst showed good activity in the hydrogenation of CO_2 to formate at 100 ° C in 24 h and could be recycled with almost 100 % recovery of activity after 5 cycles of reaction with no evidence of catalyst sintering. Phaahlamohlaka et al [120] prepared RuCo nanoparticles inside HCSs by reduction of Co and Ru salts on the surface of polystyrene (PS) spheres. The PS was used as a template in the synthesis of the HCSs, and coating of the

RuCo/PS composite with a resorcinol-formaldehyde (RF) carbon source, followed by carbonization led to the removal of the PS template and the formation of RuCo@HCSs. The evaluation of the catalyst for the Fischer-Tropsch Synthesis (FTS) revealed that due to the confinement of the catalyst, and the microporous nature of the carbon support, diffusion limitations existed. This affected the diffusion of the reactants and products moving to and from the active catalyst inside HCSs and consequently affected the activity and selectivity. Another interesting study on catalytic hydrogenation with metal decorated HCSs was reported by Wang and co-workers [121]. Pd nanoparticles (6 nm) were placed inside HCSs (175 nm) and used in the hydrogenation of nitrobenzene and nitroanthracene to demonstrate selective hydrogenation with microporous HCSs. Nitrobenzene was hydrogenated to aminobenzene at 120 °C with a conversion of 100 % and yield of 98 in 30 minutes. Whereas the hydrogenation of nitroanthracene was unsuccessful, giving a conversion of less than 5% after 3 h. This was attributed to diffusion limits prohibiting the transportation of the bulky nitroanthracene through the small micropores of the HCSs. This was further confirmed by crushing the HCSs through grinding under liquid nitrogen to expose the catalyst and redoing the hydrogenation reaction, due to which 59 % conversion of nitroanthracene was obtained. This was an important demonstration of the importance of the pore structure in HCSs.

Metal/HCSs

Nongwe et al [122] synthesized Pt nanoparticles supported on nitrogen-doped HCSs (N-HCSs). The N-HCSs were synthesized using a silica template and the CVD method with different nitrogen-containing carbon sources (acetonitrile, triethylamine, trimethylamine and aniline). Acetonitrile was found to be the best carbon precursor, and a Pt salt was reduced using $NaBH_4$ on the surface of the pre-synthesized acetonitrile N-HCSs to produce Pt (2.8 nm) nanoparticles supported on N-HCSs. The catalyst was tested for activity in the hydrogenation of cinnamaldehyde reaction using an autoclave reactor at 80 °C. The catalyst showed very good activity, with up to 99 % cinnamaldehyde conversion, and 97 % selectivity to cinnamyl alcohol. The catalyst could be recycled 12 times, with only a 10% loss in conversion and no changes in selectivity. Zhang and co-workers [123] prepared Pd nanoparticles supported on Fe-N doped HCSs. PDA, a nitrogen-containing carbon precursor, was synthesized on the surface of SiO_2 spheres in the presence of $FeCl_3$, to introduce Fe^{3+} ions within the PDA layer. Carbonization at 750 ° C for 2h and etching with KOH at 80 °C for 2 h gave HCSs doped with Fe and N. Pd nanoparticles were loaded on the Fe-NHCSs by the reduction of Pd acetate salt using NaBH4

on the surface of the HCSs. The prepared catalysts were used for the hydrogenation of phenylacetylene to produce styrene, at room temperature. After 80 minutes, a conversion of 100% was obtained, with 96.2 % styrene selectivity. After re-using the catalyst 4 times, it was realized that the was a gradual decrease in activity. This was ascribed to minor Pd leaching, which was confirmed by doing an ICP-OES analysis of fresh (2.69 % Pd) and used catalyst (2.57 % Pd). This reaction was also done by Wu et al [124], using Pd supported on transition metal modified NHCs (Pd/Ni-NHCSs, Pd/Fe-NHCSs and Pd/Co-NHCSs). Similar activity data as Zhang et al [123] was obtained.

Metal-decorated HCSs in oxidation reactions

Metal@HCSs

Shi et al [125] encapsulated Cu nanoparticles inside HCSs by hydrothermal impregnation of Cu^{2+} ions inside pre-synthesized HCSs followed by reduction with H_2(g) to make Cu nanoparticles. Small Cu nanoparticles were formed (2.2 nm) and the catalyst was used in the oxidative carbonylation of methanol to form dimethyl carbonate at 110 ° C. Good catalyst activity was obtained and up to 50 % activity could be recovered after 5 recycling runs, however significant agglomeration (2.2 to 6.4 nm, and 5.5 to 12.2 nm) of the Cu nanoparticles was observed after 5 cycles. Furthermore, there was evidence of catalyst leaching, as the Cu concentration decreased significantly after the reaction (7.4 to 5.3 % and 7.4 to 3.0 %). Therefore the 50% loss of activity was attributed to the loss of active sites due to particle growth as well as catalyst leaching. In the work by Li et al [126] Cu nanoparticles encapsulated inside NHCSs using a hydrothermal synthesis method. The NHCSs were pre-synthesized by the coating of resorcinol formaldehyde and 3-aminophenol formaldehyde on the surface of SiO_2 spheres. This was done in a two-step process which included stirring a solution of formaldehyde, resorcinol, 3-aminophenol, ammonia and SiO2 at room temperature for 24 h followed by a 24 h hydrothermal reaction in an autoclave at 100 °C. The product was carbonized at 700 ° for 5 h and etched with HF to obtain NHCSs. Encapsulation of the Cu nanoparticles inside NHCSs was done by hydrothermal impregnation and diffusion of Cu^{2+} ions into the inside of HCSs using Cu acetate in an autoclave at 100 ° C for 1 h. The product was reduced in hydrogen at 400 °C to obtain Co@NHCSs. This catalyst was used for the oxidative carbonylation of methanol at 110 °C inside an autoclave reactor pressurized with CO

and O_2. The catalyst gave a poor activity, with a 2.1 % conversion of methanol and 96 % selectivity to dimethyl carbonate.

Metal/HCSs

Zhu et al [127] prepared Pd nanoparticles (3.6 nm) supported on N-HCSs. The N-HCSs were pre-synthesized using a self-templating method with poly(aniline-co-pyrrole) copolymer as a template and nitrogen-containing carbon source. The copolymer was synthesized in the presence of a non-ionic surfactant (octylphenol polyoxyethylene ether) at room temperature for 24 h and formed hollow polymer spheres (HPSs). Pyrolysis of the HPSs at 800-1000 °C for 20 h gave N-HCSs. Pd^{2+} ions were adsorbed on the surface of the N-HCSs over 24 hours and thereafter reduced with $NaBH_4$ to make Pd nanoparticles supported on N-HCSs. Evaluation of the catalyst in the oxidation of 5-hydroxymethylfurfural at 120 °C gave good activity with 99 % conversion and 98 % selectivity. The catalyst was stable and gave up to 88.3 % conversion and 96 % selectivity after 5 cycles. The small loss in activity was attributed to minor catalyst leaching during the reaction and washing. No particle aggregation was observed after 5 cycles. Ravat et al [128] investigated the oxidation of benzyl alcohol with Pd nanoparticles supported outside boron-doped HCSs (BHCSs). BCl_3 and toluene were used as boron and carbon sources, respectively. A solution containing a mixture of BCl_3 and toluene was injected, using an automatic syringe pump, into a quartz tube containing SiO_2 under Ar atmosphere at 900 °C over 4 h. The resulting SiO2@B-Carbon was etched with HF to remove silica and obtain BHCSs. Before loading the Pd nanoparticles, the BHCSs were functionalized using HNO_3. PdO nanoparticles were loaded onto the HCSs by deposition of Pd acetate pyridine in pyridine, followed by calcination. The obtained PdO/HCSs showed high activity in the oxidation of benzyl alcohol. 100 % conversion and 99 % selectivity to benzaldehyde were obtained at 120 °C over 5 h. After 6 cycles, the catalyst showed reduced activity (61 % conversion) due to catalyst leaching. ICP-OES analysis showed that the catalyst had lost 10 % of the initial Pd content.

2.3. Conclusion

There is a number of well-developed polymer synthesis methods, which makes it easy to prepare polymers with unique desirable properties. Different synthesis routes are also available for the synthesis of polymers spheres with variable sizes and chemical properties. Additionally,

modification of the polymer surface properties can be done to ensure they are suitable for specific applications. Such applications include the adsorption of metals and other atoms and molecules. Polymers decorated with metal nanoparticles have been widely synthesized with the use of surface-modified polymers, for various applications.

The ability to adsorb molecules makes surface-modified desirable in the synthesis of hollow spheres, where the adsorption of a precursor compound on a polymer template is sometimes required. Generally, hollow spheres can be synthesized using template-free and template-assisted routes. Both methods have their advantages and disadvantages, and the choice depends on the required properties of the final product. For instance, with the template approach various properties of the hollow spheres can be controlled, especially with hard templating. This method, therefore, becomes the most preferable, especially with the synthesis of HCSs. The ability to use various polymers as carbon precursors makes the template synthesis method even preferable and convenient when specific properties are required. For example, when a nitrogen-doped mesoporous shell is required, the properties can be tuned during the shell synthesis by selecting specific starting materials.

Various heterogeneous catalysis hydrogenation and oxidation reactions have been reported in literature using different catalysts. However, there are very few reliable reports where HCSs have been used as supports. Both catalysts supported inside and outside HCSs have been discussed, and good efficiency has been observed in hydrogenation and oxidation reactions. However, recycling studies showed a variation with each catalyst. For instance, the catalysts supported outside seemed to undergo catalyst leaching, which results in activity loss during recycling. With the catalysts supported inside, recycling also becomes an issue because of the pore blockage of the carbon shell, which limits the transportation of reactants. Further work still needs to be done to build up literature on the use of HCSs as supports for heterogeneous catalysis reactions. Our work seeks to compare activities and selectivities of catalysts supported inside and outside HCSs.

References

[1] D. I. Bower, An introduction to polymer physics, Cambridge, United Kingdom: Cambridge University Press, 2002.

[2] K. S. Vishakha, B. D. Kishor and R. S. Sudha, “Natural polymers: A comprehensive review,” Int. J. Res. Pharm. Biol. Sci., vol. 3, pp. 1597-1613, 2012.

[3] A. Sionkowska, “Current research on the blends of natural and synthetic polymers as new biomaterials: Review,” Prog. Polm. Sci., vol. 36, pp. 1254-1276, 2011.

[4] A. P. Anwunobi and M. O. Emeje, “Recent applications of natural polymers in nanodrug delivery,” Nanomed. Nanotechnol., vol. 2, no. 4, 2011.

[5] D. Feldman and A. Barbalata, Synthetic polymers: technology, properties, applications, London: Chapman and Hall, 1996.

[6] I. Kucuk, “Polymer spheres formed by microfluidic technique with evans blue dye,” Polym. Adv. Technol., vol. 28, pp. 940-946, 2017.

[7] X. Sonng, Y. Ma, X. Ge, H. Zhou, G. Wang, H. Zhang, X. Tang and Y. Zhang, “Europian-based infinite coordination polymer nanospheres as an effective fluorescence probe for phosphate sensing,” RSC Adv., vol. 7, p. 8661, 2017.

[8] K. Klucinska, E. Jaworska, P. Gryczan, K. Maksymiuk and A. Michalska, “Synthesis of conducting polymer nanospheres of high electrochemical activity,” Chem. Commun., vol. 51, p. 12645, 2015.

[9] P. J. Rao and K. E. Geckeler, “Polymer nanoparticles: Preparation techniques and size control parameters,” Prog. Polym. Sci., vol. 36, pp. 887-913, 2011.

[10] Z.-Z. Gu, H. Chen, S. Zhang, L. Sun, Z. Xie and Y. Ge, “Rapid synthesis of monodisperse polymer spheres for self-assembled photonic crystals,” Colloids Surf. A Physicochem. Eng. Asp., vol. 302, pp. 312-319, 2007.

[11] H. Yoon, M. Choi, J. K. Lee and J. Jang, “Versatile strategies for fabrication nanomaterials with controlled size and morphology,” Macromol. Res., vol. 16, no. 2, 2008.

[12] T. Liu, C. Burger and B. Chu, “Nanofabrication in polymer matrices,” Prog. Polym. Sci, vol. 28, pp. 5-26, 2003.

[13] A. Khanal, Y. Inuoe, M. Yada and K. Nakashima, “Synthesis of silica hollow nanoparticles templated by polymeric micelle with core-shell-corona structure,” J. Am. Chem. Soc., Vol. 129, pp. 1534-1535, 2007.

[14] G. Zhao, X. Huang, Z. Tang, Q. Huang, F. Niu and X. Wang, “Polymer-based nanocomposites for heavy metal ions removal from aqueous solution: A review,” Polym. Chem, vol. 9, pp. 3562-3582, 2018.

[15] E. V. Zolotukhina and T. A. Kravchenko, “Synthesis and kinetics of growth of metal nanoparticles inside ion-exchange polymers,” Electrochemica Acta, vol. 56, no. 10, pp. 3597-3604, 2011.

[16] C. Saldias, S. Bonardd, C. Quezeda, D. Radic and A. Leiva, “The role of polymers in the synthesis of noble metal nanoparticles: a review,” J. Nanosci. Nanotechnol, vol. 17, no. 1, 2017.

[17] M. Akay, Introduction to polymer science and technology, Bookboon.com, 2012.

[18] A. Yokoyama and T. Yokozawa, “Converting step-growth to chain-growth condensation polymerization,” Macromolecules, vol. 40, pp. 4093-4101, 2007.

[19] D. I. Bower, An introduction to polymer physics, New York: Cambridge University Press, 2002.

[20] X. Shi, M. Nishiura and Z. Hou, “Simultaneous chain-growth and step-growth polymerization of methoxystyrenes by rare-earth catalysts,” Angew. Chem, vol. 55, pp. 14812-14817, 2016.

[21] F. J. Davis, Polymer chemistry, Oxford: Oxford University Press, 2004.

[22] S. Koltzenburg, M. Maskos and O. Nuyken, Polymer Chemistry, Berlin Heidelberg: Springer-verlag, 2017.

[23] J. K. Stille, “Step-growth polymerization,” J. Chem. Educ., vol. 58, p. 862, 1981.

[24] S. Zhu and A. Hamielec, “Polymerization kinetic modelling and macromolecular reaction engineering,” in Polymer Science: A comprehensive reference, K. Matyjaszewski and M. Moller, Eds., Elsevier, 2012, pp. 779-831.

[25] T. L. Tartamella, W. M. Cole and M. Smale, “Bulk polymerization process”. United States Patent US7351776B2, 01 April 2008.

[26] J. S. Hubby, “Solution polymerization process”. United States Patent US4271060A, 02 06 1981.

[27] L. L. Bohm, “The slurry polymerization process with super-active Ziegler-type catalyst systems: from the 2L glass autoclave to the 200 m3 stirred tank reactor,” in Polyolefins: 50 years after Zeigler and Natta I, W. Kaminsky, Ed., Berlin, Heidelberg: Springer, 2013.

[28] “Crow Polymer Properties Database,” CROW, 2015. [Online]. Available: http://polymerdatabase.com/polymer%20chemistry/Suspension%20Polymerization.html. [Accessed February 2021].

[29] J. W. Gooch, “Emulsion polymerization,” in Encyclopedic dictionary of polymers, J. W. Gooch, Ed., New York, Springer, 2011.

[30] H. Reiss, “Gas-phase polymerization: Ultraslow chemistry,” Science, vol. 238, pp. 1368-1373, 1987.

[31] S. Galindo-Rodriguez, E. Allemann, H. Fessi and E. Doelker, “Physicochemical parameters associated with nanoparticle formation in the salting-out, emulsion diffusion and nanoprecipitation methods,” Pharm. Res., vol. 21, no. 8, 2004.

[32] H. Yabu, T. Higuchi, K. Ijiro and M. Shimomura, “Spontaneous formation of polymer nanoparticles by good-solvent evaporation as a nonequilibrium process,” Chaos, vol. 15, no. 047505, 2005.

[33] S. Desgouilles, C. Vauthier, D. Brazile, J. Vacus, J.-L. Grossiord, M. Veillard and P. Couvreur, “The design of nanoparticles obtained by solvent evaporation: A comparative study,” Langmuir, vol. 19, pp. 9504-9510, 2003.

[34] S. Schubert, J. T. Delaney and U. S. Schybert, “Nanopreciptation and nanoformation of polymers from history to powerful possibilities beyond poly (lactic acid),” Soft Matter, vol. 7, pp. 1581-1588, 2011.

[35] C. J. M. Rivas, M. Tarhini, W. Badri, K. Miladi, H. Greige-Gerges, Q. A. Nazari, S. A. G. Rodriguez, R. A. Roman, H. Fessi and A. Elaissari, “Nanoprecipitation process: From encapsulation to drug delivery,” Int. J. Pharm., vol. 532, pp. 66-81, 2017.

[36] C. P. Reis, R. J. Neufeld, A. Ribeiro and F. Viega, “Nanoencapsulation I. Methods for preparation of drug-loaded polymeric nanoparticles,” Nanomed. Nanotech. Biol. Med., vol. 2, pp. 8-21, 2006.

[37] C. Vautheir and K. Bouchemal, “Methods for the preparation and manufacture of polymeric nanoparticles,” Pharm. Res., vol. 26, pp. 1025-1058, 2009.

[38] J. M. Asua, “Miniemulsion polymerization,” Progress in Polymer Science, vol. 27, no. 7, pp. 1283-1346, 2002.

[39] F. M. Pavel, “Microemulsion polymerization,” Journal of Dispersion Science and Technology, vol. 25, no. 1, pp. 1-16, 2006.

[40] M. J. Raaijmakers and N. E. Benes, “Current trends in interfacial polymerization chemistry,” Progress in Polymer Science, vol. 63, pp. 86-142, 2016.

[41] Y. Hu, T. Zhao, P. Zhu, Y. Zhu, X. Liang, R. Sun and C.-P. Wong, “Tailoring size and coverage density of silver nanoparticles on monodispersed polymer spheres as highly sensitive substrates,” Chem. Asian J., vol. 11, no. 17, pp. 2428-2435, 2016.

[42] F. Caruso, “Nanoengineering of particle surfaces,” Advanced Materials, vol. 13, pp. 11-22, 2001.

[43] H. P. Hentze and M. Antonietti, “Template synthesis of porous organic polymers,” Current opinions in solid state and materials science, vol. 5, pp. 343-353, 2001.

[44] I. Pastoriza-Santos and L. M. Liz-Marzan, “Formation of PVP-protected metal nanoparticles in DMF,” Langmuir, vol. 18, pp. 2888-2894, 2002.

[45] A. Cao, R. Lu and G. Veser, “Stabilizing metal nanoparticles for heterogeneous catalysis,” Phys. Chem. Chem. Phys., vol. 12, pp. 13499-13510, 2010.

[46] G. Chen, J. Lu, C. Lam and Y. Yu, “A novel green synthesis approach for polymer nanocomposites decorated with silver nanoparticles and their antibacterial activity,” Analyst, vol. 139, p. 5793, 2014.

[47] J. Virkutyte and R. S. Varma, “Green synthesis of metal nanoparticles: Biodegradable polymers and enzymes in stabilization and surface functionalization,” Chemical Science, vol. 2, pp. 837-846, 2011.

[48] T. Sakai and P. Alexandridis, “Single-step synthesis and stabilization of metal nanoparticles in aqueous pluronic block copolymer solutions at ambient temperature,” Langmuir, vol. 20, pp. 8426-8430, 2004.

[49] J.-Y. Lee, Y. Liao, R. Nagahata and S. Horiuchi, “Effect of metal nanoparticles on thermal stabilization of polymer/metal nanocomposites prepared by a one-step dry process,” Polymer, vol. 47, pp. 7970-7979, 2006.

[50] A. B. R. Mayer, “Colloid metal nanoparticles dispersed in amphiphilic polymers,” Polymers for Advanced Technologies, vol. 12, pp. 96-106, 2001.

[51] P. M. Budd, “Polyelectrolytes,” in Comprehensive polymer science and supplements, G. Allen and C. Bevington, Eds., UK, Pergamon, 1989, pp. 215-230.

[52] B. K. G. Theng, “Uncharged (nonionic) polymers,” in Developments in clay science, Elsevier, 2012, pp. 79-110.

[53] F. S. Bates and G. H. Fredrickson, “Block copolymer thermodynamics: Theory and experiment,” Annu. Rev. Phys. Chem, vol. 41, pp. 525-409, 1990.

[54] T. Smart, H. Lomas, M. Massignani, M. V. Flores-Merino, L. R. Perez and G. Battaglia, “Block copolymer nanostructures,” nanotoday, vol. 3, pp. 38-46, 2008.

[55] T. Uchida, T. Serizawa, H. Ise, T. Akaike and M. Akashi, “Graft copolymer having a hydrophobic backbone and hydrophilic branches: Interaction of hepatocytes and polystyrene nanospheres having lactose-immobilized hydrophilic polymers and their surfaces,” Biomacromolecules, vol. 2, pp. 1343-1346, 2001.

[56] A. B. Mayer and J. E. Mark, “Transition metal nanoparticles protected by amphiphilic block copolymers as tailored catalyst systems,” Colloid and Polymer Science, vol. 275, pp. 333-340, 1997.

[57] G. Zhang, Y. Yu, X. Chen, Y. Han, Y. Di, B. Yang, F. Xiao and J. Shen, “Silica nanobottles templated from functional polymer spheres,” Journal of Colloid and Interface Science, vol. 263, pp. 467-472, 2003.

[58] S. N. Sidorov, L. M. Bronstein, P. M. Valetsky, J. Hartman, H. Colfen, H. Schnablegger and M. Antonietti, “Stabilization of metal nanoparticles in aqueous medium by polyethylene oxide-polyethyleneimine block copolymers,” J. Colloid and Interface Sci., vol. 212, pp. 197-211, 1999.

[59] X. Cao, Q. Wang, S. Wang and R. Man, “Preparation of novel polystyrene -poly (hydroxamic acid) copolymer and its use adsorption properties for rare earth metal ions,” Polymers, vol. 12, no. 9, p. 1905, 2020.

[60] Y. Yang, Y. Chu, F. Yang and Y. Zhang, “Uniform hollow conductive polymer microspheres synthesized with the sulfonated polystyrene template,” Materials Chemistry and Physics, vol. 92, pp. 164-171, 2005.

[61] X. He, X. Ge, H. Liu, M. Wang and Z. Zhang, “Synthesis of cagelike polymer microspheres with hollow core/porous shell structures by self-assembly of latex particles at the emulsion droplet interface,” Chemistry of Materials, vol. 17, pp. 5891-5892, 2005.

[62] Q. Yuan, L. Yang, M. Wang, H. Wang, X. Ge and X. Ge, “The mechanism of the formation of multi hollow polymer spheres through sulfonated polystyrene particles,” Langmuir, vol. 25, pp. 2729-2735, 2009.

[63] N. P. Wickramaratne and M. Jaroniec, “Facile synthesis of polymer and carbon spheres decorated with highly dispersed metal nanoparticles,” Chemical Communication, vol. 50, p. 12341, 2014.

[64] J. Han, L. Li and R. Guo, “Novel approach to the controllable synthesis of gold nanoparticles supported on polyaniline nanofibers,” Macromolecules, vol. 43, pp. 10636-10644, 2010.

[65] X. Liu, H. Chen, C. Wang, R. Gu, C. Ji, C. Sun and Y. Zhang, “Synthesis of porous acrylonitrile/ methyl acrylate copolymer beads by suspended emulsion polymerization and their adsorption properties after amidoximation,” J. Hazardous Mater. , vol. 15, pp. 1014-1021, 2010.

[66] T. Godjevargova, A. Simeonova and A. Dimov, “Adsorption of lead and copper on modified polyacrylonitrile bead,” J. Appl. Polym. Sci., vol. 79, no. 2, pp. 283-288, 2001.

[67] P. Schuetz and F. Caruso, “Semiconductor and metal nanoparticle formation of polymer spheres coated with weak polyelectrolyte multilayers,” Chem. Mater., vol. 16, pp. 3066-3073, 2004.

[68] P. Schuetz and F. Caruso, “Copper-assisted weak polyelectrolyte multilayer formation on microspheres and subsequent film crosslinking,” Adv. Funct. Mater., vol. 13, no. 12, 2003.

[69] Q. Yang, L. Li, F. Zhao, Y. Wang, Z. Ye, C. Hua, Z. Liu, K. Bohinc and X. Guo, "Spherical polymeric brushes as templates to prepare hollow silica spheres encapsulating metal nanoparticles," Nanomaterials, vol. 10, no. 4, p. 799, 2020.

[70] T. K. Mandal, M. S. Fleming and D. R. Walt, "Production of hollow polymeric microspheres by surface-confined living radical polymerization on silica templates," Chemistry of Materials, vol. 12, pp. 3481-3487, 2000.

[71] S. H. Im, U. Jeong and Y. Xia, "Polymer hollow particles with controllable holes in their surfaces," Nature Materials, vol. 4, pp. 671-675, 2005.

[72] C. C. Nguyen, N. N. Vu and T.-O. Do, "Recent advances in the development of sunlight-driven hollow structure photocatalysts and their applications," J. Mater. Chem. A, vol. 3, pp. 18345-18359, 2015.

[73] J. Han and R. Guo, "A facile solution route for polymeric hollow spheres with controllable size," Advanced Materials, vol. 18, pp. 3140-3144, 2006.

[74] B. Li and H. Zeng, "Architecture and preparation of hollow catalytic devices," Adv. Mater., vol. 31, no. 38, 2018.

[75] H. C. Zeng, "Synthesis and self-assembly of complex hollow materials," J. Mater. Chem., vol. 21, pp. 7511-7526, 2011.

[76] Y. Li and J. Shi, "Hollow-structured mesoporous materials: Chemical synthesis, functionalization and applications," Adv. Mater., vol. 26, no. 20, pp. 3176-3205, 2014.

[77] Y. Bao, C. Shi, T. Wang, X. Li and J. Ma, "Recent progress in hollow silica: Template synthesis, morphologies and applications," Micropor. Mesopor. Mater., vol. 227, pp. 121-136, 2016.

[78] S. S. Park and C.-S. Ha, "Hollow mesoporous functional hybrid materials: Fascinating platforms for advanced applications," Adv. Funct. Mater. , vol. 28, no. 27, p. 1703814, 2017.

[79] S. Li, A. Pasc, V. Feirro and A. Celzard, "Hollow carbon spheres, synthesis and applications - A review," J. Mater. Chem. A, vol. 4, pp. 12686-12713, 2016.

[80] J. Wang, N. Yang, H. Tang, Z. Dong, Q. Jin, M. Yang, D. Kisailus, H. Zhao, Z. Tang and D. Wang, "Accurate control of multishelled Co3O4 hollow microspheres as high-performance anode materials in lithium-ion batteries," Angew. Chem., vol. 125, pp. 6545-6548, 2013.

[81] S. Yuan, Q. Zhang, B. Xu, Z. Jin, Y. Zhang, Y. Yang, M. Zhang and T. Ohno, "Porous cerium dioxide hollow spheres and their photocatalytic performance," RSC Adv., vol. 4, pp. 62255-62261, 2014.

[82] X. Fang, X. Zhao, W. Fang, C. Chen and N. Zheng, “Self-templating synthesis of hollow mesoporous silica and their applications in catalysis and drug delivery,” Nanoscale, vol. 5, pp. 2205-2218, 2013.

[83] J. Feng and Y. Yin, “Self-templating approaches to hollow nanostructures,” Adv. Mater., vol. 31, no. 38, p. 1802349, 2019.

[84] S. Huang, L. Yang, G. Xu, T. Wei, J. Tian, X. Liu, H. Li, Z. Xiang, J. Cao and X. Wei, “Hollow Co3O4@N-doped carbon nanocrystals anchored on carbon nanotubes for freestanding anode with superior Li/Na storage performance,” Chemical Engineering Journal, vol. 415, no. 128861, 2021.

[85] W. Wang, M. Dahl and Y. Yin, “Hollow nanocrystals through the nanoscale Kirkendall effect,” Chem. Mater., vol. 25, pp. 1179-1189, 2013.

[86] X. W. Lou, Y. Wang, C. Yuan, J. Y. Lee and L. A. Archer, “Template-free synthesis of SnO2 hollow nanostructures with high lithium storage capacity,” Adv. Mater., vol. 18, pp. 2325-2329, 2006.

[87] W. Weng, J. Lin , Y. Du, X. Ge, X. Zhou and J. Bao, “Template-free synthesis of metal oxide hollow micro-/nanospheres via Ostwald ripening for lithium-ion batteries,” J. Mater. Chem. A, vol. 6, pp. 10168-10175, 2018.

[88] A.-A. El Mel, R. Nakamura and C. Bittencourt, “The Kirkendall effect and nanoscience: hollow nanospheres and nanotubes,” Beilstein J. Nanotechnol., vol. 6, pp. 1348-1361, 2015.

[89] S. Chu, C. Yang and X. Su, “Synthesis of NiO hollow nanospheres via Kirkendall effect and their enhanced gas-sensing performance,” Appl. Surf. Sci., vol. 492, pp. 82-88, 2019.

[90] Q. Yu, P. Wang, S. Hu, J. Hui, J. Zhuang and X. Wang, “Hydrothermal synthesis of hollow silica spheres under acidic conditions,” Langmuir, vol. 27, pp. 7185-7191, 2011.

[91] Q. Zhang, W. Wang, J. Goebl and Y. Yin, “Self-templated synthesis of hollow nanostructures,” nanotoday, vol. 4, no. 6, pp. 494-507, 2009.

[92] Q. Zhang, T. Zhang, J. Ge and Y. Yin, “Permeable silica shell through surface-protected etching,” Nano. Lett., vol. 8, no. 9, pp. 2867-2871, 2008.

[93] Y. Chen, H. Chen, L. Guo, Q. He, F. Chen, J. Zhou, J. Feng and J. Shi, “Hollow/rattle-type mesoporous nanostructures by a structural difference-based selective etching strategy,” ACS Nano, vol. 4, no. 1, pp. 529-539, 2010.

[94] N. Ren, B. Wang, Y.-h. Yang, Y.-h. Zhang, W.-l. Yang, Y.-h. Yue, Z. Gao and Y. Tang, “General method for the fabrication of hollow microcapsules with adjustable shell compositions,” Chem. Mater., vol. 17, pp. 2582-2587, 2005.

[95] Y. Yu, J. Liu, L. Yu, C. Wu, Y. Wen, K. Yin, F.-K. Chiang, R. Hu, J. Liu, L. Sun, L. Gu, J. Maier and M. Zhu, "New nanoconfined galvanic replacement synthesis of hollow Sb@C yolk-shell spheres constituting a stable anode for high-rate Li/Na-ion batteries," Nano Lett., vol. 17, no. 3, pp. 2034-2042, 2017.

[96] A. S. Falchevskaya, A. Y. Prilepskii, S. A. Tsvetikova, E. I. Koshel and V. V. Vinogradov, "Facile synthesis of a library of hollow metallic particles through the galvanic replacement of liquid gallium," Chem. Mater., vol. 33, no. 5, pp. 1571-1580, 2021.

[97] Y. Liu, B. Zhou, S. Liu, Q. Ma and W.-H. Zhang, "Galvanic replacement synthesis of highly uniform Sb nanotubes: Reaction mechanism and enhanced sodium storage performance," ACS Nano, vol. 13, no. 5, pp. 5885-5892, 2019.

[98] T. Zhang, Q. Zhang, J. Ge, J. Goebl, M. Sun, Y. Yan, Y. Liu, C. Chang, J. Guo and Y. Yin, "A self-templated route to hollow silica microsphere," J. Phys. Chem. C, vol. 113, pp. 3168-3175, 2009.

[99] D. Qui, J. Guan, M. Li, C. Kang, J. Wei, Y. Li, Z. Xie, F. Wang and R. Yang, "Kinetics enhanced nitrogen-doped hierarchical porous hollow carbon spheres boosting advanced potassium-ion hybrid capacitors," Adv. Funct. Mater., vol. 29, no. 32, p. 1903494, 2019.

[100] M. J. Lawrence, "Surfactant systems: Microemulsions and vesicles as vehicles for drug delivery," Eur. J. Drug Metab. Pharmacokinetic., no. 3, pp. 257-269, 1994.

[101] T.-Z. Ren, Z.-Y. Yuan and B.-P. Su, "Surfactant-assisted preparation of hollow microspheres of mesoporous TiO2," Chem. Phys. Lett., vol. 374, pp. 170-175, 2003.

[102] H.-P. Hentze, S. R. Raghavan, C. A. McKelvey and E. W. Kaler, "Silica hollow spheres by templating of cationic vesicles," Langmuir, vol. 19, pp. 1069-1074, 2003.

[103] G.-H. Wang, J. Hilgert, F. H. Richter, F. Wang, H.-J. Bongard, B. Spliethoff, C. Weidenthaler and F. Schuth, "Platinum-cobalt bimetallic nanoparticles in hollow nanospheres for hydrogenolysis of 5-hydroxymethylfurfural," Nat. Mater., vol. 13, pp. 293-300, 2014.

[104] X. Lai, J. E. Halpert and D. Wang, "Recent advances in micro-/nano-structured hollow spheres for energy applications: From simple to complex systems," Energy Environ. Sci., vol. 5604, no. 5, pp. 5604-5618, 2012.

[105] J. Han, G. Song and R. Guo, "Synthesis of polymer hollow spheres with holes in their surfaces," Chemistry of Materials, vol. 19, pp. 973-975, 2007.

[106] A.-H. Lu, W.-C. Li, G.-P. Hao, B. Spliethoff, H.-J. Bongard, B. B. Schaack and F. Schuth, "Easy synthesis of hollow polymer, carbon and graphitized microspheres," Angewandte Chemie International Edition, vol. 2010, pp. 1615-1618, 2010.

[107] R. Liu, S. M. Mahurin, C. Li, R. R. Unocic, J. C. Idrobo, H. Gao, S. J. Pennycook and S. Dai, "Dopamine as a carbon source: The controlled synthesis of hollow carbon spheres and york-structured carbon nanocomposites," Angew. Chem. Int. Ed., vol. 50, pp. 6799-6802, 2011.

[108] F. Su, X. S. Zhao, Y. Wang, L. Wang and J. Y. Lee, "Hollow carbon spheres with controllable shell structure," J. Mater. Chem., vol. 16, pp. 4413-4419, 2006.

[109] C. Galeano, J. C. Meier, M. Soorholtz, H. Bongard, C. Baldizzone, K. J. Mayrhofer and F. Schuth, "Nitrogen-doped hollow carbon sphere as a support for platinum-based electrocatalysts," ACS Catal., vol. 4, pp. 3856-3868, 2014.

[110] X. Li, M. Chi, S. M. Mahurin, R. Liu, Y.-J. Chuang, S. Dai and Z. Pan, "Graphitized hollow carbon spheres and yolk-structure carbon spheres fabricated by metal-catalyst free chemical vapour deposition," Carbon, vol. 101, pp. 57-61, 2016.

[111] S. Mezzavilla, C. Baldizzone, K. J. Mayrhofer and F. Schuth, "General method for the synthesis of hollow mesoporous carbon spheres with tunable textural properties," ACS Appl. Mater. Interfaces, vol. 7, pp. 12914-12922, 2015.

[112] S. Wang, M. Zhang, D. Wang, W. Zhang and S. Liu, "Synthesis of hollow mesoporous silica microspheres through surface sol-gel process on polystyrene-co-poly(4-vinyl pyridine) core-shell microspheres," Micropor. Mesopor. Mater., vol. 139, pp. 1-7, 2011.

[113] J. Du, Y. Zhang, H. Wu, S. Hou and A. Chen, "N-doped hollow mesoporous carbon spheres by improved dissolution-capture for supercapacitors," Carbon, vol. 156, pp. 523-528, 2020.

[114] J. Xi, S. Yang, L. Silviolu, S. Cao, P. Liu, Q. Chen, Y. Zhao, H. Sun, J. N. Hansen, J.-P. B. Haraldsted, J. Kibsgaard, J. Rossmeisi, S. Bals, S. Wang and I. Chorkendorff, "Highly active, selective, and stable Pd single-atom catalysts anchored on N-doped hollow carbon sphere for electrochemical H2O2 synthesis under acidic conditions," J. Catal., vol. 393, pp. 313-323, 2021.

[115] D. Ni, W. Sun, Z. Wang, Y. Bai, H. Lei, X. Lai and K. Sun, "Heteroatom-doped mesoporous hollow carbon spheres for fast sodium storage with an ultralong cycle life," Adv. Energy Mater., vol. 9, no. 19, p. 1900036, 2019.

[116] J. Ding, H. Zhang, H. Zhou, J. Feng, X. Zheng, C. Zhong, E. Paek, W. Hu and D. Mitlin, "Sulfur-grafted hollow carbon spheres for potassium-ion battery anodes," Adv. Mater., vol. 31, no. 30, p. 1900429, 2019.

[117] H. Wang, L. Wei, J. Liu and J. Shen, "Hollow N-doped bimetal hollow spheres with superior ORR catalytic performance for microbial fuel cells," J. Colloid Interf. Sci., vol. 575, pp. 177-182, 2020.

[118] S. L. Zhang, B. Y. Guan and X. W. Lou, “Co-Fe alloy/N-doped carbon hollow spheres derived from dual metal-organic frameworks for enhanced catalytic oxygen reduction,” Small, vol. 15, no. 13, p. 1805324, 2019.

[119] G. Yang, Y. Kuwahara, S. Masuda, K. Mori, C. Louis and H. Yamashita, “PdAg nanoparticles and amino polymer confined within mesoporous hollow carbon spheres,” J. Mater. Chem. A, vol. 8, pp. 4437-4446, 2020.

[120] T. N. Phaahlamohlaka, M. W. Dlamini, D. O. Kumi, R. Forbes, L. L. Jewell and N. J. Coville, “Co inside hollow carbon spheres as a Fischer-Tropsch catalyst: Spillover effects from Ru placed inside and outside the HCS,” Appl. Catal. A Gen., vol. 599, p. 117617, 2020.

[121] G.-H. Wang, K. Chen, J. Engelhardt, H. Tuysuz, H.-J. Bongard, W. Schmidt and F. Schuth, “Scalable one-pot synthesis of yolk-shell carbon nanospheres with yolk-supported Pd nanoparticles for size-selective catalysis,” Chem. Mater., vol. 30, pp. 2483-2487, 2018.

[122] I. Nongwe, V. Ravat, R. Meijboom and N. J. Coville, “Pt supported nitrogen doped hollow carbon spheres for the catalysed reduction of cinnamaldehyde,” Appl. Catal. A Gen., vol. 517, pp. 30-38, 2016.

[123] W. Zhang, F. Wang, X. Li, Y. Liu, Y. Liu and J. Ma, “Fabrication of hollow carbon nanospheres introduced with Fe and N species immobilized palladium nanoparticles as catalysts for the semihydrogenation of phenylacetylene under mild reaction conditions,” Appl. Surf. Sci, vol. 404, pp. 398-408, 2017.

[124] W. Wu, W. Zhang, Y. Long, J. Qin, H. Wen and J. Ma, “Ni modified Pd nanoparticles immobilized on hollow nitrogen-doped carbon spheres for the semihydrogenation of phenylacetylene,” J. Colloid Interf. Sci., vol. 531, pp. 642-653, 2018.

[125] R. Shi, J. Wang, J. Zhao, S. Liu, P. Hao, Z. Li and J. Ren, “Cu nanoparticles encapsulated with hollow carbon spheres for methanol oxidative carbonylation: Tuning catalytic properties by particle size control,” Appl. Surf. Sci., vol. 459, pp. 707-715, 2018.

[126] H. Li, J. Zhao, R. Shi, P. Hao, S. Liu, Z. Li and J. Ren, “Remarkable activity of nitrogen-doped hollow carbon spheres encapsulated Cu on the synthesis of dimethyl carbonate: Role of effective nitrogen,” Appl. Surf. Sci, vol. 436, pp. 803-813, 2018.

[127] Y. Zhu, F. Wang, M. Fan, Q. Zhu and Z. Dong, “Ultrafine Pd nanoparticles immobilized on N-doped hollow carbon nanospheres with superior catalytic performance for the selective oxidation of 5-hydroxymethylfurfural and hydrogenation of nitroacenes,” J. Colloid Interf. Sci., vol. 553, pp. 588-597, 2019.

[128] V. Ravat, I. Nongwe, R. Meijboom, G. Bepete and N. J. Coville, “Pd on boron-doped hollow carbon spheres- PdO particle size and support effects,” J. Catal., vol. 305, pp. 36-45, 2013.

Chapter 3: Polystyrene-*b*-poly(acrylic acid) templates for the synthesis of size-controlled cobalt nanoparticles encapsulated inside hollow carbon spheres[1]

3.1. Introduction

Catalyst efficiency is dependent on factors that include metal particle size, phase composition, and surface properties [1] [2]. The control of metal particle size is thus important for achieving high catalytic efficiency and optimal activity [154] [4]. Size-controlled metal nanoparticles with a narrow size distribution can be made through the control of particle nucleation and growth and the elimination of sintering and agglomeration processes [5]. Sintering can be reduced by separating the nanoparticles from each other using a physical barrier or by using chemical approaches in which strong metal-support interactions are created (with or without promoters). One approach to using a physical barrier is by means of a hollow structure in which metal particles are placed inside the separated hollow structures. This approach has been effective when using hollow carbon spheres (HCSs) to separate metal particles [6]. However, this does not necessarily reduce sintering *within* the hollow structure. In a recent study, Dong and co-workers [7] explored the catalytic behaviour of metal nanoparticles supported outside and inside (encapsulated) HCSs to investigate mass transfer limitations, sieving effects and reactants accumulation inside the hollow void of the HCSs. Their work provides a fundamental understanding of the void confinement effects when using HCSs as nanoreactors.

HCSs are typically grown using a sacrificial template [8], however, several template-free synthesis methods have been reported. For instance, Bin and co-workers [9] have successfully prepared HCSs by selective dissolution of the inner core of 3-aminophenol-formaldehyde resin spheres in acetone. The resin used in their study was complex and multifunctional with a soluble core and an insoluble shell. Pyrolysis of the insoluble shell at high temperature under inert conditions gave a carbon shell with a hollow interior. This template-free synthesis method further allowed for the synthesis of multi-shelled HCSs as well as the use of other phenol monomers such as resorcinol, phenol and nitrophenol. Another interesting template-free

[1] This chapter has been published as: Pumza Mente, Tumelo N. Phaahlamohlaka, Victor Mashindi and Neil J. Coville, Polystyrene-b-poly(acrylic acid) nanospheres for the synthesis of size-controlled cobalt nanoparticles encapsulated inside hollow carbon spheres, *J. Mater, Sci.* (2021), 56, 2113-2128. DOI: 10.1007/s10853-020-05323-w.

synthesis method was reported by Xu et al. [10], involving the carbonization of polyaniline-co-polypyrrole hollow spheres. Other interesting template-free synthesis methods were reported by various researchers [11] [12] [13].

When using the template method for the synthesis of M@HCSs, metal particles can be added to the HCSs post-reaction (by diffusion) [14] or by adding a metal nanoparticle to the template before the template removal [15]. In the latter case, a key factor would be the initial interaction between the template and the metal. The metal nanoparticles are usually grown on the surface of the sacrificial template, as shown in Scheme 1, and the metal nanoparticle size, shape and composition are controlled at this point. After the synthesis of the metal nanoparticles on the surface of the template, a carbon source is used to coat a carbon layer around the template/metal composite (Scheme 3.1). Upon pyrolysis and carbonization, the template can be removed by chemical means, or by thermal decomposition, and the nanoparticles transferred to the HCS surface (Scheme 3.1).

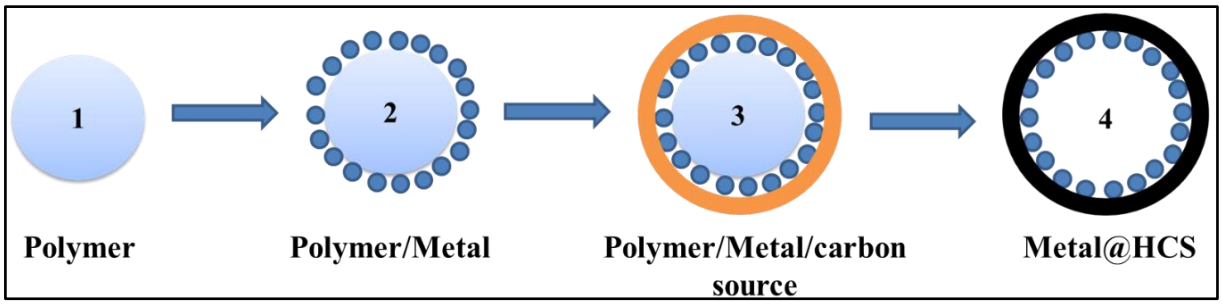

Scheme 3.1: Preparation of metal nanoparticles encapsulated inside HCSs (M_xO_y@HCSs)

A good template-metal interaction is required to ensure the growth of well dispersed and stabilized metal nanoparticles [16]. This interaction is dependent on the surface functional groups found on the template surface. A typical template used to support metal nanoparticles is polystyrene (PS). PS does not have functional groups, and therefore when using PS spheres (PSSs) as a template, there is generally a poor template-metal interaction. This can result in the formation of nanoparticles with random shapes and a broad size range. Other parameters such as the reducing agent, solvent composition, temperature and reaction time, also influence the growth of the nanoparticles [17]. The presence or introduction of functional groups on a polymer surface modifies their acid-base properties and therefore enhances any polymer-metal interactions [5] [18]. Preparation of functionalized polymers can be achieved by ex-situ reactions, where unfunctionalized polymers are decorated with functionalized compounds, or, by in-situ polymerization where block copolymers are formed from functionalized and un-

functionalized monomers [19] [20] [21]. Block copolymers have been shown to impact on the synthesis of size- and shape-controlled metal nanoparticles [16] [22] [23]. An example of this type of block copolymer is the asymmetric PS-*b*-PAA copolymer which has been synthesized by Zhang and Eisenberg [24]. By varying the monomer compositions, they made different polymer morphologies which included spheres and rods, with the polystyrene forming the core and the poly(acrylic acid) the outer surface.

In this study, styrene was polymerized in the presence of acrylic acid to give a PS-*b*-PAA block copolymer, with the objective of producing functionalized polymer spheres. The synthesized polymer spheres were used for the deposition of Co nanoparticles. Coverage of the spheres with resorcinol-formaldehyde (RF) and template removal gave Co_xO_y@HCSs, where Co_xO_y refers to the mixture of Co, CoO and Co_3O_4. The effect of PAA on the Co particle size was investigated.

3.2. Experimental Section

3.2.1. Materials

Styrene, acrylic acid, polyvinylpyrrolidone (PVP, MW 40 000), resorcinol, formaldehyde solution (37%), cetyltrimethylammonium bromide (CTAB), cobalt nitrate hexahydrate and hydrazine hydrate (78-82%) were all purchased from Sigma Aldrich and used as received. Ammonia solution (25%, Fluka) potassium persulfate (Eimer and Amend) and ethanol (98%, Merck) were also used as received. Distilled water was used for all experiments and washings.

3.2.2. Methods

Synthesis of polystyrene spheres (PSSs)

For the synthesis of PSSs, 100 mL distilled water, 25 mL ethanol and 0.1 g polyvinylpyrrolidone (PVP) were added into a 250 mL round-bottom flask. After all the PVP had dissolved, 8 mL of styrene was added, and the solution was stirred for 15 minutes using a magnetic stirrer. In a beaker, 0.13 g of potassium persulfate (KPS) was dissolved in 10 mL of distilled water and then added to the round bottom flask above, while stirring. The mixture was heated up to 80 °C and the reaction continued for 24 hours. The mixture was then filtered by centrifuge at 18000 rpm for 15 minutes at 10 °C and washed with ethanol. The product (PSSs),

produced in high yield, was dried in an oven at 60 ^{0}C for 12 hours, crushed with a mortar and pestle and then stored in a glass sample vial [25].

Synthesis of polystyrene-b-polyacrylic acid spheres

For the synthesis of PS-*b*-PAA (PAA = poly(acrylic acid)), the same procedure used for the synthesis of polystyrene spheres was followed. However, in this case 0.43 mL or 0.65 mL acrylic acid (AA) was added to the styrene to synthesize 8 mol% and 12 mol% PAA functionalized PSSs (PS-*b*-PAA), respectively. The polymer made with 8% AA was denoted as PS-*b*-PAA_8, and the polymer made with 12% AA was denoted as PS-*b*-PAA_{12}.

Synthesis of Co_xO_y/polymer composites

For the synthesis of 5% Co_xO_y@HCSs, 4 g of polymer spheres (PSSs, PS-*b*-PAA_8 or PS-*b*-PAA_{12}) were dispersed in a mixture of 36 mL ethanol and 100 mL distilled water. Thereafter, the mixture was sonicated for 30 minutes or until the polymer spheres were well dispersed. following on from this step, 0.36 g of cobalt nitrate hexahydrate was added to the mixture, while stirring. The stirring continued until all the cobalt precursor was dissolved (mixture turned pink). Hydrazine hydrate (13 mL, 2 M) was added slowly (dropwise), while stirring, and the reaction continued for 12 hours at room temperature. The mixture was filtered by vacuum filtration and the product was washed with water, dried in the oven at 60 °C for 12 hours, crushed with a mortar and pestle and stored in a glass sample vial. Two and three times the amount of cobalt nitrate and hydrazine were used to make 10% Co_xO_y@HCSs and 15% Co_xO_y@HCSs respectively.

Synthesis of HCSs encapsulated cobalt nanoparticles

The Co_xO_y/PSSs (or Co_xO_y /PS-*b*-PAA_8 or Co_xO_y/PS-*b*-PAA_{12}) composite (3 g) was dispersed in a mixture of 150 mL ethanol, 76 mL distilled water and 12 mL ammonia solution. The mixture was sonicated for 30 minutes or until all the Co_xO_y/PSSs particles were well dispersed. A beaker containing a mixture of 76 mL ethanol; 1.1 g of resorcinol, 1.5 g of CTAB and 2.3 mL of formaldehyde was sonicated until all the CTAB and resorcinol were dissolved. This mixture was added to the Co_xO_y/PSSs (or Co_xO_y/PS-*b*-PAA_8 or Co_xO_y/PS-*b*-PAA_{12}) mixture, while stirring. This reaction continued for 20 hours at room temperature. A brown layer of

resorcinol-formaldehyde (RF) was observed forming around the Co_xO_y-polymer composites. The product was filtered by vacuum filtration, washed with distilled water and ethanol, dried in the oven at 60 °C for 12 hours, crushed with a mortar and pestle and stored in a glass vial.

The dried product was loaded into a quartz boat, placed inside a quartz tube and then placed inside a horizontal tube furnace. The quartz tube was subject to a controlled flow of N_2 gas at 50 mL/min and the furnace was heated to 350 °C at 10°C/min and kept isothermal for 1 hour to decompose all the polymer spheres. It was further heated up to 600 °C at a rate of 10 °C/min and kept isothermal for 2 hours to pyrolyze and carbonize the RF forming a carbon shell that encapsulated the Co nanoparticles. The materials were characterized without any further modification or treatment.

3.2.3. Characterization techniques

FTIR spectroscopy analysis was done using a Bruker Tensor 27 Fourier Transform Infrared spectrometer. SEM analysis was performed on a ZEISS SIGMA 03-39 FE-SEM operating at 20 kV. Samples were dispersed in ethanol, deposited onto carbon tape and coated with a layer of gold-palladium (10 nm) and a layer of carbon (10 nm). TEM analysis was done on a Technai Spirit T12 operating at 120 kV. Samples were dispersed in ethanol by ultrasonication and thereafter loaded onto a lacey carbon copper grid. Metal particle sizes were determined from the TEM data using Mipar image analysis software. More than 400 nanoparticles (for the different samples) were sampled for the particle sizes measured from the TEM images. Thermal analysis was done using a Perkin Elmer TGA 6000 thermogravimetric analyser using high purity nitrogen and air at a heating rate of 10 °C/min and a gas flow rate of 10 mL/min. Powder x-ray diffraction patterns (PXRD) were collected on a Bruker D2 Phaser x-ray diffractometer equipped with a $CuK\alpha_{1/2}$ radiation ($\lambda_{K\alpha}$=0.15406 nm) source and a Lynxeye detector. Samples were scanned over the 2θ range from 5 - 90 °2θ. The metal particle sizes were determined from the PXRD data using Bruker's DIFFRAC.EVA (Release 2014) software. using the Scherrer method. A Micromeritics Tristar 3000 surface area and porosity analyser operating in liquid nitrogen (-195 °C) was used to determine the surface area and porosity of the materials. The samples (100 mg) were degassed at 150 °C for 12 h, under flowing nitrogen. Raman spectroscopy measurements were performed on a Bruker Senterra Raman spectrometer, equipped with a 532 nm laser source.

3.3. Results and discussion

3.3.1. Characterization of polymer spheres

Polymer spheres with uniform morphology and narrow size distribution were successfully prepared, as is evident from the TEM and SEM images collected on these samples (Figures 3.1 and 3.2). From the data contained in Figures 3.1 and 3.2, we observed that the PSSs had an average diameter of 350 nm, while the PS-*b*-PAA_8 and PS-*b*-PAA_{12} had smaller average diameters of 274 nm and 343 nm, respectively. Generally, the diameter of polymer spheres can be controlled by varying the solvent and monomer compositions as well as the initiator and surfactant concentrations [26] [27].

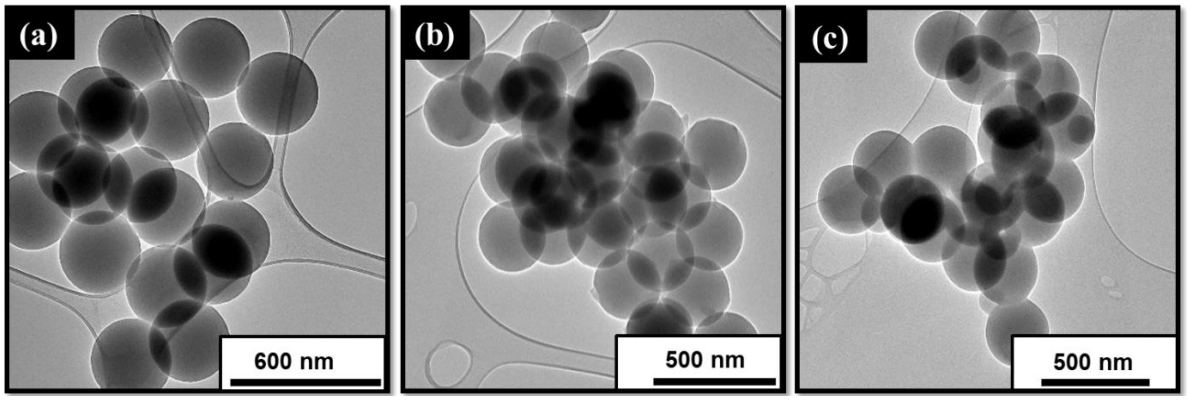

Figure 3.1: TEM images of (a) PSSs, (b) PS-b-PAA8 and (c) PS-b-PAA12

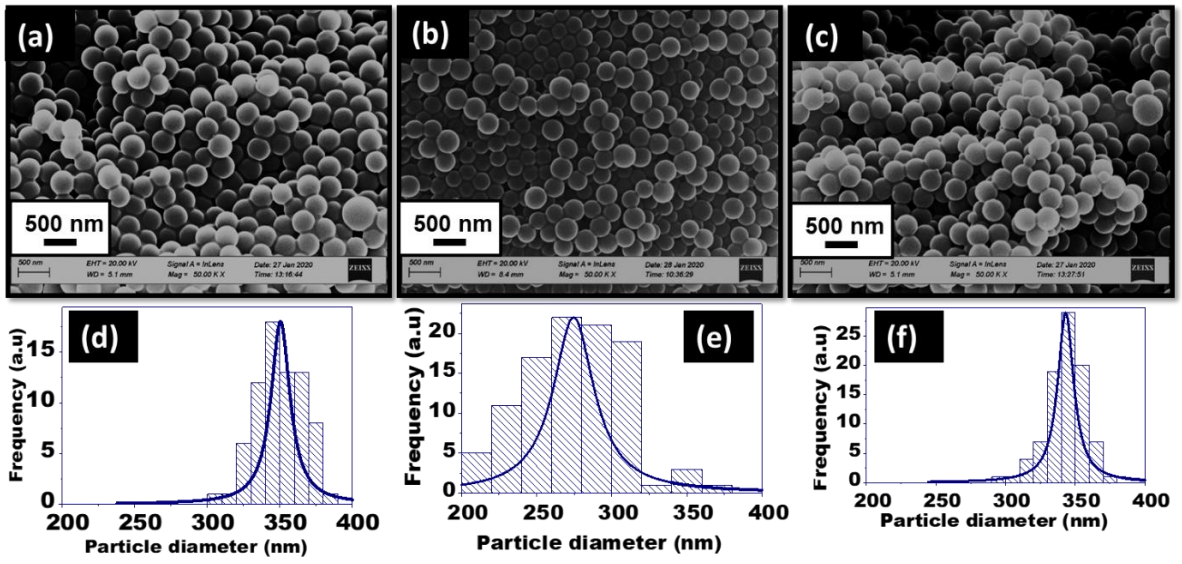

Figure 3.2: SEM micrographs and particle size distribution curves of (a,d) PSSs, (b,e) PS-b-PAA8 and (c,f) PS-b-PAA12.

The FTIR spectra (Figure 3.3) collected on the samples confirmed the successful incorporation of PAA into the PS backbone. The highlighted peak at 1732 cm^{-1} is characteristic of the C=O functional group in PAA [28]. Relative to the rest of the spectra, this peak is of lower intensity due to the small amounts of AA monomer that were used (8 mol% and 12 mol%, relative to styrene monomer). The use of a higher amount of AA monomer generated a PS-*b*-PAA polymer containing a nominal 50 mol% PAA and the IR spectrum of this sample contained a C=O peak with higher relative intensity compared to the samples containing 8 and 12 % PAA (Figure S3.1). However, the morphology of the spheres at the 50% loading was compromised, resulting in the formation of irregularly shaped spheres with high surface roughness (Figure S3.2). The other peaks in the FTIR spectra were due to PS aromatic and aliphatic C-H bonds (1604, 2845, 2925, 3068 and 3025 cm^{-1}) and the PS backbone (1356 and 1493 cm^{-1}) [29]. The OH functionality of the PAA was not readily detected by an absorption between ~3100 and 3400 cm^{-1} [28]. However, when the 50% PAA material was analysed a slight shift in the baseline of the PS-*b*-PAA spectrum in the region between 3000 and 3500 cm^{-1} was observed (Figure S3.1).

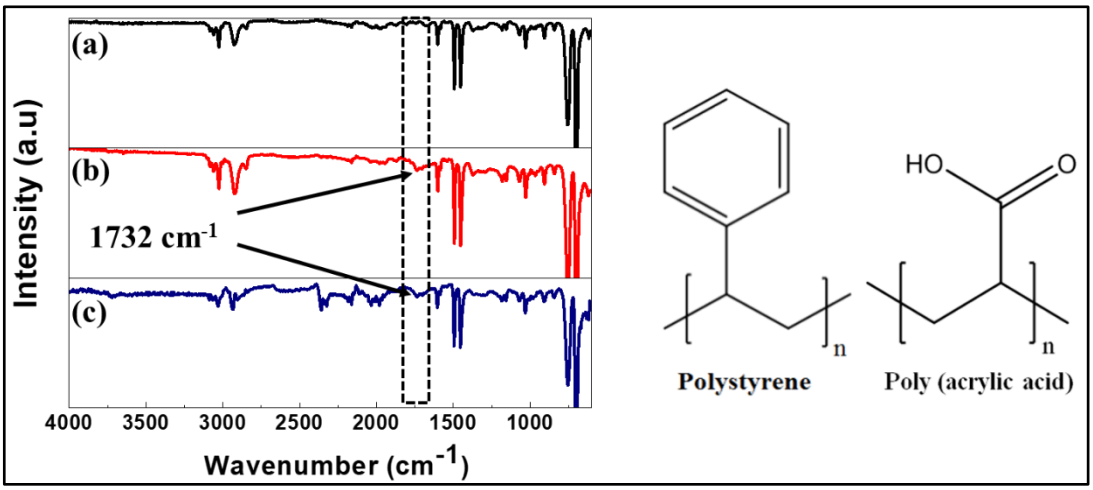

Figure 3.3: FTIR spectra of (a) PSSs, (b) PS-b-PAA8 and (c) PS-b-PAA12 and chemical structures of polystyrene and poly(acrylic acid)

The synthesis of HCSs using polymer spheres as sacrificial templates requires a polymer that has a low decomposition temperature to allow for successful removal of the polymer before the pyrolysis of the carbon RF shell. The maximum decomposition (Figure 3.4) occurs at ~414 °C for PS and PS-*b*-PAA_{12} and ~398 °C for the PS-b-PAA_8. The onset of decomposition occurs at ca. 300 °C and therefore an isothermal treatment at 350 °C for an extended period ensures complete removal of the template. The onset of decomposition occurs at ca. 300 °C for

all polymers and therefore an isothermal treatment at 350 °C for an extended period ensures the complete removal of the template. Higher temperature treatment, for example, such as 400 °C may result in the metal sintering before the successful transfer of the small metal particles to the inner surface of the HCSs. Ideally, a lower template removal temperature is desirable for minimizing metal sintering. Removal of the polymer templates was thus performed by holding the furnace isothermal at 350 °C for 1 hour under N_2. The TGA analysis of the polymers under N_2 is shown in Figure S3.3. The decomposition profile of the polymers is similar under both air and nitrogen atmosphere, the maximum decomposition temperature remained at ca. 410 °C.

The TGA analysis (Figure 3.4) in air confirmed the presence of the PS structure and also revealed some evidence for the presence of the PAA [30] as indicated by small changes in the peak positions and the possibility of a small decomposition event at 503 °C (Figure 3.4a insert) [30]. This was further confirmed by the TGA and DTGA curves of PS-*b*-PAA containing 50% PAA that showed a small mass loss between 200 – 400 °C and at *ca.* 500 °C (Figure S3.4).

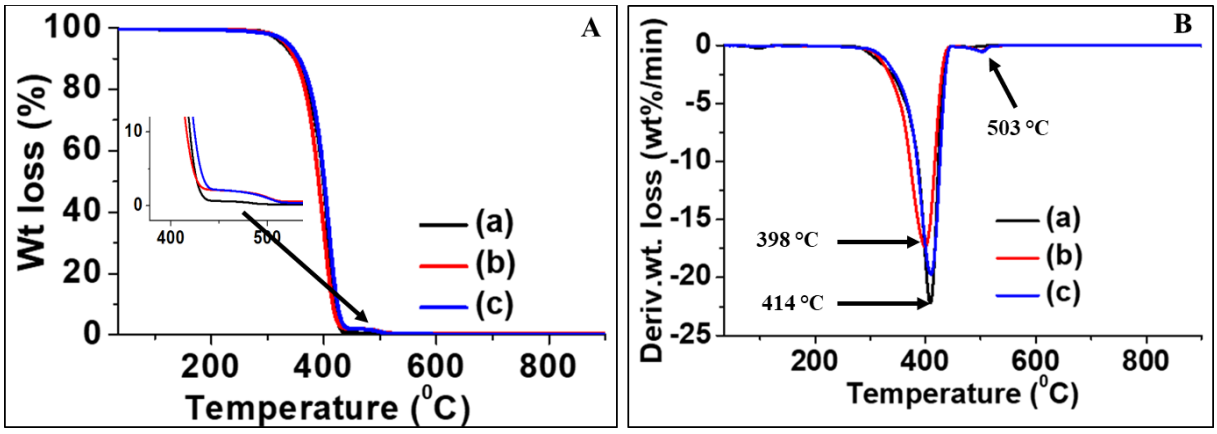

Figure 3.4: TGA (A) and derivative TGA (B) curves of (a) PSSs, (b) PS-b-PAA8 and (c) PS-b-PAA12

3.3.2. Characterization of Co_xO_y@HCSs

The synthesized polymer spheres were used for the synthesis of the Co_xO_y/polymer composites. The loading of Co on the polymer materials was small (ca. 2-5 %) and the PXRD peak intensity of the polymers is very high. It was thus not possible to reliably detect Co in these PXRD patterns. We have added the data to the supplementary section (Figure S3.5). Accordingly, it is not possible to positively identify the metal phases present on the polymer using PXRD.

The Co_xO_y/polymer composites were further used to prepare Co_xO_y nanoparticles encapsulated inside the HCSs (Co_xO_y@HCSs). The HCSs prepared with RF generally have high porosity

and surface area [31]. Furthermore, CTAB was added to the RF during the synthesis of the shell to enhance the mesoporosity of the final HCSs [32].

Table 3.1: BET data for all the catalysts

Catalyst	BET Surface area (m^2/g)	Micropore area (m^2/g)	Pore diameter (nm)	Pore volume (cm^3/g)
5%Co@HCSs_PS	612	320	4.8	0.57
5%Co@HCSs_PS-*b*-PAA$_8$	515	263	5.3	0.54
5%Co@HCSs_PS-*b*-PAA$_{12}$	506	273	4.7	0.45
10%Co@HCSs_PS	316	154	7.0	0.47
10%Co@HCSs_PS-*b*-PAA$_8$	433	255	5.0	0.39
10%Co@HCSs_PS-*b*-PAA$_{12}$	479	267	5.0	0.46
15%Co@HCSs_PS	388	270	5.1	0.36
15%Co@HCSs_PS-*b*-PAA$_8$	348	209	5.9	0.41
15%Co@HCSs_PS-*b*-PAA$_{12}$	441	180	6.6	0.63

The BET isotherms and pore size distributions of the 5% Co_xO_y@HCSs catalysts are reported in Figure 3.5 and Figures S3.6 and S3.7 for the 10% and 15% catalysts, respectively. The catalysts have similar adsorption isotherms which are typical of a material with a combination of type I and type IV pore structures [33]. This is an indication of the presence of micropores and mesopores in these catalysts. The pore size distribution plots also confirmed this and showed a high content of pore diameters <10 nm. The tabulated data (Table 3.1) showed that ~50% of the total BET surface area was due to the micropores. Comparison of the data at the different Co loadings indicated a decreased surface area with increasing Co loading. It has previously been reported that Co nanoparticles can block some of the pores of the carbon shell and therefore reduce the surface area and this could potentially account for the loss of surface area seen here [15]. The effect of PAA loading on the surface area is however less clear. For example, for the 5% catalysts, (where the Co particle size remained constant at *ca.* 6 nm; see below) the HCSs prepared with the PS template had a higher surface area (612 m^2/g) than the catalysts PS-*b*-PAA_8 (515 m^2/g) and PS-*b*-PAA_{12} (506 m^2/g). However, data collected on the 10 % and 15% Co-loaded PAA samples (Co particle size similar) generally indicated an increased surface area with an increase in PAA loading. The catalysts 10%Co_yO_x@HCSs_PS and 15%Co_yO_x@HCSs_PS both have large metal nanoparticles which are poorly distributed

on the inner surface of the support. However, the TEM images of the 10%Co_yO_x@HCSs_PS showed the presence of some small nanoparticles that can easily block the micropores, as opposed to the 15%Co_yO_x@HCSs_PS which only had large particles that can easily block mesopores. This was also confirmed by the high micropore surface area (270 m^2/g) of the 15% catalyst, which is 70% of the total BET surface area (388 m^2/g). Meanwhile, the 10% catalyst has a micropore surface area (154 nm) which is 50% of the total BET surface area (316 nm), which indicated that this catalyst had a relatively lower volume of micropores.

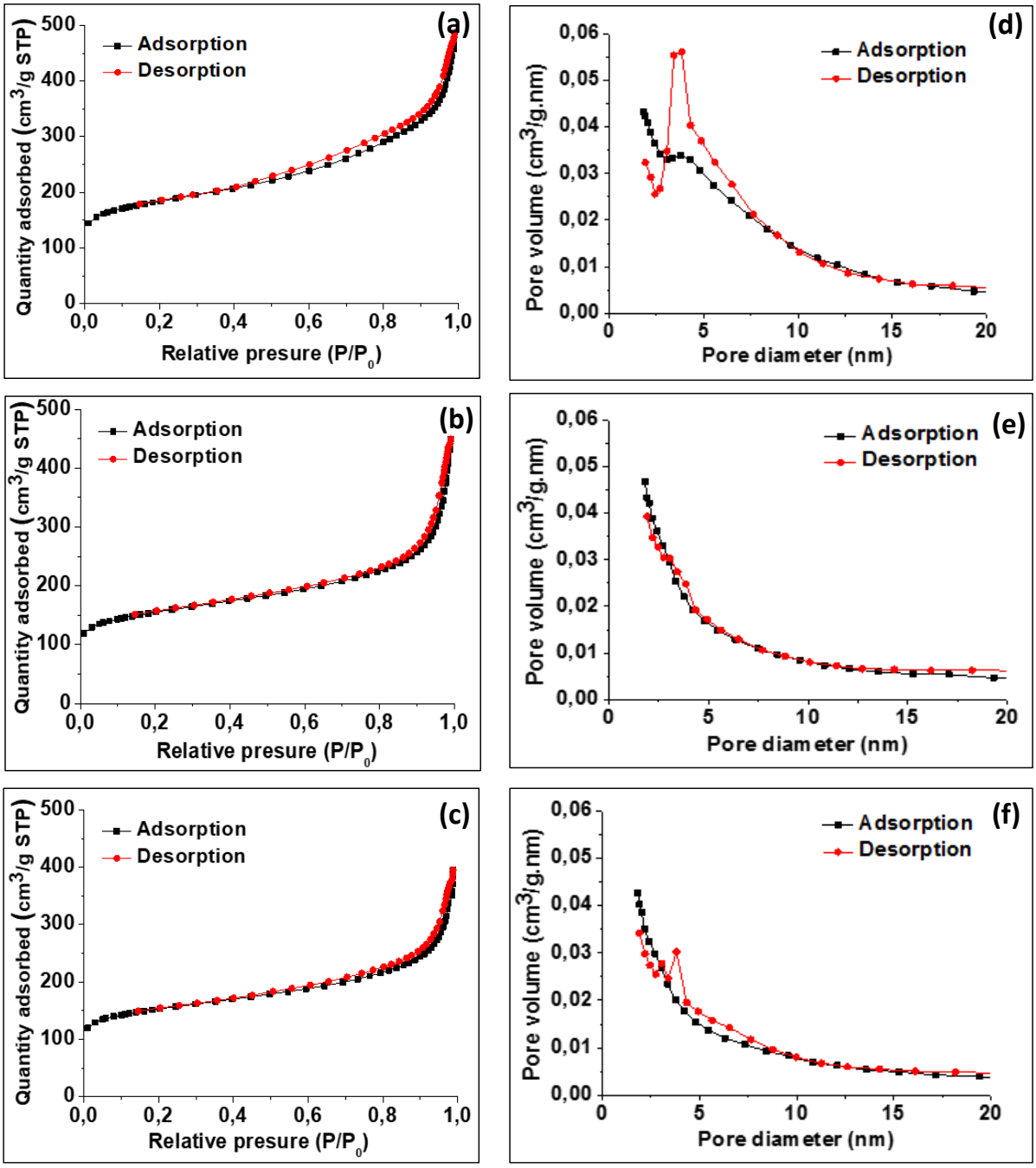

Figure 3.5: BET isotherms and pore size distribution plots of 5% CoxOy@HCSs, prepared with different templates, (a,d) PS, (b,e) PS-b-PAA8 and (c,f) PS-b-PAA12.

Raman spectra (Figure 3.6) of the samples showed the typical peaks expected for carbon materials, which are characterized by broad D (~1340) and G bands (~1585) [34]. The peak positions showed a little variation for the different samples. The area ratios of the D and G (I_D/I_G) peaks were used to measure the extent of structural defects and disorders in the carbon materials (Table 3.2). The different samples showed I_D/I_G ratios ranging from 0.8 to 1.3 which is indicative of a mix of sp^2 and sp^3 components, but no clear trends could be observed that correlated the data with the carbon structures or the Co loaded onto it. The presence of Co_3O_4 was observed in the Raman spectra at ca. 675 cm^{-1} [35]. It is suspected that the peaks observed at 880 and 1300 cm^{-1} could be related to the presence of residual poly(acrylic acid) [36] [37] [38].

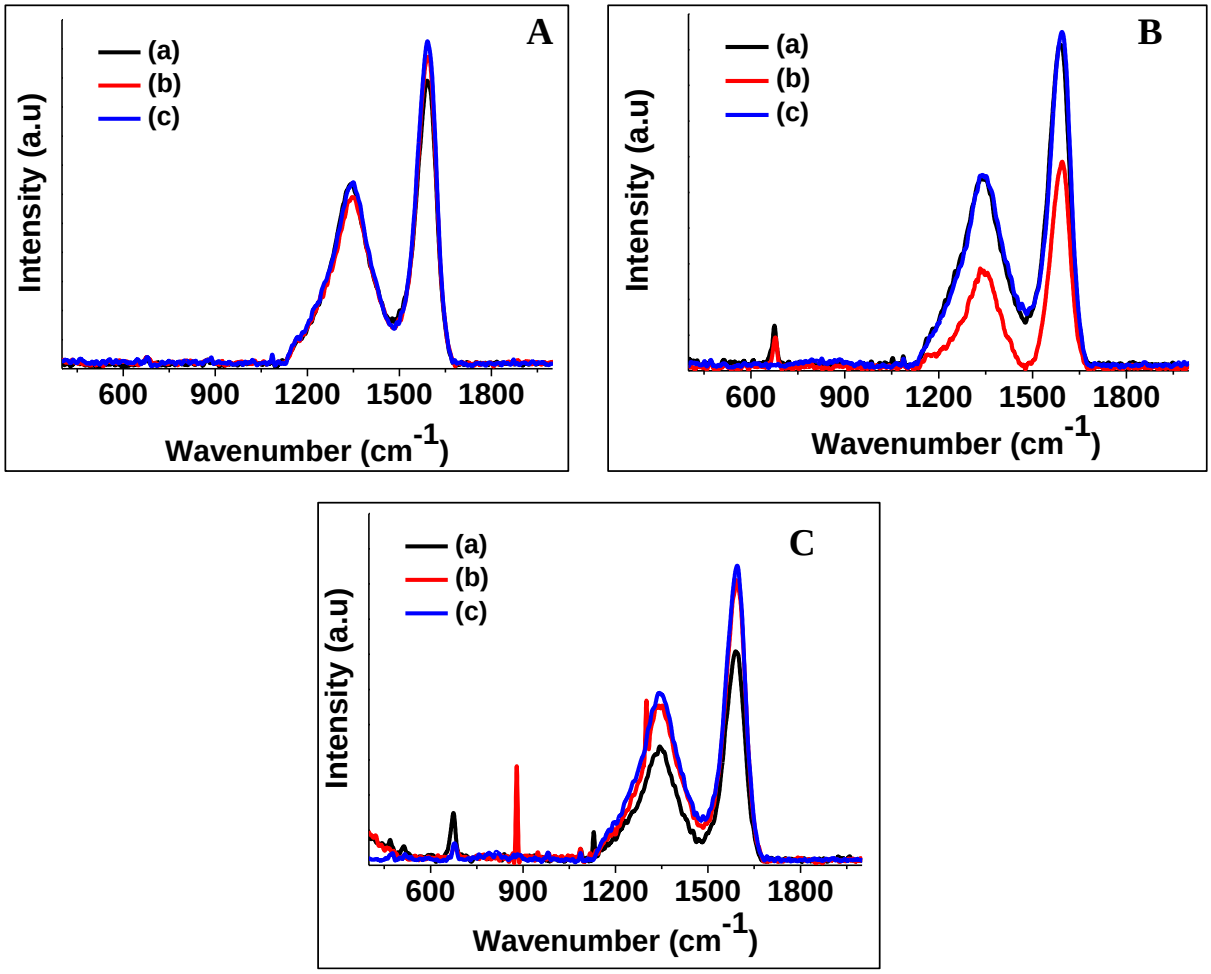

Figure 3.6: Raman spectra of 5% (A), 10% (B) and 15% (C) CoxOy@HCSs prepared with different templates PS (a), PS-b-PAA8 (b) and PS-b-PAA12 (c)

Table 3.2: Raman analysis data

Catalyst	Raman shift (cm^{-1})		I_D/I_G
	D-band	G-band	
5%Co@HCSs_PS	1342	1588	1.3
5%Co@HCSs_PS-*b*-PAA$_8$	1344	1588	1.1
5%Co@HCSs_PS-*b*-PAA$_{12}$	1342	1589	1.2
10%Co@HCSs_PS	1339	1584	1.2
10%Co@HCSs_PS-*b*-PAA$_8$	1338	1589	0.8
10%Co@HCSs_PS-*b*-PAA$_{12}$	1341	1588	1.2
15%Co@HCSs_PS	1340	1587	0.9
15%Co@HCSs_PS-*b*-PAA$_8$	1344	1587	1.0
15%Co@HCSs_PS-*b*-PAA$_{12}$	1343	1589	1.2

Figure 3.7 shows the TEM images of the Co loaded HCSs. The average internal diameters for the HCSs prepared with PS, PS-*b*-PAA$_8$ and PS-*b*-PAA$_{12}$ were measured and found to be 344, 245 and 284 nm, respectively. These values are smaller than the diameters measured on the polymer templates. The shrinkage was larger for the polymers containing the PAA. The polymer shrinkage relates to the high-temperature treatment used during synthesis as well as a possible role for the Co catalysing carbon decomposition. The average carbon shell thicknesses were similar for the HCSs prepared with PS, PS-*b*-PAA$_8$ and PS-*b*-PAA$_{12}$ (27, 20 and 25 nm). Figure 3.7(a,d,g) show TEM images of the Co_xO_y@HCSs prepared with different templates (PS, PS-b-PAA$_8$ and PS-b-PAA$_{12}$) at 5% Co loading. The corresponding particle size distribution curves are reported in Figure S3.8 and average particle diameters are reported in Table 3.3. No substantial differences were noted with regards to the size of the Co nanoparticles (5.4 to 6.1 nm, Table 3.3). However, on increasing the Co loading to 10% and 15%, the Co nanoparticles synthesized with the PS template were observed to be very large (38 – 44 nm), poorly dispersed and irregularly shaped (Figure 3.7(b,c)). In contrast, the Co nanoparticles prepared from the copolymer (PS-*b*-PAA$_8$ and PS-*b*-PAA$_{12}$) templates at these Co loadings only showed small Co nanoparticles with an expected small increase in Co size with loading (5.8 to 6.6 nm, Table 3). Thus, from this evidence we can conclude that the use of the PS-*b*-PAA templates had led to the synthesis of stabilized Co nanoparticles with high metal loading

and good dispersion. The PS-*b*-PAA catalysts have smaller Co metal particle sizes indicating that this template had a stronger interaction with the metal and was better at stabilizing the metal particles. It has been previously reported in literature that highly asymmetric block-copolymers facilitate metal nanoparticle interactions [5]. The data obtained also indicates that the small Co nanoparticles synthesized on the template have readily been transferred to the HCS shell.

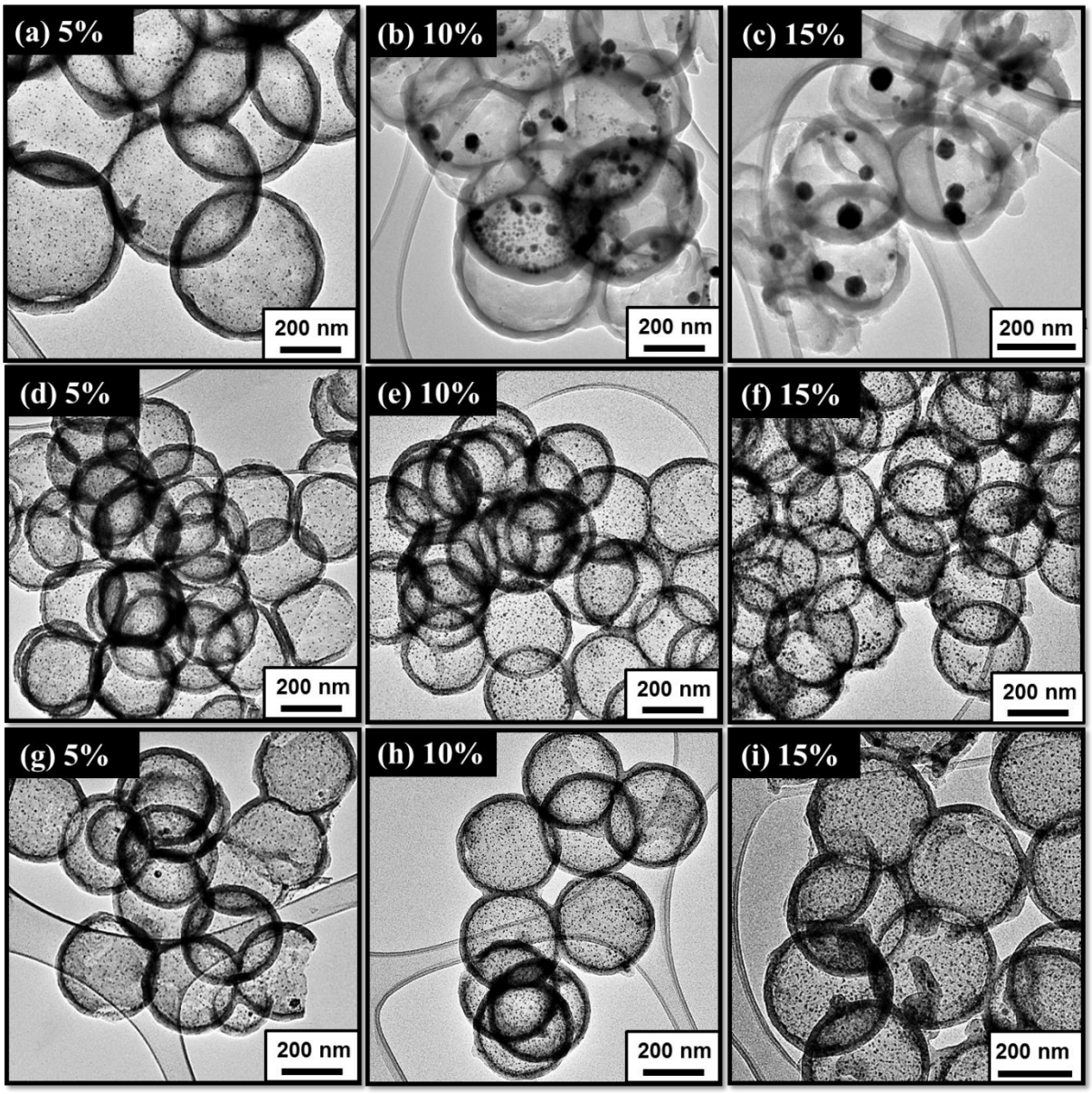

Figure 3.7: TEM micrographs of 5%, 10% and 15% CoxOy@HCSs prepared with different templates PS (a,b,c), PS-b-PAA8 (d,e,f) and PS-b-PAA12 (g,h,i)

The metal nanoparticle sizes/diameters were also measured by PXRD using EVA software by applying the Scherrer equation to the most prominent peaks from the corresponding PXRD diffractograms (Table 3.3). The PXRD measured sizes of the Co catalyst particles prepared

with the PS template were 12.7, 18.1 and 18.7 nm for the 5%, 10% and 15% Co_xO_y@HCSs, respectively, showing the expected increase in size with loading. As expected, the PXRD particle sizes were not the same as those measured from TEM images [15], but similar trends in the data sets can be seen. The TEM and PXRD data both confirm that the functional groups on the templates assisted with controlling the metal particle size.

An unexpected finding was the detection of the growth of a small number of carbon nanofibers inside the Co_xO_y/PS-b-PAA samples (e.g. see Figures 3.7f and 3.7i). Co is a well-known catalyst that is used to make carbon nanotubes (CNTs) and carbon nanofibers (CNFs) [39] [40]. Clearly, at the high Co loadings the small Co nanoparticles were able to make CNFs/CNTs from the carbon materials produced during the template removal and shell construction from the RF at the reaction temperatures employed (600 ^oC).

Table 3.3: Particle size and metal loading

Catalyst	TEM Co[a] diameter (nm)	PXRD Co[b] diameter (nm)	% Co_3O_4 (TGA)	% Co (TGA)	% Co (ICP-OES)
5%Co@HCSs_PS	6.1	12.7[c]	6.3	4.6	8.7
5%Co@HCSs_PS-*b*-PAA$_8$	5.4	4.0	6.3	4.6	5.0
5%Co@HCSs_PS-*b*-PAA$_{12}$	6.1	6.6[d]	6.3	4.6	4.4
10%Co@HCSs_PS	38	18.1	17.0	12.1	11.2
10%Co@HCSs_PS-*b*-PAA$_8$	5.8	3.9	15.0	11.0	7.4
10%Co@HCSs_PS-*b*-PAA$_{12}$	6.0	> 4[e]	15.0	11.0	10.1
15%Co@HCSs_PS	44	18.7	22.5	16.4	13.6
15%Co@HCSs_PS-*b*-PAA$_8$	6.6	6.1	22.5	16.4	20.7
15%Co@HCSs_PS-*b*-PAA$_{12}$	6.3	-	31.7	23.1	19.4

[a]based on Co particles, [b]based on Co size in Figure 9, [c]based on Co_3O_4, [18]based on CoO, [e]overlapping Co and CoO

SEM images (Figure 3.8) showed that the HCSs are hollow, as indicated by the holes that were present in some of the spheres (circled in red). The holes indicated poor coverage of some of the template spheres by the RF. There are fewer holes present on the catalysts prepared with the PS-*b*-PAA templates (Figure 3.8(d-i)), relative to the PSS derived samples which is an indication of a better RF coating on these templates. This is expected as the RF would interact

with PAA better than with the PSS. The role of the Co loading on the morphology of the HCSs could also be seen in the SEM images. The 5% catalyst prepared from the PSSs template (Figure 3.8a) had some spheres with holes, while the 10% and 15% catalysts prepared from the PSSs template (Figure 3.8(b, c)) showed more spheres with holes as well as some broken spheres and some with an irregular shape (Figures S3.9, S3.10). It is thus possible that the Co_xO_y species may also remove the carbon during the high temperature RF carbonization step.

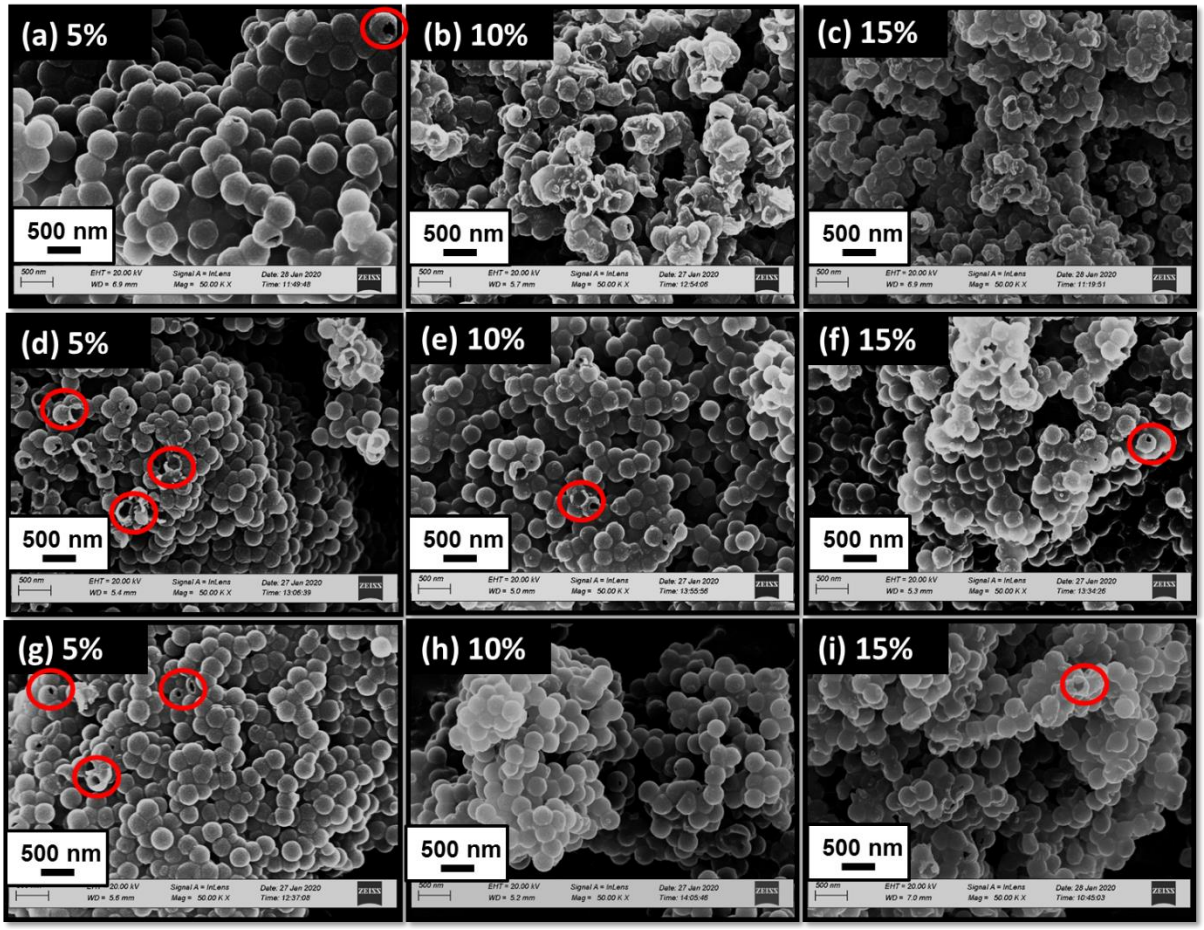

Figure 3.8: SEM micrographs of (5%, 10% and 15%) CoxOy@HCSs prepared with different templates PS (a,b,c), PS-b-PAA8 (d,e,f) and PS-b-PAA12 (g,h,i)

The size of the metal nanoparticles could also have an impact on the polymerization of the RF coating of the polymer spheres. The catalysts with the small metal nanoparticles are seen to have fully spherical HCSs with fewer holes. There is a possibility that the Co nanoparticles act as nucleation sites for the synthesis of the RF polymer resulting in a more uniform coating around the template spheres. It was previously reported that transition metals can catalyse the formation of graphitic structures [41] and there is evidence that transition metal ions influence

the synthesis of RF [42]. In other studies, Pt, Pd, Ag, Fe, Co and Ni salts were used as catalysts for the synthesis of resorcinol-formaldehyde to obtain metal-doped carbon [43] [44].

The PXRD data of pristine HCSs synthesized with the three different templates are shown in Figure S3.9. Two peaks corresponding to the (002) and (100) planes of carbon are observed for all the diffractograms at ~20 °2θ and ~44 °2θ, respectively. The peak broadening indicates the presence of amorphous carbon with a low degree of graphitization [6] [45] [46]. The PXRD data of Co_xO_y@HCSs catalysts are shown in Figure 3.9. The data showed that the samples contained Co in various oxidation states with the Co_3O_4, CoO and Co phases observed and that the presence and relative amounts of these phases were influenced by Co loading and the Co particle size. The PS template showed a mixture of all these three oxidation states, while the PS-*b*-PAA_8 template appeared to form mainly Co, at the different Co loadings. The PS-*b*-PAA_{12} template formed mainly the CoO phase at the 5 % loading and a mixture of Co, CoO and Co_3O_4 at higher Co loadings. It thus appeared that there was a competition between the air oxidation of cobalt to produce Co_yO_x phases and carbon reduction of the Co_yO_x, to produce Co metal. These effects will be dependent on the Co particle size, Co-C interactions as well as surface area/porosity of the HCS. The synthesized Co@HCS materials can be oxidized in air or oxygen at elevated temperatures for an extended period to produce pure Co_3O_4 inside HCSs. This oxidation must be done at temperatures below the onset of decomposition of the carbon materials to avoid oxidation of the carbon to carbon dioxide. In our study, the TGA data (Figure 3.10) indicated that the onset of decomposition of the carbon material is < 350 °C and therefore the oxidation can be done at 200 °C or below. In cases where pure Co is required, the materials can be reduced in hydrogen to produce Co inside HCSs. The hydrogenation should be done at the reduction temperature of the metal oxide. This hydrogenation temperature must be below the methanation temperature of the carbon. Temperature-programmed reduction (TPR) studies have been used to investigate the cobalt oxide reduction temperature as well as the carbon methanation temperature. TPR studies have indicated that the onset of reduction of Co_3O_4 to CoO occurs at ca. 200 °C and the onset of reduction of CoO to Co occurs at ca. 350 °C. Therefore, treatment of these materials at 350 °C under flowing H_2 for an extended period should yield Co inside HCSs. The TPR studies have further indicated that the methanation of the carbon shell occurred above 500 °C, therefore any hydrogen treatments below 500 °C should not result to methanation.

The °2θ positions of the peaks observed in the PXRD data are reported in Tables S3.1, S3.2 and S3.3 for the 5%, 10% and 15% Co loaded catalysts, respectively. It is to be noted that only a small C peak is observed in the PXRD for the Co_xO_y/PS samples. The absence of carbon in Figure 3.9A(a) is caused by the fluorescence effect of cobalt oxide under copper radiation which results to a high background [47].

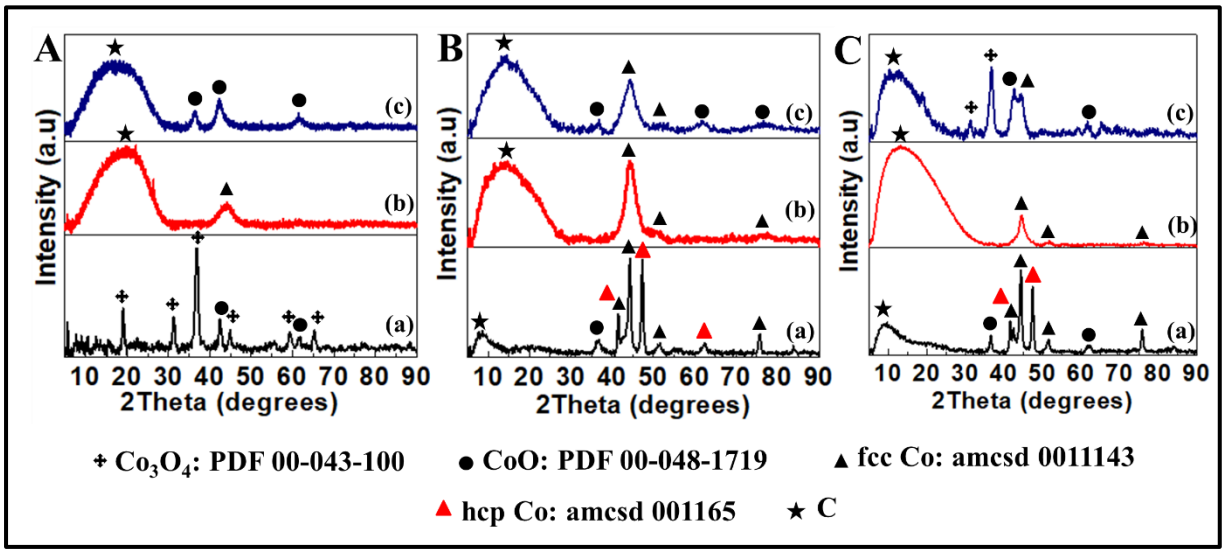

Figure 3.9: PXRD of 5% (A), 10% (B) and 15% (C)) Co_xO_y@HCSs prepared with different templates, (a) PS, (b) PS-b-PAA8 and (c) PS-b-PAA12

The TGA curves of the HCSs, before Co addition, indicated complete decomposition after thermal treatment (Figure S3.10), indicating 100% removal of the carbon shell. TGA and DTA curves for the Co containing HCSs are shown in Figure 3.10 and allow for the determination of the Co loading on the HCSs from the residue of Co_3O_4 remaining after combustion in air. The TGA data show that the Co loadings are in general close to the nominal values used in the synthesis procedure. ICP-OES analysis was also performed on the Co/HCS samples and the data are given in Table 3.3. The ICP-OES data, although showing the correct trends in Co content, appear to be less reliable than the TGA data.

The thermal decomposition of the HCSs without metal nanoparticles occurred from 500 °C to 600 °C (Figure S3.10) [48]. The data showed very little change in the maximum decomposition point in the three different samples. The TGA profile of the pristine HCSs (Figure S10) suggested a two-step decomposition at high temperature with a shoulder peak at ca 650 ^oC due to a highly graphitic component of the carbon shell.

Figure 3.10 contains the TGA and DTA curves of the Co_xO_y@HCS samples. The samples decompose above 300 ^oC but a peak at ca. 150 ^oC, pronounced for the 5% loaded catalysts, was also observed; this could be related to moisture. It has been previously reported that the presence of Co nanoparticles can accelerate carbon decomposition such that the HCSs decompose at temperatures < 500 °C (Figure S3.10) [15] [49]. The decomposition of the Co/HCSs between 300 ^oC and 600 ^oC appears to be made up of at least three peaks that vary with the samples (Table S3.1). The low temperature peak (< 380 ^oC) is proposed to be due to the Co catalysed decomposition of disordered carbon structures, with the middle peak (395 – 470 ^oC) thought to be due to the Co catalysed decomposition of graphitic segments of the carbon shell. The peak at *ca.* 560 ^oC was thought to be related to carbon decomposition with little impact of any catalytic effect of the Co.

At the 5% Co loading (Figure 3.10 A, D; Table S3.1) two peak maxima were observed for all three Co samples. In these three samples, the Co particle sizes were very similar (6 nm) and thus differences relate to the Co oxidation state/small changes in particle size/carbon graphiticity. The Co in the PAA derived Co_xO_y@HCS samples appeared to oxidize the HCS more readily than the Co in the PSS derived sample.

At the 10% loadings (Figure 3.10 B, E) and 15% loadings (Figures 3.10 C, F) the HCSs prepared from PSSs both showed two broad peaks at ca. 420 and 550 ^oC (Table S3.1). This is consistent with the presence of large Co particles such that less carbon was in contact with Co relative to 5% Co loaded sample. Thus, the carbon that interacted with the Co would decompose at the lower T (*ca.* 400 ^oC) while the carbon that had little contact with the Co would decompose close to that expected where catalysis played a little role (550 ^oC) (see Figure S3.10 and Table S3.1). In contrast, the two catalysts prepared with PS-*b*-PSAA templates both had well dispersed small Co particles and thus decomposed at *ca*. 330 and 420 ^oC (Table S3.1) due to interaction with the different types of carbon species. Furthermore, at the higher Co loading a sharper decomposition T was observed as predicted when more carbon was in contact with the Co.

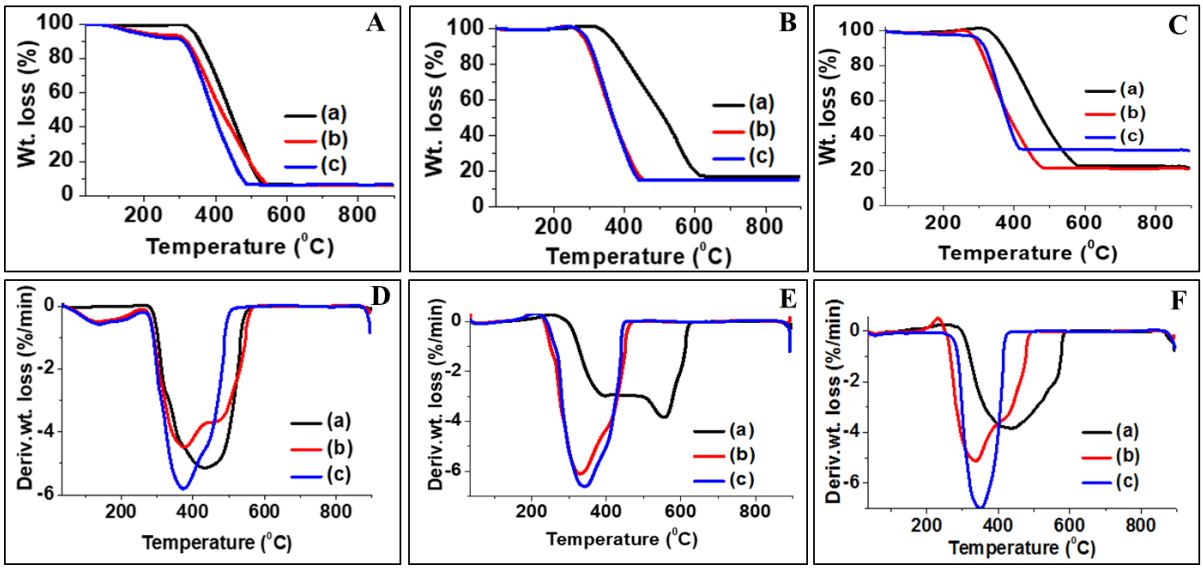

Figure 3.10: TGA and derivative TGA curves of 5% (A,D), 10% (B,E) and 15% (C,F)) CoxOy@HCSs prepared with different templates PS (a), PS-b-PAA8 (b) and PS-b-PAA12 (c)

Conclusion

The aim of this work was to establish a method to control metal nanoparticle growth during the synthesis of Co_xO_y@HCSs. Small amounts of acrylic acid added to the styrene polymerization mixture were sufficient to introduce functional groups on the surface of polystyrene spheres. The presence of the functional groups was confirmed by FTIR and TGA analysis. The metal nanoparticles synthesized varied in size and composition. Smaller nanoparticles were synthesized due to the presence of functional groups introduced by poly(acrylic acid) at high Co concentrations (10% and 15% loadings). The composition of the cobalt nanoparticles showed variation between Co, CoO and Co_3O_4 that was influenced by the particle size and metal loading. The structural integrity and thermal decomposition of the carbon shell were also influenced by the size of the metal nanoparticles. The materials had a relatively high BET surface area with a mesoporous carbon shell. The method here suggested that it should be possible to use other functional polymers such as poly(methyl methacrylate) and poly(ethylene imine) to control the growth of other metal nanoparticles inside HCSs.

References

[1] L. Perez, M. R. Axet, D. Yi, P. Serp and K. Soulantica, “Selective hydrogenation of cinnamaldehyde by unsupported and few layer graphene supported platinum concave nanocubes exposing {110} facets stabilized by long-chain amine,” Catalysis Today, 2019.

[2] L. J. Garces, B. Hincapie, R. Zerger and S. L. Suib, “The effect of temperature and support on the reduction of cobalt oxide: An in-situ X-ray diffraction study,” Journal of Physical Chemistry C, vol. 119, pp. 5484-5490, 2015.

[3] E. Iglesia, S. L. Soled and R. A. Fiato, “Fischer-Tropsch synthesis on cobalt and ruthenium metal dispersion and support effects on reaction rate and selectivity,” J. Catal., vol. 137, pp. 212-224, 1992.

[4] M. Lualdi, “Fischer-Tropsch synthesis over cobalt based catalysts for BTL applications,” Unpublished Ph.D. thesis, Department of chemical engineering, Stockholm, Sweden, 2012.

[5] A. D. Pomogailo and G. I. Dzhadimalieva, “Reduction of metal ions in polymer matrices as a condensation method of nanocomposite synthesis,” in Nanostructure materials preparation via condensation ways, Dordrecht, Springer, 2014.

[6] T. N. Phaahlamohlaka, D. O. Kumi, M. W. Dlamini, L. L. Jewell and N. J. Coville, “Ruthenium nanoparticles encapsulated inside porous hollow carbon spheres: A novel catalyst for Fischer-Tropsch synthesis,” Catalysis Today, vol. 275, pp. 76-83, 2016.

[7] C. Dong, Q. Yu, R.-P. Ye, P. Su, J. Liu and G.-H. Wang, “Hollow carbon spheres nanoreactors loaded with PdCu nanoparticles: Void-confinement effects in liquid-phase hydrogenations,” Angew. Chem. Int. Ed, p. 10.100/anie.202007297.

[8] I. Nongwe, V. Ravat, R. Meijboom and N. J. Coville, “Pt supported nitrogen doped hollow carbon spheres for the catalysed reduction of cinnamaldehyde,” Applied Catalysis A: General, vol. 517, pp. 30-38, 2016.

[9] S. Bin, Z.-X. Chi, Y. Li, K. Zhang, X. Yang, Y.-G. Sun, J.-Y. Piao, A.-M. Cao and L.-J. Wan, “Controlling the compositional chemistry in single nanoparticles for functional hollow carbon nanospheres,” J. Am. Chem. Soc, vol. 139, no. 10.1021/jacs.7b07027, pp. 13492-13498, 2017.

[10] F. Xu, Z. Tang, S. Huang, L. Chen, Y. Liang, W. Mai, H. Zhong, R. Fu and D. Wu, “Facile synthesis of ultrahigh-surface-area hollow carbon nanospheres for enhanced adsorption and energy storage,” Nature Commun., vol. 6, no. 7221, p. 12 pages, 2015.

[11] F. Xu, B. Ding, Y. Qiu, R. Dong, W. Zhuang, X. Xu, H. Han, J. Yang, B. Wei, H. Wang and S. Kaskel, “Generalized domino-driven synthesis of hollow hybrid carbon spheres with ultrafine metal nitrides/oxides,” Matter, vol. 3, pp. 246-260, 2020.

[12] L.-P. Yang, X.-J. Lin, X. Zhang, W. Zhang, A.-M. Cao and L.-J. Wan, “A general synthetic strategy for hollow hybrid microspheres through a progressive-inward-crystallization process,” J. Am. Chem. Soc, vol. 138, pp. 5916-5922, 2016.

[13] F. Xu, Y. Lu, J. Ma, Z. Huang, Q. Su, R. Fu and D. Wu, “Facile, general and template-free construction of monodisperse yolk-shell metal@carbon nanospheres,” Chem. Commun., vol. 53, pp. 12136-12139, 2017.

[14] P. M. Gangatharan, M. S. Maubane-Nkadimeng and N. J. Coville, “Building carbon structures inside hollow carbon spheres,” Scientific Reports, vol. 9, p. 10642, 2019.

[15] T. N. Phaahlamohlaka, D. O. Kumi, M. W. Dlamini, R. Forbes, L. L. Jewell, D. G. Billing and N. J. Coville, “Effects of Co and Ru intimacy in Fischer-Tropsch catalysis using hollow carbon sphere supports: Assessment of the hydrogen spillover processes,” ACS Catalysis, vol. 7, pp. 1568-1578, 2017.

[16] S. Forster, “Amphilic block copolymers for templating applications,” Topic in Current Chemistry, vol. 226, pp. 1-28, 2003.

[17] P. Alexandridis and M. Tsianou, “Block copolymer-directed metal nanoparticle morphogenesis and organization,” European Polymer Journal, vol. 47, pp. 569-583, 2011.

[18] S. Forster and M. Konrad, “From self-organizing polymers to nano- and biomaterials,” Journal of Materials Chemistry, vol. 13, pp. 2671-2688, 2003.

[19] Y. Cai-Li, “Preparation of the monodispersed carboxyl-functionalized polymer microspheres with disproportionated rosin moiety and adsorption of methylene blue,” Adsorption Science and Technology, vol. 36, pp. 1260-1273, 2018.

[20] S. M. Cho, G. Song, C. Park, Y. Lee, H. S. Kang, W. Lee, S. Park, J. Huh, D. Y. Ryu and C. Park, “Surface functionalized nanostructures via position registered supramolecular polymer assembly,” Nanoscale, vol. 10, pp. 6333-6342, 2018.

[21] H. J. Martin, B. T. White, C. J. Scanlon, T. Saito and M. D. Dadmun, “Tunable synthetic control of soft polymeric nanoparticles morphology,” Soft Matter, vol. 13, pp. 8849-8857, 2017.

[22] Y. Wang, A. V. Biradar, G. Wang, K. K. Sharma, C. T. Duncan, S. Rangan and T. Asefa, “Controlled synthesis of water-dispersible faceted crystalline copper nanoparticles and their catalytic properties,” Chemistry: A European Journal, vol. 16, pp. 10735-10743, 2010.

[23] S. Klingelhofer, W. Heitz, A. Greiner, S. Forster and M. Antonietti, “Preparation of palladium colloids in block copolymer micelles and their use for the catalysis of the heck reaction,” Journal of the American Chemical Society, vol. 119, pp. 10116-10120, 1997.

[24] L. Zhang and A. Eisenberg, “Multiple Morphologies of "Crew-Cut" Polystyrene-b-poly(acrylic acid) Block Copolymers,” Science, vol. 268, pp. 1728-1731, 1995.

[25] J. Fu, Q. Xu, J. Chen, X. Huang and X. Tang, “Controlled fabrication of uniform hollow core porous shell carbon spheres by the pyrolysis of core/shell polystyrene/crosslinked polyphosphazene composites,” Chem. Comm., vol. 46, pp. 6563-6565, 2010.

[26] J. Liu, S. Z. Qiao, H. Lui, J. Chen, A. Orpe, D. Zhao and G. Q. Lu, “Extension of the Stober method to the preparation of monodisperse resorcinol-formaldehyde resin polymer and carbon spheres,” Angewandte Chemistry International Edition, vol. 50, pp. 5947-5951, 2011.

[27] L. Luo and A. Eisenberg, “Thermodynamic size control of block copolymer vesicles in solution,” Langmuir, vol. 17, pp. 6804-6811, 2001.

[28] N. Ayres, S. G. Boyes and W. J. Brittain, “Stimuli-responsive polyelectrolyte polymer brushes prepared via atom-transfer radical polymerization,” Langmuir, vol. 23, pp. 182-189, 2007.

[29] M. Arslan, G. Yilmaz and Y. Yagci, “Synthesis of polystyrene-b-poly(ethylene glycol) block copolymers by radical exchange reactions of RAFT agents,” Designed Monomers and Polymers, vol. 17, pp. 238-244, 2014.

[30] M. a. a.-H. Abood, “Synthesis and characterization of grafted polystyrene with acrylic acid using gamma-irradiation,” Australian Journal of Basic and Applied Science, vol. 7, pp. 746-750, 2013.

[31] S. A. Al-Muhtaseb and J. A. Ritter, “Preparation and properties of resorcinol formaldehyde organic and carbon gels,” Advanced Materials, vol. 15, pp. 101-114, 2003.

[32] W. Cai, M. Gu, W. Jin and J. Zhou, “CTAB functionalized C@SiO2 double-shelled hollow microspheres with enhanced and selective adsorption performance for Cr(VI),” Journal of Alloys and compounds, vol. 777, pp. 1304-1312, 2019.

[33] X. Lui, S. Li, J. Mei, W. M. Lau, R. Mi, Y. Li, H. Liu and L. Liu, “From melamine-resorcinol-formaldehyde to nitrogen-doped carbon xerogels with micro and mesopores for lithium batteries,” Journal of Materials Chemistry A, vol. 2, p. 14429, 2015.

[34] T. H. Mongwe, B. J. Matsoso, B. K. Mutuma, N. J. Coville and M. S. Maubane, “Synthesis of chain-like carbon nano-onions by a flame assisted pyrolysis technique using different collecting plates,” Diamond & Related Materials, vol. 90, pp. 135-143, 2018.

[35] C.-W. Tang, C.-B. Wang and S.-H. Chien, “Characterization of cobalt oxides studied by FT-IR, Raman, TPR and TG-MS,” Thermochimica Acta, vol. 473, pp. 68-73, 2008.

[36] J. Koo, J. Kim, H. Lee, H. Chung, Y. Lee, W. Yi and D. Sohn, “Formation and characterization of poly(acrylic acid) on silica particles irradiated by y-ray radiation,” Macromolecular Research, vol. 20, pp. 138-142, 2012.

[37] M. Todica, R. Stefan, C. V. Pop and L. Olar, “IR and Raman investigation of some poly(acrylic) acid gels in aqueous and neutralized state,” Acta Physica Polonica A, vol. 128, pp. 128-135, 2015.

[38] C. Murli and Y. Song, “Pressure-induced polymerization of acrylic acid: A Raman spectroscopic study,” J. Phys. Chem. B, vol. 114, pp. 9744-9750, 2010.

[39] L. R. Mosiane, B. J. Matsoso, A. Makhongoana, B. K. Mutuma, T. H. Mongwe, N. J. Coville and M. S. Maubane-Nkadimeng, “Tuning the properties of CVD-grown multiwalled carbon nanotubes by ex-situ codoping with boron and nitrogen heteroatoms,” Journal of Nanoparticle Research, vol. 21, no. 207, 2019.

[40] B. O. Boskovic, V. B. Golovko, M. Cantoro, B. Y. Kleinsorge, A. T. H. Chuang, C. Ducati, S. Hofmann, J. Robertson and B. F. G. Johnson, “Low temperature synthesis of carbon nanofibres on carbon fibre matrices,” Carbon, vol. 43, pp. 2643-2648, 2005.

[41] R. Fu, T. F. Baumann, S. Cronin, G. Dresselhaus, M. S. Dresselhaus and J. H. J. Satcher, “Formation of graphitic structures in cobalt-nickel doped carbon aerogels,” Langmuir, vol. 21, pp. 2647-2651, 2005.

[42] S. Chandra, S. Bag, R. Bhar and P. Pramanik, “Effect of transition and non-transition metals during the synthesis of carbon xerogels,” Microporous and Mesoporous Materials, vol. 138, pp. 149-156, 2011.

[43] F. J. Maldonado-Hodar, M. A. Ferro-Garcia, J. Rivera-Utrilla and C. Moreno-Castilla, “Synthesis and textural properties of organic aerogels, transition-metal-containing organic aerogels and their carbonized derivatives,” Carbon, vol. 37, pp. 1199-1205, 1999.

[44] Z. Liu, J. Li, Y. Yang, J. H. Mi and X. L. Tan, “Synthesis, characterization and magnetic examination of Fe, Co and Ni-doped carbon xerogels,” Materials Research Innovations, vol. 16, pp. 362-367, 2012.

[45] D. Zhu, Y. Huang, J.-j. Cao, C. S. Lee, M. Chen and Z. Shen, “Cobalt nanoparticles encapsulated in porous nitrogen-doped carbon- Oxygen activation and efficient catalytic removal of formaldehyde at room temperature,” Applied Chemistry B: Environmental, vol. 258, p. 117981, 2019.

[46] A. S. Alex, A. M. Lekshmi, V. Sekkar, B. John, C. Gouri and S. Ilangovan, “Microporous carbon aerogel prepared through ambient pressure drying routes as anode material for lithium-ion cells,” Polymers Advanced Technologies, vol. 28, pp. 1945-1950, 2017.

[47] Y. M. Mos, A. C. Vermeulen, C. J. N. Buisman and J. Weijma, “X-Ray diffraction of iron-containing samples: The importance of a suitable configuration,” Geomicrobiology Journal, vol. 35, pp. 511-517, 2018.

[48] M. W. Dlamini, T. N. Phaahlamohlaka, D. O. Kumi, R. Forbes, L. L. Jewell and N. J. Coville, “Post doped nitrogen-decorated hollow carbon spheres as a support for Co Fischer-Tropsch catalysts,” Catalysis Today, vol. 342, pp. 99-110, 2020.

[49] M. W. Dlamini, D. O. Kumi, T. N. Phaahlamohlaka, A. S. Lyadov, D. G. Billing, L. L. Jewell and N. J. Coville, “Carbon spheres prepared by hydrothermal synthesis - A support for bimetallic iron cobalt Fischer-Tropsch catalysts,” ChemCatChem, vol. 7, pp. 3000-3011, 2015.

Chapter 4: The synthesis of Co@HCSs using polystyrene spheres functionalized with poly(acrylic acid), poly(ethyl cyanoacrylate) and poly(ethylene glycol)

4.1. Introduction

Metal nanoparticles are usually synthesized by the reduction of a metal salt in the presence of a support material that can stabilize and immobilize the nanoparticles [1]. The support can play a critical role in this process. There are different types of materials that can be used as supports, including carbon and metal oxides (silica, alumina, titania) [2]. The carbon can be made from various sources – one of these methods involves the polymerization of appropriate monomers. These polymers can stabilize metal nanoparticles by controlling the nucleation and growth stages to prevent agglomeration and this can lead to the control of the final metal particle size [3] [4]. The polymer interacts with the metal precursor by ion-pair or complex formation and this leads to an interaction of the polymer surface with the metal nanoparticle [5]. If the polymer is highly crosslinked it can form cavities that can restrict the growth of the nanoparticles by steric stabilization or by having functional groups that can stabilize the nanoparticles by covalent bonding [204] [7]. The polymer functional groups (or side chains) that have previously shown the ability to stabilize metal nanoparticles include amine, hydroxyl, carboxylic acid, and ester groups [206]. The shape of a support ranges from sheets to rods to spheres. Spherical polystyrene (PS) is one of the most used sphere-shaped polymeric supports that have been used for the growth and support of metal nanoparticles. This is because it is relatively inexpensive, easy to synthesize, has a controllable particle diameter and also has a narrow size diameter distribution [9] [10]. However, due to a lack of functional groups, PS interacts poorly with metal nanoparticles, resulting in poor stabilization and agglomeration of nanoparticles.

Several studies involving the use of PS for the stabilization of metal nanoparticles have been reported, wherein the surface of the PS has been modified with compounds containing functional groups to make it more compatible with the metal surface. For example, Tian and co-workers functionalized PS by coating the PS spheres with polyethyleneimine (PEI) [11]. The PEI was successfully adsorbed on the surface of the spheres through the amine groups. Introduction of the amine functional groups assisted with stabilizing Ag nanoparticles with small particle sizes on the polymer surface [11]. In other work, Li et al. reported that

functionalized PS spheres were prepared by polymerization of aniline on the surface of PS, to produce PS-polyaniline spheres [9]. In studies by Chen et al., Ag and Pt nanoparticles were stabilized on PS microspheres coated with poly(*N*-isopropyl acrylamide) (PNIPAAm). They reported that the PNIPAAm chains were responsible for the steric stabilization of the nanoparticles on the surface of the PNIPAAm-coated PS spheres. The PNIPAAm adsorbed the metal nanoparticles through the amide group nitrogen atoms and the nanoparticles were well dispersed on the surface of the PNIPAAm-PS [12] [13].

Polymers other than PS have also been used to stabilize metal nanoparticles. For example, polyethylene glycol (PEG) has been used as a reducing agent and stabilizer for metal nanoparticles [14] [15] such as Pd, Ag, Pt and Co. The PEG properties were found to be dependent on its molecular weight [16] [17]. PEG is inexpensive, non-toxic, environmentally friendly and contains oxyethylene functional groups which make it possible for metal nanoparticles to interact and stabilize on its polymer surface [16] [18]. Other polymers have also been used and include poly(ethyl cyanoacrylate) (PECA) and poly(acrylic acid) (PAA). PECA is a multifunctional polymer with nitrile and carbonyl functional groups. It belongs to the family of poly(alkyl cyanoacrylates) (PACAs), which have numerous biological applications due to their biodegradability and adhesive properties [19] [20]. PACAs have been investigated in several studies for their applications in drug delivery systems, where they have shown an ability to encapsulate biologically active compounds [21] [22]. PAA has also been widely used and investigated for the growth and stabilization of metal nanoparticles [23]. Indeed, PAA spheres (100 nm) have been previously synthesized by Gröschel and co-workers [24] and Pd nanoparticles (3-5 nm) were successfully stabilized and homogeneously loaded on the surface of the spheres due to the presence of PAA carboxylic acid functional groups.

An alternative procedure to stabilize PS is by reaction of PS with another polymer. For example, functionalization of PS spheres with PAA was achieved by Guo et al. by photo-polymerization of acrylic acid (AA) on the surface of PS spheres [25]. Lu et al. simultaneously synthesized PAA and Ag nanoparticles on the surface of PS spheres. This was achieved by coating the surface of the PS spheres with a functional monomer, silver acrylate, followed by UV radiation of the PAA/Ag which stabilized Ag nanoparticles with particle sizes below 5 nm [26]. In this example the metal was placed on top of the solid polymer.

In all the examples discussed a metal (M) has been placed on the surface of a support that is then used in applications such as heterogeneous catalysis. However, in this study we have used

the principle of making a M/polymer support (using a spherical polymer) that is then covered by a layer of carbon to give M/polymer@carbon in which the polymer is then removed to give M@carbon. In essence, the carbon shell is viewed as a hollow carbon sphere (HCS). In the process, the metal particle has been transferred from the polymer to the inner surface of the carbon shell. The fabrication of metal nanoparticles encapsulated inside HCSs (M@HCSs) by this process is achieved by what is called a hard-templating method.

The polymer template must be a material that can stabilize and immobilize the metal nanoparticles to avoid agglomeration under the template removal conditions. Removal of the template is normally achieved by thermal decomposition. A spherical polymer such as PS, which decomposes at relatively low temperatures, has been shown to be an appropriate template for the synthesis of M@HCSs. However, PS lacking functional groups may not stabilize metal nanoparticles by the above process.

Literature reports, as indicated above, have shown that the presence of functional groups on a polymer (template) surface can improve the degree of interaction between the polymer and the metal (ions and nanoparticles). In this study, we have synthesized *functionalized PS spheres* and have studied their impact on metal particle growth. The three polymers chosen, PAA, PECA and PEG were coated on the surface of PS spheres to decorate the surface with C=O, C-O, O-H and C≡N functional groups. Figure 4.1 shows the chemical structures of PS and the functionalizing polymers containing the desired functional groups used in this study. Co nanoparticles were then reacted with the functionalized PS spheres and the Co particle sizes and Co size distribution were investigated. The Co/polymer materials were then coated with resorcinol (R), CTAB and formaldehyde (F) using well-known procedures. After appropriate reaction conditions, a carbon shell formed from the RF on the Co/polymer. Thermal removal of the polymers gave the Co@HCS materials that were characterized with particular reference to the impact of the initial polymer on the Co agglomeration in the HCS.

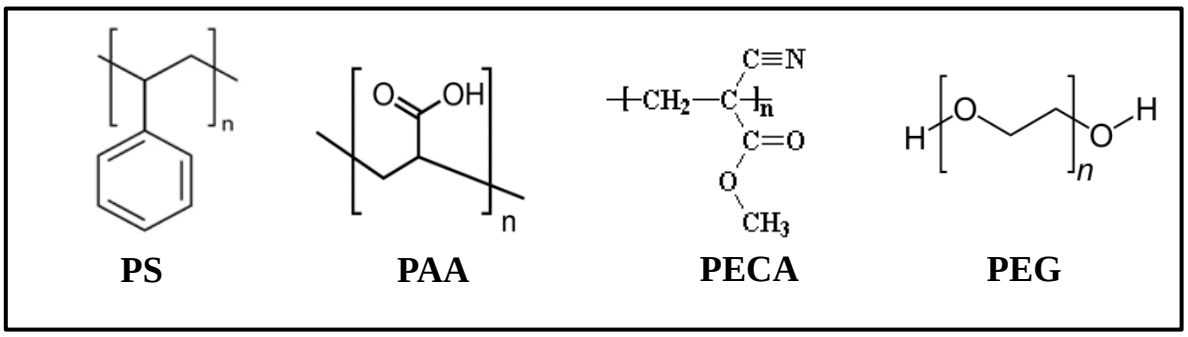

Figure 4.1: Chemical structures of PS, PAA, PECA and PEG

4.2. Experimental section

4.2.1. Materials

Styrene, acrylic acid, ethyl cyanoacetate, ethylenediamine, polyvinylpyrrolidone (PVP, MW 40 000), resorcinol, formaldehyde solution (37%), cetyltrimethylammonium bromide (CTAB), cobalt nitrate hexahydrate and hydrazine hydrate (78-82%) were all purchased from Sigma Aldrich and used as received. Poly (ethylene glycol) (MW = 35000, Fluka), ammonia solution (25%, Fluka) potassium persulfate (Eimer and Amend) and ethanol (98%, Merck) were also used as received. Distilled water was used for all experiments and washings.

4.2.2. Methods

Synthesis of PS spheres (PSSs)

The PSSs were synthesized following the procedure reported in Chapter 3 [27].

Coating of PSSs with PAA (PS-PAA)

PSSs (6 g) were dispersed in 150 ml distilled water and 50 ml ethanol by ultrasonication for 30 minutes. Acrylic acid (0.7 ml), potassium persulfate (0.3 g) was mixed with 21 ml distilled water. The two mixtures were added together, while stirring, and heated to 65 °C for 2 hours. The mixture was further stirred at room temperature overnight, filtered by centrifuge, washed with ethanol and dried at 60 °C overnight.

Coating of PSSs with PEG (PS-PEG)

PSSs (5.2 g) in 56 ml ethanol and 168 ml distilled water were dispersed for 30 minutes by ultrasonication. Poly(ethylene glycol) (0.52 g), pre-dissolved in a small amount of distilled water, was added while stirring. Thereafter, ethylenediamine (0.25 M) was added until a pH of 11 was reached [28]. The reaction was stirred at room temperature overnight, filtered by centrifuge, washed with ethanol, and dried overnight in the oven at 60 °C.

Coating of PSSs with PECA (PS-PECA)

Ethyl cyanoacrylate monomer was prepared from ethyl cyanoacetate following a method reported in the supplementary section (S4.1) [29]. The synthesized ethyl cyanoacrylate monomer was polymerized to give poly(ethyl cyanoacrylate) (S4.2, [30]) which was used to functionalize the PS spheres. PSSs (4.5 g) in 38 ml ethanol and 110 ml distilled water were

dispersed for 30 minutes by ultrasonication. Then, poly(ethyl cyanoacrylate) (0.4 g) was mixed with 11 ml distilled water and 30 ml acetone. The two mixtures were added together and 0.25 M ethylenediamine was added until a pH of 11 was reached [28]. The mixture was stirred overnight at room temperature, filtered by centrifuge, washed with ethanol, and dried overnight in the oven at 60 °C.

Synthesis of Co/polymer composites

The Co/polymer composites were synthesized following the procedure reported in Chapter 3.

Synthesis of HCSs encapsulated cobalt nanoparticles

The HCSs encapsulated cobalt nanoparticles were synthesized following the procedure reported in Chapter 3.

4.2.3. Characterization techniques

FTIR, TEM, SEM, TGA, PXRD and surface area and porosity analysis procedures were done under similar conditions as reported in Chapter 3. TPR analysis was carried out with a Micromeritics Auto Chem II instrument. Approximately 50 mg of the catalyst was placed inside a quartz tube and pre-treated under helium (30 ml/min) at 150 °C for 30 minutes and cooled down to 50 °C. Then the catalyst was re-heated to 900 °C at a rate of 10 °C/min under 5%H2/Ar flowing at 50ml/min.

4.3. Results and discussions

Coating of pre-synthesized PS polymers with functional polymers was done to introduce functional groups onto the surface of the PS. Preparation of PAA-coated PS spheres was achieved by synthesis of PAA in the presence of pre-synthesized PS spheres. This was done to ensure that the PAA polymerized on the PS surface and formed a uniform coated layer. The coating with PEG and PECA was done by coating pre-synthesized PS spheres with pre-synthesized PEG and PECA polymers in the presence of ethylenediamine. Ethylenediamine was used to crosslink the PS chains with the PEG and PECA chains and obtain a coated layer on the PS surface [31].

4.3.1. Characterization of the polymer spheres

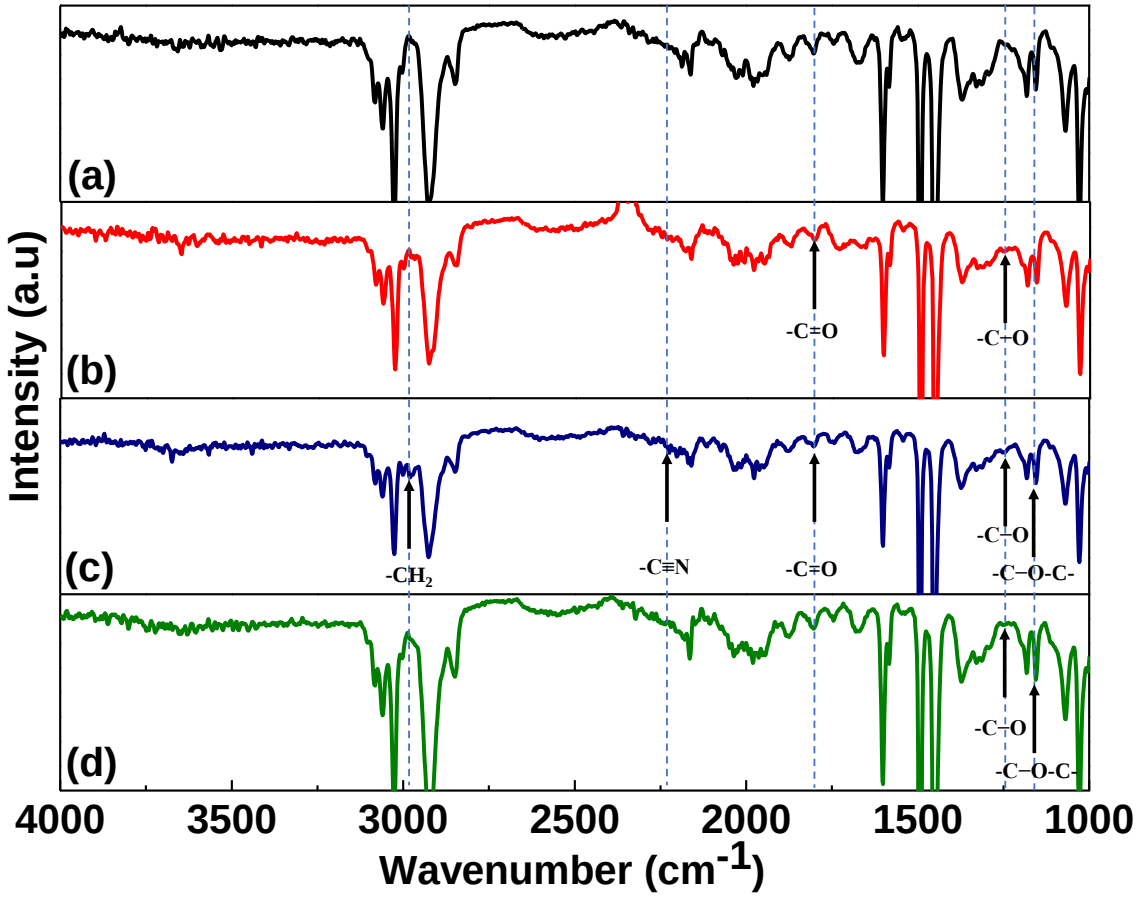

Figure 4.24: FTIR spectra of (a) PS, (b) PS-PAA, (c) PS-PECA and (d) PS-PEG

Figure 4.2 shows the FTIR spectra of the PS and functionalized PS spheres. The intensities of the absorption peaks observed in the IR spectra of the functionalised PS materials made in this study are very weak due to the low concentration of functional groups used. To obtain an accurate location of the functional groups in the IR spectra, PS spheres functionalized with 50 % PAA and 50% PEG were synthesized (Figure S2). The appropriate peak intensities were relatively larger and hence visible. Unfortunately, the corresponding SEM images (Figure S4.1) showed that the higher coating compromised the morphology of the spheres giving a lumpy coating (circled in red) around the spheres.

All the spectra showed peaks characteristic of PS, corresponding to the aromatic and aliphatic -C-H bonds (1604, 2845, 2925, 3068 and 3025 cm^{-1}) and the PS backbone (1356 and 1493 cm^{-1}) [32]. The polymers contained > 90% PS and therefore the PS absorption bands dominated the IR spectra. Low intensity peaks related to the -C=O and -C-O stretching vibrations of PAA are observed from the PS-PAA spectrum at 1730 and 1250 cm^{-1}, respectively [33]. The PS-

PECA spectrum showed small peaks at 2990, 2260, 1750 and 1250 cm^{-1} corresponding to -CH_2, -C≡N, C=O and -C-O stretching vibrations, respectively [34]. The CO peak at 1750 cm^{-1} peak overlapped with a peak associated with the PS. The PS-PEG spectrum contained a peak at 1170 cm^{-1} corresponding to the -C-O-C- vibration of PEG [35], which overlapped with a peak related to PS. The PAA and PEG -O-H vibrations at 3500 cm^{-1} are not visible in the PS-PAA and PS-PEG spectra due to the low concentration of PAA and PEG used.

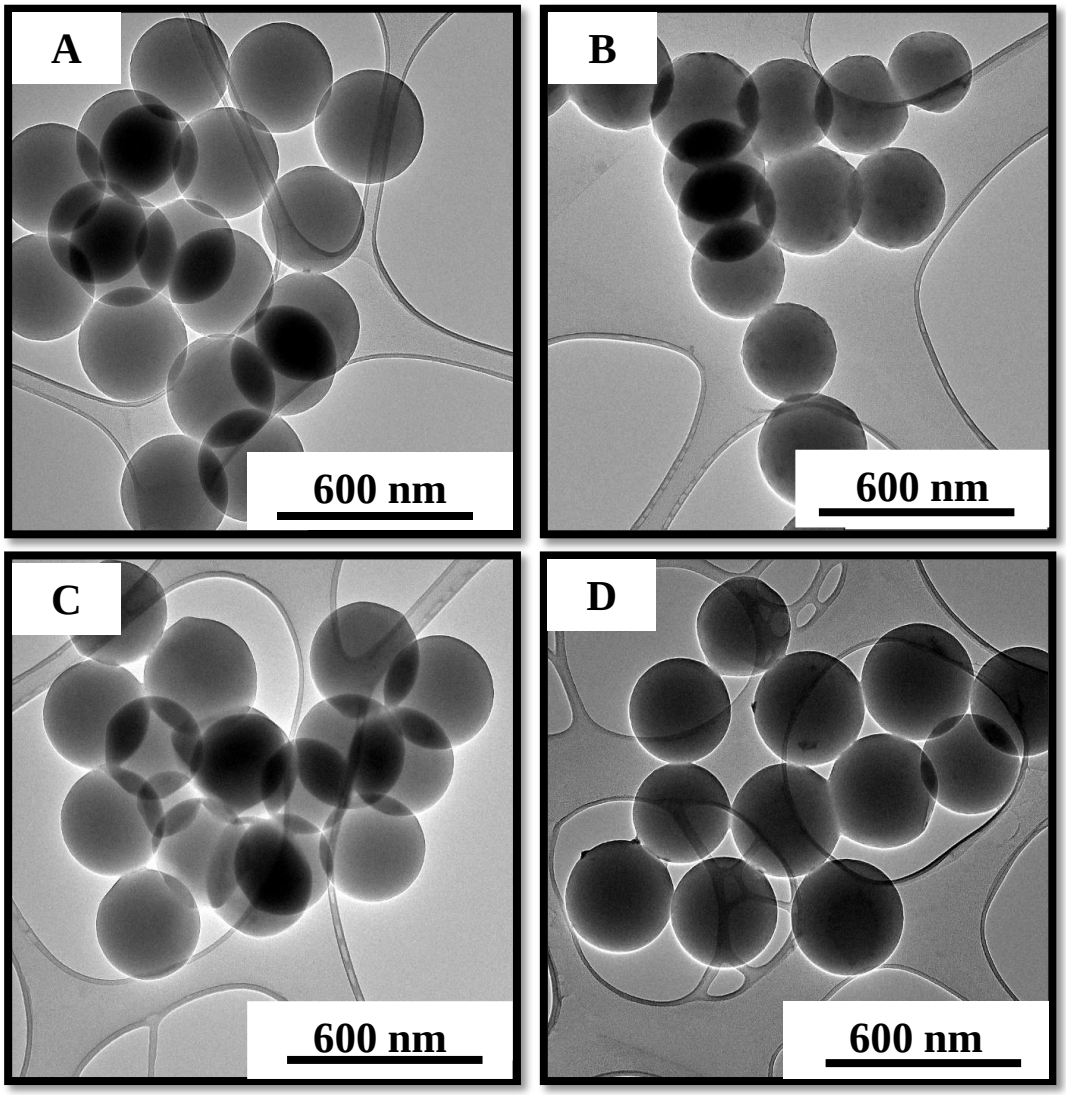

Figure 4.3: TEM images of (A) PS, (B) PS – PAA (C) PS – PECA and (D) PS – PEG

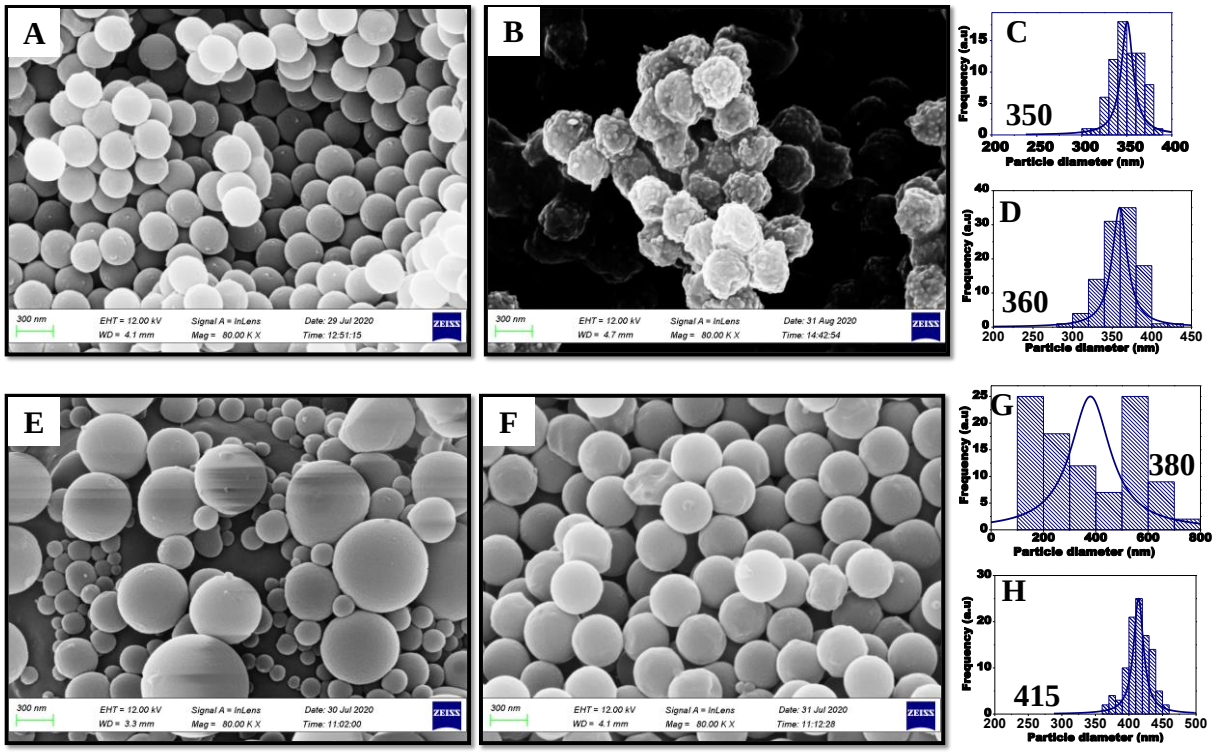

Figure 4.4: SEM images and particle size distribution plots of (A, C) PS, (B, D) PS – PAA (E,G) PS – PECA and (F,H) PS – PEG

Figure 4.3 and Figure 4.4 show the TEM and SEM images of the PS and functionalized PS spheres. The spheres appear to have a smooth and uniform surface; the SEM images (Figure 4) show more surface features than are observed in the TEM images. The SEM images and particle size distribution curves of the PS and functionalized PS spheres are shown in Figure 4.4. The PS spheres (4.4 A) have a smooth surface, with an average diameter of 350 nm with a narrow particle size distribution (250 – 400 nm) (4.4 C). The surface of the PS-PAA spheres (4.4 B) is rough and uneven, indicating the successful coating with PAA. Furthermore, the average diameter of the PS-PAA spheres is 360 nm (4.4 D) with a narrow particle size distribution (300 – 450 nm). This indicates a small increase in diameter due to the coated layer. The PS-PECA template was prepared by mixing PS dispersed in a water/ethanol mixture with PECA dispersed in ethanol. The SEM and particle size distribution of the PS-PECA spheres are shown in Figure S4.3. The average diameter of the spheres is 360 nm with a narrow particle size distribution (300 – 400 nm). The corresponding FTIR spectra are reported in Figure S4.4, and no visible peaks are corresponding to PECA. The PS-PECA spheres were also made in which PECA was dissolved in acetone but these spheres were polydisperse with a particle size distribution between 100 – 800 nm (4.4 E, G). PS is soluble in acetone, and therefore the outer surface of the spheres may presumably dissolve in the acetone during functionalization, leading to the formation of the smaller spheres (100 – 250 nm). The dissolved polymer also re-coated

on the surface of the spheres, producing larger particles (400 – 800 nm). The average particle diameter, however, was determined to be 380 nm, which is 30 nm larger than the average diameter of the PS spheres. The PS-PEG spheres have a smooth surface (4.4 F) with an average diameter of 415 nm and narrow particle size distribution (350 – 450 nm).

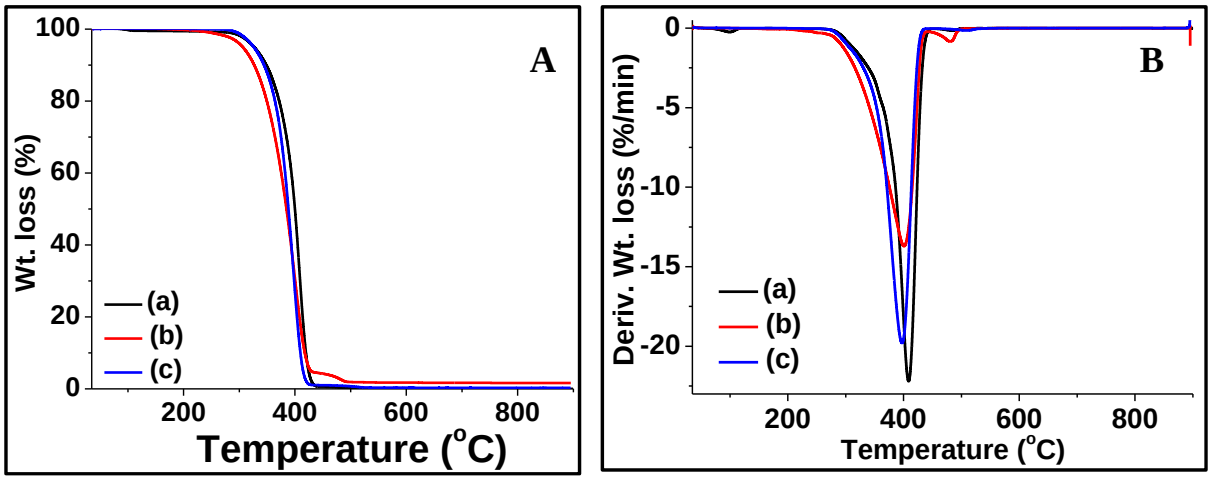

Figure 4.5: TGA (A) and derivative TGA (B) of (a) PS, (b) PS-PAA, (c) PS-PECA and (d) PS-PEG

The TGA and derivative TGA curves of PS and functionalized PS spheres are shown in Figure 4.5. The spheres all have similar decomposition profiles, with maximum decomposition at ca. 400 °C. Mass losses at 200, 250 and 507 °C can be observed in the TGA (4.5 A) profiles and derivative TGA (4.5 B) profiles of the PS-PAA spheres (b). This indicated the loss of the PAA functional groups at 200 and 250 °C and the loss of a PS-PAA component at 507 °C. This confirmed the successful coating of the PAA on the PS surface. The derivative TGA (c) curve for the PS-PECA spheres showed a shoulder peak at 304 °C, corresponding to the loss of the PECA functional groups. This confirmed the presence of the PECA on the coated spheres. The TGA and derivative TGA curves of the PS-PEG spheres are similar to the TGA and derivative TGA of the unfunctionalized PS spheres. Here there is no evidence for the presence of PEG.

4.3.2. Characterization of Co@HCSs

The internal diameters and shell thickness of the Co@HCSs catalysts were measured from the TEM images (Figure 4.8) and are presented in Table 4.1. The catalysts synthesized with PS, PS-PAA and PS-PEG all have similar internal diameters of 344, 359 and 348 nm, respectively. However, the PS-PECA catalyst has a smaller internal diameter of 273 nm. The PS-PECA spheres have been dissolved by the acetone during functionalization, leading to a shrinkage of

the sphere diameter as seen in the SEM image of the spheres (Figure 4.4). No significant differences were observed from the shell thickness (~ 30 nm) of the catalysts, indicating a uniform and consistent coating with the RF layer.

Table 4.1: Internal diameter, carbon shell thickness and surface area and porosity properties of the Co@HCSs catalysts

Sample	I.D (nm)	S.T (nm)	BET S.A (m^2/g)	M.S.A (m^2/g)	P.D (nm)	P.V (cm^3/g)
Co@HCS_PS	344 ± 21	27 ± 4	612	320	4.8	0.57
Co@HCS_PS-PAA	359 ± 25	31 ± 3	646	347	4.9	0.60
Co@HCS_PS-PECA	273 ± 13	31 ± 3	379	275	3.3	0.18
Co@HCS_PS-PEG	348 ± 24	29 ± 4	426	240	4.6	0.37

I.D = internal diameter, S.T = shell thickness, BET S.A = BET surface area, M.S.A = micropore surface area, P.D = average pore diameter, P.V = pore volume

The BET isotherms and pore size distribution curves of the 5% Co/HCSs are shown in Figure 4.6 and the data are summarized in Table 4.1. The BET isotherms of the catalysts are characteristic of a combination of type I and type IV isotherms which are due to the presence of micropores and mesopores [36]. The pore size distribution curves of the catalysts showed that the catalysts had high volumes of pores with diameters < 5 nm. Larger surface areas were observed for the PS (612 m^2/g) and PAA (646 m^2/g) catalysts, while relatively smaller surface areas were observed for the PECA (379 m^2/g) and PEG (426 m^2/g) catalysts. This indicated pore blockage in the PECA and PEG catalysts which may have been influenced by the presence of the PECA and PEG polymers. Furthermore, the PECA and PEG catalysts had smaller pore volumes (0.18 and 0.37 cm^3/g, respectively) than the PS (0.57 cm^3/g) and PAA (0.60 cm^3/g) catalysts. This further pointed to a possibility of pore blockage. The micropore surface areas of the PS, PAA and PEG catalysts contribute ca. 50% of the total BET surface areas, however, with the PECA catalyst the micropore surface area is ca. 75 % of the total surface area.

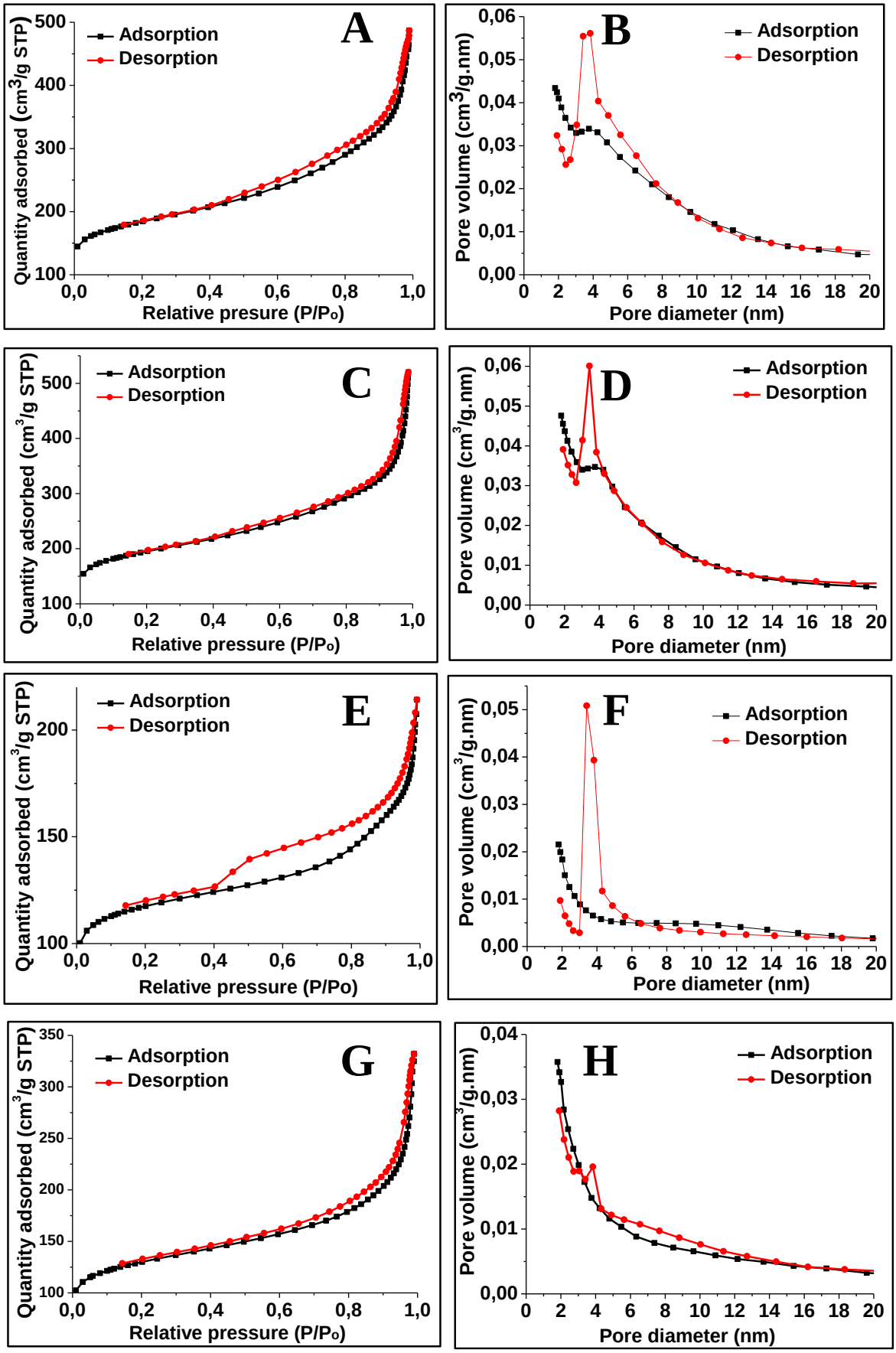

Figure 4.6: BET isotherms and pore size distribution curves of 5%Co@HCSs synthesized with (A, E) PS, (B, F) PS-PAA, (C, G) PS-PECA and (D, H) PS-PEG

Figure 4.7A shows the PXRD data of the synthesized catalysts. The °2θ positions and peak assignments are reported in Table S4.3. A difference in the oxidation states of the Co is noted in the different templates. The PS and the PS-PECA catalysts PXRD data showed the presence of both Co_3O_4 (Co^{2+}, Co^{3+}) and CoO (Co^{2+}), the PS-PEG catalysts contained mainly Co_3O_4, while the PS-PAA catalyst consisted of Co (Co^o, fcc and hcp). PAA is a better metal stabilizing agent than PECA and PEG, as also observed in this study. Hydrazine is a well-known reducing agent for Co. It would be responsible for the Co reduction. On top of this, the poly(acrylic acid) could also possibly aid the reduction reaction. The reducing ability of the poly(acrylic acid) could be investigated by eliminating the use of the reducing agent. Furthermore, other reducing agents such as sodium nitrite and sodium borohydride could be used. The carbon peak was not visible on the PS, PS-PAA and PS-PECA catalysts due to the fluorescence of Co under Cu radiation.

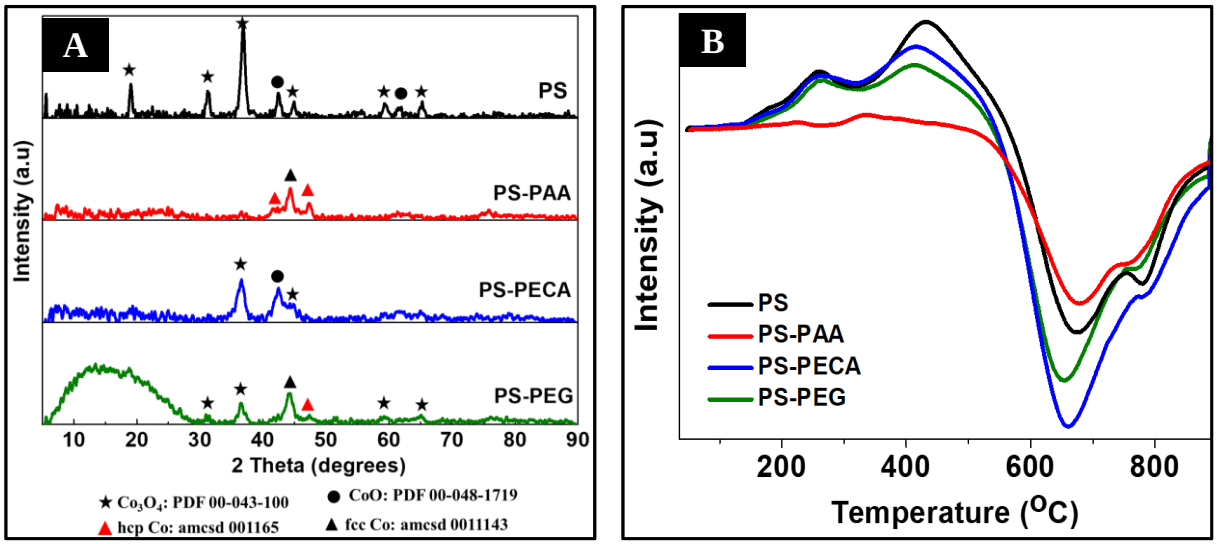

Figure 4.7: PXRD spectra (A) and TPR curves (B) of 5%Co@HCSs catalysts prepared with different templates

The TPR curves for the Co complexes are presented in Figure 4.7B and show two distinct reduction peaks, characteristic of the two-step reduction of cobalt oxide (Co_3O_4 → CoO → Co) [37]. The reduction peak temperatures are reported in Table S4.2. The PS-PECA and PS-PEG catalysts showed similar reduction profiles to the first reduction temperature at ~ 259 °C and the second reduction event at ~416 °C. The PS catalyst had a first reduction that occurred at 255 °C and a second reduction event that occurred at 433 °C. The three catalysts behaved similarly, however, the PS-PAA catalyst had very small reduction peaks that occurred at the relatively low temperatures of 225 °C and 334 °C. This was an indication that very little hydrogen was consumed, and therefore very little reduction had occurred. This was in

accordance with the presence of Co metal, not the oxide, as confirmed by the PXRD data. The event with the 'peak' at ca. 600 °C was due to the production of CH_4 due to the Co catalysed reaction of the HCS with H_2. The reducibility was found to be influenced by the polymer used with reducibility order PAA > PECA > PEG = PS.

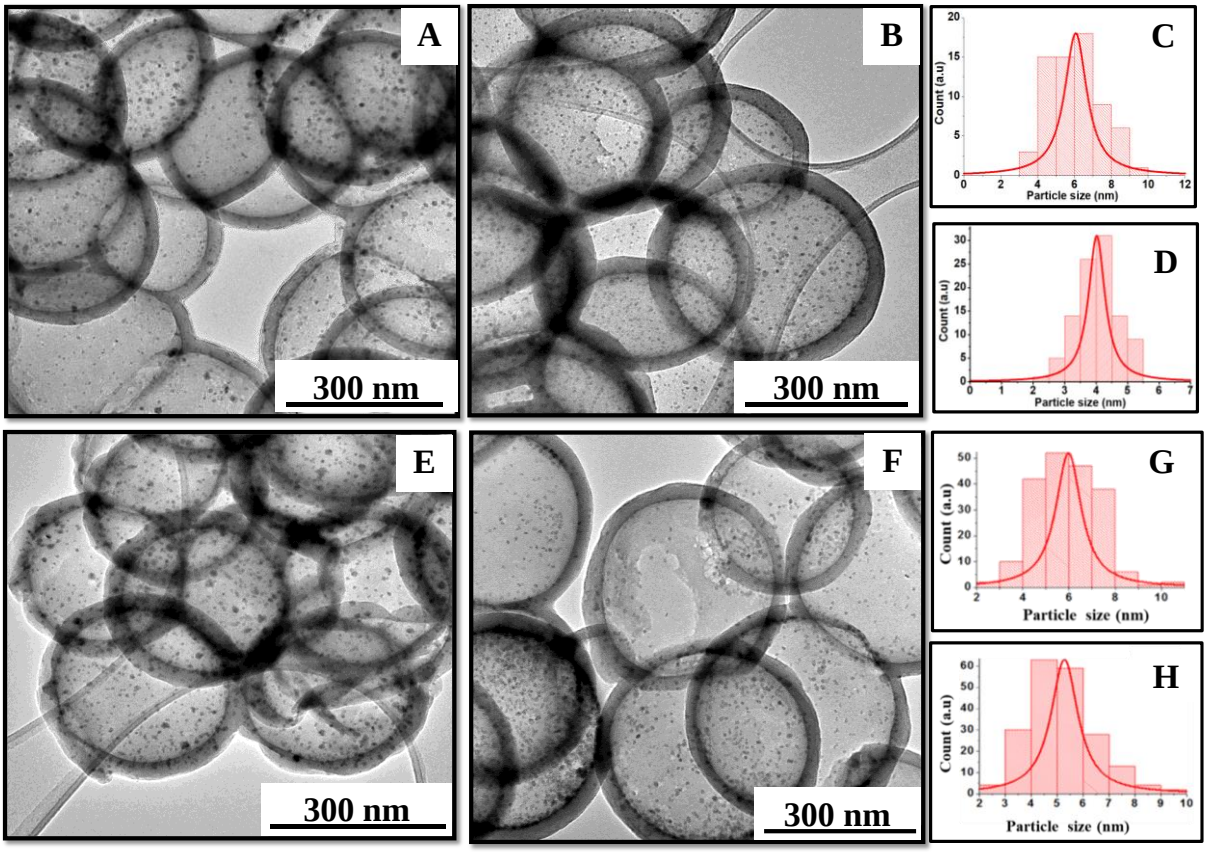

Figure 4.8: TEM micrographs and particle size distribution curves of 5%Co@HCSs synthesized with (A, C) PS, (B, D) PS-PAA, (E, G) PS-PECA and (F, H) PS-PEG

Table 4.2: Particle size and metal loading of the catalysts prepared with different templates

Template	TEM Co size (nm)	% Co_3O_4 (TGA)	% Co (TGA)
PS	6.1	6.3	4.6
PS-PAA	4.0	6.3	4.6
PS-PECA	6.0	4.9	3.6
PS-PEG	5.2	6.9	5.0

The Co nanoparticles were readily detected in TEM images and were observed to be well dispersed inside the HCSs (Figure 4.8). It was clear that small nanoparticles were successfully transferred to the inner surface of the HCSs on removal of the polymers. The average Co diameters are reported in Table 4.2 and the size distribution curves are shown in Figure 4.8. The measured particle sizes were between 4.0 and 6.1 nm. The catalysts synthesized with PS-PAA had the smallest average Co particle size (4.0 nm) but as described above, this was the measurement of Co metal particles. The other three samples had Co at ca. 6.0 nm were due to Co_3O_4. The data are similar, and this was unexpected as hydroxy groups (OH) and carboxylic acid groups could act as adsorption sites for particle growth. [38] [39].

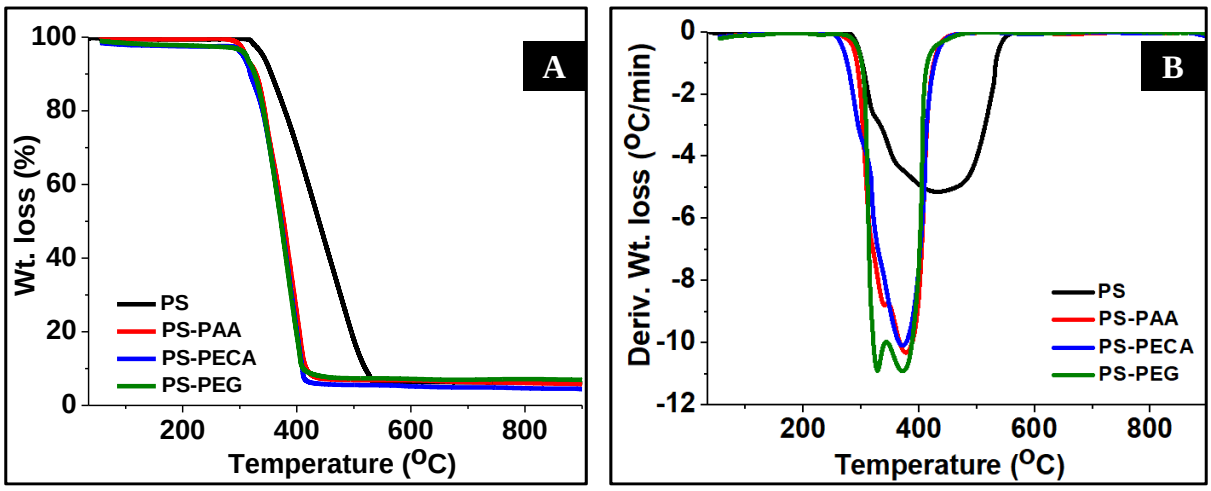

Figure 4.9: TGA (A) and derivative TGA (B) curves of 5%Co@HCSs synthesized with (a) PS, (b) PS-PAA, (c) PS-PECA and (d) PS-PEG templates.

TGA data (Figure 4.9A) were used to estimate the Co loading on the catalysts. The estimated Co and Co oxide loading are reported in Table 4.2. Co loadings close to the targeted 5% were obtained for the PS (4.6 %), PS-PAA (4.6 %) and PS-PEG (5%) catalysts. This is an indication that most of the metal was stabilized on the polymer templates and successfully transferred to the HCSs. The PS-PECA catalyst has a much lower loading of 3.6 %. It may have been possible that this template did not stabilize all the metal and some of the metal ions may have been removed during purification steps.

The derivative TGA curves (Figure 4.9B) showed the maximum carbon decomposition temperature of the different catalysts and the decomposition data is also reported in Table S1. The thermal decomposition was made up of at least two peaks. Raman studies have previously shown that the mesoporous carbon shell prepared from pyrolysis of resorcinol-formaldehyde (RF) is typically a mixture of amorphous and graphitic carbon with structural defects. The more

disordered carbon tends to decompose at relatively lower temperatures. Therefore, the low temperature decomposition peak was due to the degradation of the more disordered carbon. The decomposition temperature of the carbon is also influenced by the type and size of the metal nanoparticles. The presence of certain metal nanoparticles such as Co usually accelerates the decomposition of carbon. The PS catalyst had relatively higher decomposition temperatures of T_1=365 °C and T_2=440 °C as opposed to the PS-PAA, PS-PECA and PS-PEG catalysts which have similar decomposition temperatures at T_1= ~330 °C and T_2= ~370 °C. The difference in decomposition temperature of the PS catalyst could have been a result of the different Co metal particle sizes and a possible difference in the carbon defects.

Conclusions

The functionalization of PS was achieved by coating the PS spheres with PAA, PECA and PEG to introduce functional groups. The presence of the functional groups was confirmed by FTIR. The FTIR peak intensities were weak, relating to a low concentration of functional groups present in the polymers. The observation of a rough and uneven surface from SEM images showed a modification of the PS surface by PAA. TGA analysis of the functionalized polymers confirmed the presence of PAA and PECA on the polymers. Co nanoparticles inside HCSs were successfully synthesized using the functionalized polymers as templates. Particle size analysis of the Co nanoparticles showed a variation in the particle sizes related to the use of different templates, which indicated that the PAA and PEG treatments contributed to the stabilization of the metal nanoparticles. The PXRD and TPR data showed the presence of different Co oxidation states in the different catalysts, further indicating the influence of the templates on the growth of the nanoparticles. There was no clear indication that the PECA treatment contributed to the metal growth and stabilization. The data showed similarities in the behaviour of the PS and PS-PECA templates. It might be possible to use the templates PS-PAA and PS-PEG templates to grow other metal nanoparticles and load higher amounts of metal with small particle diameters.

References

[1] L. Groschel, R. Haidar, A. Beyer, K.-H. Reichert and R. Schomacker, “Characterization of palladium nanoparticles adsorption on polyacrylic acid particles as hydrogenation catalyst,” Catalysis Letters, vol. 95, pp. 67-75, 2004.

[2] G. Liao, J. Chen, W. Zeng, C. Yu, C. Yi and Z. Xu, “Facile preparation of uniform nanocomposite spheres with loading silver nanoparticles on polystyrene-methyl acrylic acid spheres for catalytic reduction of 4-nitrophenol,” Journal of Physical Chemistry C, vol. 120, pp. 25935-25944, 2016.

[3] L. M. Bronstein, D. M. Chernyshov, G. I. Timofeeva, L. V. Dubrovina, P. M. Valetsky, E. S. Obolonkova and A. R. Khokhlov, “Interaction of polystyrene-block-poly(ethylene oxide) micelles with cationic surfactant in aqueous solutions. Metal colloid formation in hybrid systems,” Langmuir, vol. 16, pp. 3626-3632, 2000.

[4] C.-W. Chen, D. Tano and M. Akashi, “Colloidal platinum nanoparticles stabilized by vinyl polymers with amide side chains: Dispersion stability and catalytic activity in aqueous electrolyte solutions,” Journal of Colloid and Interface Science, vol. 225, pp. 349-358, 2000.

[5] A. B. Mayer and J. E. Mark, “Transition metal nanoparticles protected by amphiphilic block copolymers as tailored catalyst systems,” Colloid and Polymer Science, vol. 275, pp. 333-340, 1997.

[6] S. N. Sidorov, L. M. Bronstein, V. A. Davankov, M. P. Tsyurupa, S. P. Solodovnikov and P. M. Valetsky, “Cobalt nanoparticle formation in the pores of hyper-cross-linked polystyrene: Control of nanoparticle growth and morphology,” Chemistry of Materials, vol. 11, pp. 3210-3215, 1999.

[7] L. D. Pachon and G. Rothenberg, “Transition-metal nanoparticles: Synthesis, stability and the leaching issues,” Applied Organometallic Chemistry, vol. 22, pp. 288-299, 2008.

[8] C. Saldias, S. Bonardd, C. Quezada, D. Radic and A. Leiva, “The role of polymers in the synthesis of noble metal nanoparticles: A review,” Journal of nanoscience and nanotechnology, vol. 17, pp. 87-114, 2017.

[9] Y. Li, Y. Hu, S. Ye, Y. Wu, C. Yang and L. Wang, “Functional polyaniline-assisted decoration of polystyrene microspheres with noble metal nanoparticles and their enhanced catalytic properties,” New Journal of Chemistry, vol. 40, pp. 10398-10405, 2016.

[10] S. H. Im, U. Jeong and Y. Xia, “Polymer hollow particles with controllable holes in their surfaces,” Nature Materials, vol. 4, pp. 671-675, 2005.

[11] C. Tian, E. Wang, Z. Kang, B. Mao, C. Zhang, Y. Lan, C. Wang and Y. Song, “Synthesis of Ag-coated polystyrene colloids by an improved surface seeding and shell growth technique,” Journal of Solid State Chemistry, vol. 179, pp. 3270-3276, 2006.

[12] C.-W. Chen, M.-Q. Chen, T. Serizawa and M. Akashi, “In-Situ formation of silver nanoparticles on poly(N-isopropyl acrylamide)-coated polystyrene microspheres,” Advanced Materials, vol. 10, pp. 1122-1126, 1998.

[13] C.-W. Chen, T. Serizawa and M. Akashi, “Preparation of platinum colloids on polystyrene nanospheres and their catalytic properties in hydrogenation,” Chemistry of Materials, vol. 11, pp. 1381-1389, 1999.

[14] F. A. Harraz, S. E. El-Hout, H. M. Killa and I. A. Ibrahim, “Palladium nanoparticles stabilized by polyethylene glycol: Efficient, recyclable catalyst for hydrogenation of styrene and nitrobenzene,” Journal of Catalysis, vol. 286, pp. 184-192, 2012.

[15] M. Popa, T. Pradell, D. Crespo and J. M. Calderon-Moreno, “Stable silver colloidal dispersions using short-chain polyethylene glycol,” Colloids and Surfaces A: Physicochemical Engineering Aspects, vol. 303, pp. 184-190, 2007.

[16] H. Cheng, X. Meng, L. He, W. Lin and F. Zhao, “Supported polyethylene glycol stabilized platinum nanoparticles for chemoselective hydrogenation of halonitrobenzenes in scCO2,” Journal of Colloid and Interface Science, vol. 415, pp. 1-6, 2014.

[17] H. Cheng, C. Xi, X. Meng, Y. Hao, Y. Yu and F. Zhao, “Polyethylene glycol-stabilized platinum nanoparticles: The efficient and recyclable catalysts for selective hydrogenation of o-chloronitrobenzene to o-chloroaniline,” Journal of Colloid and Interface Science, vol. 336, pp. 675-678, 2009.

[18] O. A. Kalayci, F. B. Comert, B. Hazer, T. Atalay, K. A. Cavicchi and M. Cakmak, “Synthesis, characterization, and antimicrobial activity of metal nanoparticles embedded into amphiphilic comb-type graft copolymers,” Polymer Bulletin, vol. 65, pp. 215-226, 2010.

[19] J. Nicolas and P. Couvreur, “Synthesis of poly(alkyl cyanoacrylate)-based colloidal nanomedicines,” Wiley Interdisciplinary Reviews-Nanomedicine and Nanobiotechnology, vol. 1, pp. 111-127, 2009.

[20] Y. Barkan, M. Levinman, I. Veprinsky-Zuzuliya, T. Tsach, E. Merqioul, G. Blum, A. J. Domb and A. Basu, “Comparative evaluation of polycyanoacrylates,” Acta Biomaterialia, vol. 48, pp. 390-400, 2017.

[21] G. Fontana, M. Licciardi, S. Mansueto, D. Schillaci and G. Giammona, “Amoxicillin-loaded polyethylcyanoacylate nanoparticles: Influence of PEg coating on the particle size, drug release rate and phagocytic uptake,” Biomaterials, vol. 22, pp. 2857-2865, 2001.

[22] M. G. Han, S. Kim and S. X. Liu, “Synthesis and degradation behaviour of poly(ethyl cyano acrylate),” Polymer degradation and stability, vol. 93, p. 12431251, 2008.

[23] J. W. Hotchkiss and B. G. Mohr, “Gold nanorods surface modified with poly(acrylic acid) as a template for the synthesis of metallic nanoparticles,” Journal of Nanoparticle Research, vol. 12, pp. 915-930, 2009.

[24] L. Groschel, R. Haidar, A. Beyer, K.-H. Reichert and R. Schomacker, “Characterization of palladium nanoparticles adsorpt on polyacrylic acid particles as hydrogenation catalyst,” Catalysis Letters, vol. 95, pp. 67-75, 2004.

[25] X. Guo, A. Weiss and M. Ballauff, “Synthesis of spherical polyelectrolyte brushes by photo emulsion polymerization,” Macromolecules, vol. 32, pp. 6043-6046, 1999.

[26] Y. Lu, M. Schrinner, M. Ballauff, M. W. Moller and J. Breu, “In situ formation of Ag nanoparticles in spherical polyacrylic acid brushes by UV irradiation,” Journal of Physical Chemistry C, vol. 111, pp. 7676-7681, 2007.

[27] J. Fu, Q. Xu, J. Chen, Z. Chen, X. Huang and X. Tang, “Controlled fabrication of uniform hollow core porous shell carbon spheres by the pyrolysis of core/shell polystyrene/crosslinked polyphosphazene composites,” Chem. Commun, vol. 46, pp. 6563-6565, 2010.

[28] M. Anbarasu, M. Anandan, E. Chinnasamy, V. Gopinath and K. Balamurugan, “Synthesis and characterization of polyethylene glycol (PEG) coated Fe3O4 nanoparticles by chemical co-precipitation method for biomedical applications,” Spectrochimica Acta Part A: Molecular and Biomolecular Spectroscopy, vol. 135, pp. 536-539, 2015.

[29] A. E. Ardis, “Preparation of monomeric alkyl alpha-cyano-acrylates”. United States Patent 2,467,927, 19 April 1949.

[30] L. Z. Zhaparova, Y. M. Tazhbayev, M. Z. Burkeev, A. T. Kazhmuratova, T. S. Zhumagaliyeva, S. I. Ali and A. M. van Herk, “Synthesis and characterization of poly (ethyl cyanoacrylate) nanoparticles loaded with capreomycin sulfate,” Pharmaceutical Chemistry Journal, vol. 46, pp. 6-9, 2012.

[31] W.-S. Hung, C.-H. Tsou, M. D. Guzman, Q.-F. An, Y.-L. Liu, Y.-M. Zhang, C.-C. Hu, K.-R. Lee and J.-Y. Lai, “Cross-linking with diamine monomers to prepare composite graphene oxide-framework membranes with varying d-spacing,” Chem. Mater, vol. 26, pp. 2983-2990, 2014.

[32] E. Geraud, V. Prevot and F. Leroux, “Synthesis and characterization of macroporous MgAl LDH using polystyrene spheres as template,” Journal of Physics and Chemistry of Solids, vol. 67, pp. 903-908, 2006.

[33] M. Kohestanian and H. Bouhendi, “Novel cross-linking mechanism for producing PAA microgels synthesized by precipitation polymerization method,” Colloid and Polymer Science, vol. 293, pp. 1983-1995, 2015.

[34] Y. Cui, J. Chai, H. Du, Y. Duan, G. Xie, Z. Liu and G. Cui, “Facile and reliable in situ polymerization of poly(ethyl cyanoacrylate)-based polymer electrolytes toward flexible lithium batteries,” ACS Applied Materials and Interfaces, vol. 9, pp. 8737-8741, 2017.

[35] K. Shameli, M. B. Ahmad, S. D. Jazayeri, S. Sedaghat, P. Shabanzandeh, H. Jahangirian, M. Mahdavi and Y. Abdollahi, “Synthesis and characterization of polyethylene glycol mediated silver nanoparticles by green method,” International Journal of Molecular Sciences, vol. 13, pp. 6639-6650, 2012.

[36] F. J. Sotomayer, K. A. Cychosz and M. Thommes, “Characterization of micro/mesoporous materials by physisorption: concepts and case studies,” Acc. Mater. Surf. Res., vol. 3, pp. 34-50, 2018.

[37] C.-W. Tang, C.-B. Wang and S.-H. Chien, “Characterization of cobalt oxides studied by FT-IR, Raman, TPR and TG-MS,” Thermochemica Acta, vol. 473, pp. 68-73, 2008.

[38] G. Guo, D. Yang, C. Wang, H. Xu and S. Yang, “Synthesis of platinum nanoparticles supported on poly(acrylic acid) grafted MWNTs and their hydrogenation of citral,” Chem. Mater., vol. 20, pp. 2291-2297, 2008.

[39] C.-P. Chang, C.-C. Tseng, J.-L. Ou, W.-H. Hwu and M.-D. Ger, “Growth mechanism of gold nanoparticles decorated on polystyrene spheres via self-regulated reduction,” Colloid Polym Sci, vol. 288, pp. 395-403, 2010.

Chapter 5: The synthesis of poly(styrene-b-methyl methacrylate) copolymer spheres as templates for the synthesis of Co@HCSs

5.1. Introduction

Polymers produced from a single monomer are classified as homopolymers, while polymers produced from more than one monomer are referred to as copolymers [1]. Classification of copolymers depends on the arrangement of the monomers in the polymer chain. They can be classified as alternating, statistic, block, and graft copolymers [2] [3]. The various structures are shown in Figure 5.1.

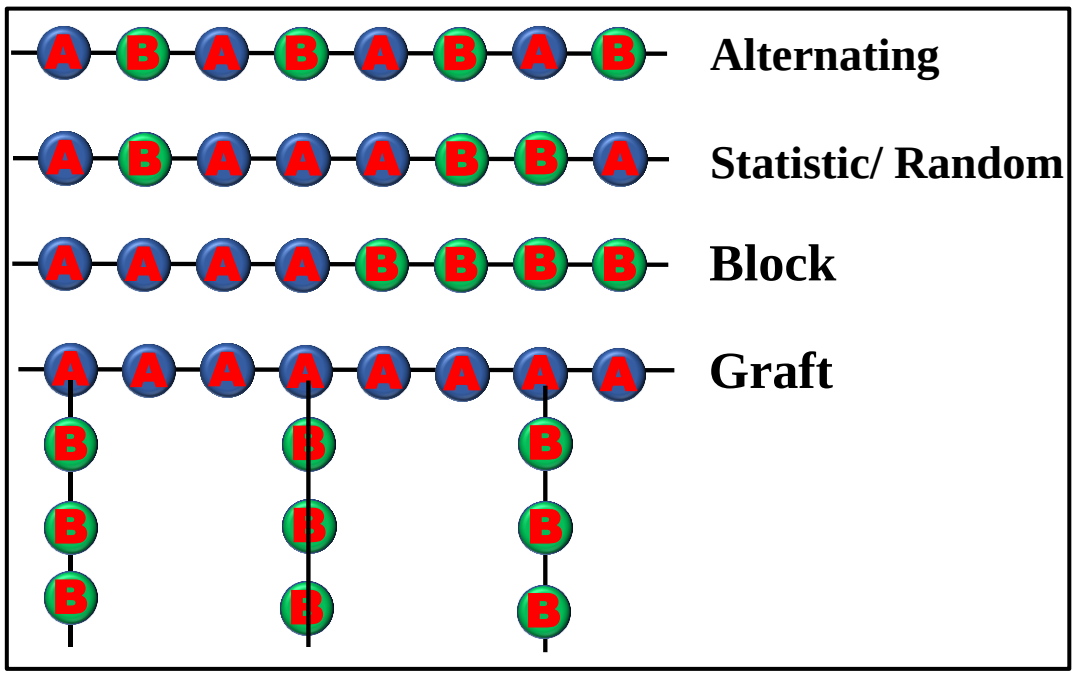

Figure 5.1: Classification of copolymers showing the monomer arrangement in each type of copolymer. A= monomer 1 and B= monomer 2

Block co-polymers have potential applications in the fields of photovoltaics, membranes, photonic materials, biomaterials, textile materials and high-capacity storage devices [4] [5] [6] [7]. After encapsulation of a polymer by other materials, they have the potential to be used as templates in the synthesis of hollow structures because the copolymer can be easily removed by thermal decomposition. Furthermore, their ability to stabilize metal nanoparticles allows metal/copolymer materials to be used as templates in the synthesis of small metal nanoparticles supported inside hollow structures [8]. Loading small nanoparticles in hollow structures is usually challenging as the metal nanoparticles tend to sinter and agglomerate during template removal under thermal conditions. This is especially true if the template has few functional groups to stabilize the metal particles. The use of block copolymers containing functional

groups that can stabilize metal nanoparticles could allow higher metal loadings to be achieved inside hollow structures. Additionally, the diameter of block copolymer spheres can be easily controlled [9]. This is important in the synthesis of hollow spheres for use as catalyst support as it can allow for the synthesis of small hollow spheres with a high surface area.

A combination of monomers with different functionalities can give copolymers with varied structural and functional properties. Researchers have focused their interests on controlling the polymer synthesis processes. Polymer nanoparticles with a controlled shape, size and functionality have found use in various applications, including biomedicine, drug delivery, electronics, and catalysis [10] [11] [12] [13] [14].

Dispersion polymerization is one of the commonly used polymerization processes because it is simple and produces nanoparticles of uniform size [15]. The formation of polymer spheres by dispersion polymerization occurs in the presence of an organic solvent that is miscible with the monomer but immiscible with the polymer [16]. During the synthesis of monodispersed nanoparticles, the particle formation stage plays a key role in generating the final diameter of the particles [17]. The particle formation mechanism was reported by Shen et al [18], where it was stated that the polymerization begins when the initiator decomposes and forms free monomer radicals. These radicals grow until they reach a critical chain length where they can form nuclei. The nuclei that are formed agglomerate together while absorbing the surfactant/stabilizer. The aggregates become particles once they absorb enough surfactant and become stabilized. The particle formation stage is complete when all radicals and nuclei have transformed into particles. Various reaction parameters can be changed to control the final particle size of the polymer. These include temperature, initiator concentration, surfactant concentration, monomer concentration and solvent composition [19].

An increase in temperature usually increases final particle diameter because a higher temperature leads to an increase in the critical chain length. This due to the faster decomposition of the initiator, which leads to the formation of more radicals and consequently leads to a faster chain growth. Increasing initiator concentration increases the average particle size and beyond 10% initiator concentration the nanoparticles may become polydisperse. A higher initiator concentration results in the formation of more radicals and consequently a more enhanced aggregation process, leading to bigger particles. Increasing stabilizer concentration and increasing stabilizer molecular weight reduces the average particle size. Increasing monomer concentration increases the polymerization rate, leading to the formation of larger

particles. Addition of water in polymerization systems with monomers that have low water solubility results in the formation of smaller particles and the size of the particles decreases as the water concentration increases. This is because the low solubility of the monomer leads to the formation of shorter chain lengths. It has been reported that a variation in monomer ratios can result in different morphologies such as spherical, vesicular, tubular, worm-like and rod-like particles [20].

In this study, three solvents (ethanol, isopropanol, and methanol) were used to investigate their influence on the diameter and shape of poly (styrene-block-methyl methacrylate) (PS-b-PMMA) spheres. The solvent composition was further varied by increasing the amount of water in ethanol. The monomer composition was also varied by increasing the concentration of the MMA co-monomer while keeping the total amount of monomer constant. Some of the polymers synthesized here were used in the synthesis of small cobalt nanoparticles encapsulated inside hollow carbon spheres (HCSs). The aim was to prepare small polymer spheres that can be used to make small HCSs.

5.2. Experimental section

5.2.1. Materials

Styrene, methyl methacrylate and polyvinylpyrrolidone (PVP, MW 40 000) was purchased from Sigma Aldrich; ethanol (98%), methanol (98%) and isopropanol (98%) were purchased from MK labs; and Potassium persulfate (Eimer and Amend). All reagents were used as received while distilled water was used for all experiments and product washing steps.

5.2.2. Methods

Synthesis of PS-b-PMMA

The synthesis of polystyrene spheres was modified to synthesize copolymer spheres containing poly (methyl methacrylate). In a typical polymerization reaction 100 ml distilled water, 25ml alcohol (ethanol/ methanol/ isopropanol) and 0.1 g polyvinylpyrrolidone (PVP) was added into a 250 mL round-bottom flask. After all the PVP had dissolved, 8 mL of monomer (1:1 mol ratio styrene: methyl methacrylate) was added, and the solution was stirred for 15 minutes using a magnetic stirrer. In a beaker, 0.15 g of potassium persulfate (KPS) was dissolved in 10 mL of distilled water and then added to the round bottom flask above, while stirring. The

mixture was heated up to 80 °C and the reaction continued for 24 hours. The mixture was then filtered by centrifuge at 18000 rpm for 15 minutes at 10 °C and washed with ethanol. The product (copolymer spheres), produced in high yield, was dried in an oven at 60 °C for 12 hours, crushed with a mortar and pestle and stored in a glass sample vial. The solvent composition was further varied by changing the water: ethanol ratio and using 20%, 80%, 90%, 97% and 100 % volume ratios of distilled water. The monomer composition was also varied by using 10%, 20%, 30%, 40%, 60%, 70%, 80% and 90% mol ratios of methyl methacrylate. The total amount of solvent and the total amount of monomer were kept constant in all reactions.

Synthesis of HCSs

The hollow carbon spheres were prepared following the procedures reported in Chapter 3.

5.2.3. Characterization techniques

FTIR, TEM, SEM, TGA, PXRD and surface area and porosity analysis procedures were done under similar conditions as reported in Chapter 3.

5.3. Results and discussion

5.3.1. Polymer characterization

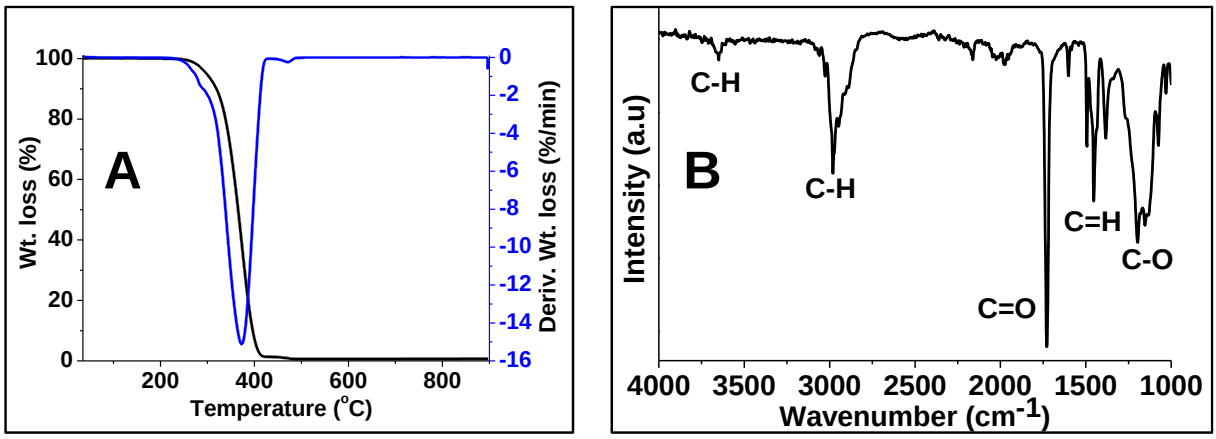

Figure 5.2: (A) TGA and derivative TGA curves and (B) FTIR of PS_{50}-b-$PMMA_{50}$

Figure 5.2A shows the TGA and derivative TGA curves of the PS_{50}-b-$PMMA_{50}$ copolymer. The maximum decomposition temperature of the polymer occurred at about 370 °C, consistent with previously reported studies [21] . This was lower than the decomposition temperature of the PS homopolymer (415 °C) [22], implying that methyl methacrylate lowered the PS

decomposition temperature. The template decomposition temperature is one of the important factors in the synthesis of HCSs by polymer templating. A template with a lower decomposition temperature is preferred as it is easier to remove and leads to a successful transfer of the small metal nanoparticles from the polymer to the HCSs. The FTIR spectrum of the co-polymer (Figure 5.2 B) confirms that PS-b-PMMA was successfully synthesized. This is shown by the presence of the C=O bond and C-O bonds, which are due to methyl methacrylate. The PS backbone is characterized by the presence of the aromatic C-H and C=H bonds.

Effect of using different solvents

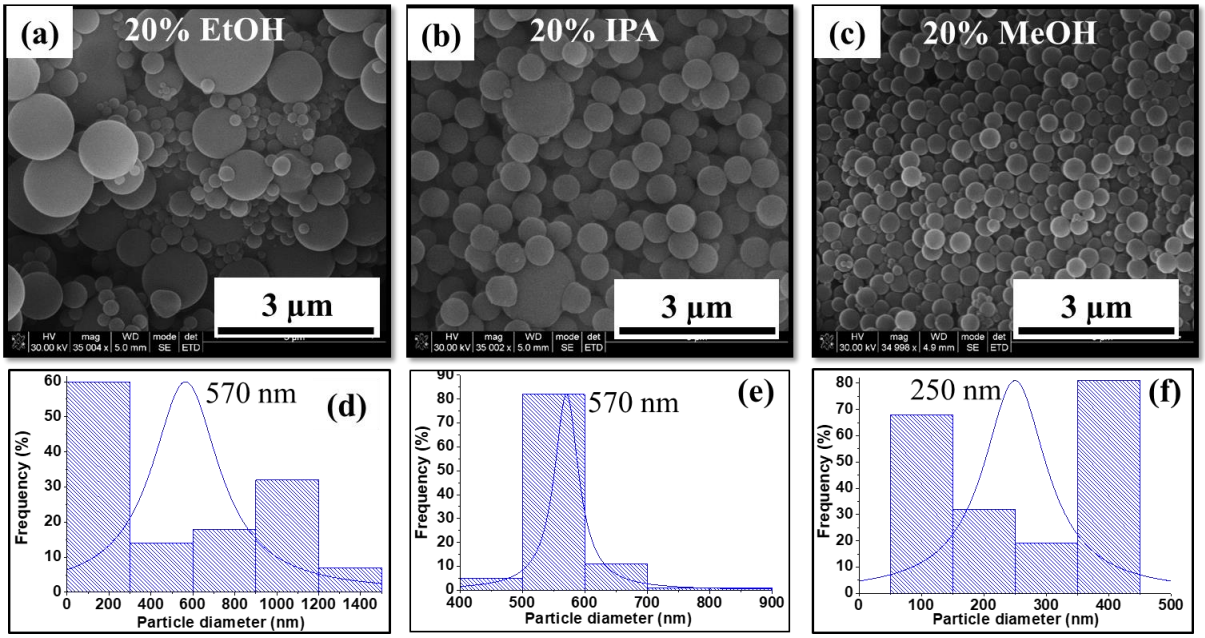

Figure 5.3: SEM images (a-c) and particle size distribution curves (d-f) of PS-b-PMAA spheres synthesized in different solvents: (a, d) ethanol, (b, e) isopropanol and (c, f) methanol.

The synthesis of PS-*b*-PMAA spheres was investigated by making use of three solvents, ethanol, methanol, and isopropanol. A 20 % volume of each alcohol mixed with distilled water was used in the three separate reactions. The type of solvent used in the synthesis of polymer spheres influences the size, dispersion, and shape of the resulting spheres. Figure 5.3 shows the SEM images of the PS-*b*-PMMA spheres synthesized in different solvents and the average diameters of the spheres are reported on the particle size distribution curves. The spheres prepared in ethanol were polydisperse with an average diameter of 570 nm and a wide size distribution between 100 to 1400 nm (a, d). Isopropanol resulted in spheres with an average diameter of 570 nm and a narrow size distribution between 400 and 700 nm (b, e). Most of the particles were distributed between 500 and 600 nm, therefore these particles were nearly

monodispersed. Methanol produced the smallest spheres that were polydisperse, with an average diameter of 250 nm, distributed between 50 and 450 nm.

The shape of the particles remained the same with all solvents, indicating that the solvent has very little influence on the shape. For most polymer applications smaller spheres are preferred because they provide a relatively high surface area. Since ethanol gave the most polydisperse sphere, it was further used to investigate how the solvent composition affects the sphere diameter by increasing the amount of water in the solvent.

Effect of increasing the amount of water

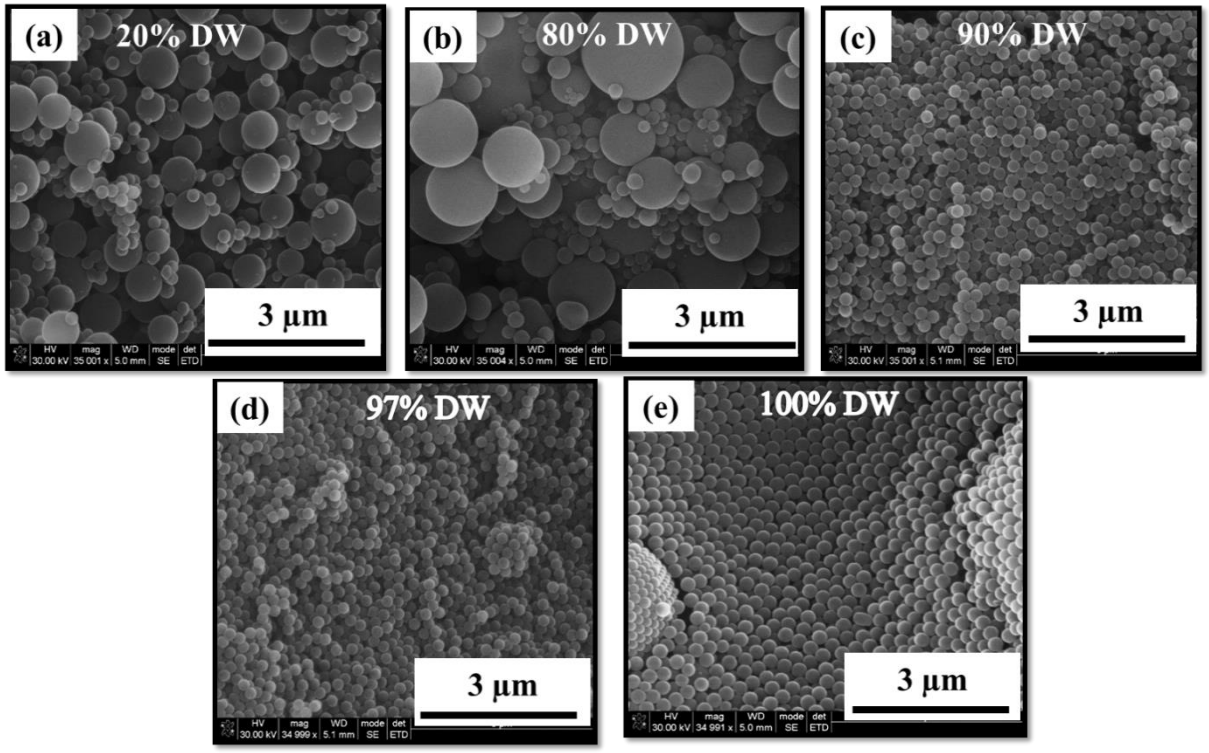

Figure 5.4: SEM images of PS-b-PMAA spheres synthesized in varying amounts of distilled water: (a) 20%, (b) 80%, (c) 90%, (d) 97 % and (e) 100 %

The volume of distilled water was varied to investigate the effect of using different amounts of ethanol on the size and dispersion of the polymer spheres. Figure 5.4 reports the SEM images of PS-*b*-PMMA spheres synthesized with varying solvent compositions. The particle size distribution curves and average diameters are reported in Figure S5.1. The use of a low volume of water (20 %, (a)) produced big and polydisperse polymer spheres with an average diameter of 480 nm and a wide particle size distribution between 100 and 1000 nm. Even with 80 % water (b), polydispersed and big particles were produced (570 nm distributed between 100 and 1400 nm). As the volume of water was increased to 90% (c), 97% (d) and 100%, the average diameter of the spheres also decreased to 240 nm, 210 nm and 230 nm, respectively. It was

further noted that the particle size distribution also narrowed to 210 – 260 nm (90 %), 200 – 235 nm (97 %) and 180 – 300 nm (100 %). It is therefore evident that the lowest volume of ethanol gave the smallest copolymer spheres with a very narrow size distribution. Only small amounts of ethanol were necessary for the synthesis of small PS-*b*-PMMA spheres with a narrow size distribution. The shape of the spheres was not influenced by the change in solvent composition. The use of organic solvents in the synthesis of copolymer spheres can be avoided because distilled water alone is a good solvent for the synthesis of small PS-*b*-PMMA copolymer spheres with a narrow size distribution. Therefore, the use of pure water as a solvent was further explored by changing the monomer composition.

Varying monomer composition

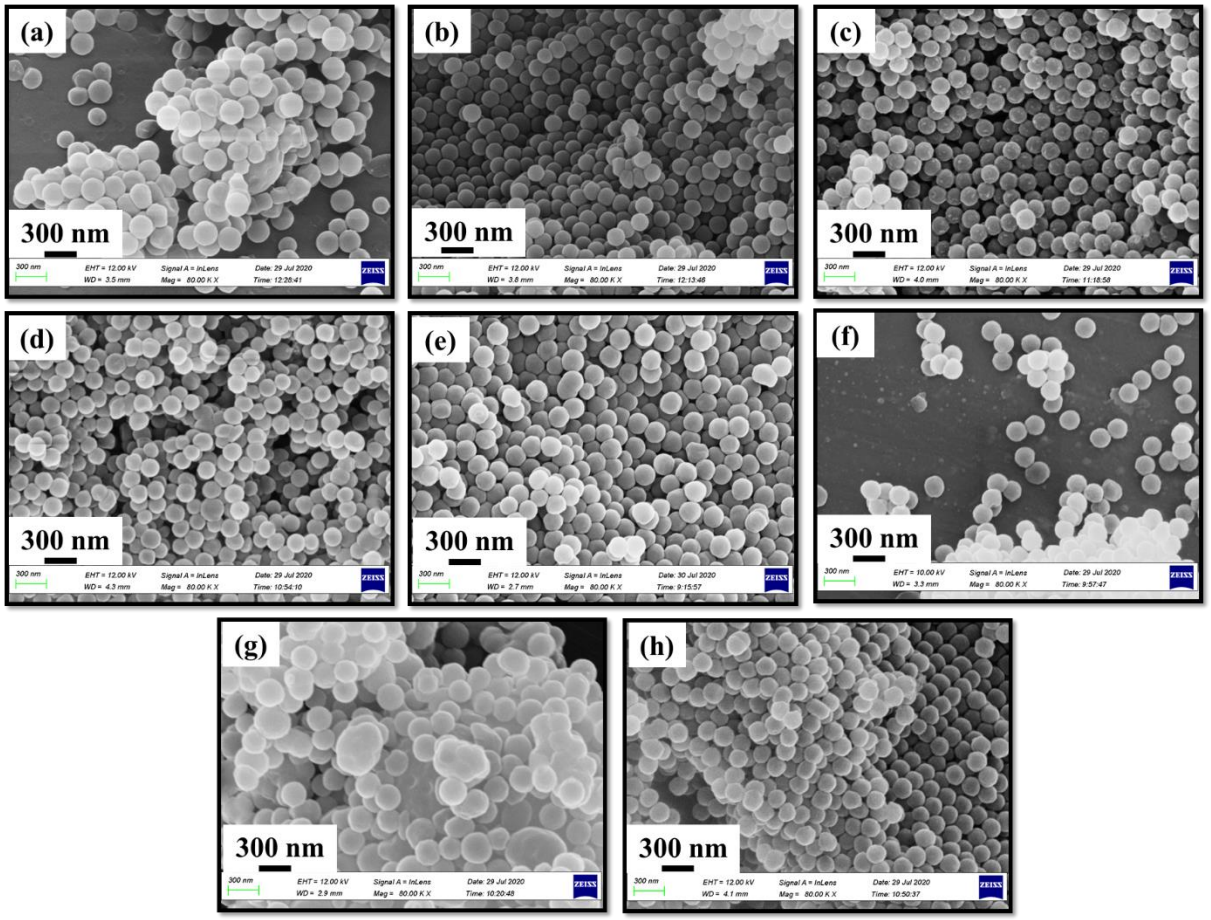

Figure 5.5: SEM images of PS-b-PMAA spheres synthesized in varying MMA monomer composition: (a) 10%, (b) 20%, (c) 30%, (d) 40 %, (e) 60 % (f) 70 %, (g) 80 % and (h) 90 %

The monomer composition was varied by using different ratios of styrene: methyl methacrylate in pure distilled water. Figure 5.5 shows the SEM images of the various PS-*b*-PMMA copolymer spheres and the corresponding particle size distribution curves, while the average

particle size diameters are reported in Figure S2. The amount of the MMA monomer was increases from 10 % to 90 %, in increments of 10 %. The average particle size diameter remained between 190 nm and 250 nm with the varying monomer composition. There was no observable trend with the change in particle size as the amount of MMA was increased. The spheres remained monodispersed and there were no changes observed in the shape of the particles. Therefore, changing the monomer composition did not seem to have a noticeable effect on the co-polymer spheres. However, it seemed possible to manipulate the diameter of the polymer template by changing the polymer composition. This was important in the synthesis of HCSs when trying to obtain spheres of a preferred diameter. The variations in monomer composition could be combined with the control of other reaction parameters such as the amount of stabilizer, reaction temperature, amount of solvent, etc. to try and obtain functionalized templates that are smaller than 100 nm.

5.3.2. Characterization of Co@HCSs

Three of the synthesized polymers were used to prepare Co@HCSs catalysts loaded with 15% Co. These were named 15%Co@HCSs_PS_{90}-b-$PMMA_{10}$, 15%Co@HCSs_PS_{50}-b-$PMMA_{50}$ and 15%Co@HCSs_PS_{10}-b-$PMMA_{90}$ for the catalysts prepared with templates containing 10%, 50% and 90% MMA, respectively. Figure 5.6 shows the TEM images and particle size distribution curves of the catalysts, and Table 5.1 reports the summary of the HCS internal diameter and shell thickness data.

As can be seen from the TEM images the HCSs are uniformly shaped and monodisperse, with varying internal diameter and carbon shell thickness for the HCSs made with different templates. The 90% MMA template gave the smallest HCSs (164 nm) with the thickest carbon shell (48 nm). The small internal diameter is related to the initial diameter of the polymer (192 nm, Figure 5.5). Due to the high temperature used during carbonization, the final diameter of the HCSs was reduced and became slightly smaller than the initial diameter of the polymers. The 50% MMA polymer had the largest diameter (260 nm) and therefore gave the largest HCSs (204 nm) with a shell thickness of 37 nm. The 10% MMA template gave HCSs with a diameter of 185 nm, related to the initial diameter of this template (245 nm). The HCSs internal diameters showed a simple trend where they increased with an increase in the polymer diameters. However, the shell thickness showed a trend where it increased with an increase in the amount of MMA in the polymer. The TGA of the polymer spheres (Figure S5.3) showed that the polymers do not decompose completely under N_2(g), a residue remained and varied

depending on the amount of MMA in the polymer. This residue was caused by the PMMA grafted into the PS and seemed to increase as the amount of MMA increased.

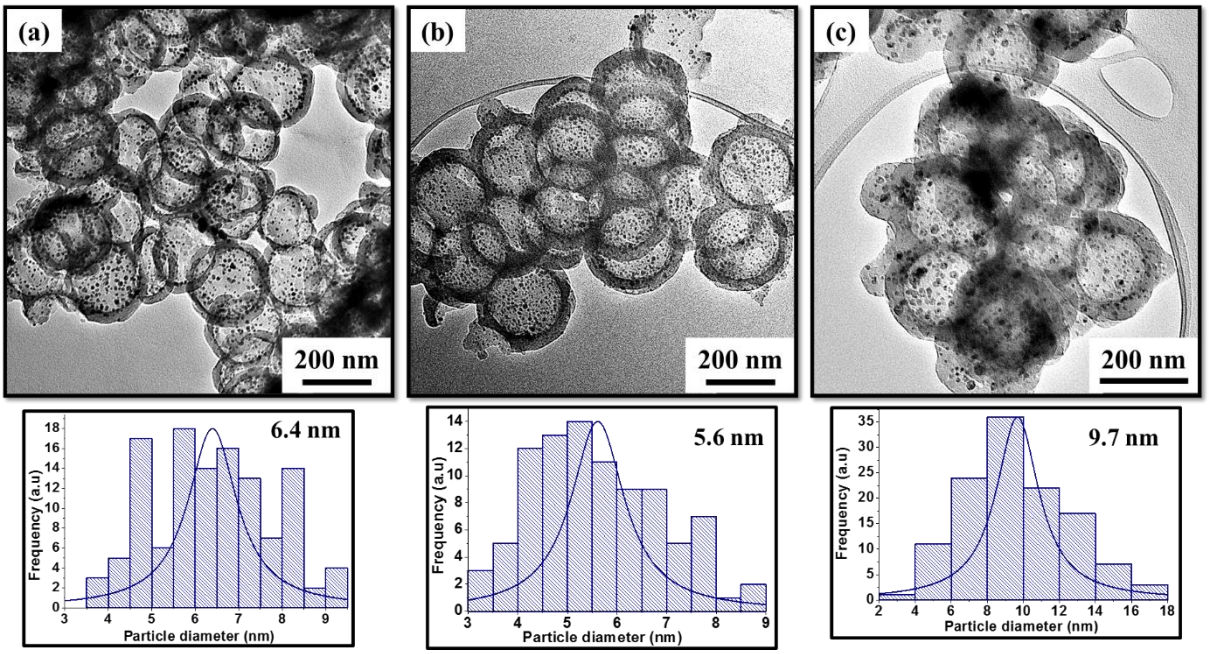

Figure 5.6: TEM images and particle size distribution curves for (a) 15%Co@HCSs_PS90-b-PMAA10, (b) 15%Co@HCSs_PS50-b-PMMA50, and (c) 15%Co@HCSs_PS10-b-PMMA90

The particle diameters of the metal nanoparticles loaded inside the HCSs were measured from the TEM images and reported in Table 5.1. The amount of cobalt loaded was determined using TGA and reported in Table 5.1. It was observed from the TEM images that small nanoparticles were synthesized, with varying average particle diameters for the different catalysts. The variations in particle size are related to the variations in Co metal loading. The nominal Co loading was 15 %, however, the catalysts contained 16.5 %, 14.3 % and 17.3 % Co for the 10, 50 and 90 % MMA catalysts, respectively. The catalyst containing the least amount of Co (14.3 %) had the smallest Co particles (5.6 nm), while the catalyst containing the most amount of Co (17.3 %) had the largest Co particles (9.7 nm). It is well known that the size of metal nanoparticles tends to grow with an increasing amount of metal loading. Here we have shown that the PS-b-PMMA templates successfully stabilized the Co nanoparticles as they produced nanoparticles with average diameters of less than 10 nm. These particles were much smaller than the particles produced when using an unfunctionalized PS template that gave particles that were larger than 30 nm at 15 % Co loading (Chapter 3). The amount of MMA present in the template does not seem to influence the particle size of the Co nanoparticles. However, it does have a large impact on the diameter and shell thickness of the HCSs. This has the potential to

produce smaller HCSs by simply controlling the size of the PS-b-PMMA spheres via monomer composition.

Table 5.1: Summary of the Co@HCSs_PS-b-PMMA properties

Sample	Polymer d (nm)	HCS Id (nm)[a]	HCS St(nm)[b]	Co diameter (nm) TEM	Co diameter (nm) PXRD	%Co[d]
15%Co@HCSs_PS$_{90}$-b-MAA$_{10}$	245	185	27	6.4	10.5	16.5
15%Co@HCSs_PS$_{50}$-b-MAA$_{50}$	260	204	37	5.6	7.9	14.3
15%Co@HCSs_PS$_{10}$-b-MAA$_{90}$	192	164	48	9.7	12.1[c]	17.3

[a] Internal Diameter, [b]Shell Thickness, [c]determined using CoO peak, [d] determined by TGA.

The metal crystallite sizes were also determined using PXRD and reported in Table 5.1. The PXRD sizes were larger than seen in the TEM images, but a similar trend was noted where the particle size increased as the metal loading increased.

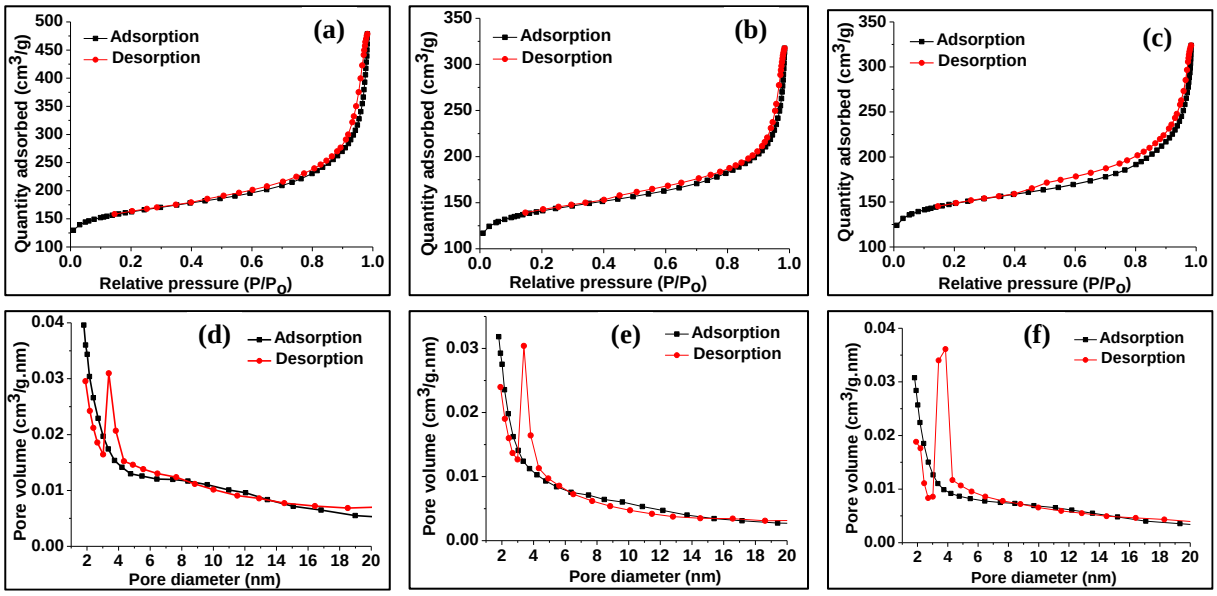

Figure 5.7: BET isotherms and pore size distribution curves of the catalysts (a, d) 15%Co@HCSs_PS90-b-PMAA10, (b, e) 15%Co@HCSs_PS50-b-PMMA50, and (c, f) 15%Co@HCSs_PS10-b-PMMA90

The BET isotherms and pore size distribution curves of the polymers are presented in Figure 5.7, and the data are summarized in Table 5.2. The materials contained a mixture of micropores and mesopores. This evident from the BET isotherms which were a combination of type I and type IV adsorption isotherms. The pore size distribution curves showed a high volume of pores with a diameter below 2 nm, which further confirmed the presence of

micropores. Pores with diameters above 2 nm were also observed, which indicated the presence of mesopores. This is typical of HCSs prepared with resorcinol-formaldehyde (RF) in the presence of CTAB, which creates pores on the RF shell. The catalysts had relatively high BET SA's (Table 5.2), however, the catalyst prepared with the PS_{90}-b-$PMMA_{10}$ template had the highest surface area (534 m^2/g). This could be related to the small diameter (185 nm) and shell thickness (27 nm) of the HCSs for this catalyst. The 15%Co@HCSs_PS_{10}-b-MAA_{90} catalyst had the second-highest BET SA (481 m^2/g), with the highest micropore SA (324 m^2/g). This could be related to the thick HCS shell (48 nm) and the small HCSs diameter (164 nm). The SA's of the catalysts generally showed a variation that seemed to the related to the diameter and shell thickness of the HCSs. However, the size and % loading of the metal nanoparticles also influence the surface area.

Table 5.2: Summary of the surface area properties of the catalysts

Sample	BET SA (m^2/g)	Micropore SA (m^2/g)	Pore diameter (nm)	Pore Volume (cm^3/g)
15%Co@HCSs_PS_{90}-b-MAA_{10}	534	306	5.4	0.73
15%Co@HCSs_PS_{50}-b-MAA_{50}	459	299	4.2	0.48
15%Co@HCSs_PS_{10}-b-MAA_{90}	481	324	4.1	0.49

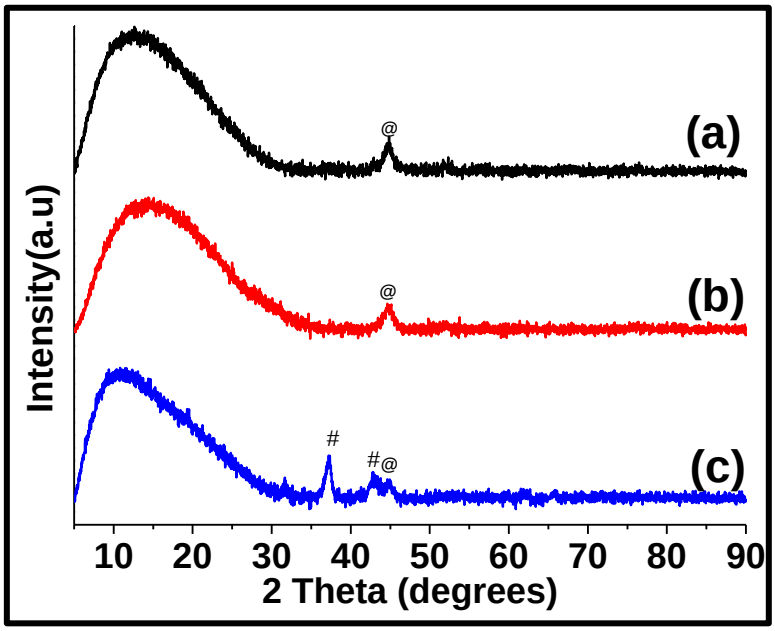

Figure 5.8: PXRD diffractograms of the catalysts (a) 15%Co@HCSs_PS90-b-PMAA10, (b) 15%Co@HCSs_PS50-b-PMMA50, and (c) 15%Co@HCSs_PS10-b-PMMA90. #: CoO PDF 00-048-1719, @: fcc Co amcsd 0011143

The PXRD patterns of the catalysts are shown in Figure 5.8. The broad peak at ~15 °2θ is characteristic of amorphous carbon. This is typical of carbon produced from the pyrolysis of resorcinol-formaldehyde. The catalysts showed domination of Co, even though the 15%Co@HCSs_PS_{10}-b-$PMMA_{90}$ showed the presence of both CoO and Co. The surface functional groups on the copolymer may have assisted with the metal reduction process. It has been previously reported that some polymers can act as metal reducing agents [23].

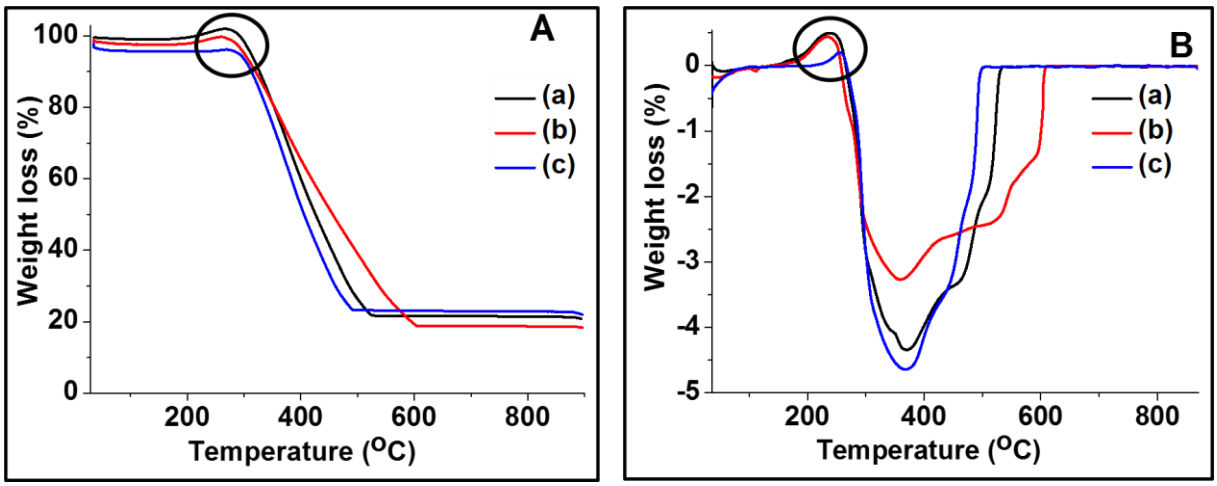

Figure 5.9: (A) TGA and (B) derivative TGA curves of the catalysts (a) 15%Co@HCSs_PS90-b-PMAA10, (b) 15%Co@HCSs_PS50-b-PMMA50, and (c) 15%Co@HCSs_PS10-b-PMMA90

Figure 5.9 contains the TGA and derivative TGA curves of the catalysts. The TGA curves were used to estimate the amount of Co loading on the catalysts. The catalysts had similar residue, corresponding to the amount of Co loaded on each catalyst. An oxidation peak at ~ 250 °C can be observed on both the TGA and DTG curves (circled in black). This oxidation peak is due to the oxidation of Co to CoO and Co_3O_4. This is a further confirmation of the presence of Co (0), as observed on the PXRD. The decomposition occurred in a 3-step process and was catalysed by the Co nanoparticles. The low temperature peak was due to the decomposition of amorphous carbon, while the high temperature peak was due to the decomposition of graphitic carbon. This was expected because the carbon produced with RF usually contains a mixture of amorphous and graphitic carbon. The first decomposition was observed at ~ 300 °C, which showed that the catalysts have good thermal stability. There was no significant variation in the decomposition temperatures of the catalysts. The 15%Co@HCSs_PS_{10}-b-$PMMA_{90}$ catalyst had a slightly higher decomposition temperature, this was because this catalyst contained relatively less metal than the other catalysts, as was observed in the TGA residue. Therefore, all three catalysts showed very similar thermal stabilities.

Conclusions

This chapter focused on tuning the template properties and evaluated how the different templates influenced the properties of HCSs encapsulating metal nanoparticles. The synthesized copolymers contained functional groups which assisted with stabilizing and reducing Co nanoparticles. As a result, small Co nanoparticles dominated by Co (0) were successfully synthesized and encapsulated inside the HCSs. Variations in synthesis parameters of the co-polymer templates resulted in templates with varying particle diameters, this led to the synthesis of HCSs varying internal diameters and shell thickness. It was further observed that the varying HCSs properties resulted in a variation in the surface properties of the catalysts. Surface area is one of the important properties which influence the activity and selectivity of catalysts. Therefore, the templates synthesized in this study can be further modified to synthesize smaller templates that can be used to tune the surface area properties of HCSs.

References

[1] T. P. Lodge, "Block copolymers: Past successes and future challenges," Macromol. Chem. Phys., vol. 204, pp. 265-273, 2003.

[2] A. Noshay and J. E. McGrath, Block copolymers: overview and critical survey, New York: Academic Press, 1997.

[3] S. koltzenburg, M. Maskos and O. Nuyken, Polymer Chemistry, Berlin Heidelberg: Springer-Verlag, 2017.

[4] C. Shi, Y. Yao, Y. Yang and Q. Pei, "Regioselective copolymers of 3-akoxythiophene and their photovoltaic application," J. Am. Chem. Soc., vol. 128, pp. 8980-8986, 2006.

[5] A. C. Obermeyer and B. D. Olsen, "Synthesis and application of protein-containing block copolymers," ACS Macro Lett., vol. 4, pp. 101-110, 2015.

[6] M. W. Meshram, V. V. Patil, S. T. Mhaske and B. N. Thorat, "Graft copolymers of starch and its application in textiles," Carbohyd. Polym., vol. 75, pp. 71-78, 2009.

[7] K. S. Lee, J. Lee, J. Kwak, H. C. Moon and J. K. Kim, "Reduction of line edge roughness of polystyrene-block-poly(methyl methacrylate) copolymer nanopatterns by introducing hydrogen bonding at the junction point of two block chains," Applied Materials and Interfaces, vol. 9, pp. 31245-31251, 2017.

[8] T. Sakai and P. Alexandris, "Single-step synthesis and stabilization of metal nanoparticles in aqueous pluronic block copolymer solutions at ambient temperature," Langmuir, vol. 20, pp. 8426-8430, 2004.

[9] R. J. Hickey, A. S. Haynes, J. M. Kikkawa and S.-J. Park, “Controlling the self-assembly structure of magnetic nanoparticles and amphiphilic block copolymers: from micelles to vesicles,” J. Am. Chem. Soc., vol. 133, pp. 1517-1525, 2011.

[10] E. Raoufian, H. Eslami and M. Darafarin, “Synthesis of spike-ball-like polystyrene/poly(methyl methacrylate) composite particles via seeded polymerization,” Polym. Int, vol. 67, pp. 61-67, 2018.

[11] Y. Cong, W. Zhai and C. Wu, “Morphology evolution of block copolymer blend thin films induced by solvent vapor annealing,” Soft Materials, p. 10.1080/1539445X.2020.1775648, 2020.

[12] Y. Seo, S. Jang, S. Ahn, A. K. Mishra and J. K. Kim, “Phase behaviour of 18-arm star-shaped polystyrene-block-poly(methyl methacrylate) copolymers with different second block initiations,” Macromolecules, vol. 51, pp. 2750-2755, 2018.

[13] H. Miyazoe, A. V. Jagtiani, H.-Y. Tsai, S. U. Engelmann and E. A. Joseph, “Highly selective dry etching of polystyrene-poly(methyl methacrylate) block copolymer by gas pulsing carbon monoxide-based plasmas,” Journal of Physics D: Applied Physics, vol. 50, no. 204001, 2017.

[14] I. H. Ifijen and E. U. Ikhuoria, “Monodisperse polystyrene microspheres: studies on the effects of reaction parameters on particle diameter and colloidal stability,” Tanzania Journal of Science, vol. 46, pp. 19-30, 2020.

[15] X. Zhang, Y. Cao, Q. Jiang , Y. Zhang and W. Yang, “Preparation of cross-linked poly(methyl methacrylate) microspheres using an asymmetric cross-linker via dispersion polymerization and its application in light diffusers,” Colloid and Polymer Science, vol. 298, pp. 495-504, 2020.

[16] R. Arshaday, “Suspension, emulsion and dispersion polymerization,” Colloid Polym. Sci., vol. 270, pp. 717-732, 1992.

[17] C. K. Ober and K. P. Lok, “Formation of large monodisperse copolymer particles by dispersion polymerization,” Macromolecules, vol. 20, pp. 268-273, 1987.

[18] S. Shen, E. D. Sudol and M. S. El-Aasser, “Control of particle size in dispersion polymerization on methyl methacrylate,” Journal of Polymer Science: Part A: Polymer Chemistry, vol. 31, pp. 1393-1402, 1993.

[19] S. Kawaguchi and K. Ito, “Dispersion polymerization,” in Advances in Polymer Science, vol. 175, M. Okubo, Ed., Berlin, Heidelberg: Springer, 2005, pp. 299-328.

[20] A. Abdollahi, H. Roghani-Mamaqani and M. Salami-Kalajahi, “Morphology evolution of functionalized styrene and methyl methacrylate copolymer latex nanoparticles by one-step emulsifier-free emulsion,” European Polymer Journal, vol. 133, no. 109790, 2020.

[21] D. Debnath and B. B. Khatua, “Preparation by suspension polymerization and characterization of polystyrene (PS)-poly(methyl methacrylate)(PMMA) core-shell nanocomposites,” Macromolecular Research, vol. 19, pp. 519-527, 2011.

[22] P. Mente, T. N. Phaahlamohlaka, V. Mashindi and N. J. Coville, “Polystyrene-b-poly(acrylic acid) nanospheres for the synthesis of size-controlled cobalt nanoparticles encapsulated inside hollow carbon spheres,” J. Mater. Sci., vol. 56, pp. 10-16, 2021.

[23] C. Huang, Y. Ding, C. Hao, S. Zhou, X. Wang, H. Gao, L. Zhu and J. Wu, “PVP-assisted growth of Ni-Co oxide on N-doped reduced graphene oxide with enhanced pseudocapacitive behavior,” Chem. Eng. J., vol. 378, p. 122202, 2019.

Chapter 6: The oxidation of benzyl alcohol using cobalt oxide supported inside and outside hollow carbon spheres[2]

6.1. Introduction

The catalytic performance and efficiency of a material are evaluated based on its activity, selectivity and stability [1]. Many catalysts are placed on a support to enhance the metal particle surface concentration, and the catalyst support material is thus an important factor that influences catalytic efficiency [2]. Catalyst support materials include titania, alumina, silica, tungsten oxide, and carbon [3,4]. Metal oxide supports have the advantage that they can be used at high temperatures but have the disadvantage of forming strong interactions with metal nanoparticles, leading to reduced catalytic activity via the formation of metal-support compounds, which are not catalytically active [5]. In contrast, carbon supports are relatively chemically inert, and therefore do not form strong metal-support interactions [6]. Many carbon based supports that have been used in catalytic reactions include nanofibers, nanotubes, spheres, hollow spheres, nanodiamonds, graphene and carbon black [7-9]. In this study, the focus was placed on using hollow carbon spheres (HCSs) as a support and we studied the effect of placing a catalyst (Co_xO_y) either inside or outside a HCS.

HCSs have found applications in many fields such as catalysis, gas storage, electrocatalysis, as templates for the synthesis of other hollow spheres, electrode materials for lithium-ion batteries and water purification [10-12]. They find use in all these applications because they have unique and desirable structural characteristics that include a high surface area, low density, a mesoporous shell, uniform particle size, narrow pore size distribution and a relatively high oxidation stability [13-15]. The catalytically active materials can be supported either inside and/or outside of the HCSs. By varying the shell porosity, access to/from the HCS interior by reactants/products can be modified. Numerous studies that have been reported in which metals have been placed outside a HCS revealed that the carbon acts as a classical carbon support [9,16-20]. Fewer studies have been reported in which a metal catalyst has been placed inside the HCSs; these studies include reports on Pt, Pd, Cu, Co, Au, and alloys as catalysts [21-28]. Comparative studies in which metals have been placed both inside and outside HCSs are rare.

[2] This chapter has been accepted for publication as: Pumza Mente, Victor Mashindi, Tumelo N. Phaahlamohlaka, Thabo Monyatsi, Roy P. Forbes and Neil J. Coville, The oxidation of benzyl alcohol using cobalt oxide supported inside and outside hollow carbon spheres. (Accepted Manuscript, ChemistryOpen, 2021).

In this study, we have supported Co oxide nanoparticles both inside and outside HCSs compared their different catalytic activities/selectivities.

The catalytic oxidation of benzyl alcohol to benzaldehyde was used in this study as a model reaction to evaluate these new Co catalysts. The oxidation of alcohols to the corresponding carbonyl compounds (aldehyde, ketones, carboxylic acids) has been widely investigated and reported in the scientific literature [20, 29]. These oxidation reactions produce starting materials to produce important organic compounds that are used for the synthesis of various industrial and consumer products [30, 31]. Benzaldehyde is useful in the production of pharmaceuticals, pesticides, perfumes, dyes and aromatic compounds [32,33]. Different oxidizing agents have been used for the oxidation of benzyl alcohol, including the use of hydrogen peroxide, manganese dioxide, permanganate and dichromate [34-37]. Catalytic oxidation, using air or molecular oxygen in the presence of a heterogeneous catalyst, is a more environmentally friendly approach than compared to other methods and this oxidant has also shown good efficiency [38,39]. Many current methods for the oxidation of benzyl alcohol can suffer disadvantages, such as long reaction times and low efficiencies [33].

Oxidation of simple small-chain alcohols is normally straightforward. However, the oxidation of complex molecules is usually complicated by the production of unwanted carboxylic acid compounds that may cause catalyst deactivation [39-41]. The oxidation of benzyl alcohol to benzaldehyde usually leads to the formation of benzoic acid, benzyl benzoate and toluene as by-products [29,30]. Therefore, the ideal catalyst for this reaction will selectively produce benzaldehyde in large amounts. Noble metal catalysts such as Pt, Pd, Au, Rh, Ir and Ru have been investigated for this process and good activity and selectivity have been achieved [31, 38]. However, these metals are expensive and, in some cases, require the use of promoters such as NaOH and K_2CO_3 to control the selectivity during the reaction [29, 42]. Base metals like Co, Ni, Fe and Cu are relatively cheaper alternatives that have also been used without the use of promoters and can provide high selectivity [43]. These catalysts, however, suffer from low activity [33, 43] and therefore there is still a need for the development of efficient heterogeneous catalysts for the oxidation of benzyl alcohol to benzaldehyde. This can be achieved through manipulation of the material properties by tuning the metal particle size and support material properties such as surface area, porosity, and electronic structure.

In this study, Co oxide nanoparticles were supported either inside or outside HCSs viz. Co_xO_y@HCSs and Co_xO_y/HCSs, respectively. The Co_xO_y@HCSs catalysts were synthesized

using two different types of templates, polystyrene (PS) and the copolymer, PS-b-poly(acrylic acid) containing 12% acrylic acid (PS-b-PAA_{12}) and were named CoxOy@HCSs_PS and CoxOy@HCSs_PS-b-PAA_{12}, respectively (Chapter 3,[44]). Catalysts with different Co loadings, different Co sizes and different Co oxidation states were studied.

6.2. Experimental Section

6.2.1. Materials

Styrene, acrylic acid, polyvinylpyrrolidone (PVP, MW 40 000), resorcinol, formaldehyde solution (37%), cetyltrimethylammonium bromide (CTAB), cobalt nitrate hexahydrate, hydrazine hydrate (78-82%) and benzyl alcohol were all purchased from Sigma Aldrich and used as received. Ammonia solution (25%, Fluka), potassium persulfate (Eimer and Amend), ethanol (98%, MK Labs) and N,N-dimethylformamide (Merck) were also used as received. Distilled water was used for all experiments and product washing steps. Oxygen (technical grade) was purchased from Afrox.

Synthesis of polymer spheres (PSs):

Polystyrene spheres (PS) (d = 350 nm) and the co-polymer, polystyrene-b-poly (acrylic acid) with 12% PAA (PS-b-PAA12) (d = 343 nm) were synthesized as described previously (see Chapter 3, ([44]).

Synthesis of CoxOy inside HCSs (CoxOy @HCSs):

The synthesis of 5% Co_xO_y@HCSs, 10% Co_xO_y@HCSs and 15% Co_xO_y@HCSs were done as described previously using PSSs and PS-b-PAA_{12} templates (see Chapter 3 [44]). The synthesis of the corresponding Co_xO_y/PS and resorcinol-formaldehyde (RF) covered Co_xO_y/PS (RF/ Co_xO_y/PS) were also made as described in Chapter 3 [44].

Synthesis of Co_xO_y outside HCSs (Co_xO_y/HCSs):

The RF/PS composites were synthesized using the method reported above by making use of PS instead of a Co_xO_y/PS composite. The RF/PS composite (2 g) was dispersed in 50 mL distilled water and 28 mL ethanol by ultrasonication and 0.07 g of cobalt nitrate hexahydrate was added to this mixture while stirring. After 5 minutes (or until all the cobalt salt dissolved), 3.3 mL of 2 M hydrazine hydrate was added slowly (dropwise), and the reaction continued for

12 h, at room temperature. The mixture was filtered by vacuum filtration and the product (Co_xO_y/RF/PS) was washed with water, dried in the oven at 60 °C for 12 h, crushed with a mortar and pestle and stored in a glass sample vial. The dry product was annealed to produce 5% Co_xO_y/HCSs. Two and three times the amount of cobalt nitrate hexahydrate and hydrazine hydrate were used to synthesize 10% Co_xO_y/HCSs and 15% Co_xO_y/HCSs, respectively.

Catalyst calcination:

The catalysts were calcined by placing ~70 mg of the as-synthesized catalyst between two plugs of quartz wool, inside a glass tube reactor. The reactor was placed inside a vertical furnace and heated to 200 °C at a rate of 5 °C/min, under 5%O_2/He flowing at 20 mL/min and kept isothermal for 2 h. Thereafter the catalyst was cooled to room temperature. The 15% metal loaded catalysts were calcined for 4 h to ensure the complete conversion of Co and CoO to Co_3O_4.

6.2.2. Characterization techniques:

TEM, TGA, PXRD and surface area and porosity analysis procedures were done under similar conditions as reported in Chapter 3. The XPS measurements were carried out using a Thermo Scientific ESCALAB 250Xi spectrometer with a Monochromatic Al Kα source (1486.7eV) operating with an X-ray power of 300 W, X-ray spot size of 900 µm, low resolution pass energy of 100 eV, high resolution pass energy of 20 eV and a pressure of 10-8 mBar.

6.2.3. Catalytic reactions:

Catalyst (50 mg) was added to a 100 mL 3-neck round bottom flask fitted with a reflux condenser, gas inlet and a rubber septum. N, N-dimethylformamide (DMF, 25 mL) and benzyl alcohol (2 mL, 19.2 mmol) were added to the flask and the reaction was heated to 110 °C under 40 mL/min O_2 flow and constant stirring. The reaction was continued for 8 hours, during which time 0.5 mL aliquots were sampled every hour and analysed by gas chromatography with an FID, using a capillary column (Phenomenex Zebrox, 30 m x 0.53 mm) and N_2 as the carrier gas. The products were also analysed with a GC-MS. All the variables were kept constant for the different reactions.

6.3. Results and Discussion

6.3.1. Catalyst Characterization

Figure 6.1 shows TEM images and particle size distribution curves for the Co_xO_y nanoparticles supported outside the HCSs (Co_xO_y/HCSs). The nanoparticles are well dispersed on the surface of the HCSs with small particle sizes of 6.2 nm, 5.2 nm and 5.4 nm for the 5%, 10% and 15% metal loaded catalysts, respectively. The synthesis and characterization of Co_xO_y nanoparticles loaded inside the HCSs (5, 10 and 15% Co_xO_y@HCSs) were described previously (Chapter 3 [44]). The catalyst properties (particle sizes, Co loadings and BET surface area, pore size and pore volumes) are summarized in Table 1. The particle sizes for the Co_xO_y/HCSs are comparable to the values reported for the Co_xO_y@HCSs catalysts (Table 6.1, [44]). The measured internal diameters of the CoxOy/HCSs were 263, 311 and 271 nm for the 5%, 10% and 15% catalysts, respectively. The HCS shell thicknesses were found to be 19, 23 and 19 nm for the 5%, 10% and 15% catalysts, respectively. These internal diameters and shell thickness were found to be comparable to the values observed for the metal loaded Co_xO_y@HCSs catalysts (Chapter 3 [44]). The similarities in these properties allowed for a comparison of the effect of the Co location on the benzyl alcohol oxidation reaction.

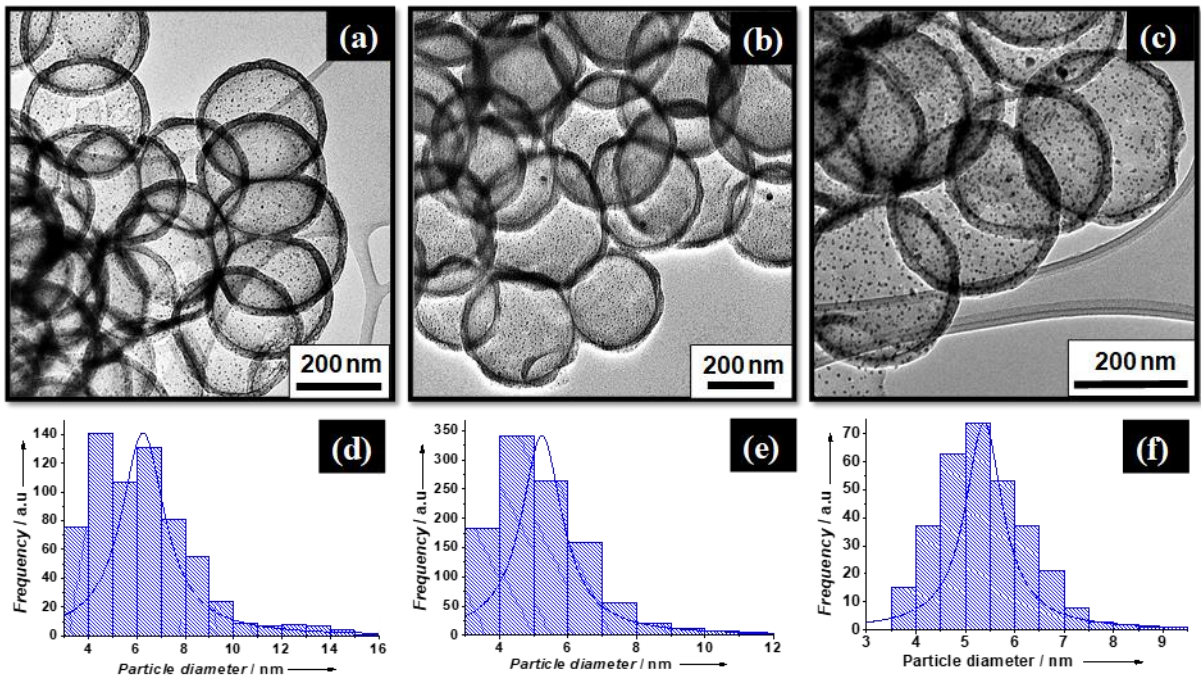

Figure 6.1: TEM micrographs (a,b,c) and particle size distribution curves (d,e,f) of (a,d) 5%CoxOy/HCSs, (b,e) 10%CoxOy/HCSs and (c,f) 15%CoxOy/HCSs

Table 6.1: Summary of catalyst properties (Co diameter, Co loading and BET surface area)

Catalyst	TEM Co diameter (nm)	PXRD Co diameter (nm)	% Co (TGA)	% Co_3O_4 (TGA)	BET SA (m^2/g)	Pore diameter (nm)	Pore volume (cm^3/g)
[a]**5%Co@HCSs_PS**	6.1	12.7	4.6	6.3	612	4.8	0.57
[a]**5%Co@HCSs_PS-*b*-PAA_{12}**	6.1	6.6	4.6	6.3	506	4.7	0.45
5%Co/HCSs	6.2	6.8	6.0	8.2	540	5.0	0.67
[a]**10%Co@HCSs_PS**	38	18.1	12.1	17.0	316	7.0	0.47
[a]**10%Co@HCSs_PS-*b*-PAA_{12}**	6.0	> 4	11.0	15.0	479	5.0	0.46
10%Co/HCSs	5.2	7.5	9.5	12.9	530	4.7	0.63
[a]**15%Co@HCSs_PS**	44	18.7	16.4	22.5	388	5.1	0.41
[b]**15%Co@HCSs_PS-*b*-PAA_{12}**	5.6	>4	14.3	19.6	536	4.5	0.43
15%Co/HCSs	5.4	6.3	13.0	17.5	498	5.2	0.51

[a] Data were taken from Chapter 3 [44]. [b] Characterizations for this catalyst are contained in supplementary Figures S6.1, S6.2 and S6.3.

The PXRD patterns of the CoxOy/HCSs catalysts are shown in Figure 6.2. The Co crystallite sizes were calculated using the Scherrer equation by integrating the main Co/CoO/Co_3O_4 peak in the corresponding PXRD diffractograms (Figure 6.2) are reported in Table 6.1. The calculated crystallite sizes were 6.8 nm, 7.5 nm and 6.3 nm for the 5%, 10% and 15% catalysts, respectively. The broad peaks observed between ~8.4° and ~14° for the 5%, 10% and 15% catalysts, are due to the presence of amorphous carbon [45]. The amorphous carbon was expected as it has been previously observed with carbon prepared from resorcinol-formaldehyde [46]. The spectra show the presence of mainly Co_3O_4 for the 5% and 10% catalysts. However, the PXRD of the 5% catalyst also indicates the presence of a small amount of CoO. The 15% catalyst contained mainly fcc Co and CoO. The PXRD peak positions are summarized in Tables S6.1, S6.2 and S6.3. The PXRD patterns of the CoxOy@HCSs were previously reported and also showed the presence of a mixture of Co_3O_4, CoO and Co nanoparticles (Chapter 3 [44]). It is clear that the reduction of the Co was affected by the Co loading (see below).

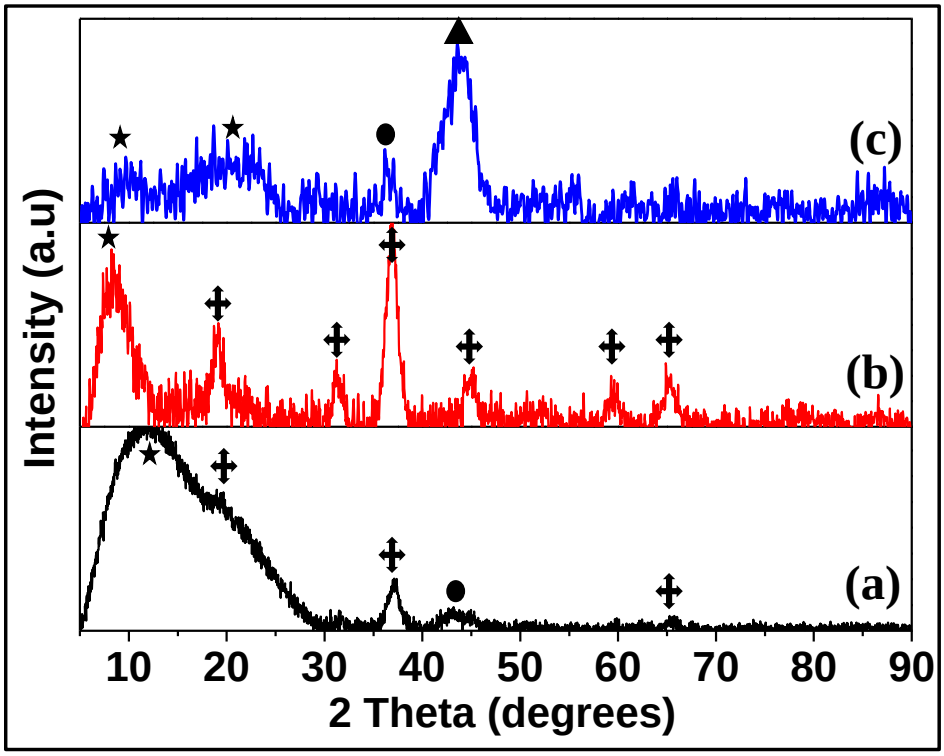

Figure 6.2: PXRD patterns of (a) 5% Co_xO_y/HCSs, (b) 10% Co_xO_y/HCSs and (c) 15% Co_xO_y/HCSs. ★ Carbon, ✣ Co_3O_4: PDF 00-043-100, ● CoO: PDF 00-048-1719, ▲ fcc Co: PDF 00-015-0806

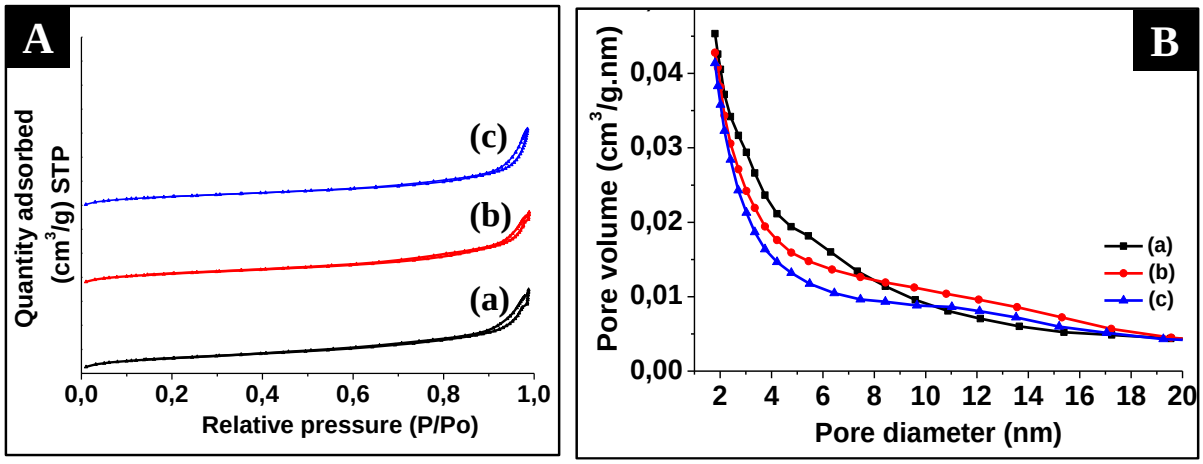

Figure 6.3: BET isotherms (A) and pore size distribution curves (B) of (a) 5%Co_xO_y/HCSs, (b) 10%Co_xO_y/HCSs and (c) 15%Co_xO_y/HCSs

Figure 6.3 shows the BET isotherms (A) and pore size distribution curves (B) of the Co_xO_y/HCSs catalysts. The adsorption-desorption curves are characteristic of a combination of type IV and type I isotherms, which indicate the presence of mesopores and some micropores [47]. The pore size distribution curves further confirm the presence of micropores and mesopores, as shown by the high volume of pores with diameters less than 2 nm. The BET surface areas, pore volumes and pore diameters of all catalysts are reported in Table 3.1. The

surface areas of the 5%, 10% and 15% Co_xO_y/HCSs catalysts were 540, 530 and 498 m2g-1, respectively. Similar pore diameters (5.0, 4.7 and 5.2 nm) and pore volumes (0.67, 0.63 and 0.51 m^3/g^{-1}) were reported for the 5%, 10% and 15% Co_xO_y/HCSs catalysts, respectively. The N_2 adsorption-desorption properties of the Co_xO_y/HCSs were comparable to the properties reported for the Co_xO_y@HCSs catalysts (Table 1, Chapter 3 [44]).

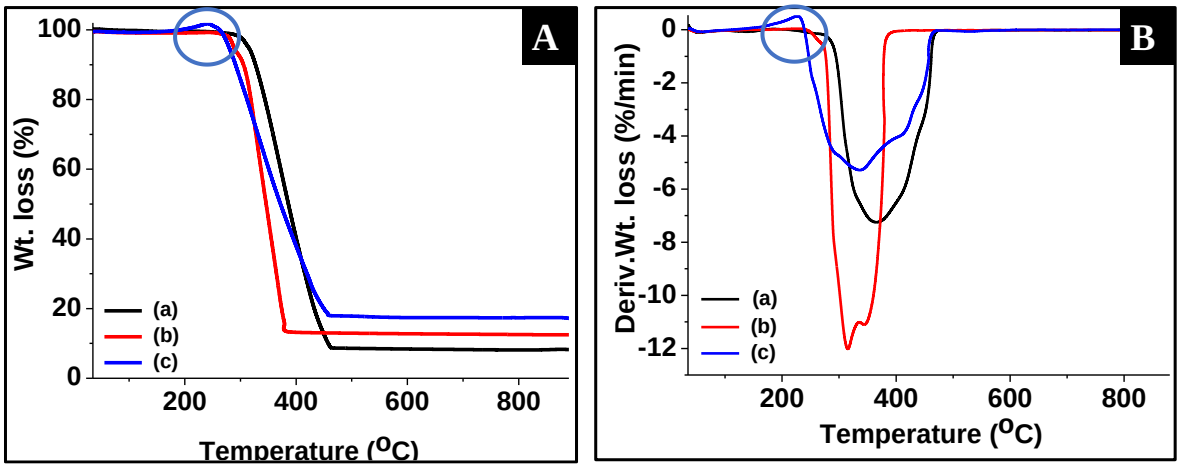

Figure 6.4: TGA (A) and derivative TGA curves (B) of (a) 5%Co_xO_y/HCSs, (b) 10%Co_xO_y/HCSs and (c) 15%Co_xO_y/HCSs

The TGA and derivative TGA curves of the Co_xO_y/HCSs catalysts are shown in Figure 6.4. The TGA curves (6.4A) were used to estimate the content of Co_3O_4 present in the catalysts. The Co_3O_4 contents were 8.2, 12.9 and 17.5 % for the 5, 10 and 15% Co_xO_y/HCSs catalysts, respectively (Table 6.1) and thus the corresponding Co metal contents (6.0, 9.5 and 13.0 %) were close to the loadings used in the synthesis. The estimated metal loadings of all the catalysts are reported in Table 6.1, and the expected trends can be seen for 5%, 10% and 15% catalysts. An oxidation peak (blue circle, Figure 6.4) can be observed for the 15% catalyst at ~240 °C (onset = 190 °C) indicating oxidation of Co to CoO and Co_3O_4. This is expected as the PXRD of the 15% catalyst indicated the presence of mainly Co.

The derivative TGA curves (6.4B) show a relatively higher decomposition temperature for the 5% catalyst relative to the 10% and 15% catalysts. This was expected as the carbon decomposition temperature is influenced by the presence of metal nanoparticles. Deconvoluted curves indicated the presence of possibly 3 decomposition maxima for the 5% (326, 363 and 414 °C), 10% (288, 314 and 344 °C) and 15% (284, 337 and 413 °C) Co_xO_y/HCSs catalysts. The position and breadth of the peaks are due to the catalytic effect of the oxidation of the HCS carbon by Co. The higher loading of Co led to the peaks for the 10% and 15% loaded catalysts being observed at lower oxidation temperatures than for the 5% loaded HCSs. Importantly, all

the catalysts showed comparable thermal stability and they were all stable at the temperature (110°C) used in the catalytic oxidation reactions.

6.3.2. Catalyst activity: oxidation of benzyl alcohol

The new materials were studied as catalysts by using a model reaction: the conversion of benzyl alcohol into benzaldehyde using molecular oxygen as the oxidant. The same amount of reactants, solvents and the same gas flow rates were used in all reactions. The activity was investigated by comparing metal loading as well as the effect of supporting the metal nanoparticles inside or outside HCSs at similar Co loadings. The catalysts were also calcined at 200 °C for 2 h (4 h for the 15% loaded catalysts) in 5%O_2/He and the catalytic activity before and after calcination was recorded. This arises since the Co was heated to 600 °C under N_2 to polymerize the RF and at these temperatures the carbon can reduce the Co (see below). Furthermore, the use of a PAA functionalized template in the synthesis of the Co_xO_y@HCSs catalysts resulted in different Co oxidation states. The activity data for the calcined catalysts are shown in Figures 6.5 and 6.6, and the data are summarized in Table 6.2. The data relates to the activity at 110 °C after 8 h, at atmospheric pressure for reactions performed after catalyst calcination. This data allowed for an exploration of the factors responsible for the variation in catalyst activity.

Effect of cobalt oxidation state

Since the catalysts had Co with different oxidation states (see PXRD data in Figure 2 and Chapter 3 [44]), the catalysts were also all calcined at 200 °C for 2 h (or 4 h). This calcination was performed at a low temperature to ensure that there was no catalytic conversion of the HCSs to CO_2 in the presence of air (see TGA, Figure 6.3). As expected, this resulted in improved catalyst activity for most of the catalysts (Table 6.2). This arose since Co_3O_4 was the required form of the catalysts for the oxidation reaction. In a previous study by Cordoba and co-workers [31] it was observed (after determining Co^{3+}/Co^{2+} ratios using XPS) that an activation period was required for the catalysts to convert from Co^{2+} to Co^{3+} in the oxidation of benzyl alcohol. They further reported that Co^{3+} was responsible for the catalytic activity while the Co^{2+} was non-active and therefore required activation. In another study by Xie et al. [48] it was reported that both Co^{2+} and Co^{3+} were responsible for the catalytic CO oxidation to CO_2. They reported a mechanism based on theoretical studies, showing that CO molecules

adsorb on the Co^{2+} sites, and CO_2 forms by reaction of CO with an O-atom from the Co^{3+} sites. Therefore, the Co^{2+} was responsible for the surface adsorption of CO, while Co^{3+} provided O-atoms. The presence of Co_3O_4 is therefore responsible for the catalytic efficiency of cobalt-based catalysts as it contains both Co^{2+} and Co^{3+} sites.

Table 6.2: Conversion, selectivity and catalyst activity of all the catalysts after 8 h of reaction

Catalyst	Benzyl alcohol Conversion (%)	Benzaldehyde selectivity (%)	Activity (mol_{conv}/g_{Co})
5%Co@HCSs_PS	35.8	86.1	2.99
5%Co@HCSs_PS-*b*-PAA$_{12}$	5.2	100	0.43
5%Co/HCSs	40.8	82.0	2.61
***C-5%Co@HCSs_PS**	47.5	76.7	3.96
***C-5%Co@HCSs_PS-b-PAA$_{12}$**	48.3	73.7	4.03
***C-5%Co/HCSs**	50.0	63.1	3.20
10%Co@HCSs_PS	41.5	78.2	1.31
10%Co@HCSs_PS-*b*-PAA$_{12}$	2.5	100	0.09
10%Co/HCSs	29.9	87.0	1.21
***C-10%Co@HCSs_PS**	42.4	75.6	1.34
***C-10%Co@HCSs_PS-b-PAA$_{12}$**	27.8	90.4	0.97
***C-10%Co/HCSs**	25.3	91.1	1.02
15%Co@HCSs_PS	53.0	61.3	1.24
15%Co@HCSs_PS-*b*-PAA$_{12}$	2.8	100	0.05
15%Co/HCSs	1.1	100	0.03
***C-15%Co@HCSs_PS**	30.9	71.3	0.72
***C-15%Co@HCSs_PS-b-PAA$_{12}$**	46.3	78.8	1.25
***C-15%Co/HCSs**	48.1	73.9	1.42

*Catalysts calcined at 200 °C for 2 h in 5%O_2/He.

The Co oxidation state varied with the type of support used.

i) The conversion for the 5%Co_xO_y/HCSs catalyst increased from 40.8 % to 50 % after calcination while the 10%Co_xO_y/HCSs decreased marginally from 29.9 % to 25.3 % (Table 6.2). Both these catalysts thus showed small changes with calcination consistent with a dominance of Co_3O_4 in the uncalcined catalysts (Figure 6.2, Tables S6.1, S6.2). This was expected. However, the 15%Co_xO_y/HCSs catalyst showed a large improvement in conversion after calcination (1.1% to 48.1%). This was consistent with the presence of Co metal in the sample (as seen in the PXRD spectrum in Figure 6.2) before calcination.

The TEM images and particle size distributions of the 5% and 10%Co_xO_y/HCSs after 8 h of benzyl alcohol oxidation were recorded (Figure S6.8) and the particle diameters are summarized in Table S6.4. The TEM data showed no clear evidence of any catalyst sintering after the reaction. The measured particle diameters were 5.2 nm for both catalysts and the initial diameters were 6.2 and 5.2 nm, for the 5% and 10% catalysts, respectively.

ii) The PXRD data for the 5%Co_xO_y@HCSs_PS indicated that the catalyst before calcination consisted mainly of Co_3O_4 [44] and thus showed limited improvement after calcination (35.8 % to 47.5 %, Table 6.2). Initial analysis of the 10% and 15%Co_xO_y@HCSs_PS catalysts however showed that they consisted mainly of fcc and hcp Co and CoO (Table S6.2, [44]) due to the reduction of Co by carbon, but that the particle has sintered in the synthesis reaction. Oxidation to Co_xO_y readily occurred, and these catalysts showed unexpected high conversions and the conversion only increased marginally (41.5 % to 42.4 %) for the 10% catalyst after calcination, and even decreased for the 15% catalyst (53 % to 30.9 %) after calcination.

The TEM images of the 5%, 10% and 15%Co_xO_y@HCSs_PS catalysts after 24 hours of reaction are reported in Figure S6.4 and the particle diameters are summarized in Table S6.4. There is no observable evidence of further particle sintering in the TEM images taken after 24 h catalytic reaction. The average particle diameters measured from the TEM images are 5.3 nm, 40 nm and 42 nm compared to the initial diameters of 6.1, 38 and 44 nm for the 5%, 10% and 15% catalysts, respectively. The TEM images of the 15%Co_xO_y@HCSs_PS catalyst after the catalytic oxidation reaction showed the formation of small hollow spheres within the HCSs (Figures S6.4, S6.5) and the diameter of these small hollow particles was determined to be 45 nm (Table S6.4). The observation relates to the change in morphology of large Co and CoxOy particles as they interconvert. The oxidation of supported metal Co nanoparticles to

generate hollow CoOx particles (the Kirkendall effect) is well known in Co catalysed reactions [49][50]. It is presumed that this new morphology was related to the decreased activity.

iii) Large changes in activity occurred for the PS-b-PAA12 catalysts after calcination. Here, the conversion improved from 5.2 % and 2.5 % to conversions of 48.3 % and 27.8 % after calcination, for the 5 and 10 % Co loaded catalysts, respectively. The PXRD data (Figure S6.7) indicated that most of the Co and CoO that were initially seen in the uncalcined catalyst, was converted to Co_3O_4 after calcination but even here some fcc Co was still present. A longer calcination time or higher calcination temperature may be required for the 10%Co_xO_y@HCSs_PS-b-PAA12 catalyst to convert all Co to Co_3O_4 to improve the catalytic activity even further. The 15% catalyst was calcined for 4 h and an improved conversion was also observed (from 2.8 % to 46.3%), consistent with the high metal loading in this catalyst. The TEM images and particle size distributions of the reacted 5%, 10% and 15% PS-b-PAA12 catalysts after 24 h of reaction shown in Figure S6.6 and the particle diameters are summarized in Table S6.4. The measured particles diameters were 5.0 nm, 5.2 nm and 8.9 nm for the 5%, 10% and 15% catalysts, respectively. The initial particles diameters were 6.1 nm, 6.0 nm and 5.6 nm, therefore there was no growth observed for the 5% and 10% catalysts. However, the 15% catalysts showed modest growth after 24 h of reaction.

The Co oxidation state, therefore, played a key role in the reaction, consistent with known studies [31,48,51]. The results reflect differences in the composition of the catalysts with regards to the quantity of Co, Co^{2+} and Co^{3+} in the initial catalysts. Our studies above confirm the importance of the high oxidation state required for Co to be used as a catalyst in the benzyl alcohol reaction. No sintering of the Co was observed post-reaction even after the calcination steps. Thus, the Co_xO_y reduction by carbon during catalyst synthesis needs to be counteracted by a subsequent calcination process, to convert the Co to Co_3O_4.

Effect of cobalt metal loading

The Co catalyst synthesis procedures used in this study generally produced Co particles with sizes between 6-8 nm on both the inside and outside of the HCSs which allowed for a comparative study. The effect of metal loading on a per gram basis for the three calcined catalysts is summarized in Figure 5. This shows the data as a function of Co metal loading, with loading determined from the TGA data. The data showed that the ($mols_{conv}$/gCo) of the three Co catalysts decreased with metal loading from 5% to 10% and then remained approximately unchanged from 10% to 15%. In general, the particle sizes from the TEM

analysis were between 5 - 6 nm for most of the catalysts indicating that this was not due to a particle size effect. The exceptions were the 10%Co_xO_y@HCSs_PS and 15%Co_xO_y@HCSs_PS catalysts that had particles larger than 35 nm. Thus, only the effect of metal loading on the Co_xO_y@HCSs_PS-b-PAA12 and Co_xO_y/HCS catalysts was evaluated in more detail.

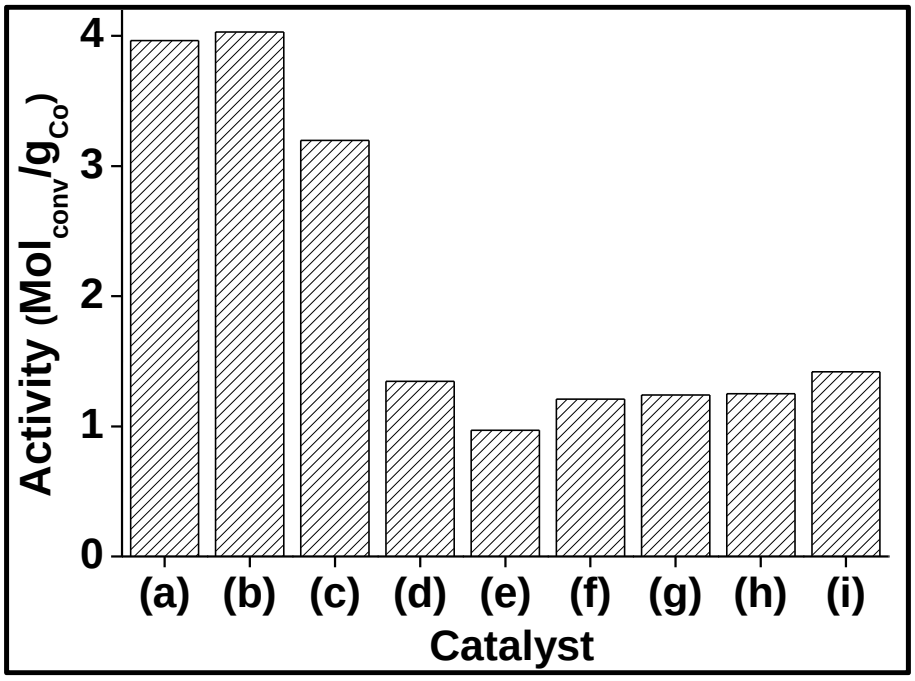

Figure 6.5: Catalytic activity of the calcined catalysts as mols of benzyl alcohol converted per gram of Co(mols$_{conv}$/gCo) for catalysts (a) 5%Co_xO_y@HCSs_PS, (b) 5%Co_xO_y@HCSs_PS-b-PAA_{12}, (c) 5%Co_xO_y/HCSs, (d) 10%Co_xO_y@HCSs_PS, (e) 10%Co_xO_y@HCSs_PS-b-PAA_{12}, (f) 10%Co_xO_y/HCSs, (g) 15%Co_xO_y@HCSs_PS, (h) 15%Co_xO_y@HCSs_PS-b-PAA_{12} and (i) 15%Co_xO_y/HCSs

i) The conversion for the as-synthesized 5% to 15% CoxOy@HCSs_PS-b-PAA12 catalysts increased slowly but at the same rate, i.e., the reactant conversion did not increase with the amount of Co. This could be associated with pore blockage since the surface area/pore volume of the catalysts decreased as the Co content increased (Table 6.1). After calcination, the conversion data for the three catalysts had increased due to the conversion of the Co to Co_3O_4, as discussed above.

ii) The CoxOy/HCS catalysts, before calcination, gave data that related to the Co oxidation state. After calcination, the 5% and 10% catalysts did not show substantial changes while the 15% catalysts did, as discussed above. Again, the key finding was that the activity did not

change with Co loading which suggested that under the reaction conditions diffusion control limits the reaction.

The Co2p XPS spectra of the catalysts are shown in Figure S6.9 and the BE's are summarized in Table S6.5. The peaks were assigned with reference to the NIST database [52], as well as other literature studies [31,53,54,55]. The 15%Co/HCSs catalyst contained $Co^{2+,}$ confirmed by the presence of the $Co2p_{3/2}$ and $Co2p_{1/2}$ and BE's of 780.0 eV and 795.6 eV, respectively. This was further confirmed by the corresponding strong satellite peaks at 785.4 eV and 802.7 eV. These satellite peaks are usually weaker for Co_3O_4, therefore the strong intensity suggests that they are due to CoO and that the sample contained mainly CoO. The surface of metal nanoparticles is prone to surface oxidation, and therefore the oxide phase was observed by XPS. The Co metal observed in the PXRD data arose since this data was recorded soon after the catalyst synthesis, and prior to substantial oxidation of the Co nanoparticles observed by XPS data at a later time. The absence of Co^{3+} in this sample explains the low catalytic activity of this material before calcination (1.1 % conversion, Table 6.2). The XPS spectra of the calcined 15%Co/HCSs catalyst (Figure S6.9b) showed the presence of Co_3O_4, indicating that the catalyst was successfully oxidized. The finding was confirmed by the presence of the $Co2p_{3/2}$ and $Co2p_{1/2}$ peaks at BE's of 778.0 and 795.3 eV, and the corresponding satellite peaks at 785.0 and 801.6 eV, respectively. A small amount of CoO could still be present, but, due to the complex nature of the XPS spectra of the two Co oxides and the similar BE's of Co and Co_3O_4, quantitative analysis and assignment of the two oxide phases were not possible. The catalytic activity of this calcined catalyst improved, giving a conversion of 48.1 % (Table 6.2), due to the presence of Co_3O_4.

The corresponding XPS spectra showing the survey, and high-resolution O1s, N1s and C1s spectra for the 15%Co/HCSs and calcined Co/HCSs are reported in Figure S6.10. The atomic percentages of the different elements are summarized in Tables S6.6 and S6.7.

Effect of the Co nanoparticles placed inside or outside the HCSs

Figure 6.6 shows the conversion and selectivity plots of the calcined catalysts and the following can be observed:

i) At 5% catalyst loading the reaction rates for the calcined catalysts are seen to be similar for all three catalysts, As the Co particle sizes are all about 6 nm this implies that Co placed

either inside or outside the HCSs gave the same rate data, this implies that under the reaction conditions used, reactant diffusion to the catalyst surface is similar.

ii) The two 10% loaded catalysts with similar particle sizes ((e) 10%Co_xO_y@HCSs_PS-b-PAA_{12}, (f) 10%Co_xOy/HCSs) followed different trends. The 10%Co_xO_y/HCSs catalyst revealed a normal initial reaction but the catalyst deactivated after ca. 4 h. In contrast, the 10%Co_xO_y@HCSs_PS-b-PAA_{12} data showed that the catalyst had to overcome an initial barrier before the rate became similar to that for the 10%Co_xO_y@HCSs_PS catalyst. The reasons for this effect are not presently understood.

iii) At 15% loading the Co_xO_y/HCSs and Co_xO_y@HCSs catalyst reactions gave similar final conversion and activity data. Given that these catalysts had similar properties in terms of metal particle size and BET surface areas, it can be deduced that the reaction rates and activity were independent of the location of the metal particles under the reaction conditions. In summary, it appears that under the reaction conditions used, the placement of the Co either inside or outside the HCS shell produced very similar activities for the reaction.

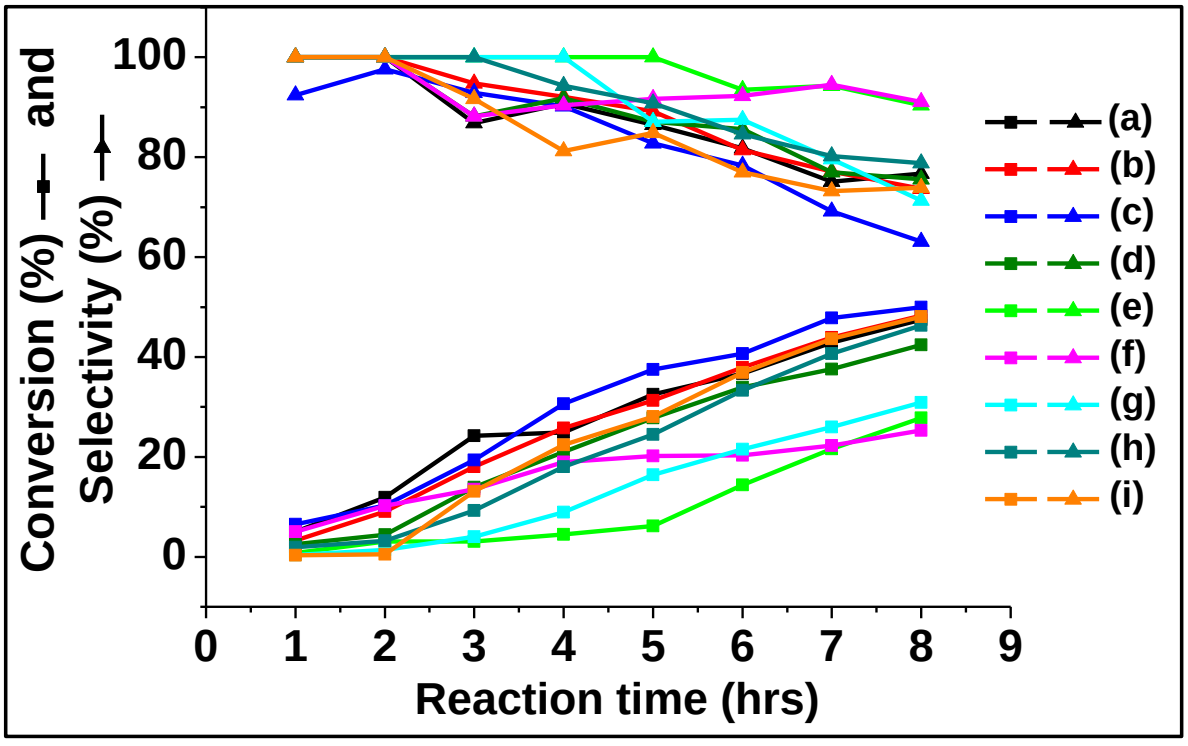

Figure 6.6: Conversion of benzyl alcohol and selectivity towards benzaldehyde over the calcined catalysts (a) 5%Co_xO_y@HCSs_PS, (b) 5%Co_xO_y@HCSs_PS-b-PAA_{12}, (c) 5%Co_xO_y/HCSs, (d) 10%Co_xO_y@HCSs_PS, (e) 10%Co_xO_y@HCSs_PS-b-PAA_{12}, (f) 10%Co_xO_y/HCSs, (g) 15%Co_xO_y@HCSs_PS, (h) 15%Co_xO_y@HCSs_PS-b-PAA_{12} and (i) 15%Co_xO_y/HCSs

Catalyst selectivity

All the catalysts showed similar selectivity data (Figure 6.6) and selectivity to the benzaldehyde (above 70 %) that decreased with time. Thus, the product selectivity did not appear to be affected by whether the Co was placed inside or outside the HCS. This has implications for the use of these catalysts to discriminate between reactants that can enter the HCS and those that are too large. The use of Co_xO_y@HCSs should allow for the preferential oxidation of small reactants and the rates should be the same as observed for oxidation using Co_xO_y/HCSs.

The product reacted further with the catalyst with time and consequently reduced the required product yield by producing secondary products. The common secondary products for this reaction include benzoic acid, toluene, benzene, benzyl ether and benzyl benzoate [56] and these were all observed in the product GC traces, building up with time. These types of secondary products are known to poison the catalyst [39-41]. A GC-FID spectrum is shown in Figure S6.10 and the trace products can be observed. The products also appear to have the same effect on the Co, in the three different catalysts. The general observation was that the selectivity towards benzaldehyde showed a gradual decrease as the reaction progressed irrespective of the location of the Co. This was consistent with findings from other studies [30,48]. This suggests that no extra poisoning of the catalyst occurs if secondary products are formed inside the HCS. A comparison of the results from this study has been made with other literature studies on the reaction (Table S6.10). The range of variable conditions (Co loading/solvent/T etc.) makes a comparison with, and between, these studies difficult.

Catalyst recycling

Figure 6.7 shows the activity and selectivity of the recycled 5%Co/HCS catalyst. Catalyst recycling was achieved by washing the used catalyst with ethanol using magnetic stirring and vacuum filtration. The catalyst was dried in an oven at 100 °C for 4 hours and reused for the oxidation of benzyl alcohol. To ensure minimal losses in mass during the cycles, an initial catalyst mass of 200 mg was used. Losses of approximately 30 mg per cycle occurred. These losses were accurately measured and subtracted when calculating the catalytic activity for each cycle. The catalytic activity showed an increase with recycling. This could be due to the oxidation of the catalyst by oxygen during recycling, therefore making it more active. The by-products which could poison the catalyst were successfully washed off with ethanol. The

selectivity is still above 90 % even after 5 cycles. This indicates that the catalyst is quite stable and re-useable.

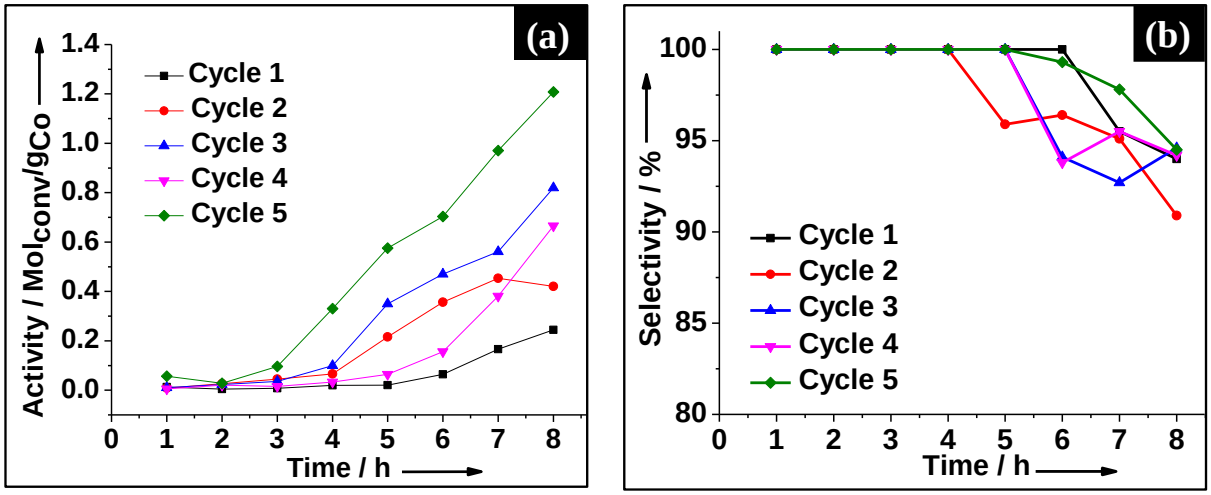

Figure 6.7: (a) Activity and (b) selectivity towards benzaldehyde during 5 cycles of benzyl alcohol oxidation with 5%Co/HCSs.

The 5%Co@HCSs_PS-b-PAA12 and 10%C0@HCSs_PS-b-PAA12 catalysts could not be recycled. Several methods were used in attempts to regenerate the catalysts and re-activate the active sites. The catalyst was washed several times with DMF, and no benzyl alcohol conversion could be observed. Washing with ethanol also did not give any activity. In another attempt, the washed catalyst was calcined in air at 200 °C for 1 h. This also did not recover the activity. The catalyst was then characterized by TEM, surface analysis and TGA, to understand why there was no activity when attempting to recycle the catalyst. The TEM data did not show any particle growth, this was expected as the reaction was done under mild reaction conditions.

Table S6.8 shows the surface area analysis of the two reacted catalysts. A significant loss in BET surface area occurred for both catalysts. However, the loss was more pronounced for the Co@HCSs catalyst. The Co/HCSs catalyst only lost 50% of the BET SA and the Co@HCSs catalyst lost almost 70%. This was accompanied by a significant loss in micropore SA, which suggested a blockage of small pores. The fresh catalyst had high micropore SA, which was almost 50% of the total SA. It is not understood why the Co/HCSs catalyst had a relatively smaller degree of pore blockage than the Co@HCSs catalyst. The corresponding BET isotherms are shown in Figure S6.13. The isotherms are typical of material with type IV pore structures. This is an indication of the presence of mesopores. The fresh catalysts contained a combination of Type I and type IV pore structures. The BET isotherms further confirm the possibility of a blockage of the small pores by possibly carbon build-up. The pore size

distribution curves are shown in Figure S6.14. It is evident that there was a high volume of pores with ~ 4 nm diameter. The fresh catalysts contained a high volume of pores less than 2 nm, which are micropores. The catalysts still contained some micropores, in smaller volumes compared to the fresh catalyst. Figure S6.15 shows the TGA and DTGA curves of the recycled catalyst. An initial weight loss of about 20 % can be observed for both catalysts, with an onset at 200 °C. This could be the loss of the reaction products that could not be properly washed off from the catalysts. The Co@HCSs catalyst was calcined at 200 °C in an attempt to remove products that could be trapped on the catalyst. This, however, did not lead to the recovery of the activity of the catalyst. Interestingly, both catalysts have a similar weight loss at the same temperature, but the Co/HCSs catalyst showed the least loss in BET SA.

Conclusions

The Co_xO_y@HCSs and Co_xO_y/HCSs catalysts showed similar activity towards the oxidation of benzyl alcohol (~ 50 % conversion) and produced benzyl alcohol in good yields (> 70 %). TEM analysis of the reacted catalysts revealed that all the catalysts showed resistance to metal sintering even after 24 h of reaction. The carbon support was found to reduce the Co_xO_y species and it was found to covert the Co and CoO to Co_3O_4 via calcination to increase the benzyl alcohol conversion. An increase in metal loading led to a decrease in catalyst efficiency and this was seen to be related to a lowered surface area due to pore blockage by the metal. The catalysts inside and outside the HCSs showed very similar activity and selectivity, indicating that the location of the metal on the HCS, under our reaction conditions was not important for this reaction.

References

[1] P. S. Lamoureux, K. T. Winther, J. A. Torres, V. Streibel, Z. Meng, M. Bajdich, F. Abild-Pedersen and T. Bligaard, "Machine learning for computational heterogeneous catalysis," ChemCatChem, vol. 11, pp. 3581-3601, 2019.

[2] L. J. Garces, B. Hincapie, R. Zerger and S. L. Suib, "The effect of temperature and support on the reduction of cobalt oxide: An in-situ X-ray diffraction study," Journal of Physical Chemistry C, vol. 119, pp. 5484-5490, 2015.

[3] S. Shama and B. G. Pollet, "Support Materials for PEMFC and DMFC electrolytes - A review," J. Power Sources, vol. 208, pp. 96-119, 2012.

[4] F. Rodrigues-Reinoso, "The role of carbon materials in heterogeneous catalysis," Carbon, vol. 36, pp. 159-175, 1998.

[5] D. I. Enache, B. Rebours, M. Roy-Auberger and R. Revel, "In situ XRD study of the influence of thermal treatment on the characteristics and the catalytic properties of cobalt-based Fischer-Tropsch catalysis," J. Catal. , vol. 205, pp. 346-353, 2002.

[6] K. Cheng, V. Subramanian, A. Carvelho, V. V. Ordomsky, Y. Wang and A. Y. Khodakov, "The role of carbon pre-coating for the synthesis of highly efficient cobalt catalysts for Fischer-Tropsch synthesis," J. Catal., vol. 337, pp. 260-271, 2016.

[7] N. J. Coville, S. D. Mhlanga, E. N. Nxumalo and A. Shaikjee, "A review of shaped carbon nanomaterials," South African Journal of Science, vol. 107, no. 418, p. 15 pages, 2011.

[8] H. Xiong, M. Moyo, N. K. Rayner, L. L. Jewell, D. G. Billing and N. J. Coville, "Autoreductin and catalytic performance of a cobalt Fischer-Tropsch synthesis catalyst supported on nitrogen-doped carbon spheres," ChemCatChem., vol. 2, pp. 514-518, 2010.

[9] C. Galeano, J. C. Meier, V. Peinecke, H. Bongard, I. Katsounaros, A. A. Topalov, A. Lu, K. J. Mayrhofer and F. Schuth, "Toward highly stable electrocatalysts via nanoparticle pore confinement," Journal of the American Chemical Society, vol. 134, pp. 20457-20465, 2012.

[10] F. bottger-Hiller, P. Kampe, G. Cox, A. Panchenko, N. Janssen, A. Petzold, T. Thurn-Albrecht, L. Borchardt, M. Rose, S. Kaskel, C. Georgi, H. Lang and S. Spange, "Twin polymerization at spherical hard templates: An approach to size-adjustable carbon hollow spheres with micro or mesoporous shells," Angew. Chem. Int. Ed., vol. 52, pp. 6088-6091, 2013.

[11] S. Ma, P. Su, W. Huang, S. P. Jiang, S. Bai and J. Liu, “Atomic Ni species anchored N-doped carbon hollow spheres as nanoreactors for efficient electrochemical CO_2 reduction,” ChemCatChem, vol.11, pp. 6092–6098, 2019.

[12] F. Zheng, M. He, Y. Yang and Q. Chen, "Nano electrochemical reactors of Fe2O3 nanoparticles embedded in shells of nitrogen-doped hollow carbon spheres as high-performance anodes for lithium-ion batteries," Nanoscale, vol. 7, pp. 3410-3417, 2015.

[13] S. Li, A. Pasc, V. Feirro and A. Celzard, "Hollow carbon spheres, synthesis and applications: a review," J, Mater. Chem. A, vol. 4, pp. 12686-12713, 2016.

[14] J. H. Kim, B. Fang, M. Kim and J. Yu, "Hollow spherical carbon with mesoporous shell as a super anode catalyst support in proton exchange membrane fuel cell," Catalysis Today, vol. 146, pp. 25-30, 2009.

[15] J. Qu, H. Zhu, D. Chen, N. Li, Q. Xu, J. Xie, H. Li, H. He, and J. Lu, “Hollow porous carbon with in situ generated monodisperse gold nanoparticles for efficient CO oxidation, ” ChemCatChem, vol. 10, pp. 837–842, 2018.

[16] J. Ding, H. Zhang, H. Zhou, J. Feng, X. Zheng, C. Zhong, E. Paek, W. Hu and D. Mitlin, “Sulfur-grafted hollow carbon spheres for potassium-ion battery anodes,” Adv. Mater., vol. 31, no. 1900429, 2019

[17] C. Galeano, J. C. Meier, M. Soorholtz, H. Bongard, C. Baldizzone, K. J. Mayrhofer and F. Schith, "Nitrogen-doped hollow carbon spheres as supports for platinum-based electrocatalysts," ACS Catalysis, vol. 4, pp. 3856-3868, 2014.

[18] K. Wenelska, B. Michalkiewicz, J. Gong, T. Tang, R. Kalenczuk, X. Chen and E. Mijowska, "In situ deposition of Pd nanoparticles with controllable diameters in hollow carbon spheres for hydrogen storage," International Journal of Hydrogen Energy, vol. 38, pp. 16179-16184, 2013.

[19] K. Ranganathan, A. Morais, I. Nongwe, C. Longo, A. F. Nogueira and N. J. Coville, "Study of photoelectrochemical water splitting using composite films based on TiO2 nanoparticles and nitrogen or boron-doped hollow carbon spheres as photoanodes," Journal of Molecular Catalysis A: Chemical, vol. 422, pp. 165-174, 2016.

[20] V. Ravat, I. Nongwe, R. Meijboom, G. Bepete and N. Coville, "Pd on boron-doped hollow carbon spheres-PdO particle size and support effects," Journal of Catalysis, vol. 305, pp. 36-45, 2013.

[21] G.-H. Wang, J. Hilgert, F. H. Richter, F. Wang, H.-J. Bongard, B. Spliethoff, C. Weidenthaler and F. Schuth, "Platinum-cobalt bimetallic nanoparticles in hollow carbon nanospheres for hydrogenolysis of 5-hydroxymethylfurfural," Nature Materials, vol. 13, pp. 293-300, 2014.

[22] Z. Zhang, F. Xiao, J. Xi, T. Sun, S. Xiao, H. Wang, S. Wang and Y. Liu, "Encapsulating Pd nanoparticles in double-shelled graphene@carbon hollow spheres for excellent chemical property," Scientific Reports, vol. 4, no. 4053, p. 5 Pages, 2015.

[23] P. M. Gangatharan, M. S. Maubane-Nkadimeng and N. J. Coville, "Building carbon structures inside hollow carbon spheres," Scientific reports, vol. 9, no. 10642, 2019.

[24] C. Lurhs, J. Philips, M. N. Richard and A. M. Knapp, "Hollow carbon spheres". United States of America Patent 0215960, 26 August 2010.

[25] T. N. Phaahlamohlaka, M. W. Dlamini, D. O. Kumi, R. Forbes, L. L. Jewell and N. J. Coville, "Co inside hollow carbon spheres as Fischer-Tropsch synthesis catalyst: spillover effects from Ru placed inside and outside the HCS," Applied Catalysis A: General, vol. 559, no. 117617, 2020.

[26] C. Zhang, R. Zhang, S. He, L. Li, X. Wang, M. Liu and W. Chen, " 4-Nitrophenol reduction by a single platinum-palladium nanocube caged within a nitrogen-doped hollow carbon nanosphere," ChemCatChem, vol. 9 pp. 980-986, 2017.

[27] C. Dong, Q. Yu, P-P. Ye, P. Su, J. Liu and G-H. Wang, "Hollow carbon sphere nanoreactors loaded with PdCu nanoparticles: void-confinement effects in liquid-phase hydrogenations," Angew. Chem. In. Ed.vol. 59, pp. 18374–18379, 2020.

[28] Y. Wang, H. Pan, Q. Lin, Y. Shi and J. Zhang, "Synthesis of Pd-M@HCS(M = Co, Ni, Cu) bimetallic catalysts and their catalytic performance for direct synthesis of H_2O_2," Catalysts, vol. 10, no. 303, 2020.

[29] G. Nagy, A. Beck, G. Safran, Z. Schay, S. Liu, T. Li, B. Qiao, J. Wang and K. Lazar, "Nanodisperse gold catalysts in the oxidation of benzyl alcohol: comparison of various supports under different conditions," Reaction Kinetics, Mechanisms and Catalysis, vol. 128, pp. 71-95, 2019.

[30] C. Rangupathi, J. J. Vijaya, S. Narayanan, S. K. Jesudoss and L. J. Kennedy, "Highly selective oxidation of alcohol to benzaldehyde with hydrogen peroxide by cobalt aluminate catalysis: A comparison of conventional and microwave methods," Ceramics International, vol. 41, pp. 2069-2080, 2015.

[31] M. Cordoba, C. Miranda, C. Lederhos, F. Coloma-Pascual, A. Ardila, G. A. Fuentes, Y. Pouilloux and A. Ramirez, "Catalytic performance of Co3O4 on different activated carbon supports in the benzyl alcohol oxidation," Catalysts, vol. 7, p. 384, 2017.

[32] S. Ji, Y. Chen, Z. Zhang, W.-C. Cheong, Z. Liu, D. Wang and Y. Li, "Single-atomic-site cobalt stabilized on nitrogen and phosphorus co-doped carbon for selective oxidation of primary alcohols," Nanoscale Horizons, vol. 4, pp. 902-906, 2019.

[33] X. Yang, S. Wu, L. Peng, J. Hu, X. Wang, X. Fu, Q. Huo and J. Guan, "Highly dispersed cobalt oxide nanoparticles on CMK-3 for selective oxidation of benzyl alcohol," RSC Advances, vol. 5, pp. 102508-102515, 2015.

[34] A. Jia, L.-L. Lou, C. Zhang, Y. Zhang and S. Liu, "Selective oxidation of benzyl alcohol to benzaldehyde with hydrogen peroxide over alkali-treated ZSM-5 zeolite catalysts," Journal of Molecular Catalysis A: Chemical, vol. 306, pp. 123-129, 2009.

[35] V. Ravat, I. Nongwe and N. J. Coville, "Palladium-supported boron-doped hollow carbon spheres as catalysts for the aerobic oxidation of alcohols," ChemCatChem, vol. 4, pp. 1930-1934, 2012.

[36] A. Mondal, D. Mukherjee, B. Adhikary and M. A. Ahmed, “Cobalt nanoparticles as recyclable catalyst for aerobic oxidation of alcohols in liquid phase,” J. Nanopart. Res. vol. 18, no.117, 2016.

[37] D. Dey and M. K. Mahanti, "Kinetics of oxidation of substituted benzyl alcohols by quinolinium dichromate," Journal of Organic Chemistry, vol. 55, pp. 5848-5850, 1990.

[38] K. Zhang, Y. Lui, J. Deng, L. Jing, W. Pei, Z. Han, X. Zhang and H. Dai, “Ru nanoparticles supported on oxygen-deficient 3DOM BiVO4: high-performance catalysts for the visible-light-driven selective oxidation of benzyl alcohol,” ChemCatChem, vol. 11, pp. 6398–6407, 2019.

[39] J. Zhu, k. Kailasam, A. Fischer and A. Thomas, "Supported cobalt oxide catalysts for aerobic oxidation of alcohols in liquid phase," ACS Catalysis, vol. 1, pp. 342-347, 2011.

[40] T. Mallat and A. Baiker, "Oxidation of alcohols with molecular oxygen on solid catalysts," Chemical Reviews, vol. 104, pp. 3037-3058, 2004.

[41] E. Ali, M. Rahman, S. Sarkar and S. B. Hamid, "Heterogeneous metal catalysts for oxidation reactions," Journal of Nanomaterials, vol. 2014, pp. 1-23, 2014.

[42] D. Mao, M. Jia, J. Qiu, X.-F. Zhang and J. Yao, "N-doped porous carbon supported Au nanoparticles for benzyl alcohol oxidation," Catalysis Letters, vol. 150, pp. 74-81, 2020.

[43] V. R. Choudhary, P. A. Chaudhari and V. S. Narkhede, "Solvent-free liquid phase oxidation of benzyl alcohol to benzaldehyde by molecular oxygen using non-noble transition metal containing hydrotalcite-like solid catalysts," Catalysis Communications, vol. 4, pp. 171-175, 2003.

[44] P. Mente, T. N. Phaahlamohlaka, V. Mashindi and N. J. Coville, "Polystyrene-b-poly(acrylic acid) nanoparticles for the synthesis of size-controlled cobalt nanoparticles encapsulated inside hollow carbon spheres," J. Mater. Sci, 2020.

[45] R. Paul, A. A. Voevodin, J. J. Hu, P. B. Amama, S. Ganguli, A. K. Roy, D. Zemlyanov and T. S. Fisher, "Boron-carbon-nitrogen foam surfaces for thermal physisorption applications," Thin Solid Films, vol. 528, pp. 187-193, 2013.

[46] L. C. Cotet, M. Gich, A. Roig, I. C. Popescu, V. Cosoveanu, E. Molins and V. Danciu, "Synthesis and structural characteristics of carbon aerogels with a high content of Fe, Co, Ni, Cu and Pd," Journal of Non-Crystalline Solids, vol. 352, pp. 2772-2777, 2006.

[47] Y. Tao, M. Endo and K. Keneko, "A review of synthesis and nanopore structures of organic polymer aerogels and carbon aerogels," Recent Patents on Chemical Engineering, vol. 1, pp. 192-200, 2008.

[48] Y. Xie, F. Dong, S. Heinbuch, J. J. Rocca and E. R. Bernstein, "Oxidation reactions on neutral cobalt oxide clusters: experimental and theoretical studies," Physical Chemistry and Chemical Physics, vol. 12, pp. 947-959, 2010.

[49] C. J. Weststrate, M. M. Hauman, D.J. Moodley, A. M. Saib, E. van Steen, J. W. Niemantsverdriet, "Cobalt Fischer–Tropsch catalyst regeneration: The crucial role of the kirkendall effect for cobalt redispersion,"Top. Catal., vol. 54, pp. 811–816, 2011.

[50] M. Varón, I. Ojea-Jimenez, J. Arbiol, L. Balcells, B. Martínez and V. F. Puntes, "Spontaneous formation of hollow cobalt oxide nanoparticles by the Kirkendall effect at room temperature at the water-air interface," Nanoscale, vol. 5, pp. 2429-2436, 2013.

[51] L. Zhong, T. Kropp, W. Baaziz, O. Ersen, D. Teschner, R. Schlogl, M. Mavrikakis and S. Zafeiratos, "Correlation between reactivity and oxidation state of cobalt oxide catalysts for CO preferential oxidation," ACS Catal., vol. 9, pp. 8325-8336, 2019.

[52] A. V. Naumkin, A. Kraut-Vass, S. W. Gaarenstroom, C. J. Powell, "NIST X-ray Photoelectron Spectroscopy Database," 2012. [Online]. Available: srdata.nist.gov/xps/EngElmSrchQuery.aspx?EType=PE&CSOpt=Retri_ex_dat_&Elm=Co. [Accessed 6 February 2021]

[53] M. C. Biesinger, B. P. Payne, A. P. Grosvenor, L. M. Lau, A. R. Gerson and R. S. C. Smart, "Resolving surface chemical states in XPS analysis of first row transition metals, oxides and hydroxides: Cr, Mn, Fe, Co and Ni," Appl. Surf. Sci., vol. 257, pp. 2717-2730, 2011.

[54] "Thermo scientific XPS," Thermo Fisher Scientific Inc., [Online]. Available: http://xpssimplified.com/elements/cobalt.php. [Accessed 5 February 2021]

[55] K. Lin and B.-J. Chen, "Magnetic carbon-supported cobalt derived from a Prussian blue analog as a heterogeneous catalyst to activate peroxymonosulfate for efficient degradation of caffeine in water," J. Colloid Interf. Sci. vol. 486, pp. 255-264, 2017.

[56] L. Gurrala, A. S. Nagpure, H. R. Gurav and S. Chilukuri, "Spinel-type mixed oxides for stable and selective partial oxidation of benzyl alcohol," ChemistrySelect, vol. 3, pp. 3751–3761, 2018.

Chapter 7: The vapour phase hydrogenation of cinnamaldehyde using cobalt supported inside and outside hollow carbon spheres[3]

7.1. Introduction

Cinnamaldehyde (CALD) belongs to the family of α,β-unsaturated aldehydes. Hydrogenation of CALD is an industrially important reaction, involving selective catalytic reduction of C=C and C=O bonds in the presence of molecular hydrogen [1] [2]. The reaction produces three main compounds, which are, hydrocinnamaldehyde (HCALD), hydrocinnamyl alcohol (3-phenyl propanol, 3PP) and cinnamyl alcohol (CAL) (Scheme 7.1) [3]. HCALD is produced when the C=C bond is selectively reduced, CAL is a product of the selective reduction of the C=O bond and 3PP is a product of the reduction of both the C=C and C=O bonds [4]. Low molecular weight fragments and other high molecular weight compounds e.g. formaldehyde, styrene, and ethylbenzene can also be produced as by-products [5] [6].

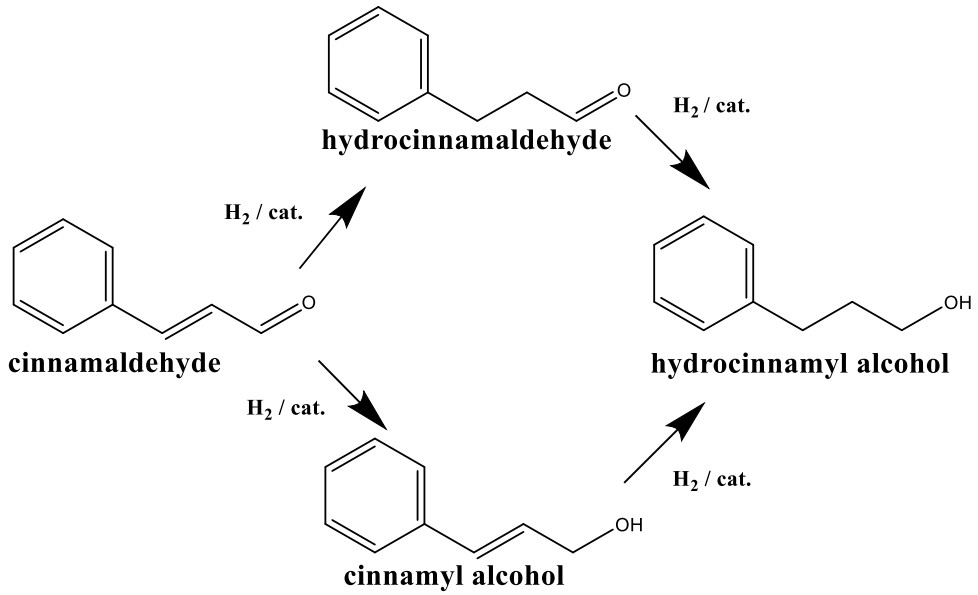

Scheme 7.1: Products of the catalytic hydrogenation of CALD

Selective reduction of the C=O bond of α,β unsaturated aldehydes is generally challenging as C=C bond reduction is thermodynamically favoured [7] over C=O reduction [8] [9] [10]. An ideal catalyst for the hydrogenation of CALD would selectively produce one main unsaturated

[3] This chapter has been submitted for publication as: Pumza Mente, Victor Mashindi, Alice Magubane, Tumelo N. Phaahlamohlaka, Prakash M. Gangatharan, Roy P. Forbes and Neil J. Coville, The hydrogenation of cinnamaldehyde using cobalt nanoparticles supported inside and outside hollow carbon spheres. (Submitted to Can. J. Chem).

compound, with no unwanted by-products, at moderate temperature and pressure. Noble metal catalysts such as Pt, Ir, Os and Pd have been successfully used for the liquid phase hydrogenation reaction and have shown good catalytic activity and selectivity [11].

Transition metal catalysts such as Co, Ni and Cu are less expensive, more abundant and have shown good catalytic activity towards the hydrogenation of CALD [5] [9] [12]. However, these catalysts also suffer from poor selectivity. Numerous approaches to enhance the catalyst activity/selectivity have been reported and they, include among others, the use of bimetallic catalysts [13], variation of support properties and optimization of catalyst particle size and shape [2]. Reaction conditions, such as the amount of catalyst, temperature, pressure and solvent, also play an important role in the success of this hydrogenation process [8]. Most of these reactions have been done in the liquid phase using batch reactors but these liquid phase hydrogenation processes use large quantities of organic solvents [14] [15] [16] [17] [18].

In the liquid phase hydrogenation of CALD, high activity and selectivity have been achieved with Co based catalysts. However, the reactions require high H_2(g) pressures and long reaction times due to the low activity of Co. In this study, we have used a vapour phase approach to evaluate Co catalysts as this allows for the use of a flow system to generate the products. Interestingly, the vapour phase hydrogenation of cinnamaldehyde has not been widely investigated.

Reddy and co-workers [9] reported on the vapour phase hydrogenation of CALD with bimetallic catalysts supported on silica. The catalysts' active metal phases included the alloys CoNi, NiCu, and CoCu. In their study it was shown that CoNi was highly selective towards HCALD while CoCu was highly selective towards CAL, reaching 45% yields. All the catalysts gave good conversion, above 60 %, and the NiCu catalyst gave the best conversion (75%). No by-products were reported at the optimal temperature used (270 °C). However, above 270 °C CALD fragmented products formed, indicating a decomposition of reactants and/or products. Chin and co-workers [5] also reported on the vapour phase hydrogenation of CALD, using Ni catalysts supported on mesoporous silica. Optimal results were obtained at 300 °C, with up to 80% conversion and up to 80 % selectivity towards HCALD. 3PP was also produced, alongside styrene and ethylbenzene as by-products, CAL was not produced. In a study by Jao and co-workers [4], the vapour phase hydrogenation of CALD with Ni supported on alumina was investigated at 200 °C. Again, HCALD was produced in high yields (up to 60 %). Other products were 3PP, styrene and ethylbenzene but CAL was not produced. The above appear to

be the only reports on studies that involve the vapour phase hydrogenation of CALD. There are no reports of Co on carbon supports that have been described in the vapour phase hydrogenation of CALD.

Continuing from earlier studies by other scientists working in our research group on the use of Co supported on carbon in catalysis [19] [20] [21] we herein report on their use for the vapour phase CALD hydrogenation reaction using hollow carbon spheres (HCSs) as a support. HCSs contain a mesoporous shell that allows for the loading of Co both inside and outside HCSs; the structure can support a high loading of small metal nanoparticles. The encapsulation of metal nanoparticles inside HCSs can protect the metal from sintering, leaching and agglomeration during harsh catalytic reaction conditions [22]. The synthesized catalysts were named Co@HCSs and Co/HCSs for catalysts supported inside and outside HCSs, respectively. The Co@HCSs catalysts were synthesized by using two different types of templates, polystyrene (PS) and the copolymer, PS-*b*-poly (acrylic acid) containing 8% acrylic acid (PS-*b*-PAA_8) and were named Co_xO_y@HCSs_PS and Co_xO_y@HCSs_PS-*b*-PAA_8, respectively [23]. The PS-*b*-PAA_8 template contained functional groups that assisted with controlling and producing small metal particles [23]. The effects of particle size, metal loading and the role of diffusion on Co loaded either inside or outside the HCSs, were investigated. The catalysts were further evaluated by varying the reaction temperature, H_2 flow rate and catalyst mass.

7.2. Materials and methods

7.2.1. Materials

Cinnamaldehyde (CALD) and tetrahydrofuran (THF) were purchased from Sigma Aldrich and used without further purification. The GC standards, cinnamyl alcohol (CAL), hydrocinnamaldehyde (HCALD) and 3-phenyl propanol (3PP) were also all purchased from Sigma Aldrich and used without further purification. Hydrogen gas (H_2 (g)) was purchased from Afrox South Africa and was passed through a gas filter before use.

2.1.Methods

The synthesis of the Co@HCSs catalysts and Co/HCSs catalysts has been previously described [23] [24]. The synthesized catalysts (100 – 500 mg) were reduced inside a down-flow vertical fixed-bed glass tube reactor (l = 42 cm, d = 2 cm). The reactor was placed inside an electrically heated vertical tube furnace equipped with a K-type thermocouple. Catalyst reduction was done

at 350 °C for 2 h under 50 mL/min H_2 flow. The reduced catalyst (100 mg - 500 mg) inside the vertical tube reactor was cooled down to 200 °C and allowed to stabilize for 30 min. CALD (2.5 mL) dissolved in THF (6.25 mL) was injected into the reactor using an automatic syringe pump (SAGE instruments, model 341B) set at 1.5 mL h^{-1}. The CALD was injected over a 5 h period under 100 mL/min H_2 flow and the reaction products were collected every hour. The reactor was connected to a glass sample collection tube (l = 6 cm, d = 2 cm) equipped with a glass tap. The sample collection tube was emptied every hour and the products were immediately diluted in THF and analysed with an offline GC-FID using a capillary column (Phenomenex Zebron, 30m x 0.53 mm I.D) and N_2 as a carrier gas. Pure chemical standards were used to identify the GC peaks. Catalyst recycling was done by re-oxidizing the reacted catalyst at 200 °C under flowing air at 50 mL/min for 1 h. The calcined catalyst was weighed and placed inside the glass tube reactor, reduced and tested for vapour phase hydrogenation of CALD following the procedures mentioned above.

Temperature-programmed reduction (TPR) analysis was carried out with a Micromeritics Auto Chem II instrument. Approximately 70 mg of the catalyst was placed inside a quartz tube and pre-treated under helium (30 ml/min) at 150 °C for 30 minutes and cooled down to 50 °C. Thereafter, the catalyst was re-heated to 900 °C at a rate of 10 °C/min under 5%H_2/Ar flowing at 50 mL/min. H_2 consumption was measured with a thermal conductivity detector (TCD).

A Micromeritics Tristar 3000 surface area and porosity analyser was used to determine the surface area and pore volumes.

7.3. Results and discussions

7.3.1. Catalyst synthesis and characterization

The catalyst synthesis procedures have been reported previously [22], [23]. Catalysts with three Co loadings (inside and outside the HCSs) were studied (5%, 10%, 15%). Characterization data has also been previously reported (metal loading, particle size and BET surface area) and is also given in Table S7.1 to provide easy access to key information [23] [24]. Similar metal particle sizes (5.4 to 6.6 nm) were obtained, both inside and outside HCSs for some of the catalysts, and this allowed for the direct comparison of their activities. The BET surface areas of the catalysts were also similar and therefore made it possible to compare the activity of the catalysts. The catalysts contained various phases of cobalt but prior to reaction were reduced and all were converted from Co_3O_4 to Co.

Temperature programmed reduction studies

Temperature programmed reduction (TPR) studies of the catalysts were performed to investigate the catalyst reducibility and the Co-carbon interactions. The TPR profile of the pristine HCSs prepared with a PS-b-PAA8 template can be found in Figure S7.2. No hydrogen adsorption was observed by the HCSs (< 300 ^{o} C) during the TPR experiment while H_2 consumption was observed above 400 °C due to the gasification of C support to form CH_4 [25] [26]. The release of CH_4 is indicated by the negative peak appearing after 500 °C, with a maximum of 700 °C [19].

Co_3O_4 is known to reduce to Co in a two-step process [27]. The two peaks are normally expected at *ca*. 180 – 250 °C (Co_3O_4 → CoO) and at ca. 250 - 450 °C (CoO → Co) in the presence of carbon supports. CH_4 formation occurs above 400 °C and this peak can overlap with the high T Co peak [28] [29].

The TPR profiles of the three catalysts (Co@HCSs_PS, Co@HCSs_PS-b-PAA_8 and Co/HCSs) at three different Co loadings (5 %, 10%, 15%) are reported in Figure 7.1 and their peak positions in Table S7.2. It is to be noted that all the 5% loaded catalysts had similar Co sizes (d = *ca*. 6 nm, Table S2) [22] [23]. At 10% and 15% Co loading the Co/HCSs and Co@HCSs_PS-b-PAA8 catalysts contained small nanoparticles (~ 6 nm) while the Co@HCSs_PS catalysts contained larger particles (>20 nm).

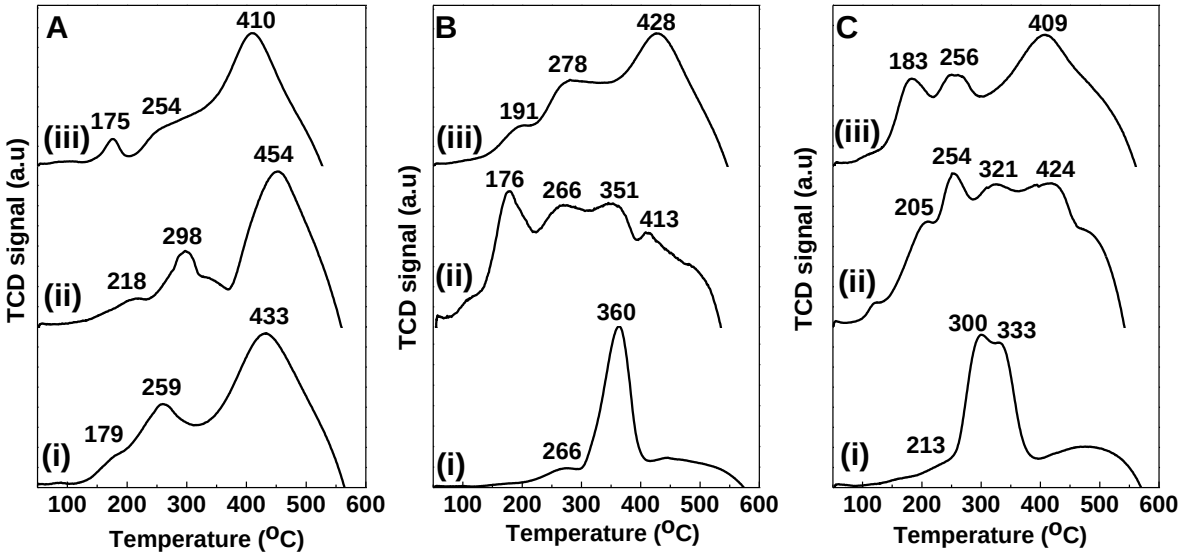

Figure 7.1: TPR profiles of the (A) 5%, (B) 10 % and (C) 15% loaded catalysts, (i) Co@HCSs_PS, (ii) Co@HCSs_PS-b-PAA8 and (iii) Co/HCSs

Figure 7.1A shows the TPR profiles of the three 5% Co loaded catalysts and their peak positions are summarized in Table S7.2. Two major peaks (ca. 250-300 °C and 410-450 °C)

related to the reduction of Co_3O_4 to Co are observed for all three catalysts. A small peak can also be seen in the three catalysts (ca. 180-220 °C) as well as a small peak for 5%Co@HCSs_PSPAA at ca. 350 °C; due to a second Co species that has been reduced. These peaks are more prominent in the TPR profiles of the 10% and 15% loaded catalysts (see Figures 7.1B and 7.21C). Peaks due to residual nitrate are not expected as the catalysts were heated to 600 °C during preparation [31]. The two major peaks are associated with species showing strong Co-carbon interactions relative to the Co species associated with the minor peak(s). The 5%Co/HCSs catalyst had the lowest reduction temperatures (254 and 410 °C) of the three catalysts, which could relate to the effect of H_2 diffusion. The 5%Co@HCSs_PS had lower reduction temperatures (259 and 433 °C) than the 5%Co@HCSs_PSPAA (298 and 454 °C). This is an indication that stronger cobalt-to-support interactions occurred with the HCS created from PSPAA, caused by the functional groups on the PAA template that was used in the synthesis of the HCSs. Carbon methanation was observed above 400 °C, consistent with previous studies [21] [28].

The TPR profiles for the 10% Co loaded catalysts are reported in Figure 1B and the data are like those for the 15% loaded catalysts shown in Figure 7.1C. For the 10%Co/HCSs catalyst, two reduction peaks for the major Co species can be observed at 278 and 428 °C. The reduction peaks occurred at higher Ts than observed for the 5%Co/HCSs catalyst, indicating the expected increase in reduction T with increasing Co loading. A minor species with a peak at 191 °C was also noted and had increased in intensity (compare Figures Aiii and Biii), and increases further at 15% loading (Figure Ciii). The data was consistent with the minor species having a weaker interaction with the carbon and could be linked to larger Co particles.

The 10%Co@HCSs_PS-b-PAA (and 15% loading) catalyst behaved similarly to the Co/HCSs catalysts, but with different ratios of the two Co species. The two species had similar concentrations as reflected by peak heights, with the four peaks at 176/351 °C and 266/413 °C (205/321 °C and 254/424 °C for the 15% loaded catalyst). The Co@HCSs catalysts had varying reduction temperature values relative to the Co/HCSs, which are related to diffusion effects and metal-to-support interactions.

The 10%Co@HCSs_PS catalyst has one major reduction peak at 360 °C (Figure Bi). This was associated with the presence of large Co particles (38-45 nm). It has been previously reported by Luisetto et al. [30] that the two cobalt oxide reduction steps can give one reduction peak in

the presence of large cobalt particles (> 20 nm). A similar profile is seen for 15%Co@HCSs_PS (Figure Ci).

From previous studies involving Co supported on carbon, where TPR analysis was performed, a reduction temperature of 350 °C was chosen to convert the Co_3O_4 on/in the HCS supports to Co, the active catalyst needed for the HCALD reduction reaction [21].

7.3.2. Catalytic study

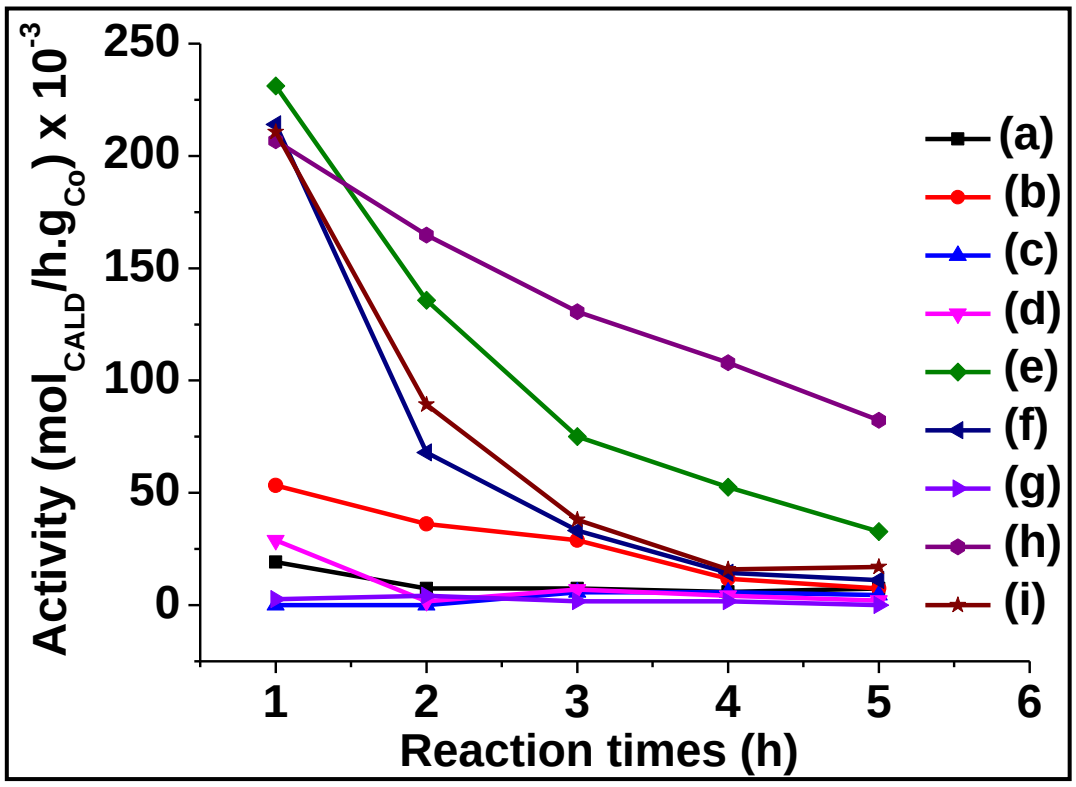

Figure 7.2: Catalytic activity of the catalysts during 5 h hydrogenation of CALD with (a) 5%Co@HCSs_PS, (b) 5%Co@HCSs_PS-b-PAA_8, (c) 5%Co/HCSs, (d) 10%Co@HCSs_PS, (e) 10%Co@HCSs_PS-b-PAA_8, (f) 10%Co/HCSs, (g) 15%Co@HCSs_PS, (h) 15%Co@HCSs_PS-b-PAA_8 and (i) 15%Co/HCSs. Reaction conditions: 100 mg catalyst at 200 °C, 100 mL/min H_2 flow rate and 1.5 mL/min CALD flow rate.

The catalytic study was carried out to explore the role of the location of the Co in/on a hollow carbon sphere (Co@HCS and Co/HCS) under conditions in which the Co loading, Co particle size and Co mass were similar. A model reaction, the hydrogenation of cinnamaldehyde was chosen for the study. This reaction can occur in the gas phase at ca. 200 °C and thus the Co loaded HCSs will be stable under these conditions. No attempt was made to optimize the reaction – established reaction conditions were used for the study as our focus was on

elaborating the effect of placing catalysts inside the HCSs relative to placing the Co outside the HCSs. This study complements an earlier vapour phase study involving an *oxidation reaction* (liquid phase oxidation of benzaldehyde) in which Co_3O_4 catalysts were supported in/on HCSs [24].

Figure 7.2 shows the plot of the catalytic activity during 5 h of hydrogenation for all nine catalysts. It was observed that the conversion decreased as the reaction progressed, for all the catalysts. This indicates catalyst deactivation/poisoning with time. This is proposed to be caused by the reaction of the Co with undesired by-products formed from CALD. It has been reported that undesired side reactions can lead to a loss of active sites in vapour phase hydrogenation reactions [31]. The loss of active sites in the gas phase hydrogenation reaction usually occurs through coke deposition on the catalyst surface [32]. As expected, the conversion rate showed a dependence on metal loading, particle size and location of the Co in/on the HCS; this issue is discussed in further detail in a later section.

Table 7.1: Conversion, activity and selectivity after 1 h hydrogenation of CALD with the catalysts [a].

Catalyst	CALD Conv (%)	Activity ($mol_{CALD}h^{-1}g_{Co}^{-1}$) $x10^{-3}$	Product Selectivity (%)			
			HCALD	3PP	CAL	Other
5%Co@HCSs_PS	2.6	19	38.3	61.7	-	-
5%Co@HCSs_PS-b-PAA_8	7.2	53	30.5	38	27.3	4.2
5%Co/HCSs	1	0	-	100	-	-
10%Co@HCSs_PS	10.3	29	17.7	28.3	-	54.0
10%Co@HCSs_PS-b-PAA_8	74.8	231	13.6	37.7	2.1	46.6
10%Co/HCSs	59.8	214	15.2	21.0	3.5	60.3
15%Co@HCSs_PS	1.3	2.7	100	-	-	-
15%Co@HCSs_PS-b-PAA_8	99.7	207	16.7	48.8	9.4	25.1
15%Co/HCSs	80.5	211	12.1	23.1	-	64.8

[a] Reaction conditions: 100 mg catalyst at 200 °C, 100 mL/min H_2 flow rate and 1.5 mL/min CALD flow rate.

Table 7.1 reports the selectivity, catalytic activity as well as conversion of CALD for the nine catalysts after 1 h of hydrogenation of CALD at 200 °C. Hydrocinnamaldehyde (HCALD), 3-phenyl propanol (3PP) and cinnamyl alcohol (CAL) were all produced alongside other low

molecular weight products. These latter products have been lumped together and termed 'other' as they were not the target products of this study.

Effect of the hydrogen flow rate

The most active catalyst (10%Co@HCSs_PS-b-PAA_8) was used to investigate the effect of varying the H_2 flow rate (50 mL/min, 100 mL/min and 150 mL/min) while keeping the temperature (200 °C) and catalyst mass (100 mg) constant. No CALD conversion was observed at 50 ml/min and 150 ml/min. An increase in the concentration of H_2 may result in a competition between the reactants (H_2, CALD) for the same adsorption sites on the catalyst surface, and this could result in the decreased activity in the presence of excess H_2 or CALD [33] [34] [35].

Effect of reaction temperature

Blank reactions were done at 200 and 300 °C using HCSs that did not contain any metal. CALD was passed through the reactor using a flow of H_2 (100 ml/min). There was no CALD conversion observed at both 200 and 300 °C. This indicated that any product formation observed was due to the Co nanoparticles.

The most active catalyst (10%Co@HCSs_PS-b-PAA_8) was also used to investigate the effect of the reaction temperature (150 °C, 200 °C, 250 °C, 300 °C) on the CALD conversion while keeping the H_2 flow rate (100 mL/min) and catalyst mass (100 mg) constant. The conversion data are reported in Figure 3A. At 150 °C there was no conversion observed over 5 h of reaction; the conversion was only observed above 200 °C. As the temperature was increased from 200 to 250 and 300 °C, the conversion, however, decreased, *viz.* after 1 h from 74.8 to 37.1 to 25% (Figure 7.3A). This was attributed to the poorer adsorption of reactant molecules with temperature [29][33].

Figure 7.3B shows the product *selectivity* at 25% conversion at the three different temperatures. It was observed that an increase in reaction temperature led to poor product selectivity of the desired products (HCALD, CAL). Instead, large quantities of the low molecular weight by-products were produced due (possibly) to the decomposition of CALD at high temperatures [9]. The best results, in terms of CAL/HCALD yields, were obtained at 200 °C, but even here

over-reduction of the 3PP was observed. At higher temperatures, large amounts of 'other' products were formed, which suggested that products readily break down at these temperatures.

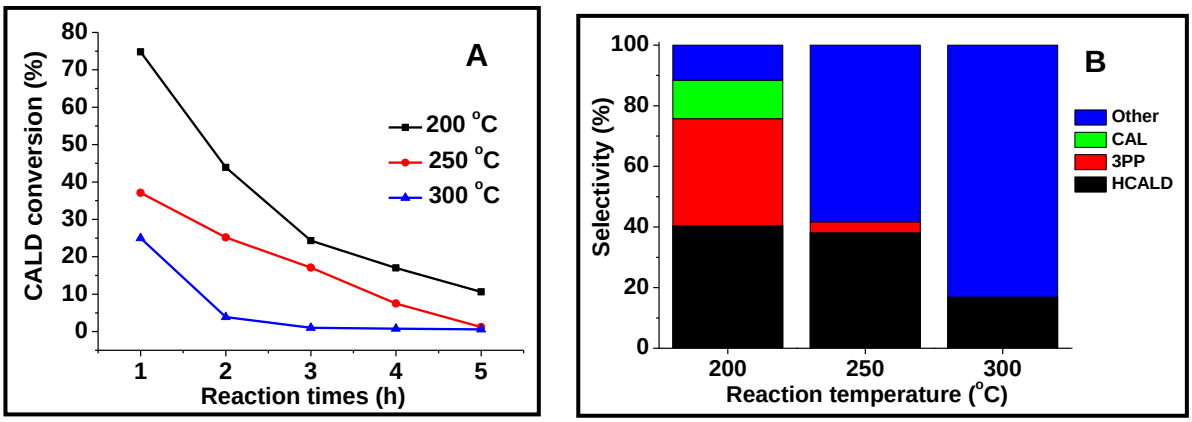

Figure 7.3: (A) Conversion of CALD during 5 h of hydrogenation over 10%Co@HCSs_PS-b-PAA_8 at different reaction temperatures. (B) Selectivity at 25% conversion of CALD over 10%Co@HCSs_PS-b-PAA_8 at different reaction temperatures. Reaction conditions: 100 mg catalyst, 100 mL/min H_2 flow rate and 1.5 mL/min CALD flow rate.

Effect of the amount of catalyst

The 10%Co/HCSs catalyst was used to investigate the effect of the amount of catalyst (100 mg, 200 mg, 300 mg, and 500 mg) on the reaction (200 °C; H_2 flow rate of 100 mL/min) and the results are shown in Figure 7.4. After 1 h, using the smaller amounts of catalyst (100 and 200 mg) only ca. 60% conversion was achieved, and the conversion dropped with increasing time. Increasing the catalyst content to 300 and 500 mg, the conversion reached 100 % and decreased with time (Figure 7.4A) [32].

Figure 7.4B shows the product selectivity when using different amounts of 10%Co/HCSs. The data indicated poor selectivity for the desired product with an increased amount of catalyst – over-reaction is evident and large quantities of unwanted by-products were produced. Figure 7.5 further shows the distribution of the product after every hour, for 5 h when using 300 mg and 500 mg catalysts. It was observed that over time the amount of the by-products formed was reduced, while the amount of HCALD and 3PP increased. This indicates that as the catalyst was poisoned the products were less liable to be over hydrogenated. Similar results were reported by Chin et al. [5] when a 10%Ni/alumina catalyst was evaluated for the hydrogenation of CALD at 300 °C. They also noted that the conversion increased with increasing contact time. The catalyst selectively produced HCALD in large quantities, and the yield increased with increasing contact time until it reached a maximum and then decreased. The drop in

HCALD yield was accompanied by the formation of high yields of side-products (ethylbenzene and phenyl-propanol).

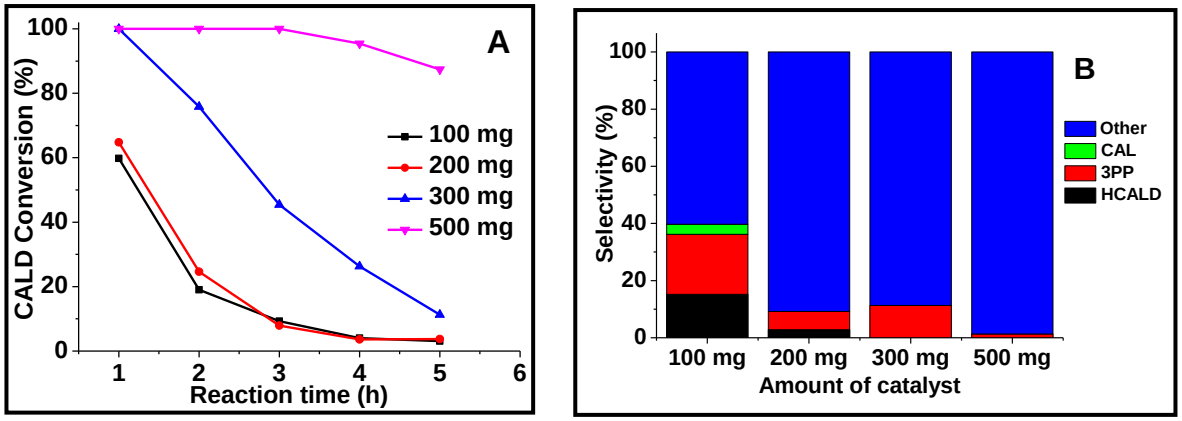

Figure 7.4: (A)Conversion of CALD during 5 h of hydrogenation over 10%Co/HCSs using different amounts of catalyst and, (B) Selectivity after 1 h of hydrogenation of CALD with different amounts of catalyst.

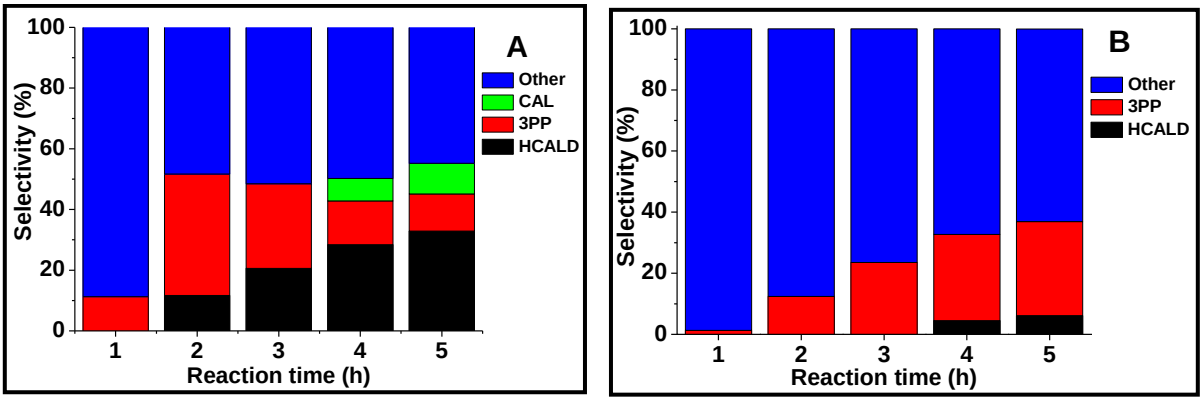

Figure 7.5: Selectivity during 5 h hydrogenation of CALD with (A) 300 mg, and (B) 500 mg of 10%Co/HCSs

Effect of particle size

The use of two templates, polystyrene (PS) and polystyrene-b-poly(acrylic acid) (PS-b-PAA8) resulted in the synthesis of Co@HCSs with variable particle sizes at similar metal loadings [23]. This allowed for the effect of metal particle size to be investigated for the catalysts supported inside the HCSs. The PS template gave larger particles with TEM average diameters of 6.1, 38, and 44 nm (Table S7.2, [23]) for the 5%, 10% and 15% Co loaded catalysts, respectively. In contrast, the PS-b-PAA_8 template gave smaller particles with average diameters of 5.4, 5.8 and 6.6 nm (Table S7.2, [23]) for the 5%, 10% and 15% Co loaded catalysts, respectively.

The large particles (Co@HCSs_PS) gave low conversion and there were no significant improvements with increased metal loading (Table 7.1). The CALD conversion increased from 2.6 to 10.3 % as the metal loading increased from 5 % to 10 % Co. As the metal loading increased from 10% to 15% Co, the conversion decreased from 10.3 % to 1.3 % due to the increase in particle size. The small particles (Co@HCSs_PS-b-PAA_8) gave a high conversion, which increased with increasing metal loading. The conversion of CALD increased from 7.2 to 74.8 and 99.7 % as the catalyst loading increased from 5 to 10 and 15% Co.

The corresponding activity data ($mol_{CALD}.h^{-1}.g_{Co}^{-1}$; Table 7.1) showed that the PS catalysts were 90% less active than the PS-b-PAA catalysts. Therefore, smaller particles are more efficient in the hydrogenation of CALD. A similar observation can be found in the study by Durndell and co-workers [10], where the conversion of CALD with Pt catalysts of different sizes dropped drastically with increasing particle size, due to a reduction in active surface area. The particle size can also affect the geometric and electronic characteristics of the catalyst that would influence the adsorption and desorption behaviour of the reactants [14]. Therefore, the careful control of the metal particle size is very important in the hydrogenation of CALD.

Comparison of the catalytic properties of Co@HCSs_PS-b-PAA_8 and Co/HCSs

Both Co@HCSs_PS-b-PAA_8 and Co/HCSs catalysts had similar loadings (5%, 10%, 15%) and Co particle sizes (*ca.* 6 nm) (Table S7.2, [23]). This allowed for the effect of placing the Co both inside and outside the HCSs to be studied. The catalytic behaviour of the 6 catalysts were compared under equivalent reaction conditions (100 mg catalyst, 100 mL/min H_2 flow rate and 1.5 mL/min CALD flow rate at 200 °C) and the selectivity data are shown in Figure 7.6, and the conversion data is summarized in Table 7.1.

- At 5% loading, the Co/HCSs catalyst did not show any conversion for the first 2 h of reaction. A conversion of 1% was observed after 3 h and remained at 1% for the remaining 5 h. It was evident that this catalyst was not active, even though it contained small active metal particles (6.2 nm).
- As the loading was increased to 10% and 15% Co, the conversion for the Co@HCSs catalysts increased to 74.8% and 99.8% respectively. These were lower than the conversions obtained with the Co/HCSs catalysts (59.8 % and 80.5 % for the 10% and 15% loaded catalysts, respectively). It was thus concluded that the encapsulation of the metal nanoparticles inside the HCSs enhanced the catalytic activity of the cobalt

catalysts. In a study by Dong and co-workers [22] the catalytic activities of PdCu catalysts supported inside and outside HCSs were investigated in liquid phase reactions. They investigated the void confinement effects and realized that mass transfer limits were not significant for hydrogenation of small molecules such as styrene but became important with big molecules that could not pass through the pores (0.6 nm) of the HCSs. Both the PdCu@HCSs and PdCu/HCSs showed similar activity for the hydrogenation of small molecules. In our study, the catalysts contained pores with diameters of *ca.* 5 nm. These were big enough to eliminate mass transfer limitations. Reactant accumulation effects can also be eliminated as the reaction was done at 200 °C. The different catalytic activities could be due to the strong metal-support interactions that were confirmed by TPR in the Co@HCSs_PS-b-PAA8 catalysts. This is suspected because the metal support interactions may have allowed for better electron transfer between the carbon and Co.

- At 5% loading, the Co/HCSs (Figure 7.6 (ii)) catalyst showed very low conversion and produced only 3PP. At 10% loading ((iv)), HCALD, 3PP and CAL were all produced, with high selectivity towards 3PP (21 %) while producing 60% of the 'other' by-products. At 15% loading ((vi)) CAL was not produced and a large quantity of the unwanted by-products (65 %) was produced. Over-hydrogenation occurs when the Co is placed outside the HCSs under the reaction conditions used.
- At 5% loading, the Co@HCSs_PS-b-PAA_8 ((i)) catalyst produced smaller amounts of the unidentified by-products (4 %), while producing similar amounts of HCALD (30%), 3PP (38%) and CAL (27 %). At higher metal loadings (10 and 15 %), the amount of the unidentified by-products increased significantly and the selectivity towards CAL decreased. This could be due to the high activity of the high metal-loaded catalysts which resulted in excess hydrogenation of the CALD. It was however evident that the Co@HCSs catalysts showed better selectivity than the Co/HCSs catalysts as they produced less by-products. Wang and co-workers [14] have reported that steric effects have an influence on catalyst selectivity, and this can be achieved by using core-shell catalysts as well as controlling metal particle diameter.

To briefly summarize the experimental work presented here, the catalysts studied generally showed an increase in conversion as the metal loading increased, due to the increase in catalytically active metal surface area.

The TEM images of the reacted 5% and 10% catalyst can be found in Figures S7.2 and S7.3. The catalysts did not show sintering after 5 h of reaction and the particle sizes were still in the range of 5 – 6 nm.

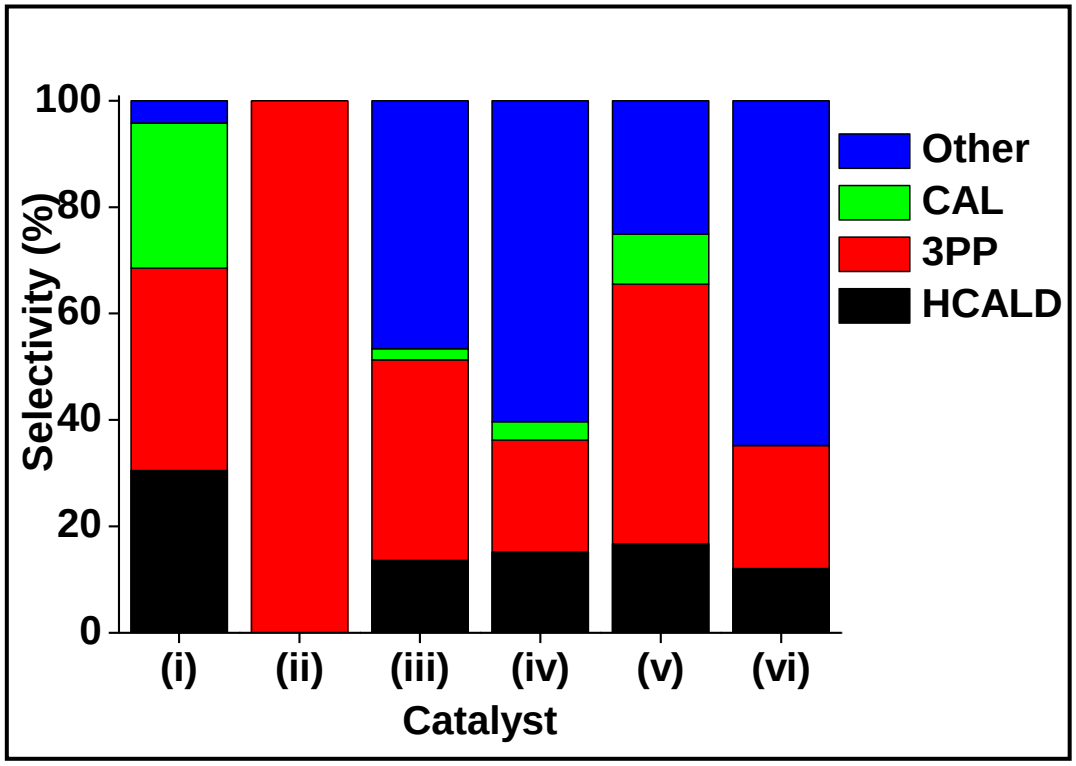

Figure 7.6: Selectivity after 1 h hydrogenation of CALD with (i) 5%Co@HCSs_PS-b-PAA_8, (ii) 5%Co/HCS, (iii) 10%Co@HCSs_PS-b-PAA_8, (iv) 10%Co/HCSs, (v) 15%Co@HCSs_PS-b-PAA_8 and (vi) 15%Co/HCSs

Catalyst recycling

Figure 7.7 shows the catalytic activity and selectivity after 5 cycles of hydrogenation with 10%Co/HCSs. The catalyst retained 80 % of its activity up to the third reaction cycle. On cycles 4 and 5, the retained activity was 65 and 25%, respectively. The data indicate that a major loss in activity only occurred after 4 reaction cycles. The stability of our catalysts was comparable to other catalysts previously reported in the literature [18] [36]. The TEM image and particle size distribution curve of the catalyst after 5 cycles can be found in Figure S7.4. No sintering was observed as the particle size was found to be 5.3 nm (initial particle size was 5.2 nm) (Table S7.2). The selectivity of the catalyst to HCALD was enhanced over the 5 cycles.

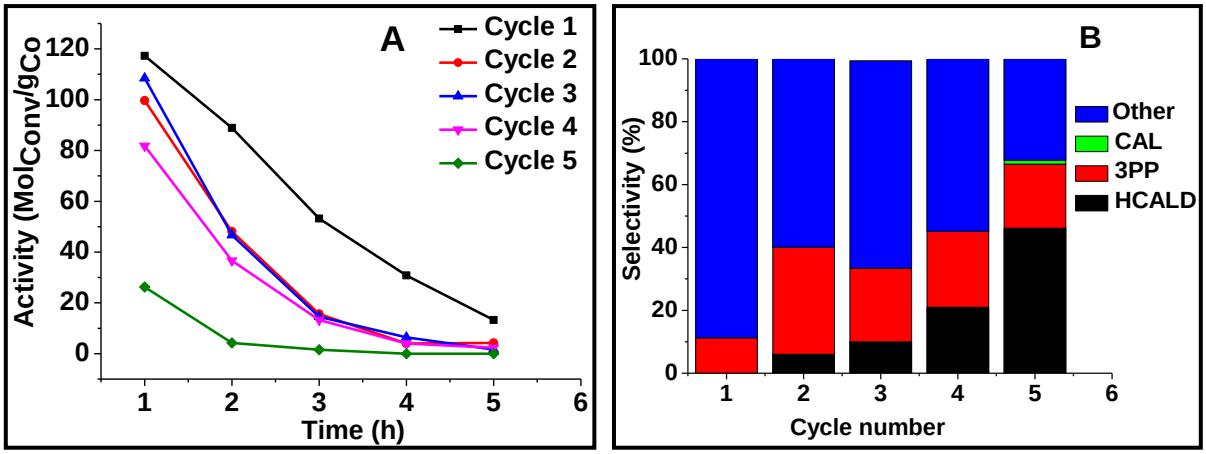

Figure 7.75: (A)catalytic activity of 10%Co/HCSs during 5 cycles of 5 h hydrogenation of CALD and (B) selectivity at 1 h of hydrogenation of CALD with10%Co/HCSs

The 10%Co@HCSs_PS-b-PAA_8 catalyst was also recycled, however, the catalyst activity could not be recovered, due to pore blockage. The recyclability of the 10%Co@HCSs_PS-b-PAA_8 catalyst was tested with a fresh catalyst (300 mg; standard conditions; 5 h reaction). After use, the catalyst was calcined at 200 °C for 1 h, under flowing air at 200 °C. The catalyst was then re-used for the hydrogenation of CALD, however, less than 5% CALD was converted. The catalyst was then calcined at 220 °C for 2 h and reused. Up to 45 % conversion of CALD was obtained. After this, the catalyst was again calcined (220 °C; 5 h) and reused for the hydrogenation of CALD, but without success.

Surface area analysis was done on the reused Co/HCSs and Co@HCSs catalysts after 5 and 4 uses, respectively. The used catalysts were calcined at 200 °C for 1h prior to the surface area analysis. The BET surface area, pore diameters and pore volumes of the catalysts are reported in Table S3. The corresponding BET isotherms and pore size distribution curves are reported in Figures S7.5 and S7.6, respectively. The surface area of both catalysts decreased significantly after the hydrogenation reaction, indicating a blockage of pores. The surface area of the 10%Co/HCSs catalyst decreased from 530 m^2/g to 95 m^2/g, and the 10%Co@HCSs_PS-b-PAA_8 decreased from 433 m^2/g to 108 m^2/g. For the Co/HCSs catalyst, the blockage of pores does not have a negative impact on the catalytic activity as the catalysts could be recycled with recovery of the catalyst activity. With the Co@HCSs catalysts, the pores are very important for the transportation of reactants to the inside of the HCSs, where the active metal nanoparticles are situated. The blockage of pores meant that the CALD could not reach the Co nanoparticles inside the HCSs, and as a result, the catalyst could not be recycled.

Conclusions

The Co@HCSs and Co/HCSs catalysts prepared were analysed by TPR studies and it was shown that the reducibility of the different catalysts varied based on the location of the Co due to diffusion and metal-support interaction effects. The catalysts were evaluated for activity in the vapour phase hydrogenation of CALD and good activity was observed for most of the catalysts. The data showed evidence of catalyst deactivation by poisoning/coke deposition due to the formation of by-products. A variation in the rate of hydrogen flow showed that the amount of hydrogen has a significant influence on the reaction as it competes for adsorption sites with CALD. Reaction temperature studies indicated that a moderate temperature gave the best results because higher temperatures led to poor reactant adsorption. Furthermore, high reaction temperatures resulted in poor selectivity due to over-hydrogenation and decomposition of the reactants and products. A similar effect was observed with an increase in catalyst mass, where higher amounts of catalyst led to over-hydrogenation and large amounts of unwanted by-products due to an increase in contact time. Careful control of particle size was required to achieve optimum results in hydrogenation reactions as larger particles gave very low activity compared to smaller particles. Better activity and selectivity were obtained with Co@HCSs than the Co/HCSs. However, an unexpected disadvantage of using Co@HCSs was the recyclability of the catalyst which was hindered by pore-blockage. The Co/HCSs catalysts could be recycled with up to 80% recovery of activity. Surface area analysis showed that the pores of the HCSs were blocked during the reaction, and this had a negative impact on the recyclability of the Co@HCSs catalysts as they depended on the pores as conduits for reactants and products to and from the active catalyst.

References

[1] Perez, L.; Axet, M. R.; Yi, D.; Serp, P.; Soulantica, K. Selective hydrogenation of cinnamaldehyde by unsupported and few layer graphene supported platinum concave nanocubes exposing {110} facets stabilized by long-chain amine. *Catal. Today*, **2020**, 357 (1), 166-175. DOI: 10.1016/j.cattod.2019.05.048

[2] Bonita, Y.; Jain, V.; Geng, F.; O'Connell, T. P.; Ramos, N. X.; Rai N.; Hicks, J. C. Hydrogenation of cinnamaldehyde to cinnamyl alcohol with metal phosphides: Catalytic consequences of product and pyridine doping. *Appl. Catal. B Environ*. **2020**, 227 (119272). DOI: 10.1016/j.apcatb.2020.119272

[3] Nongwe, I.; Ravat, V.; Meijboom, R..; Coville, N. J. Pt supported nitrogen doped hollow carbon spheres for the catalysed reduction of cinnamaldehyde. *Appl. Catal. A Gen*. **2016**, 517, 30-38. DOI: 10.1016/j.apcata.2016.02.025

[4] Jao, K.-Y.; Liu, K.-W.; Yang, Y.-H.; Ko, A.-N. Vapour phase hydrogenation of cinnamaldehyde over nano Ni and Ni/SiMCM-41 catalysts. *J. Chin. Chem. Soc*. **2009**, 56 (5), 885-890. DOI: 10.1002/jccs.200900131

[5] Chin, S.-Y.; Lin F.-J.; Ko, A.-N. Vapour phase hydrogenation of cinnamaldehyde over Ni/y-Al_2O_3 catalysts: Interesting reaction network. *Catal. Lett*. **2009**, 132 (389), 389-394. DOI: 10.1007/s10562-009-0127-4

[6] Leng, F.; Gerber, I. C.; Axet, M. R.; Serp, P. Selectivity shifts in hydrogenation of cinnamaldehyde on electron-deficient ruthenium nanoparticles. *C. R. Chimie*, **2018**, 21, 346-353. DOI: 10.1016/j.crci.2017.04.001

[7] Zhang, J.; Gao, Z.; Wang, S.; Wang, G.; Gao, X.; Zhang, B.; Xing, S.; Zhao, S.; Qin, Y. Origin of synergistic effects in bicomponent cobalt oxide-platinum catalysts for selective hydrogenation reaction, *Nat. Commun*. **2019**, 10 (4166). DOI: 10.1038/s41467-019-11970-8

[8] Coq, B.; Kumbhar, P. S.; Moreau, C.; Moreau, P.; Warawdekar, M. G.; Liquid phase hydrogenation of cinnamaldehyde over supported ruthenium catalysts: Influence of particle size, bimetallics and nature of support. *J. Mol. Catal*. **1993**, 85 (2), 215-228. DOI: 10.1016/0304-5102(93)80103-2

[9] Reddy, B. M.; Kumar, G. M.; Ganesh I.; Khan, A. Vapour phase hydrogenation of cinnamaldehyde over silica supported transition metal-based bimetallic catalysts. *J.Mol. Catal. A Chem*. **2006**, 247, 80-87. DOI: 10.1016/j.molcata.2005.11.026

[10] Durndell, L. J.; Parlett, C. M. A.; Hondow, N. S.; Isaacs, M. A.; Wilson, K.; Lee, A. F.; Selectivity control in Pt-catalyzed cinnamaldehyde hydrogenation. *Sci. Rep*. **2015**, 5 (9425). DOI: 10.1038/srep09425

[11] Raj, J. A.; Prakash, M. G.; Elangovan, T.; Viswanathan, B.; Selective hydrogenation of cinnamaldehyde over cobalt supported on alumina, silica and titania. *Catal. Lett*. **2012**, 142, 87-94. DOI: 10.1007/s10562-011-0693-0

[12] Su, H.; Zhang, K.-X.; Zhang, B.; Wang, H.-H.; Yu, Q.-Y.; Li, X.-H.; Antonietti, M.; Chen, J.-S. Activating cobalt nanoparticles via the Mott-Schotty effect in nitrogen-rich carbon shells for base-free aerobic oxidation of alcohols to esters. *J. Am. Chem. Soc*. **2017**, 139 (2), 811-818. DOI: 10.1021/jacs.6b10710

[13] Homs, N.; Llorca, J.; Piscina, P. R.; Rodriguez-Reinoso, F.; Sepulveda-Escribano, A.; Silvestre-Albero, J. Vapour phase hydrogenation of crotonaldehyde over magnesia-supported platinum-tin catalysts. *Phys. Chem. Chem. Phys*. **2001**, 3, 1782-1788. DOI: 10.1039/B100770J

[14] Wang, X.; Liang, X.; Geng, P.; Li, Q. Recent advances in selective hydrogenation of cinnamaldehyde over supported metal-based catalysts. *ACS Catal*. **2020**, 10 (4), 2395-2412. DOI: 10.1021/acscatal.9b05031

[15] Lv, Y.; Han, M.; Gong, W.; Wang, D.; Chen, C.; Wang, G.; Zhang, H.; Zhao, H. Fe-Co alloyed nanoparticles catalyzing efficient hydrogenation of cinnamaldehyde to cinnamyl alcohol in water. *Angew. Chem. Int. Ed*. **2020**, 59 (52), 23521-23526. DOI: 10.1002/anie.202009913

[16] Tan, Y.; Liu, X.; Zhang, L.; Liu, F.; Wang A.; Zhang, T. Producing of cinnamyl alcohol from cinnamaldehyde over supported gold nanocatalyst, *Chin. J. Chem*. **2021**, 42 (3), 470-481. DOI: 10.1016/S1872-2067(20)63678-6

[17] Toebes, M. L.; Zhang, Y.; Hajek, J.; Nijhuis, A. T.; Bitter, J. H.; van Dillen, A. J.; Murzin, D. Y.; Koningsberger D. C.; de Jong, K. P. Support effects in the hydrogenation of cinnamaldehyde over carbon nanofiber-supported platinum catalysts: characterization and catalysis. *J. Catal*. **2004**, 226 (1), 215-225. DOI: 10.1016/j.jcat.2004.05.026

[18] Zhao, J.; Yuan, H.; Gui, Y.; Li, X.; Qin, X.; Wei, C.; Liu, Y.; Wang, G.; Zhou, L.; Fang, S. Engineering the interface of Au nanocatalysts with FeO_x for enhanced selective hydrogenation of cinnamaldehyde. *J. Mat. Sci*. **2021**, 56, 5760-5771. DOI: 10.1007/s10853-020-05634-y

[19] Dlamini, M. W.; Kumi, D. O.; Phaahlamohlaka, T. N.; Lyadov, A. S.; Billing, D. G.; Jewell, L. L.; Coville, N. J. Carbon spheres prepared by hydrothermal synthesis - A support for bimetallic iron cobalt Fischer-Tropsch catalysts. *ChemCatChem* **2015**, 7 (18), 3000-3011. DOI: **10.1002/cctc.201500334**

[20] Dlamini, M. W.; Phaahlamohlaka, T. N.; Kumi, D. O.; Forbes, R.; Jewell L. L.; Coville, N. J. Post-doped nitrogen-decorated hollow carbon spheres as a support for Co Fischer-Tropsch catalysts. *Catal. Today* **2020**, 342, 99-110. DOI: 10.1016/j.cattod.2019.01.070

[21] Phaahlamohlaka, T. N.; Kumi, D. O.; Dlamini, M. W.; Forbes, R.; Jewell, L. L.; Billing, D. G.; Coville, N. J. Effects of Co and Ru intimacy in Fischer-Tropsch catalysts using hollow carbon sphere supports: Assessment of the hydrogen spillover processes. *ACS Catal*. **2017**, 7 (3), 568-1578. DOI: 10.1021/acscatal.6b03102

[22] Dong, C.; Yu, Q.; Ye, R.-P.; Su, P.; Liu, J.; Wang, G.-H. Hollow carbon sphere nanoreactors loaded with PdCu nanoparticles: Void confinement effects in liquid phase hydrogenations," *Angew. Chem. Int. Ed.* **2020**, 59 (42) , 18374-18379. DOI: **10.1002/ange.202007297**

[23] Mente, P.; Phahlaamohlaka, T. N.; Mashindi, V.; Coville, N. J. Polystyrene-b-poly(acrylic acid) nanospheres for the synthesis of size-controlled cobalt nanoparticles encapsulated inside hollow carbon spheres. *J. Mater. Sci.* **2021**, 56 (3), 2113-2128. DOI: 10.1007/s10853-020-05323-w

[24] Mente, P.; Mashindi, V.; Phaahlamohlaka, T. N.; Monyatsi, T. N.; Forbes, R. P.; Coville, N. J. The oxidation of benzyl alcohol using cobalt oxide supported inside and outside hollow carbon spheres. *ChemistryOpen* **2021**.

[25] Roman-Martinez, M. C.; Cazorla-Amoros, D.; Linares-Solano, A.; Salinas-Martinez De Lecea, C. TPD and TPR characterization of carbonaceous supports and Pt/C catalysts. *Carbon* **1993**, 31 (6), 895-902. DOI: 10.1016/0008-6223(93)90190-L

[26] Arnoldy, P., van Oers, E. M.; Bruinsma, O. S. L.; de Beer, V. H. J.; Moulijn, J. A. Temperature-programmed reduction of Al_2O_3-, SiO_2-, and carbon-supported Re_2O_7 catalysts. *J. Catal*. **1985**, 93 (2), 231-245. DOI: 10.1016/0021-9517(85)90171-X

[27] Fu, T.; Jiang, Y.; Lv, J.; Li, Z. Effect of carbon support on Fischer-Tropsch synthesis activity and product distribution over Co-based catalysts, *Fuel Process. Technol*. **2013,** 110, 141-149. DOI: 10.1016/j.fuproc.2012.12.006

[28] Xiong, H.; Motchelaho, M. A.; Moyo, M.; Jewell L. L.; Coville, N. J. Cobalt catalysts supported on a micro-coil carbon in Fischer-Tropsch synthesis: A comparison with CNTs and CNfs. *Catal*. Today **2013,** 214, 50-60. DOI: 10.1016/j.cattod.2012.10.018

[29] Cordoba, M.; Miranda, C.; Lederhos, C.; Coloma-Pascual, F.; Ardila, A.; Fuentes, G. A.; Pouilloux, Y.; Ramirez, A. Catalytic performance of Co_3O_4 on different activated carbon supports in the benzyl alcohol oxidation. *Catalysts* **2017**, 7 (384). DOI: **https://doi.org/10.3390/catal7120384**

[30] Luisetto, I.; Pepe, F.; Bemporad, E. Preparation and characterization of nano cobalt oxide. *J. Nanopart. Res.* **2008**, 10, 59-67. DOI: 10.1007/s11051-008-9365-4

[31] Ramos-Fernandez, E. V.; Sepulveda-Escribano, A.; Rodriguez-Reinoso, F. Enhancing the catalytic performance of Pt/ZnO in the vapour phase hydrogenation of crotonaldehyde by the addition of Cr to the support. *Cat. Commun*. **2008**, 9 (6), 1243-1246. DOI: 10.1016/j.catcom.2007.11.010

[32] Chary, K. V.; Naresh, D.; Vishwanathan, V.; Sadakane, M.; Ueda, W. Vapour phase hydrogenation of phenol over Pd/C catalysts: A relationship between dispersion, metal area and hydrogenation activity. *Catal. Commun*. **2007**, 8 (3), 471-477. DOI: 10.1016/j.catcom.2006.07.017

[33] Taimoor, A. A.; Pitault, I. Kinetics of toluene hydrogenation - Integrating a dynamic approach regarding catalyst activity. *React. Kinet. Mech. Cat*. **2011,** 102, 263-282. DOI: 10.1007/s11144-010-0270-3

[34] Keane, M. A.; Patterson, P. M. The role of hydrogen partial pressure in the gas-phase hydrogenation of aromatics over supported nickel. *Ind. Eng. Chem. Res*. **1998**, 38 (4), 1295-1305. DOI: 10.1021/ie980540t

[35] Lindfors, L. P.; Salmi, T. Kinetics of toluene hydrogenation on a supported Ni catalyst. *Ind. Eng. Chem. Res*. **1993**, 32, 34-42. DOI: 10.1021/ie00013a006

[36] Wang, G.; Xin, H.; Wang, Q.; Wu P.; and Li, X. Efficient liquid-phase hydrogenation of cinnamaldehyde to cinnamyl alcohol with a robust PtFe/HPZSM-5 catalyst. *J. Catal.* **2020**, 382, 1-12. DOI: 10.1016/j.jcat.2019.12.004

[37] Johnson, B. G.; Bartholomew C. H.; Goodman, W. D. The role of surface structure and dispersion in CO hydrogenation on cobalt. *J. Catal*. **1991**, 128 (1), 231-247. DOI: 10.1016/0021-9517(91)90080-N

[38] Van Deelen, T. W.; Mejia C. H.; de Jong, K. P. Control of metal-support interactions in heterogeneous catalysts to enhance activity and selectivity. *Nat. Catal*. **2019**, 2, 955-970. DOI: 10.1038/s41929-019-0364-x

[39] Zhan, W.; He, Q.; Liu, X.; Guo, Y.; Wang, Y.; Wang, L.; Guo, Y.; Borisevich, A. Y.; Zhang, J.; Lu, G.; Dai, S. A sacrificial coating strategy toward enhancement of metal-support interaction for ultrastable Au nanocatalysts, *J. Am. Chem. Soc*. **2016,** 138 (49), 16130-16139. DOI: 10.1021/jacs.6b10472

[40] Mahata, N. Ranghavan, K. V. Vishwanathan, V. Park C. and Keane, M. A. Phenol hydrogenation over palladium supported on magnesia: Relationship between catalyst structure and performance. *Phys. Chem. Chem. Phys.* **2001**, 3, 3712-2719. DOI: 10.1039/B100237F

[41] Wang, C.-B.; Tang, C.-W.; Tsai H.-C.; Chien, S.-H. Characterization and catalytic oxidation of carbon monoxide over supported cobalt catalysts. *Catal. Lett*. **2006**, 107, 3-4. DOI: 10.1007/s10562-005-0002-x

[42] Lapidus, A. L.; Krylova, A. Y.; Kazanskii, V. V.; Borovkov, V. Y.; Zaitsev, A. V.; Kozlova, G. V.; Zukal, A.; Ratkhouski I.; Yanchalkova, M. Effect of preliminary heating on the physicochemical

properties of 10% Co/Al_2O_3 catalyst and its behaviour in hydrogenation synthesis from Co and H. *Bulletin of the Academy of Sciences of the USSR, Division of chemical science.* **1991**, 40 (11), 2129-2134.

Chapter 8: Conclusions and recommendations

8.1. Conclusions

8.1.1. Synthesis of Co@HCSs with functionalized polymers

- The polymers PAA, PEG, PECA and PMMA were used to introduce hydroxyl and carboxyl type functional groups on the surface of polymer spheres.
- The functional groups introduced successfully stabilized and immobilized Co nanoparticles with different Co phases (Co, CoO and Co_3O_4). The copolymers PS-b-PAA and PS-b-PMAA gave better nanoparticles (small controllable size) than PS spheres coated with PECA and PEG.
- The variations in the Co phase seemed to depend on the type of polymer used to grow the nanoparticles. The polymers containing carboxylic groups gave more reduced particles (Co and CoO) than the unfunctionalized PS (Co_3O_4).
- The changes in the solvent and monomer compositions had a very significant influence on the size of the polymer spheres, and consequently on the size and shell thickness of the resultant HCSs.
- There was no direct relationship between the size of the polymer spheres and the size and shape of the resultant Co nanoparticles. Changes were seen in Co particle sizes at the size of the PS-b-PMMA spheres changed, but no exact reasons for this relationship could be determined.
- Both the polymer template and the metal particle sizes influenced the resorcinol formaldehyde polymerization reaction. This could be seen from the SEM micrographs of the HCSs. The HCSs containing smaller particles (from functionalized polymers) had less breakage on the carbon shell, as opposed to the HCSs prepared from unfunctionalized polymers containing bigger Co nanoparticles.

8.1.2. Catalysis with Co@HCSs and Co/HCSs

- The Co@HCSs and Co/HCSs catalysts showed good activity in the oxidation of benzyl alcohol and the hydrogenation of cinnamaldehyde reactions. Both catalysts showed

good selectivity in the oxidation of benzyl alcohol, whereas in the hydrogenation of CALD the catalysts showed good activity but poor selectivity.

- Dependence of activity on particle size was observed with the hydrogenation reaction, where the small particles were much more active than the bigger particles. The oxidation reaction seemed to depend more on the cobalt phase where the Co_3O_4 phase gave catalysts that were more active than Co and CoO phases.
- The activity and selectivity of both the Co@HCSs and Co/HCSs were very similar in the oxidation of benzyl alcohol, yet, the Co@HCSs catalysts showed better activity and selectivity than the Co/HCSs in the hydrogenation of CALD.
- Catalysts were tested with different Co loading (5, 10, and 15%). It was generally observed that in the oxidation of benzyl alcohol reaction, the conversion and selectivity did not necessarily change with the increase in loading. The 5%, 10% and 15% Co loaded catalysts gave very similar benzyl alcohol conversions for both Co@HCSs and Co/HCSs. In contrast, with the hydrogenation of CALD, the conversion increased significantly as the Co loading increased. From this, it can be deduced that there were other limiting factors in the oxidation of benzyl alcohol reaction.
- It was observed that both reactions led to catalyst deactivation over time, in the form of active sites blockage and HCS pore blockage. The active site blockage could be reversed for both reactions. Up to 80% activity was recovered during catalysts recycling in both reactions with the Co/HCSs. However, with the Co@HCSs catalysts the pore blockage was a bigger problem than the active site blockage. Due to the pore blockage, the activity could not be recovered with the Co@HCSs as access to the active Co catalysts was restricted.

8.2. Recommendations

- The shell porosity appeared to be a limiting factor in using the Co@HCSs materials in catalysis. A study in which the shell porosity of the HCSs is varied is recommended to overcome the pore blockage issues observed during catalysis with Co@HCSs.
- A variation in shell thickness of HCSs is recommended to investigate the influence of the HCS shell on the rate of the catalytic reactions.

- Loading of Co based bimetallic catalysts inside and outside HCSs, to mitigate the selectivity issues in the hydrogenation of CALD with Co based catalysts could enhance the activity of the catalysts.
- To evaluate the reason for the catalyst deactivation, the reacted Co@HCSs catalysts could be crushed by grinding in liquid nitrogen to expose the cobalt nanoparticles. The crushed catalyst could then be re-used in the hydrogenation and oxidation reactions to confirm if the non-recyclability of these catalysts is due to pore blockage.
- The synthesis of other smaller copolymer spheres could be undertaken to prepare small HCSs (< 100 nm) with less shell breakages. These small HCSs can be used to investigate the rate of catalyst deactivation by pore blockage when using HCSs of different diameters (100 – 1000 nm).
- These carbon sphere materials can be used for heterogeneous catalysis reactions using other metals/metal oxides at room temperature, where it is assumed that the pore blockage would not occur or would be minimal.

Supplementary information

Appendix A: Polystyrene-b-poly(acrylic acid) nanospheres for the synthesis of size-controlled cobalt nanoparticles encapsulated inside hollow carbon spheres

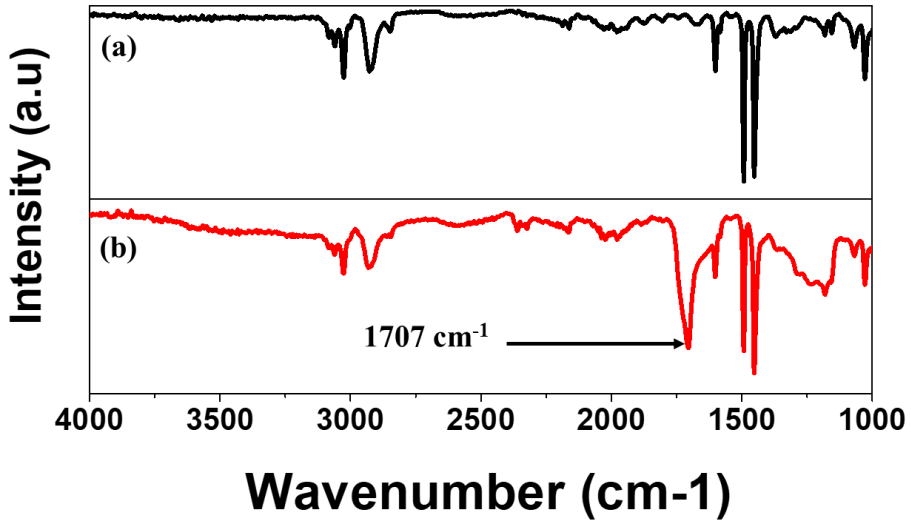

Figure S3.1: FTIR spectra of (a) PSSs, (b) PS-b-PAA prepared with 50 % acrylic acid

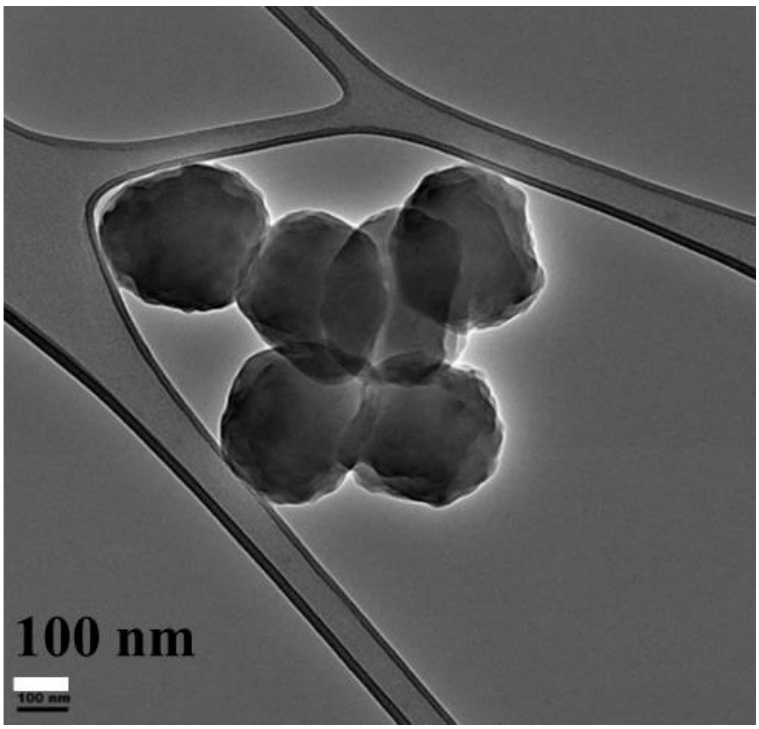

Figure S3.2: TEM image of PS-b-PAA prepared with 50 % acrylic acid

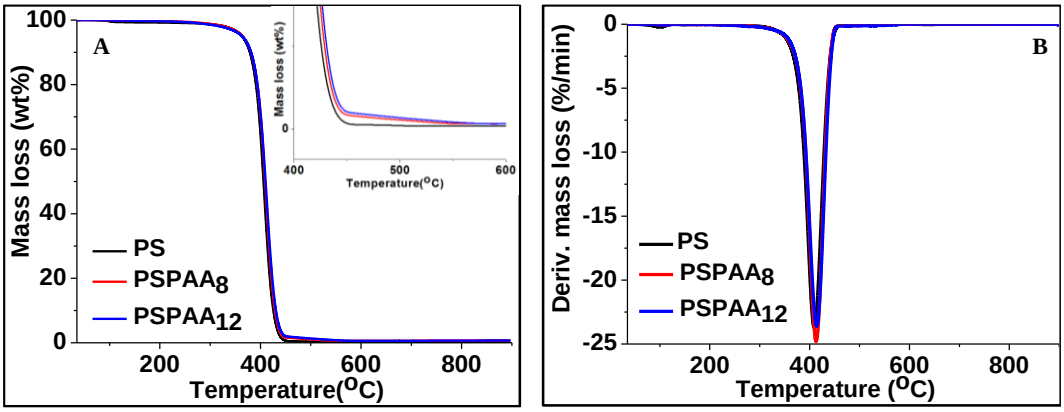

Figure S3.3: TGA and derivative TGA of PS and functionalized PS spheres analysed under nitrogen

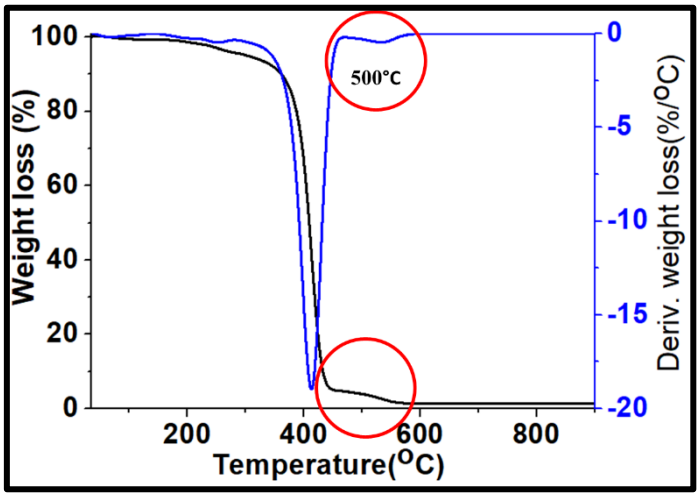

Figure S3.4: TGA and derivative TGA of PS-b-PAA prepared with 50 % acrylic acid

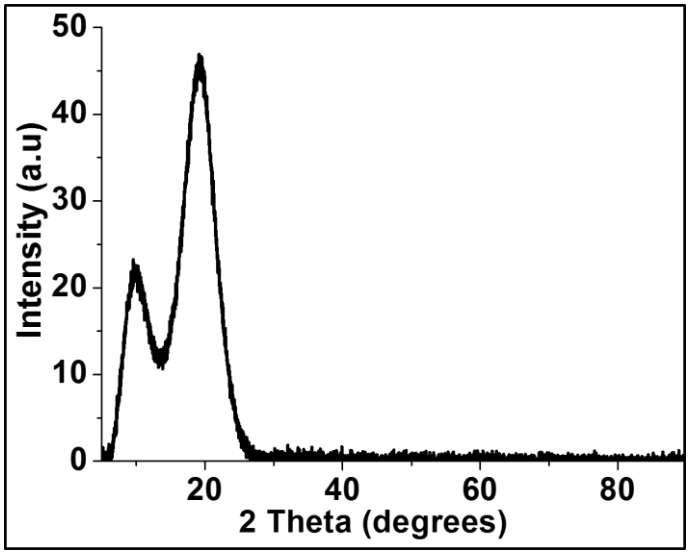

Figure S3.5: PXRD data of CoyOx/PS

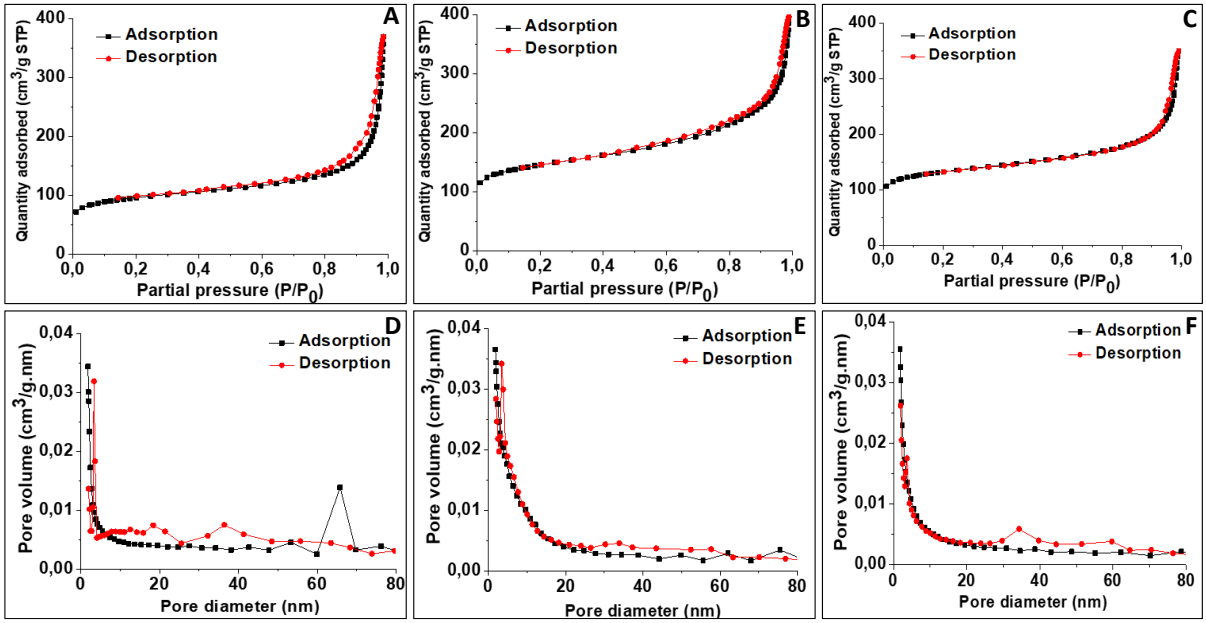

Figure S3.6: BET isotherms (A,B,C) and pore size distribution plots (D,E,F) of 10% Co_xO_y@HCSs prepared with different templates PS (A,D), PS-b-PAA_8 (B,E) and PS-b-PAA_{12} (C,F)

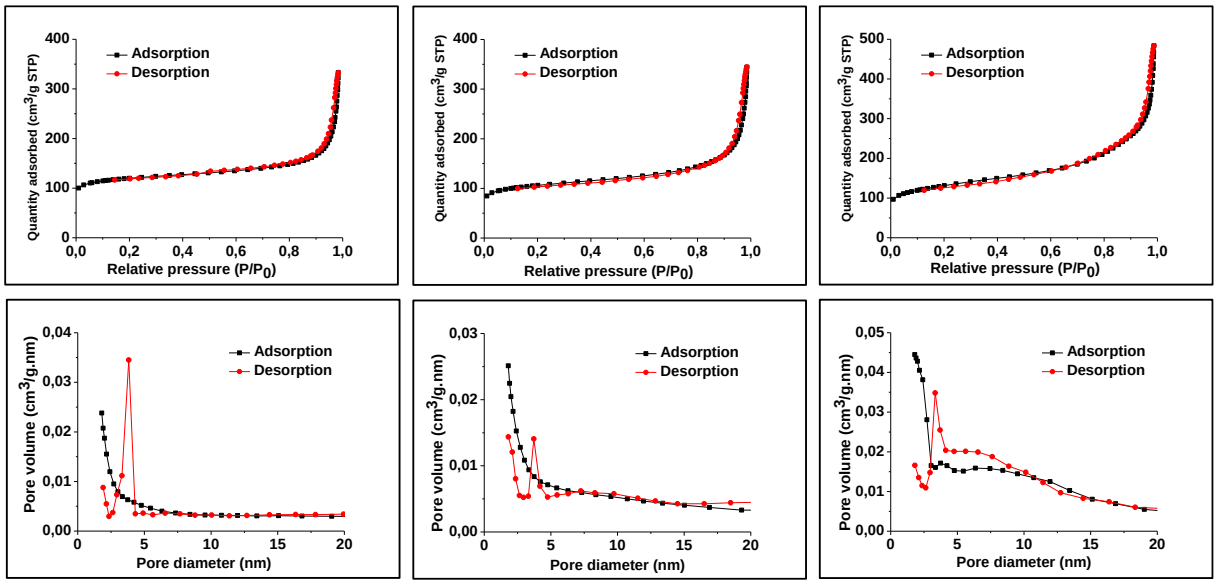

Figure S3.7: BET isotherms (A, B, C) and pore size distribution plots (D, E ,F) of 15% Co_xO_y@HCSs prepared with different templates PS (A,D), PS-b-PAA8 (B,E) and PS-b-PAA12 (C,F)

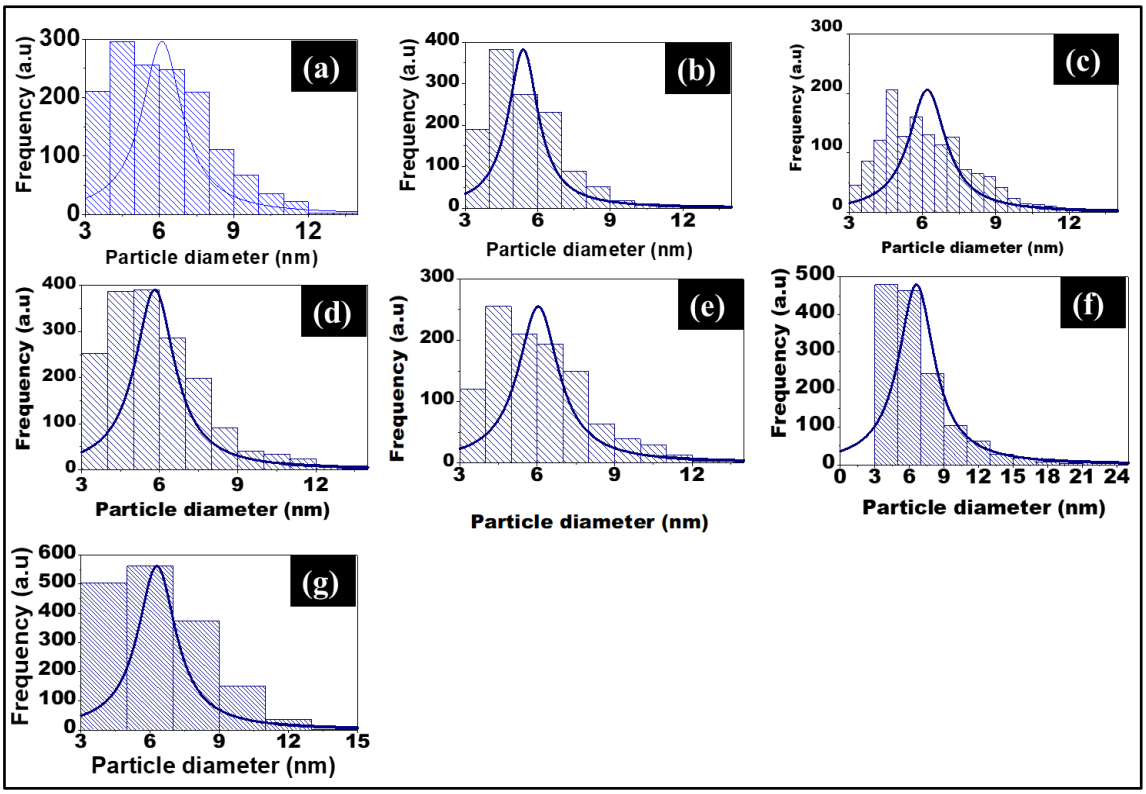

Figure S3.8: Particle size distribution curves of 5% Co_xO_y@HCSs prepared with PS (a), PS-b-PAA_8 (b) and PS-b-PAA_{12} (c), 10% Co_xO_y@HCSs prepared with PS-b-PAA_8 (d) and PS-b-PAA_{12} (e) and 15% Co_xO_y@HCSs prepared with, PS-b-PAA_8 (f) and PS-b-PAA_{12} (g)

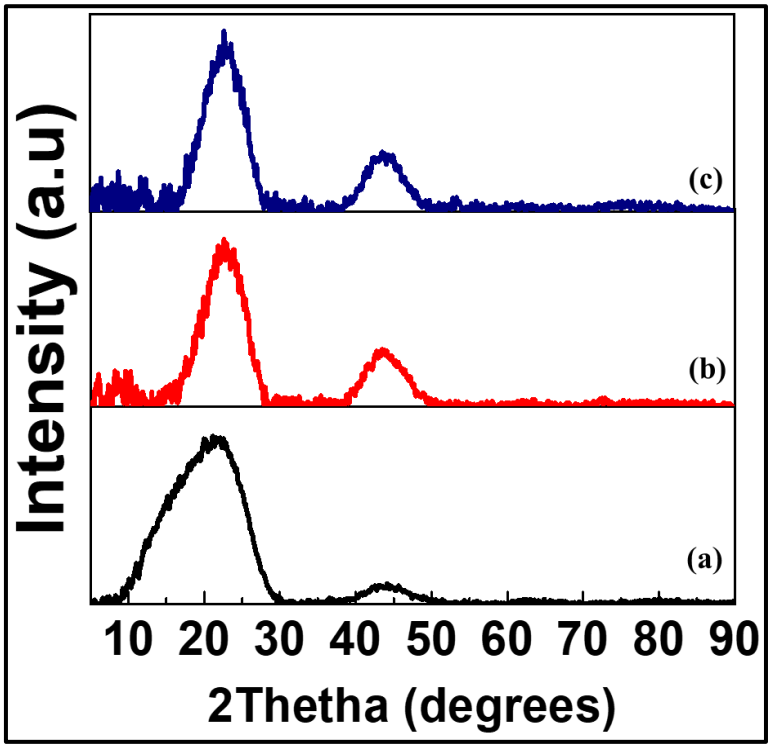

Figure S3.9: PXRD data of HCSs prepared with different polymer templates, PS (a), PS-b-PAA8 (b) and PS-b-PAA12 (c)

Table S3.1: PXRD peak positions for 5% Co loaded catalysts

Catalyst	2 Theta (degrees)	Comment	Assignment
5%Co@HCSs_PS	19.03	small	Co_3O_4
	31.28	small	Co_3O_4
	36.85	sharp (strongest)	Co_3O_4
	42.49	small	CoO
	44.89	very small	Co_3O_4
	59.42	very small	Co_3O_4
	61.59	very small	CoO
	65.23	very small	Co_3O_4
5%Co@HCSs_PS-*b*-PAA$_8$	44.22	short, broad	Co
5%Co@HCSs_PS-*b*-PAA$_{12}$	36.52	small	CoO
	42.32	medium(strongest)	CoO
	61.35	small	CoO

Table S3.2: PXRD peak positions for 10% Co loaded catalysts

Catalyst	**2 Theta (degrees)**	**Comment**	**Assignment**
10%Co@HCSs_PS	36.68	small	CoO
	41.51	small	*hcp* Co
	44.25	sharp (strong)	*fcc* Co
	47.31	sharp (strong)	*hcp* Co
	51.38	very small	*fcc* Co
	62.37	small	*hcp* Co
	75.77	small	*fcc* Co
10%Co@HCSs_PS-*b*-PAA$_8$	44.39	broad (strongest)	*fcc* Co
	49.22	very small	*fcc* Co
	76.69	very small	*fcc* Co

10%Co@HCSs_PS-*b*-PAA$_{12}$	36.55	small	CoO
	44.15	Sharp (strongest)	*fcc* Co
	50.56	very small	*fcc* Co
	61.49	small	CoO
	76.91	very small	CoO

Table S3.3: PXRD peak positions for 15% Co loaded catalysts

Catalyst	**2 Theta (degrees)**	**Comment**	**Assignment**
15%Co@HCSs_PS	36.59	small	CoO
	41.66	small	*hcp* Co
	42.53	small	CoO
	44.40	sharp (strongest)	*fcc* Co
	47.46	sharp	*hcp* Co
	51.48	small	*fcc* Co
	61.99	very small	CoO
	75.87	small	*hcp* Co
15%Co@HCSs_PS-*b*-PAA$_8$	44.40	broad (strongest)	*fcc* Co
	57.79	very small	*fcc* Co
	76.01	very small	*fcc* Co
15%Co@HCSs_PS-*b*-PAA$_{12}$	31.1	very small	Co_3O_4
	36.63	sharp (strongest)	Co_3O_4
	42.51	sharp	CoO
	44.40	sharp	*fcc* Co
	61.52	very small	CoO

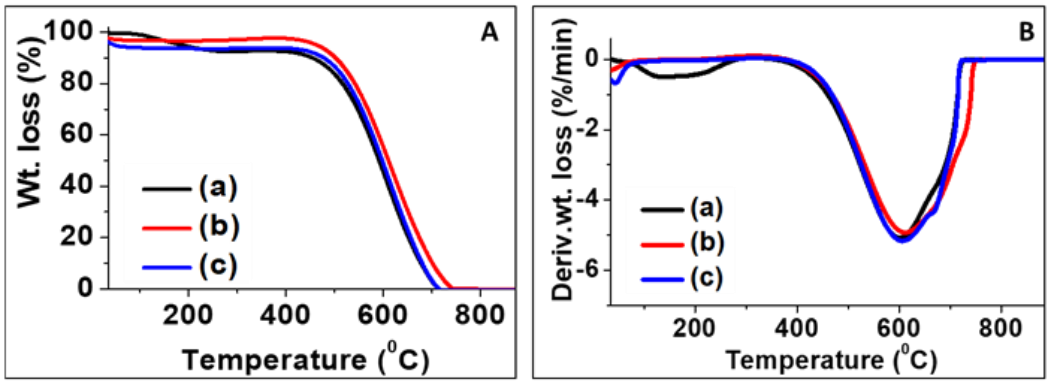

Figure S3.10: TGA (A) and DTGA curves of HCSs prepared with different polymer templates, PSS (a), PS-b-PAA8 (b) and PS-b-PAA12 (c)

Table S3.4: Carbon decomposition temperature analysis

Catalyst	Carbon maximum decomposition temperature (T_{max},°C)		
	T_1	T_2	T_3
5%Co@HCSs_PS	365	440	-
5%Co@HCSs_PS-*b*-PAA$_8$	370	472	-
5%Co@HCSs_PS-*b*-PAA$_{12}$	370	440	-
10%Co@HCSs_PS	-	394	557
10%Co@HCSs_PS-*b*-PAA$_8$	329	410	-
10%Co@HCSs_PS-*b*-PAA$_{12}$	339	410	-
15%Co@HCSs_PS	-	428	558
15%Co@HCSs_PS-*b*-PAA$_8$	332	428	-
15%Co@HCSs_PS-*b*-PAA$_{12}$	347	-	-

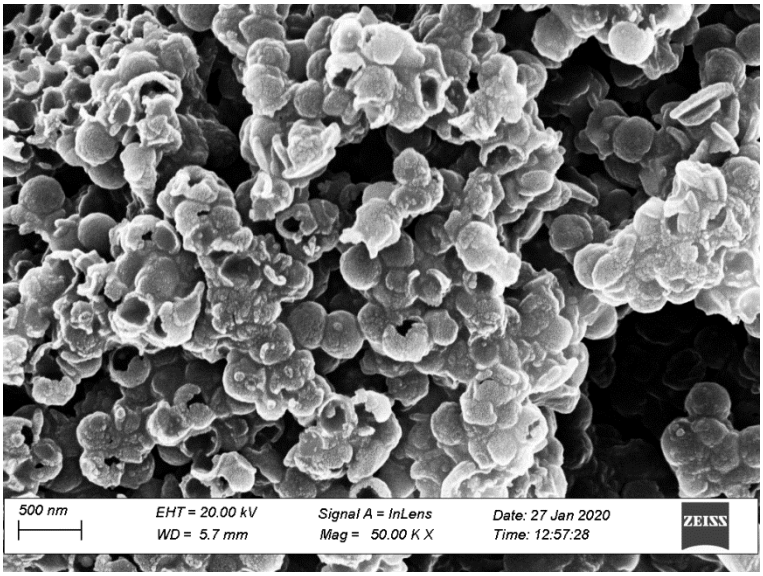

Figure S3.11: SEM Micrograph of 10% CoxOy@HCSs prepared with PS

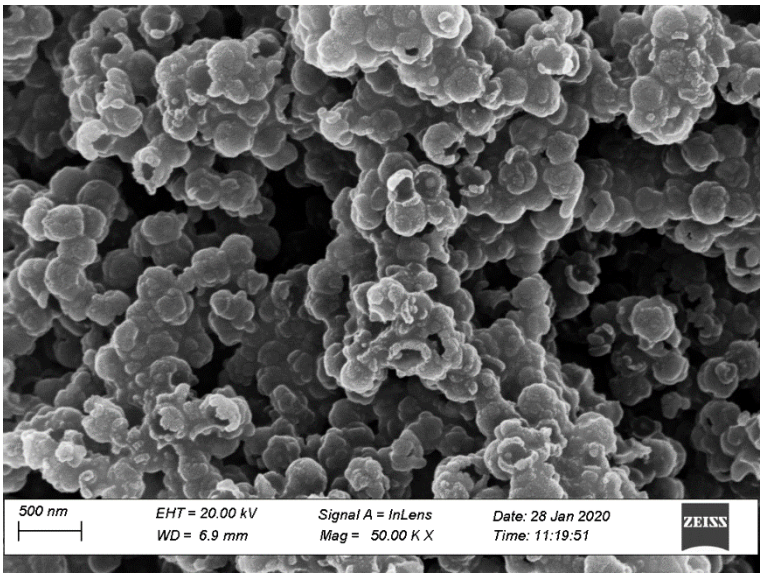

Figure S3.12: SEM Micrograph of 15% CoxOy@HCSs prepared with PS

Appendix B: The synthesis of Co@HCSs using polystyrene spheres functionalized with poly(acrylic acid), poly(ethyl cyanoacrylate) and poly(ethylene glycol)

S4.1: preparation of ethyl cyanoacrylate [1]

Ethyl cyanoacetate (10.5 mL) containing 2 drops of piperidine was added dropwise to a 7.5 mL solution of formaldehyde (37%). The temperature of the mixture increased to 60 °C and the rate of the addition of ethyl cyanoacetate was controlled such that the temperature of the mixture did not exceed 80 °C. After completing the addition of ethyl cyanoacetate the mixture was heated up to 80 °C and kept isothermal for 1 hour and then cooled down. The cooled product had a water supernatant layer which was discarded. The residue was washed with acetone and then dried over anhydrous phosphorus pentoxide and the remaining acetone was distilled using a rotary evaporator at 65 °C. The fluid clear product (ethyl cyanoacrylate) was distilled off at 76 – 93 °C and collected on a receiver containing 0.4 g of phosphorus pentoxide.

S4.2: polymerization of ethyl cyanoacrylate [2]

The monomer (4g) was added to a mixture of water (200 mL), acetone (50 mL) and PVP (0.04 g). The pH of the water was adjusted to 2.5 using 0.1 M HCl solution. The polymerization occurred at room temperature for 2 hours, under constant stirring. The product was washed with acidic distilled water and dried in an oven at 60 °C.

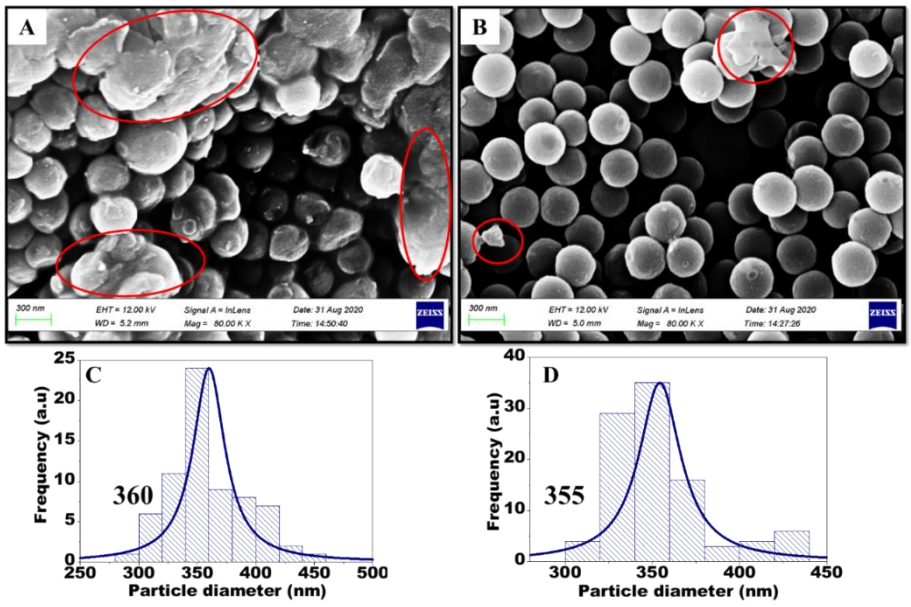

Figure S4.1: SEM images and particle size distribution plots of (A, C) PS – PAA spheres functionalized with 50% PAA and (B, D) PS – PEG spheres functionalized with 50% PEG

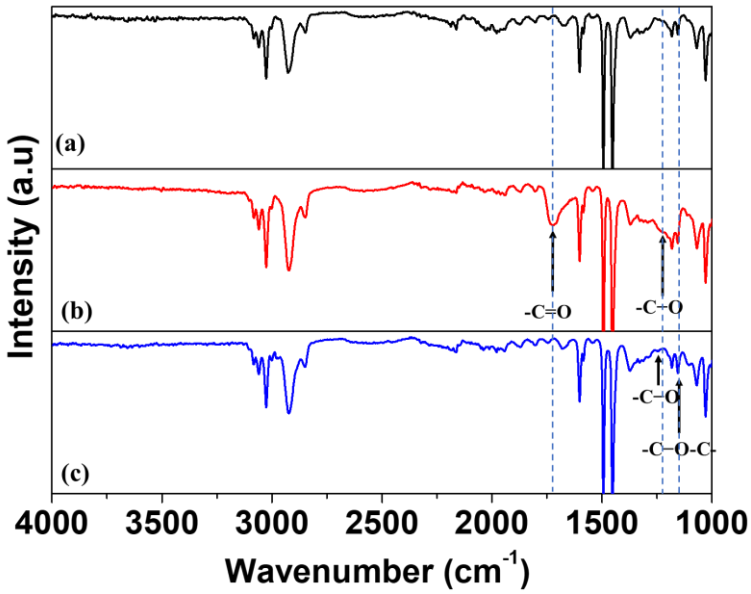

Figure S4.2: FTIR spectra of (a) PS and (b) PS-PAA and (c) PS-PEG spheres functionalized with 50% PAA and PEG

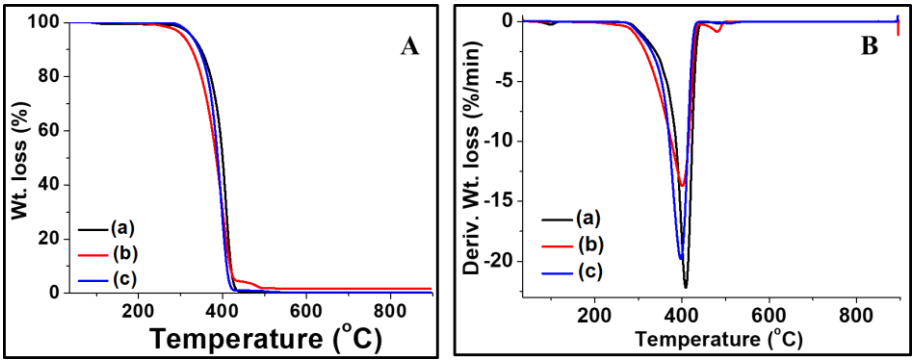

Figure S4.3: TGA (A) and derivative TGA (B) of (a) PS and (b) PS-PAA and (c) PS-PEG spheres functionalized with 50% PAA and PEG

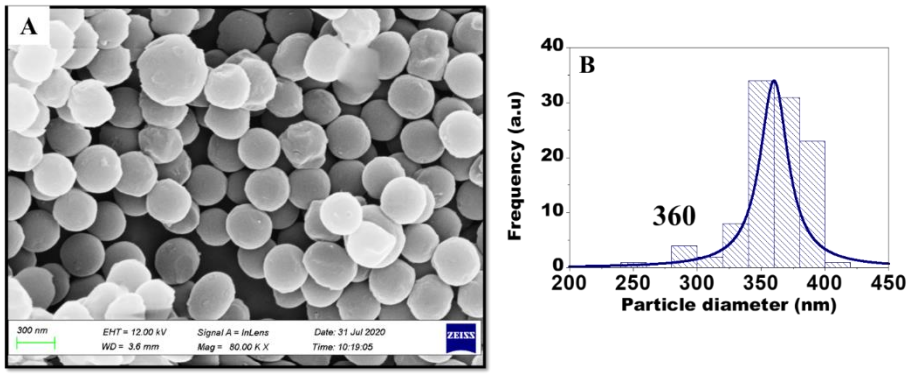

Figure S4.4: SEM image (A) and particle size distribution plot (B) PS-PECA spheres in ethanol

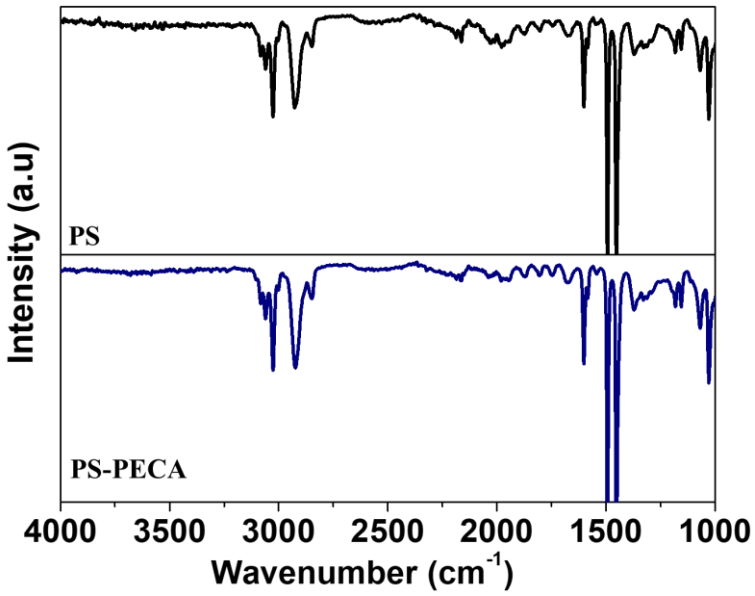

Figure S4.5: FTIR spectra of PS-PECA spheres prepared in ethanol

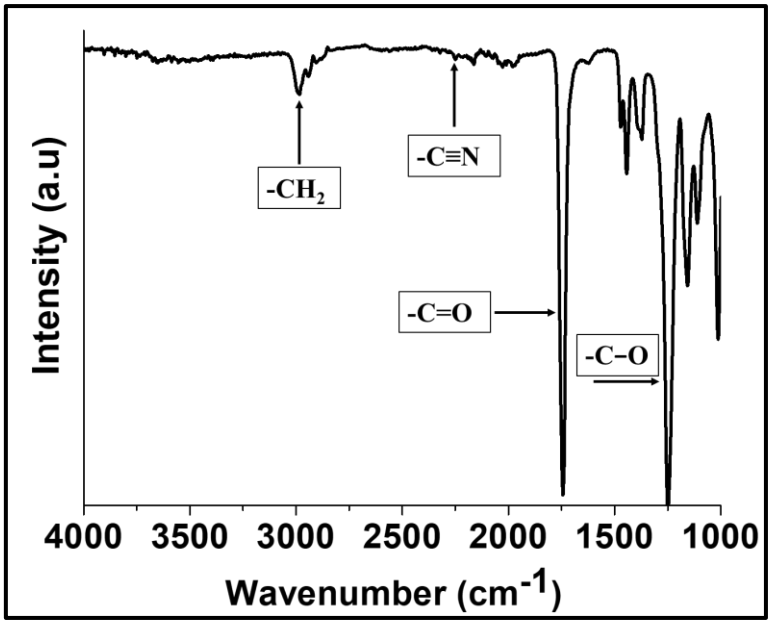

Figure S4.6: FTIR spectrum of poly(ethyl cyanoacrylate) (PECA)

Table S4.1: Carbon decomposition temperatures of the catalysts

Template	Carbon maximum decomposition temperature (T_{max}, °C)	
	T_1 (^{0}C)	T_2(^{0}C)
PS	365	440
PS-PAA	340	378
PS-PECA	298	372
PS-PEG	328	371

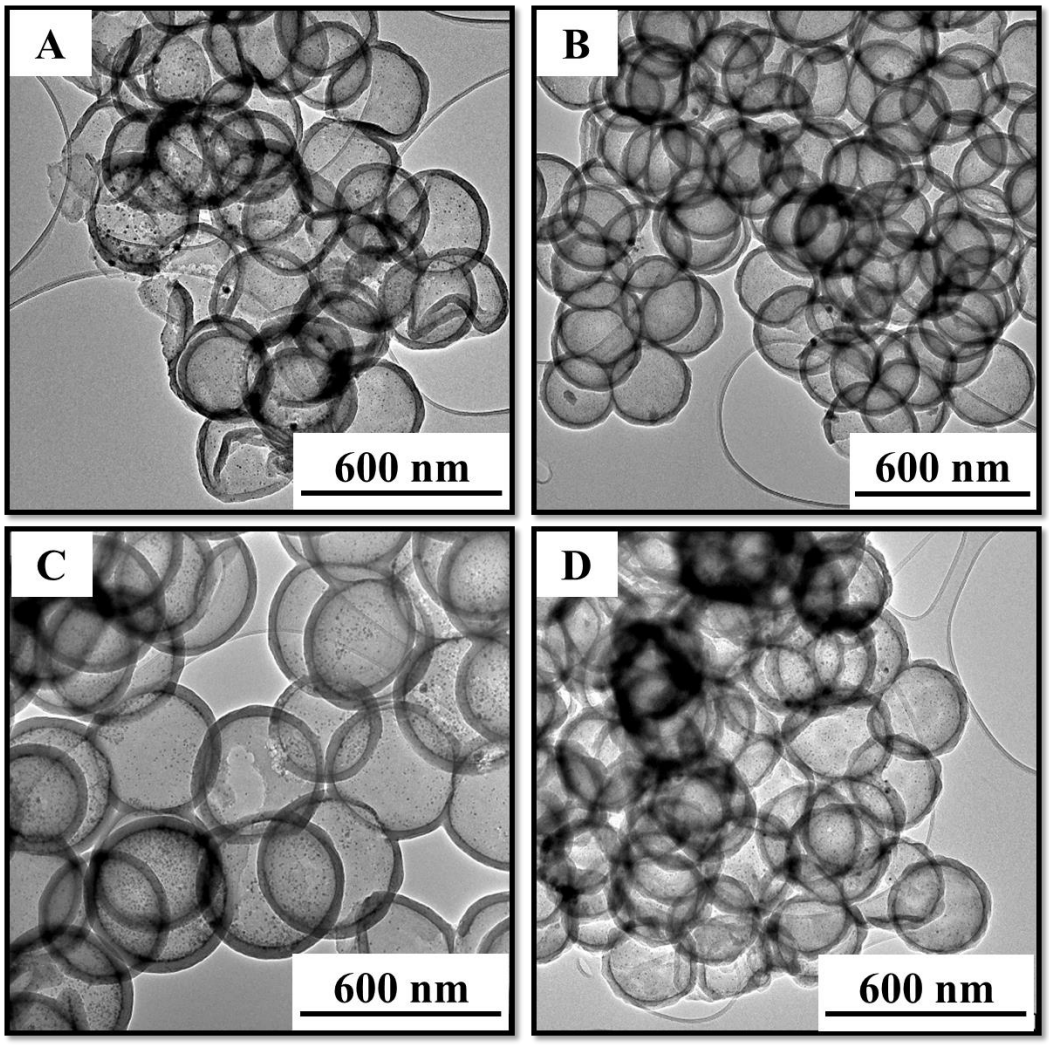

Figure S4.7: TEM micrographs of 5%Co@HCSs synthesized with (A) PS, (B) PS-PAA, (C) PS-PECA and (D) PS-PEG

Table S4.2: TPR peak positions

Template	TPR peak positions	
	T_1 (^{0}C)	T_2(^{0}C)
PS	255	433
PS-PAA	225	334
PS-PECA	259	416
PS-PEG	259	416

Table S4.3: PXRD peak positions of 5%Co@HCSs catalysts

Template	Peak position (°)	Comments	Assignment
PS	19.0	small	Co_3O_4
	31.2	small	Co_3O_4
	36.8	big, strongest	Co_3O_4
	42.4	medium	CoO
	44.9	small	Co_3O_4
	59.4	small	Co_3O_4
	61.5	small	CoO
	65.2	small	Co_3O_4
PS-PAA	41.8	small, shoulder peak	*hcp* Co
	44.3	medium, strongest	*fcc* Co

	47.3	small	*hcp* Co
PS-PECA	36.6	big, strongest	Co_3O_4
	42.5	big	CoO
	44.8	small, shoulder peak	Co_3O_4
PS-PEG	31.2	very small	Co_3O_4
	36.6	small	Co_3O_4
	44.2	big, strongest	*fcc* Co
	47.3	very small	*hcp* Co
	59.1	very small	Co_3O_4
	65.2	very small	Co_3O_4

References

[1] A. E. Ardis, "Preparation of monomeric alkyl alpha-cyano-acrylates". United States Patent 2,467,927, 19 April 1949.

[2] L. Z. Zhaparova, Y. M. Tazhbayev, M. Z. Burkeev, A. T. Kazhmuratova, T. S. Zhumagaliyeva, S. I. Ali and A. M. van Herk, "Synthesis and characterization of polyethyl cyanoacrylate nanoparticles loaded with capreomycin sulfate," Pharmaceutical Chemistry Journal, vol. 46, pp. 6-9, 2012.

Appendix C: The synthesis of poly(styrene-b-methyl methacrylate) copolymer spheres as templates for the synthesis of Co@HCSs

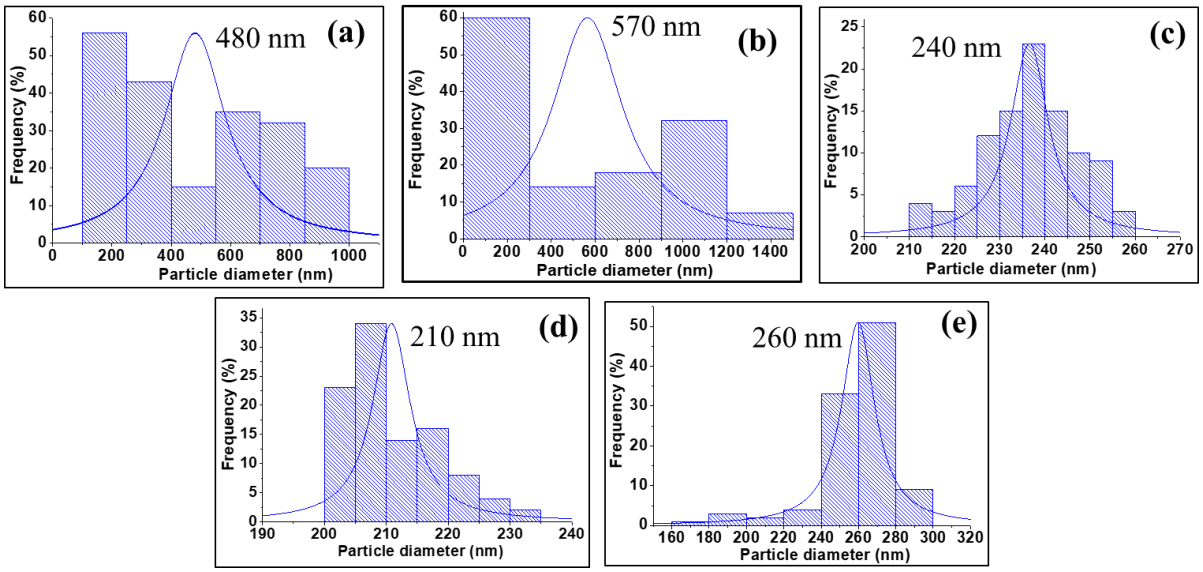

Figure S5.1: Particle size distribution curves of PS-b-PMAA spheres synthesized in varying amounts of distilled water: (a) 20%, (b) 80%, (c) 90%, (d) 97 % and (e) 100 %

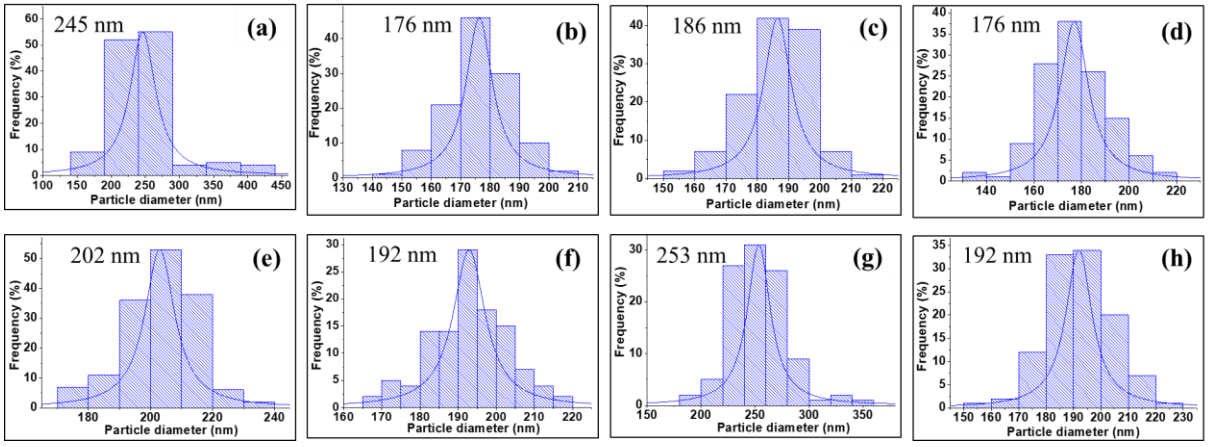

Figure S5.2: Particle size distribution curves of PS-b-PMAA spheres synthesized in varying MMA monomer composition: (a) 10%, (b) 20%, (c) 30%, (d) 40 %, (e) 60 % (f) 70 %, (g) 80 % and (h) 90 %

Appendix D: The oxidation of benzyl alcohol using cobalt oxide supported inside and outside hollow carbon spheres

S6.1 Synthesis of PSSs

For the synthesis of polystyrene spheres (PSSs), 100 mL distilled water, 25 mL ethanol and 0.1 g polyvinylpyrrolidone (PVP) were added into a 250 mL round-bottom flask. After all the PVP had dissolved, 8 mL of styrene was added, and the solution was stirred for 15 minutes using a magnetic stirrer. In a beaker, 0.15 g of potassium persulfate (KPS) was dissolved in 10 mL of distilled water and then added to the round bottom flask above, while stirring. The mixture was heated up to 80 °C and the reaction continued for 24 hours. The mixture was then filtered by centrifuge at 18000 rpm for 15 minutes at 10 °C and washed with ethanol. The product (PSSs) was dried in an oven at 60 ^{0}C for 12 hours, crushed with a mortar and pestle and then stored in a glass sample vial. For the synthesis of PS-*b*-PAA, the same procedure above was followed, however, acrylic acid (0.65 ml) was added to the styrene.

S6.2 Synthesis of Co/PSS

4 g of PSs was dispersed in a mixture of 36 mL ethanol and 100 mL distilled water, and the mixture was sonicated for 30 minutes or until the PSs were dispersed. Then 0.36 g of cobalt nitrate hexahydrate was added to the mixture while stirring, and the stirring continued until all the cobalt precursor was dissolved (mixture turned pink). Hydrazine hydrate (13 mL, 2 M) was added slowly (dropwise), while stirring, and the reaction continued for 12 hours at room temperature. The mixture was filtered by vacuum filtration and the product was washed with water, dried in the oven at 60 °C for 12 hours, crushed with a mortar and pestle and stored in a glass sample vial. Two and three times the amount of cobalt nitrate and hydrazine were added to make 10%Co@HCSs and 15%Co@HCSs respectively.

Co/PSs composite (3 g) was dispersed in a mixture of 150 mL ethanol, 76 distilled water and 12 mL ammonia solution. The mixture was sonicated for 30 minutes or until all the Co/PSSs particles were dispersed. In a beaker containing 76 mL ethanol; 1.1 g of resorcinol, 1.5 g of CTAB and 2.3 mL of formaldehyde were added and sonicated until all CTAB and resorcinol were dissolved. This mixture was added to the Co/polymer spheres mixture while stirring, and the reaction continued for 20 hours at room temperature. A brown layer of resorcinol-formaldehyde (RF) formed around the Co/PSs composite to form RF/PSSs/Co composite. The

product was filtered by vacuum filtration, washed with distilled water and ethanol, dried in the oven at 60 °C for 12 hours, crushed with a mortar and pestle and stored in a glass vial.

S6.3 Synthesis of Co@HCSs

RF/PSs/Co composite was loaded into a quartz boat, placed inside a quartz tube and then placed inside a horizontal furnace. The quartz tube was subject to a controlled flow of N_2 gas at 50 mL/min and the furnace was heated to 350 °C at 10°C/min and kept isothermal for 1 hour to decompose all the polymer spheres. It was further heated up to 600 °C at 10 °C and kept isothermal for 2 hours to pyrolyze and carbonize the RF and leave a shell of carbon that encapsulated the Co nanoparticles. The materials were characterized without any further modification or treatment.

Table S6.1: PXRD peak positions- 5% catalysts

Catalyst	2 Theta (degrees)	Comment	Assignment
5%Co@HCSs_PS	19.03	small	Co_3O_4
	31.28	small	Co_3O_4
	36.85	sharp (strongest)	Co_3O_4
	42.49	small	CoO
	44.89	very small	Co_3O_4
	59.42	very small	Co_3O_4
	61.59	very small	CoO
	65.23	very small	Co_3O_4
5%Co@HCSs_PS-*b*-PAA$_{12}$	36.52	small	CoO
	42.32	medium(strongest)	CoO
	61.35	small	CoO
5%Co/HCSs	19.1	small	Co_3O_4
	31.5	very small	Co_3O_4
	36.9	Strongest	Co_3O_4
	42.5	small	CoO
	65.7	very small	Co_3O_4

Table S6.2: PXRD peak positions- 10% catalysts

Catalyst	2 Theta (degrees)	Comment	Assignment
10%Co@HCSs_PS	36.68	small	CoO
	41.51	small	*hcp* Co
	44.25	sharp (strong)	*fcc* Co
	47.31	sharp (strong)	*hcp* Co
	51.38	very small	*fcc* Co
	62.37	small	*hcp* Co
	75.77	small	*fcc* Co
10%Co@HCSs_PS-*b*-PAA$_{12}$	36.55	small	CoO
	44.15	Sharp (strongest)	*fcc* Co
	50.56	very small	*fcc* Co
	61.49	small	CoO
	76.91	very small	CoO
10%Co/HCSs	19.1	medium	Co_3O_4
	31.2	medium	Co_3O_4
	36.9	sharp (strongest)	Co_3O_4
	44.8	medium	Co_3O_4
	59.5	medium	Co_3O_4
	65.1	medium	Co_3O_4

Table S6.3: PXRD peak positions- 15% catalysts

Catalyst	2 Theta (degrees)	Comment	Assignment
15%Co@HCSs_PS	36.59	small	CoO
	41.66	small	*hcp* Co
	42.53	small	CoO
	44.40	sharp (strongest)	*fcc* Co
	47.46	sharp	*hcp* Co
	51.48	small	*fcc* Co
	61.99	very small	CoO
	75.87	small	*hcp* Co
15%Co@HCSs_PS-*b*-PAA$_{12}$	36.63	small	Co_3O_4
	42.51	small	CoO
	44.40	sharp (strongest)	*fcc* Co
15%Co/HCSs	36.58	small	CoO
	44.0	sharp (strongest)	*fcc* Co

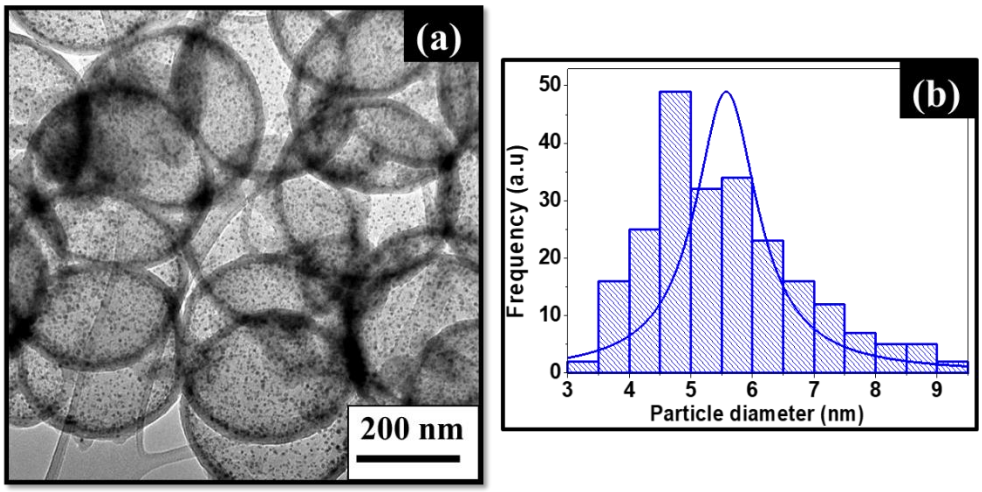

Figure S6.1: (a) TEM image and (b) particle size distribution of 15%Co@HCSs_PS-b-PAA_{12}

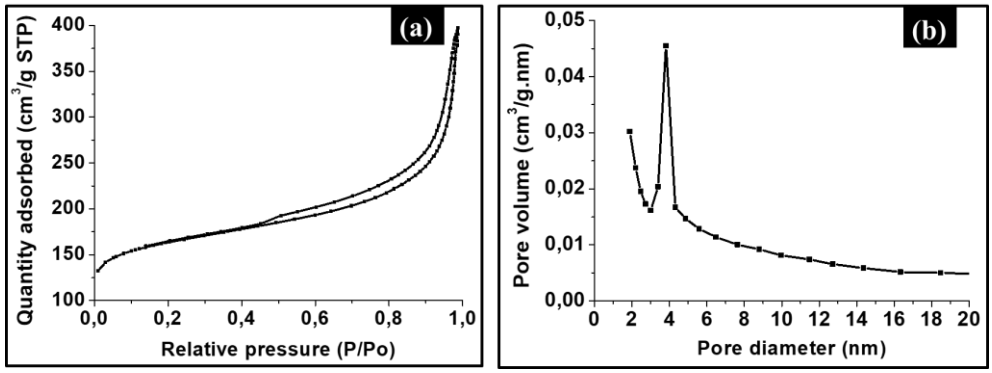

Figure S6.2: (a) BET isotherm and (b) pore size distribution of 15%Co@HCSs_PS-b-PAA_{12}

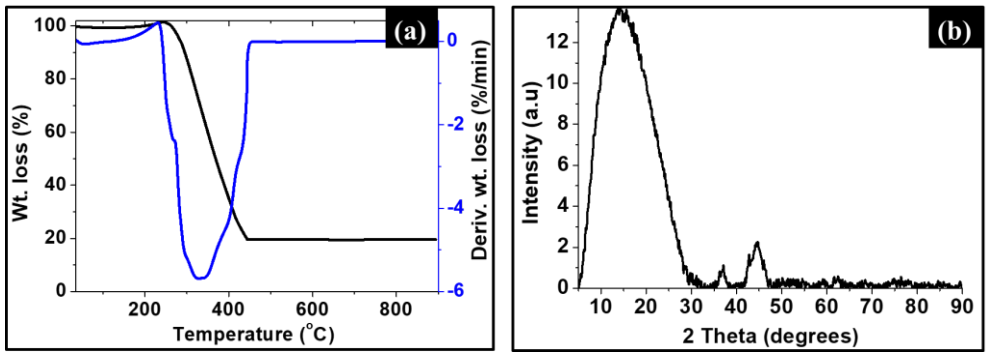

Figure S6.3: (a)TGA and derivative TGA and (b) PXRD of 15%Co@HCSs_PS-b-PAA_{12}

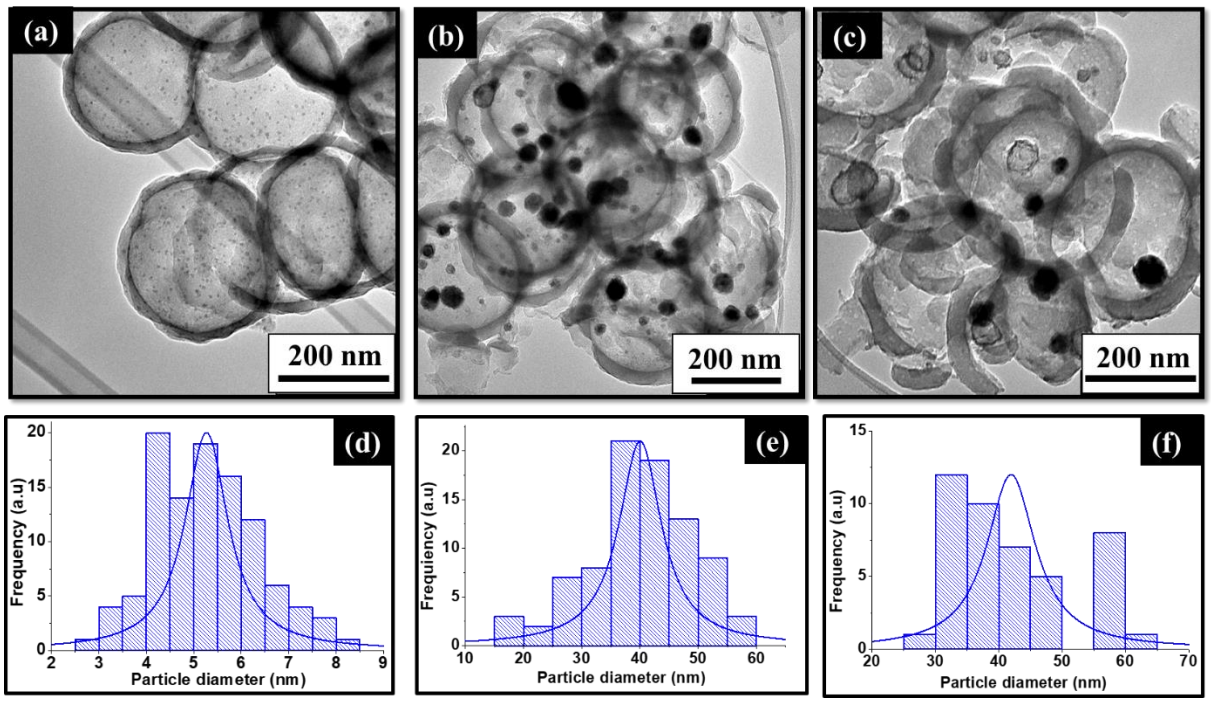

Figure S6.4: TEM images and particle size distribution of (a, d) 5%, (b, e) 10% and (c, f) 15%Co_xO_y@HCSs_PS after 24 h oxidation of benzyl alcohol

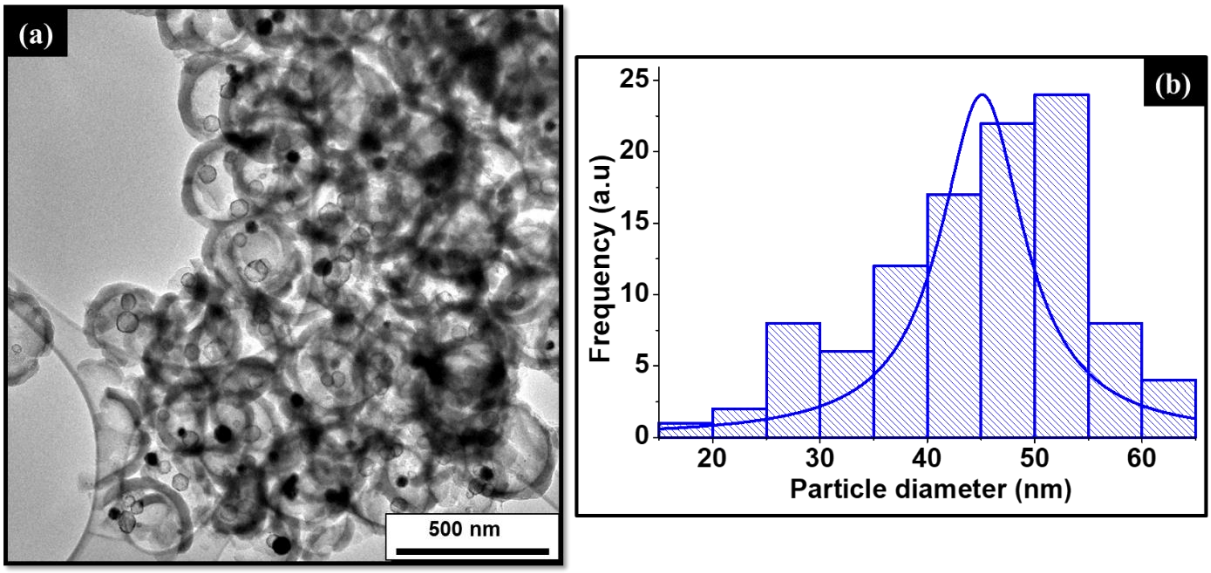

Figure S6.5: (a) TEM image and (b) particle size distribution of 15%CoxOy@HCSs_PS after 24 h oxidation of benzyl alcohol, showing the presence of small hollow nanoparticles and the particle size distribution of the small hollow particle

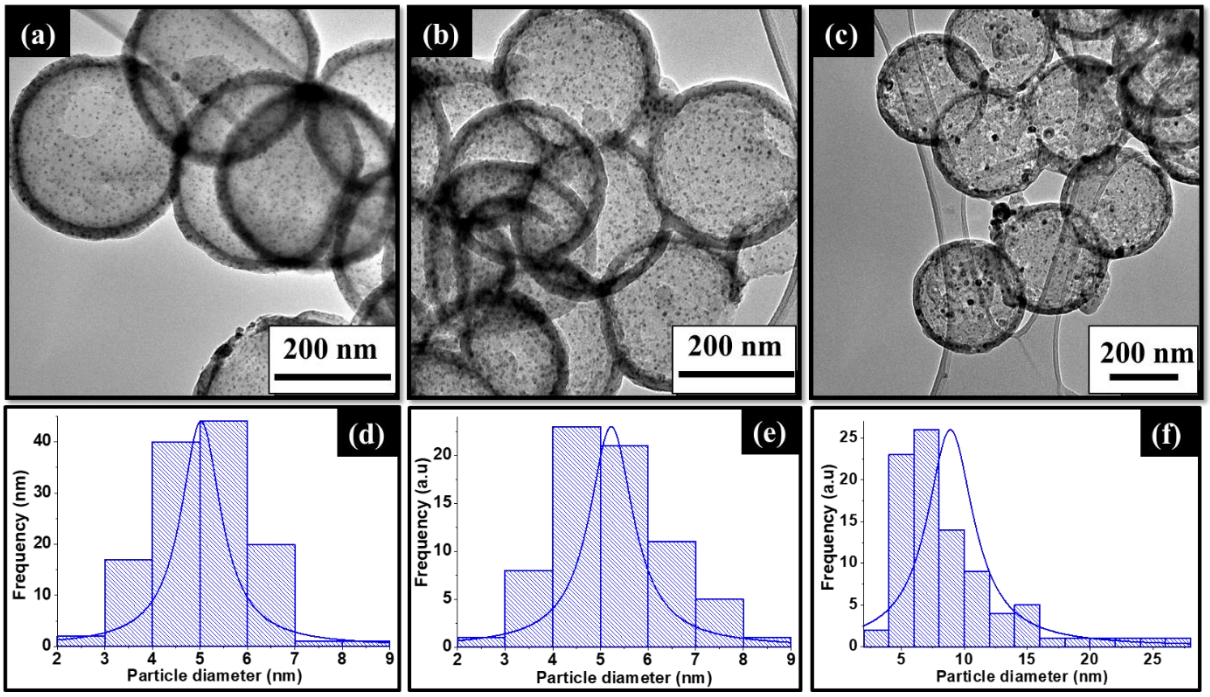

Figure S6.6: TEM images and particle size distributions of (a, d) 5%, (b, e) 10% and (c, f) 15%CoxOy@HCSs_PS-b-PAA_{12} after 24 h oxidation of benzyl alcohol

Table S6.4: Summary of Co particle size of the as-synthesized catalysts after 24 h of oxidation of benzyl alcohol

Catalyst	Average TEM Co diameter (nm) before oxidation reaction	Average TEM Co diameter (nm) after oxidation reaction
[a]**5%Co@HCSs_PS**	6.1	5.3
[a]**5%Co@HCSs_PS-*b*-PAA_{12}**	6.1	5.0
5%Co/HCSs	6.2	5.2*
[a]**10%Co@HCSs_PS**	38	40
[a]**10%Co@HCSs_PS-*b*-PAA_{12}**	6.0	5.2
10%Co/HCSs	5.2	5.2*
[a]**15%Co@HCSs_PS**	44	42 (45**)
[b]**15%Co@HCSs_PS-*b*-PAA_{12}**	5.6	8.9
15%Co/HCSs	5.4	-

*After 8 h of oxidation of benzyl alcohol

** Diameter of small hollow particles inside HCSs

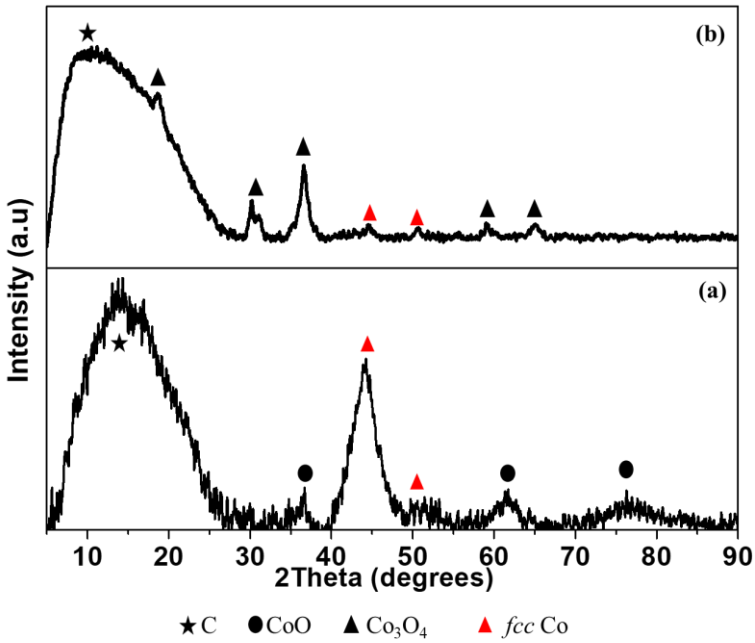

Figure S6.7: PXRD spectra of as-synthesized (a) and calcined (b) 10%Co@HCSs_PS-b-PAA_{12}

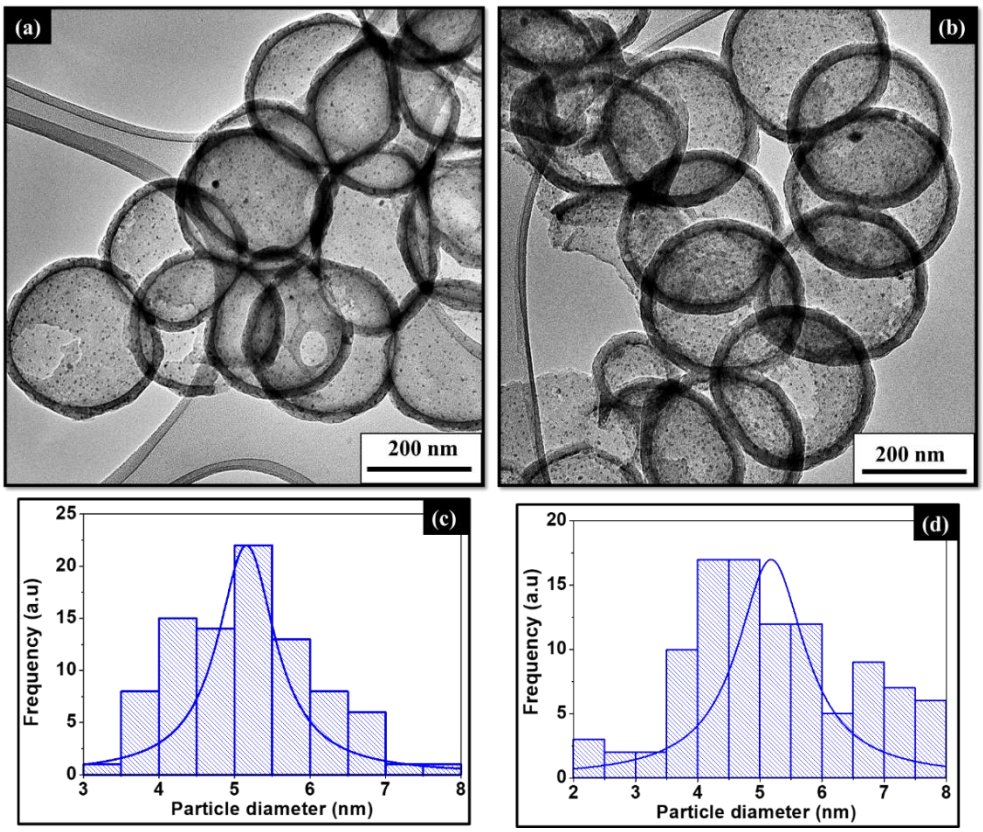

Figure S6.8: TEM images and particle size distribution of (a, c) 5%Co/HCSs and (b, d) 10%Co/HCSs after 8 h of oxidation of benzyl alcohol

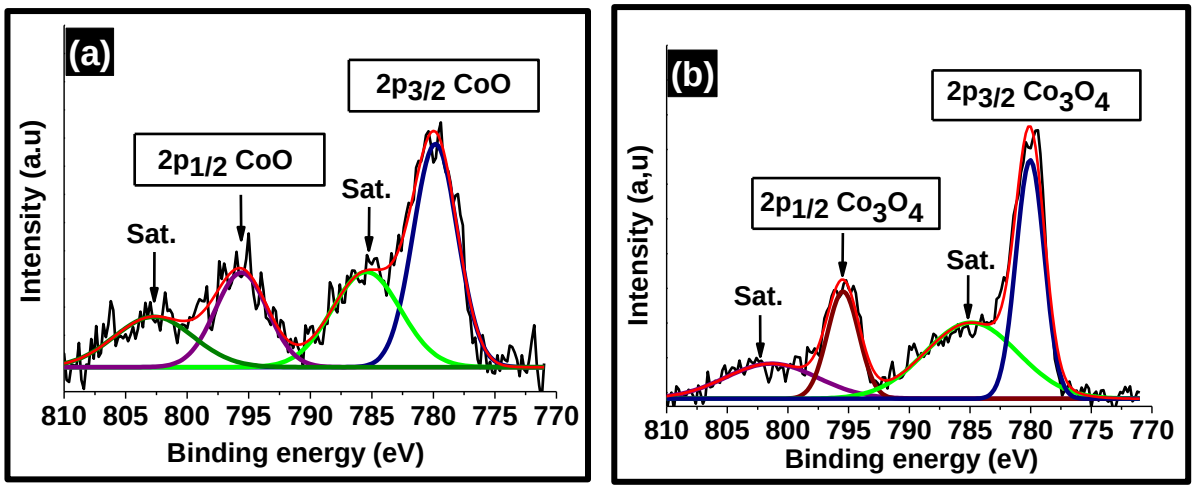

Figure S6.9: High resolution XPS spectra of Co 2P for samples (a) 15%Co/HCSs and (b) calcined 15%Co/HCSs

Table S6.5: XPS analysis data showing the $Co2p_{3/2}$ and $Co2p_{1/2}$ BE's for the catalysts

Sample	$Co2p_{3/2}$ BE (eV)				$Co2p_{1/2}$ BE (eV)			
	Co_3O_4	Sat.	CoO	Sat.	Co_3O_4	Sat.	CoO	Sat.
15%Co/ HCSs	-	-	780.0	785.4	-	-	795.6	802.7
C-15%Co/HCSs	778.0	785.0	-	-	795.3	801.6	-	-

Figures S6.10 reports the corresponding XPS spectra for the 15%Co/HCSs and calcined 15%Co/HCSs catalysts, showing the survey, and high resolution Os1, N1s and C1s spectra. The atomic percentages of the different elements are summarized in Tables S6.6 and S6.7. As expected, all catalysts contained high quantities of carbon.

Varying amounts of oxygen were observed, particularly, the calcinated catalyst contained relatively more oxygen than the other samples due to the introduction of oxygen during calcination. Furthermore, this catalyst contained twice the amount of oxygen bonded to a metal (3.0 %) than the uncalcined catalyst (1.6 %). This is an additional confirmation of metal oxidation by calcination.

An unexpected finding was the presence of nitrogen in all catalysts. The catalysts were not doped, however, the synthesis of the carbon source (resorcinol formaldehyde) occurs in the presence of a catalyst. In this case, ammonium hydroxide was used as a catalyst. A chemical

reaction is possible between ammonia and formaldehyde, as well as between ammonia and resorcinol [1]. This could be the source of the nitrogen in our catalysts. The amount of nitrogen seemed to be similar in all catalysts (1.5 -1.8 %).

The catalysts generally contained a mixture of sp^2 and sp^3 hybridized carbon, however, the sp^2 hybridized carbon was dominant due to the graphitic nature of the HCSs. The number of defect sites was relatively lower in the 15%Co/HCSs catalysts, characterized by the low quantity of sp^3 hybridized carbon (8.6 %). While the other catalysts contained approximately 14 % of sp^2 hybridized carbon. The actual % values of the sp^2 (and sp^3) carbons are affected by both the baseline and deconvolution parameters and may vary with the choices made; however, the sp^2/sp^3 ratio increased after Co calcination and this was still observed after varying these parameters. Calcination of the 15%Co/HCSs catalyst introduced structural defects in the carbon, increasing sp^3 hybridized carbon.

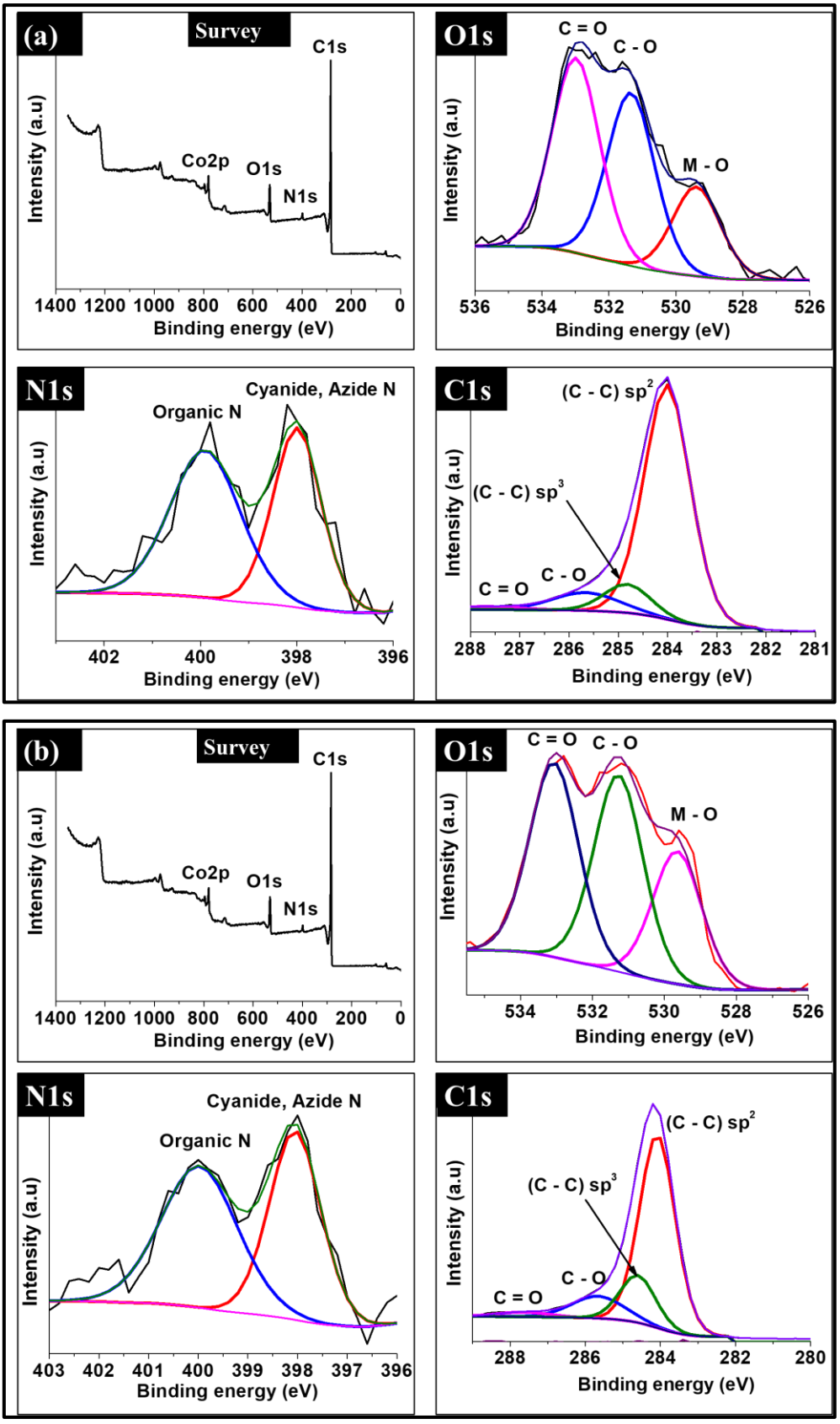

Figure S6.10: XPS spectra showing the survey, high resolution O1s, high resolution N1s and high resolution C1s for the catalysts (a) 15%Co/HCSs and (b) calcined 15%Co/HCSs

Table S6.6: Atomic percentages of the different configurations of O1s, N1s and C1s

Sample	O1s, at. %			N1s, at. %		C1s, at. %			
	[a]M-O	C-O	C=O	[b]Cyn.	[c]Org.	C-C, sp^2	C-C sp^3	C-O	C=O
15%Co/ HCSs	1.6	3.0	3.4	1.3	1.5	70.1	8.6	7.7	1.3
C-15%Co/HCSs	3.0	4.4	4.3	1.2	1.3	57.9	14.2	9.7	2.0

[a]Metal oxide ,[b]Cyanide and Azide N, [c]Organic N

Table S6.7: BE's and atomic percentages for O1s, N1s and C1s

	O1s		N1s		C1s	
	BE (eV)	At. %	BE (eV)	At. %	BE (eV)	At. %
15%Co/ HCSs	531.6	6.5	398.8	1.8	284.1	90.7
C-15%Co/HCSs	531.2	9.6	398.7	1.9	284.1	87.1

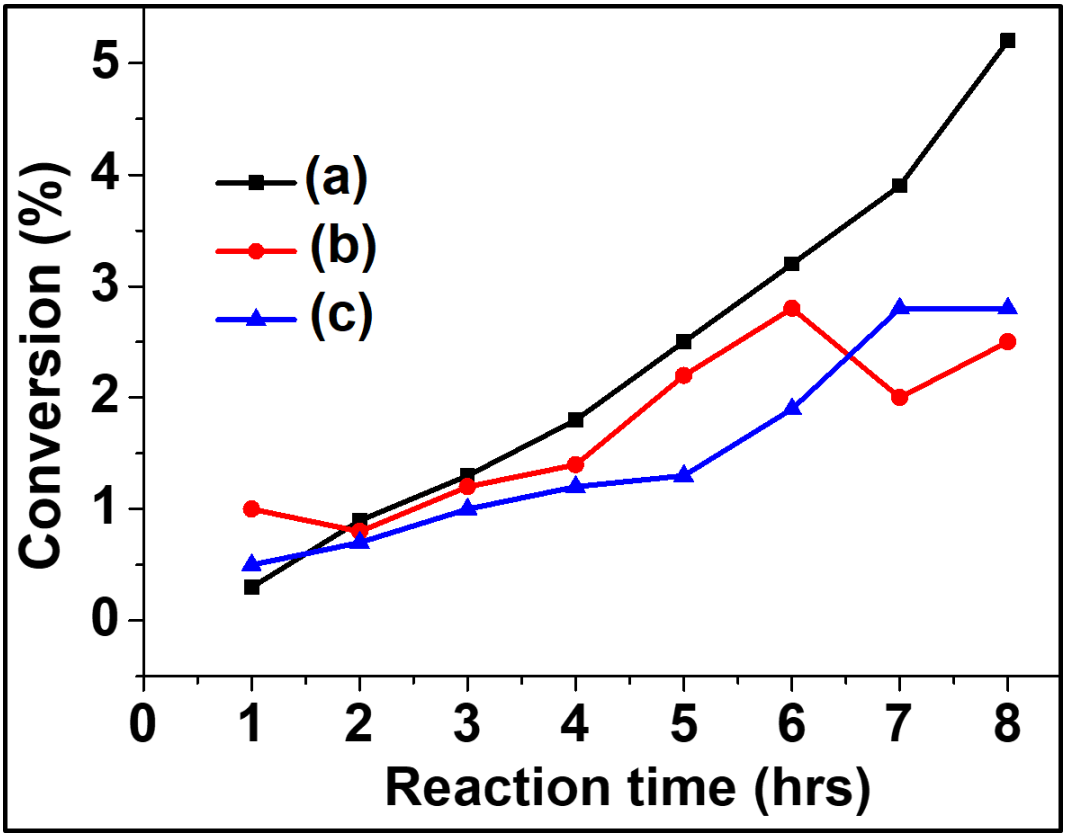

Figure S6.11: Conversion of benzyl alcohol during oxidation over as-synthesized Co@HCSs catalysts prepared with PS-b-PAA_{12} template: (a) 5%Co@HCSs, (b) 10%Co@HCSs and (c) 15%Co@HCSs

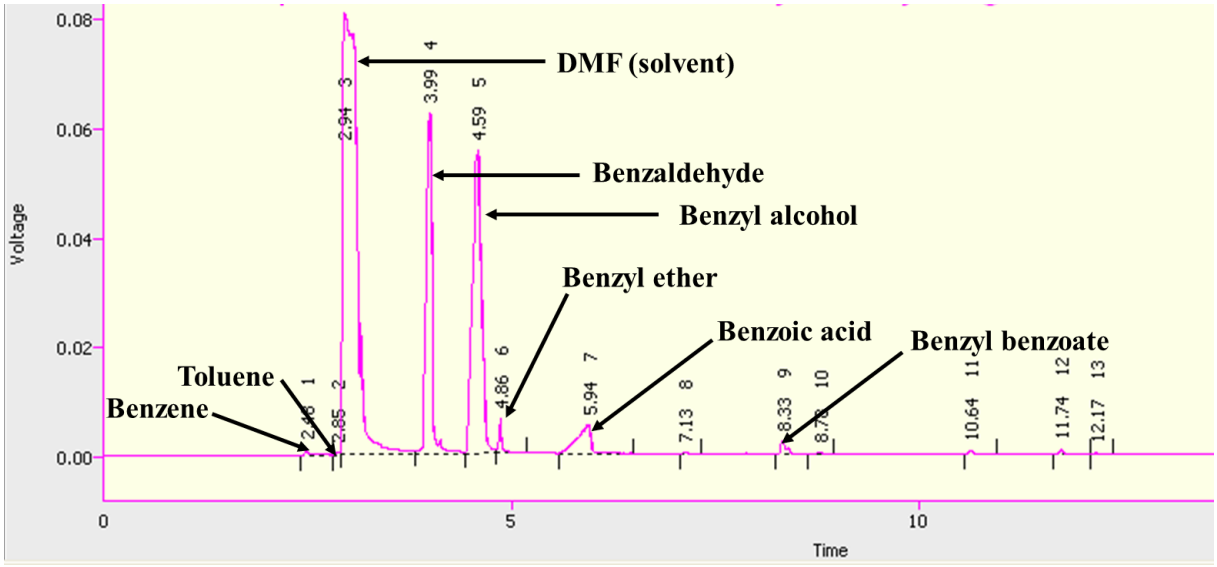

Figure S6.12: GC-FID spectrum of the benzyl alcohol oxidation reaction after 8 hours using calcined 5%Co@HCSs_PS-b-PAA_{12}

Table S6.8: Surface area data for the reacted catalysts after 5 and 4 cycles of oxidation of benzyl alcohol for the 5%Co/HCSs and 5%Co@HCSs, respectively

Sample	Used catalyst				Fresh catalyst		
	BET SA (m^2/g)	Micr. SA(m^2/g)	P.D (nm)	PV (cm^3/g)	BET SA (m^2/g)	P.D (nm)	PV (cm^3/g)
5%Co/HCSs	285	66	9.8	0.68	540	5.0	0.67
5%Co@HCSs	167	8.5	11.2	0.47	506	4.7	0.45

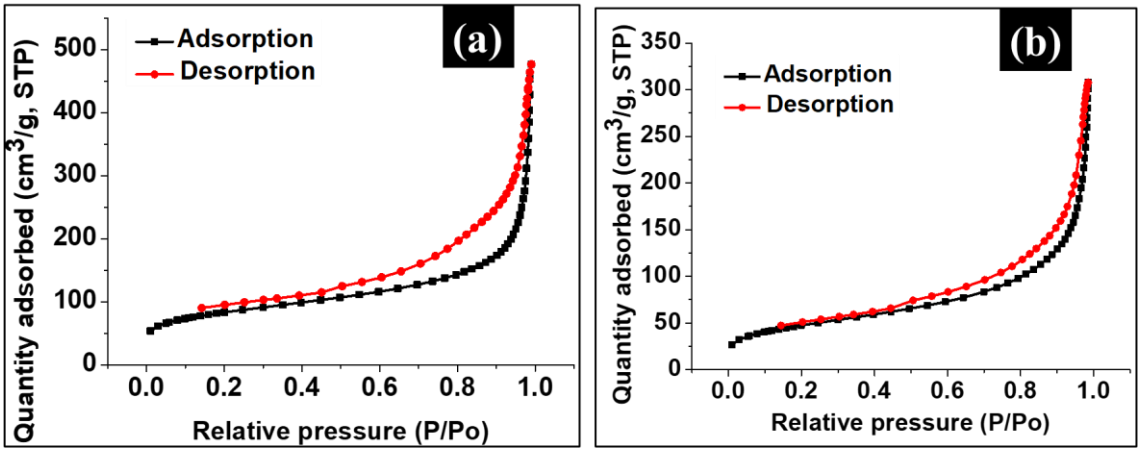

Figure S6.13: BET isotherms of the recycled catalysts (a) 5%Co/HCSs and (b) 5%Co@HCSs

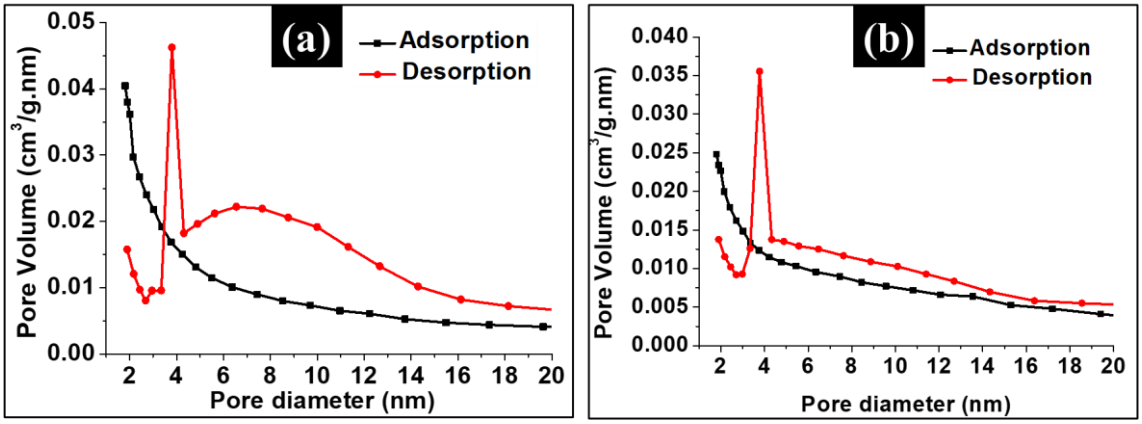

Figure S6.14: Pore size distribution curves of the recycled catalysts (a) 5%Co/HCSs and (b) 5%Co@HCSs

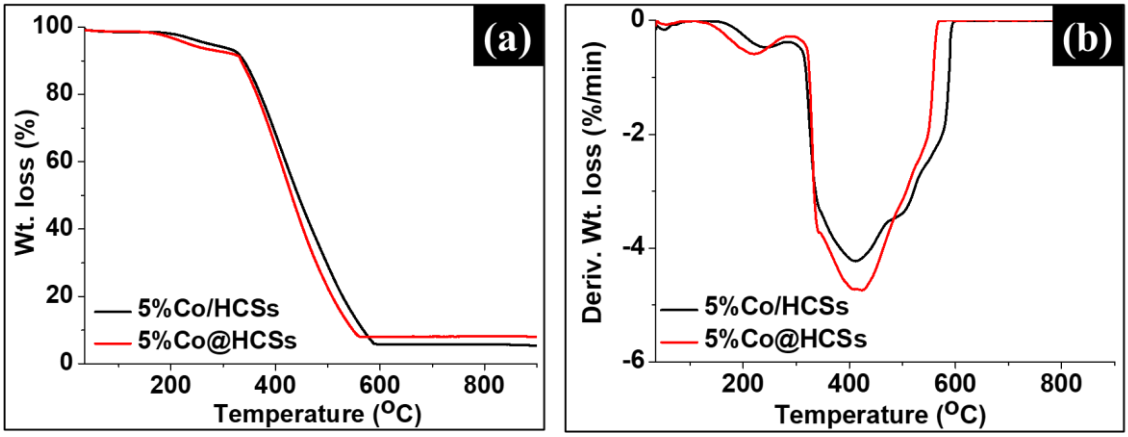

Figure S6.15: (a) TGA and (b) DTGA curves for the recycled catalysts 5%Co/HCSs and 5%Co@HCSs

Table S6.9: Data from literature studies

Ref	Catalyst/ support	Metal %/ mass (mg)	Particle diameter	Solvent/ Oxidant	Solv:Balc Vol	Time /Temp	Conv. of Balc (%)	Select. to BAld (%)
This work	Co/HCSs	5% / 50 mg	6 nm	DMF/O_2 (40 ml/min)	25: 2 ml	8 h/ 110°C	50	63
[2]	Co_3O_4	100 %/ 200 mg	10-30 µm	Toluene/ O_2 (60 ml/min)	10 ml: 2 mmol	3.5 h/ 90°C	100	8 at 100 % Conv 60 at 60% Conv

[3]	Co/Al_2O_4	500 mg	18-24 nm	Acetonitrile/ H_2O_2 (5mmol)	5 mmol: 5 mmol	8 h/ 80 °C	99	87
[4]	Co_3O_4/AC[a]	8.4-15.2 % / 100 mg	-	Toluene/ O_2 (50 ml/min)	20ml: 0.2 mmol	6 h/ 80 °C	66.2-100	> 99 [b]
[5]	Co_3O_4/ CMK-3	1.3-4.0 %/ 50 mg	2-5 nm	DMF/ O_2 (20 ml/min)	10 ml: 1 mmol	8 h/ 110 °C	67.7-83.5	97.7-96
[6]	Au/SiO_2 Au/Al_2O_3 Au/MgO $Au/MgAl_2O_4$ Au/HAP	1.8%/ 25mg - Au-SiO_2 3%/ 15mg - others	2.4 nm 1.7 nm 6.5 nm 2.7 nm 2.7 nm	Xylene/ O_2 (150 ml/min)	29.4 ml: 2.9 mmol	~3 h/ 60 °C	<1[c] / ~70[d] <7[c] / ~70[d] <5[c] / ~70 [d] <8[c] / ~70 [d] <3[c]/ ~70 [d]	>95/ 85[d] >95/ 75[d] >95/ 90[d] >95/ 83[d] >95/ 85[d]
[7]	PdCo/CM K-3	~2.9%/ 100mg	3.3 nm 4.2 nm 10.5 nm	Solvent-free/ O_2 (5 ml/min)	40 mmol	8 h/ 130 °C	55[e]/ 100[f] 50[e]/ 100[f] 20[f]	99 98 70

[a] 4 different types of commercial activated carbon. [b] Selectivity at 40% conversion. [c] without the addition of promoter. [d] K_2CO_3 was added to the reaction mixture as a promoter. [e] Catalyst tested as-synthesized [f] Catalyst tested after activation at 400 °C in H_2/Ar

References

[1] G. E. Van Gils, "Study of the reaction of resorcinol, formaldehyde and ammonia," Journal of Applied Polymer Science, vol. 13, pp. 835-849, 1969.

[2] M. Ilyas and M. Saeed, "Oxidation of benzyl alcohol in liquid phase catalyzed by cobalt oxide," International Journal of Chemical and Reactor Engineering, vol. 8, 2010.

[3] C. Rangupathi, J. J. Vijaya, S. Narayanan, S. K. Jesudoss and L. J. Kennedy, "Highly selective oxidation of alcohol to benzaldehyde with hydrogen peroxide by cobalt aluminate catalysis: A comparison of conventional and microwave methods," Ceramics International, vol. 41, pp. 2069-2080, 2015.

[4] M. Cordoba, C. Miranda, C. Lederhos, F. Coloma-Pascual, A. Ardila, G. A. Fuentes, Y. Pouilloux and A. Ramirez, "Catalytic performance of Co3O4 on different activated carbon supports in the benzyl alcohol oxidation," Catalysts, vol. 7, p. 384, 2017.

[5] X. Yang, S. Wu, L. Peng, J. Hu, X. Wang, X. Fu, Q. Huo and J. Guan, "Highly dispersed cobalt oxide nanoparticles on CMK-3 for selective oxidation of benzyl alcohol," RSC Advances, vol. 5, pp. 102508-102515, 2015.

[6] G. Nagy, A. Beck, G. Safran, Z. Schay, S. Liu, T. Li, B. Qiao, J. Wang and K. Lazar, "Nanodisperse gold catalysts in the oxidation of benzyl alcohol: comparison of various supports under different conditions," Reaction Kinetics, Mechanisms and Catalysis, vol. 128, pp. 71-95, 2019.

[7] V. Ravat, I. Nongwe and N. J. Coville, "N-doped ordered mesoporous carbon supported PdCo nanoparticles for the catalytic oxidation of benzyl alcohol," Microporous and Mesoporous Materials, vol. 225, pp. 224-231, 2016.

Appendix E: The vapour phase hydrogenation of cinnamaldehyde using cobalt supported inside and outside hollow carbon spheres

Table S7.1: Summary of catalyst properties

Catalyst	TEM Co diameter (nm)	PXRD Co diameter (nm)	% Co (TGA)	% Co_3O_4 (TGA)	BET SA (m^2/g)	Pore diameter (nm)	Pore volume (cm^3/g)
5%Co@HCSs_PS	6.1	12.7	4.6	6.3	612	4.8	0.57
5%Co@HCSs_PS-*b*-PAA_8	6.3	4.0	4.6	6.3	515	5.3	0.50
5%Co/HCSs	6.2	6.8	6.0	8.2	540	5.0	0.67
10%Co@HCSs_PS	38	18.1	12.1	17.0	316	7.0	0.47
10%Co@HCSs_PS-*b*-PAA_8	5.3	3.9	11.0	15.0	433	5.0	0.39
10%Co/HCSs	5.2	7.5	9.5	12.9	530	4.7	0.63
15%Co@HCSs_PS	44	18.7	16.4	22.5	388	5.1	0.41
15%Co@HCSs_PS-*b*-PAA_8	6.6	6.1	16.4	22.5	348	5.9	0.41
15%Co/HCSs	5.4	6.3	13.0	17.5	498	5.2	0.51

Table S7.2: Summary of TPR peak positions

Catalyst	Peak 1	Peak 2	Peak 3
	Residual salt	$Co^{3+} \rightarrow Co^{2+}$	$Co2+ \rightarrow Co^{o}$
5%Co@HCSs_PS	179	259	433
5%Co@HCSs_PS-*b*-PAA_8	218	298	454
5%Co/HCSs	175	254	410
10%Co@HCSs_PS	-	266	360
10%Co@HCSs_PS-*b*-PAA_8	176	266/351	413
10%Co/HCSs	191	278	428
15%Co@HCSs_PS	-	213	300/333
15%Co@HCSs_PS-*b*-PAA_8	205	254/321	424
15%Co/HCSs	183	256	409

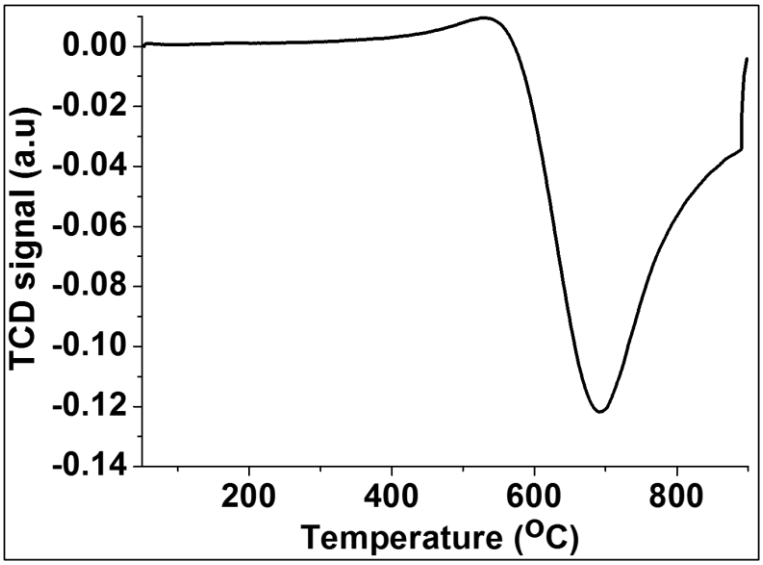

Figure S7.1: TPR profile of HCSs prepared with PS-b-PAA_8 template.

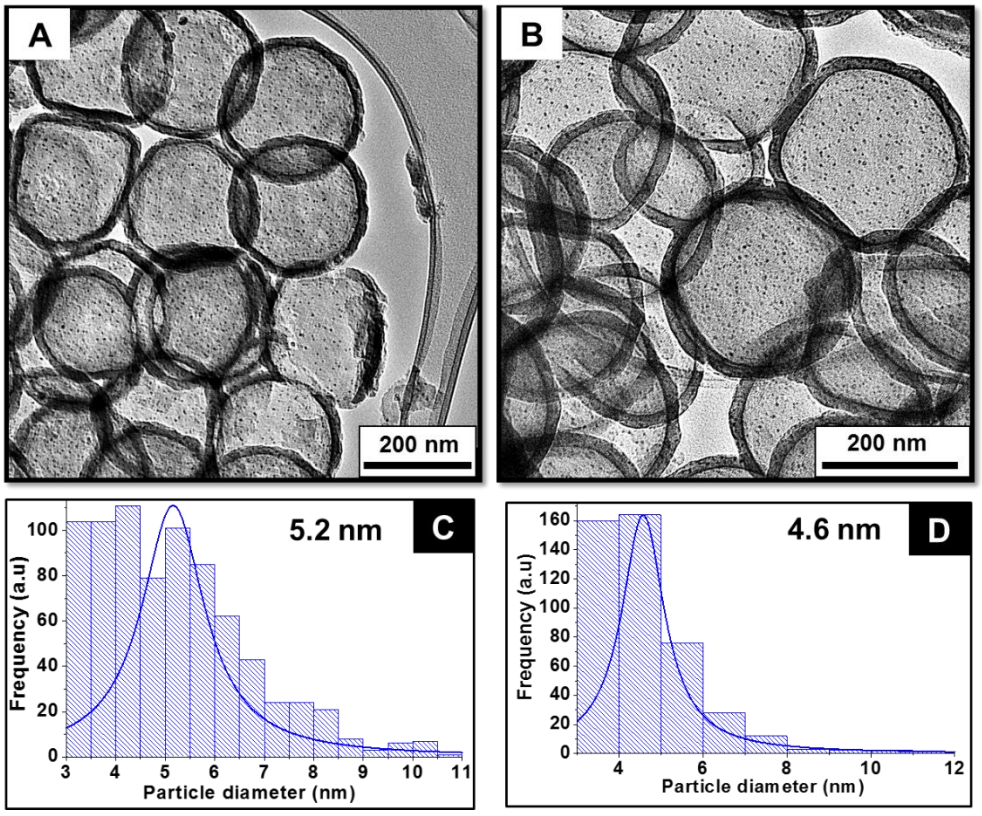

Figure S7.2: TEM images and particle size distribution curves of reacted catalysts after 5 h of hydrogenation of CALD, (A, C) 5%Co@HCSs_PS-b-PAA_8 and (B, D) 5%Co/HCSs.

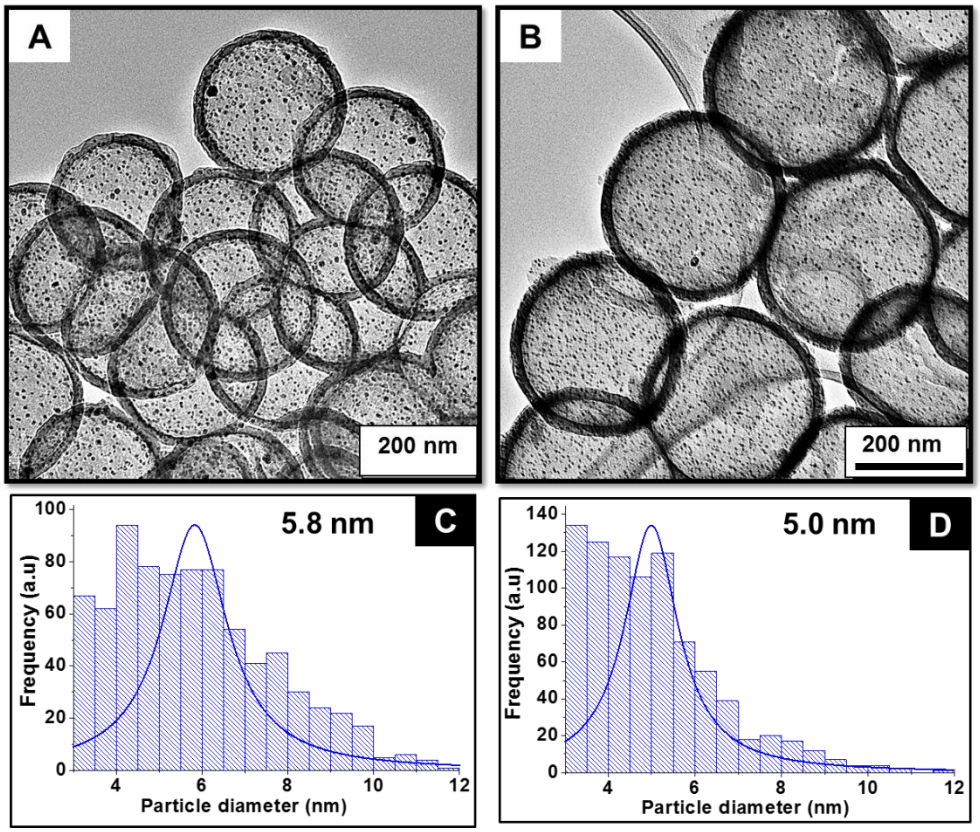

Figure S7.3: TEM images and particle size distribution curves of reacted catalysts after 5 h of hydrogenation of CALD, (A, C) 10%Co@HCSs_PS-b-PAA_8 and (B, D) 10%Co/HCSs.

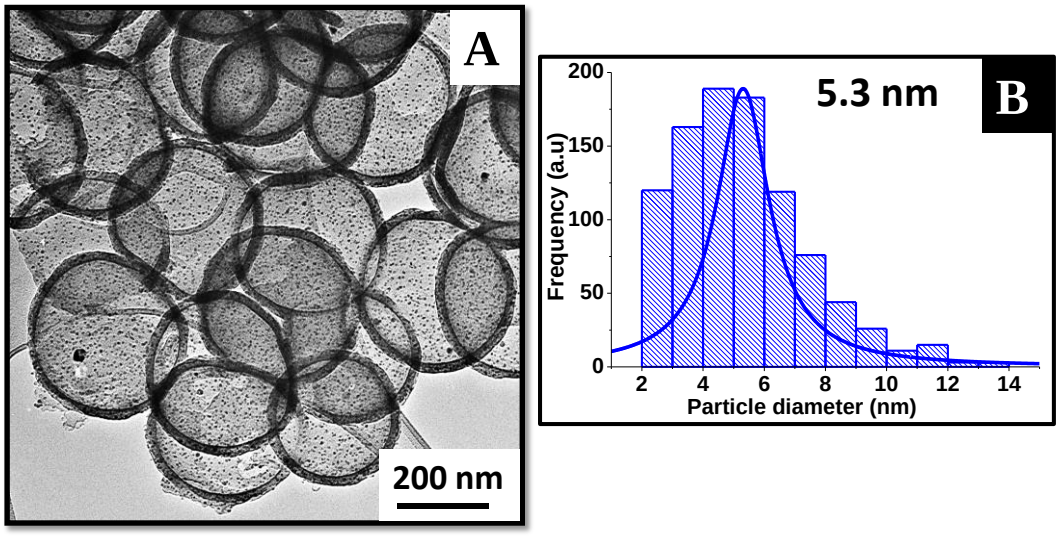

Figure S7.4: TEM image and particle size distribution of 5%Co/HCSs after 5 cycles of CALD hydrogenation.

Table S7.3: Surface area data for the reacted catalysts after 5 cycles of oxidation of hydrogenation of cinnamaldehyde

Sample	Used catalyst			Fresh catalyst		
	BET SA (m^2/g)	P.D (nm)	PV (cm^3/g)	BET SA (m^2/g)	P.D (nm)	PV (cm^3/g)
10%Co/HCSs	95	14.1	0.34	530	4.7	0.63
10%Co@HCSs	108	10.2	0.27	433	5.0	0.39

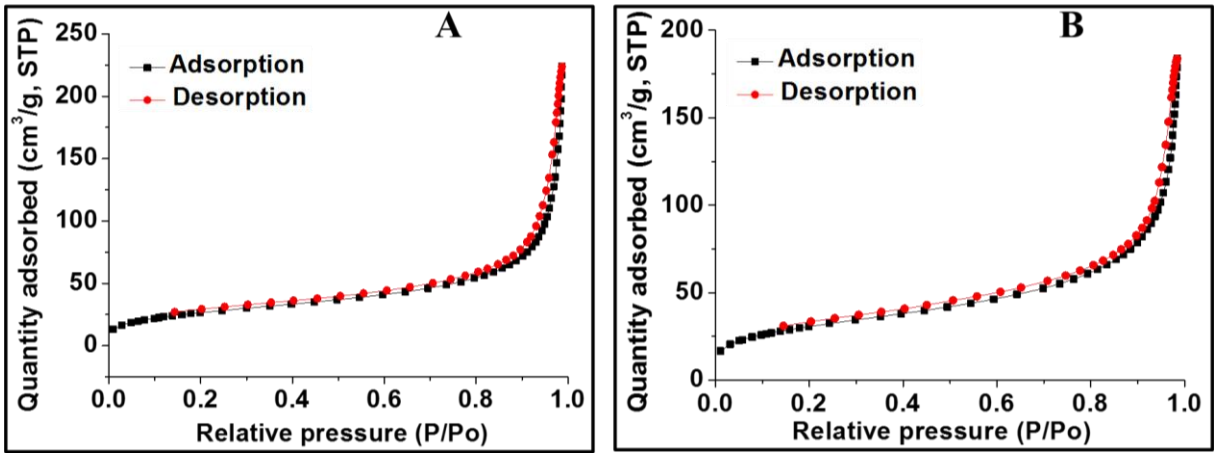

Figure S7.5: BET isotherms of the recycled catalysts (A) 10%Co/HCSs and (B) 10%Co@HCSs

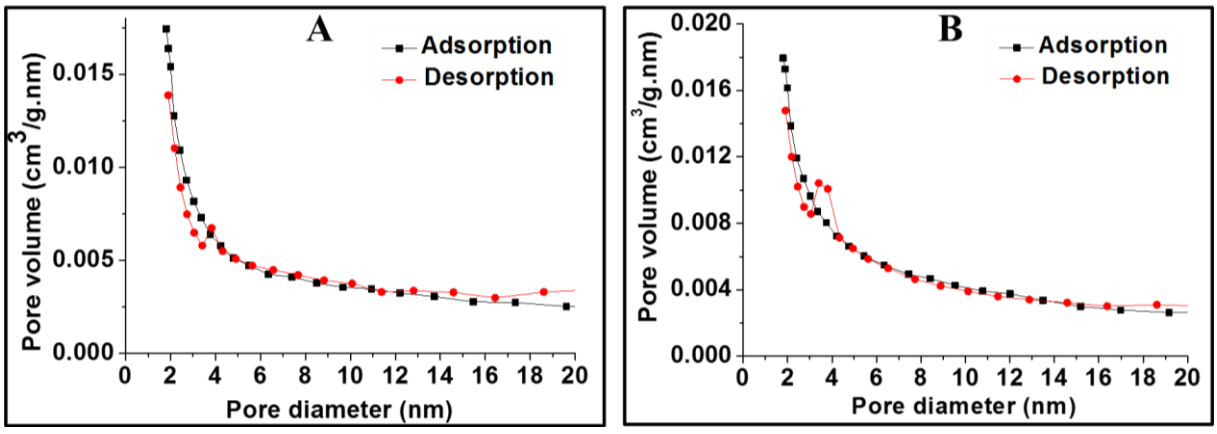

Figure S7.6: Pore size distribution curves of the recycled catalysts (A) 10%Co/HCSs and (B) 10%Co@HCSs